DOCTOR OF PHILOSOPHY

Numerical Modelling and Analysis of a New Rotor Cooling Technique for Axial Flux Permanent Magnet Machines

Fawzal, Ahmad Syahid

Award date:
2018

Awarding institution:
Coventry University

Numerical Modelling and Analysis of a New Rotor Cooling Technique for Axial Flux Permanent Magnet Machines

By

Ahmad Syahid Fawzal

PhD

October 2018

A thesis submitted in partial fulfilment of the University's requirements for the Degree of Doctor of Philosophy

Certificate of Ethical Approval

Applicant:

Ahmad Fawzal

Project Title:

Computational Modelling of Rotor Cooling Technique for Yokeless and Segmented Armature (YASA) Machine

This is to certify that the above named applicant has completed the Coventry University Ethical Approval process and their project has been confirmed and approved as Low Risk

Date of approval:

30 November 2015

Project Reference Number:

P39013

ABSTRACT

An efficient thermal management is essential for an electrical machine because it determines its durability and performance; particularly the continuous power output. Without good thermal management, the operational temperature will exceed the machine's temperature threshold limit, which may possibly lead to catastrophic failure.

YASA Motors Ltd. specialise in the design and development of high efficiency electric motors specifically aimed at the automotive industry. However, the current Yokeless and Segmented Armature (YASA) machine has limited performance due to the sealed or confined design that limits the heat transfer on the rotors and the permanent magnets. Therefore, this thesis presents a new cooling technique for the YASA machine but which can also be adapted to any Axial Flux Permanent Magnet (AFPM) design in order to maximise its continuous performance for automotive and motorsports applications.

The work begins with a detailed review on the issues of thermal challenges for electrical machines (i.e. efficiency, reliability and performance), the derivation of an AFPM machine and then the heat sources from which the electric machine losses are produced. Utilising the Computational Fluid Dynamics (CFD), the losses of a 50kW sealed YASA machine has been studied in order to understand the thermal characteristics and thermal distribution.

The novel secondary cooling strategy of the rotor has been implemented by attaching several fan designs on the rotor including other design iteration to assess its cooling performance. The idea is to allow the fan to drive the coolant (air) in the machine and become a heat exchanger at the same time. At this stage, only a single side of the rotor has studied under secondary cooling design, while the other side remained sealed. In order to aid the design assessment, a novel dimensionless number named Cooling Performance Index (CPI) has been proposed. The CPI number helps in

comparing the cooling performance, apart from the comparison in the flow and thermal characteristics of each design change.

The dual rotor cooling technique for the YASA machine is subsequently presented, where the backward curve fan has been selected as the best option based on its higher CPI number. The air outlet of the non-drive-end rotor that has an attached fan, was channelled to the drive-end to cool the other side of the rotor. The CFD analysis prove that the dual rotor cooling technique is able to maintain the rotors and magnets temperature with an increase up to 300% (150kW) continuous power compared to the 50kW on the existing sealed machine.

The work presented here is not limited to the YASA machine case; rather it can be extrapolated to any other disc-type AFPM machine.

SCIENTIFIC PUBLICATIONS

Several parts of the work carried out in this thesis have been published in a peer-reviewed international conference and 2 Q1 international scientific journals as listed below:

List of publications

- A. Fawzal, R. Cirstea, K. Gyftakis, T. Woolmer, M. Dickison and M. Blundell (2016) 'The Fan Design Impact on The Rotor Cooling of Axial Flux Permanent Magnet Machines'. *2016 XXII International Conference on Electrical Machines (ICEM)*, 2725-2731, Lausanne, Switzerland, Sept. 2016.
- A. Fawzal, R. Cirstea, K. Gyftakis, T. Woolmer, M. Dickison and M. Blundell (2017) 'Fan Performance Analysis for Rotor Cooling of Axial Flux Permanent Magnet Machines'. *IEEE Transactions on Industry Applications*, Vol. 53, no. 4, 3295-3304.
- A. Fawzal, R. Cirstea, T. Woolmer, M. Dickison, M. Blundell and K. Gyftakis (2018) 'Air Inlet/Outlet Arrangement for Rotor Cooling Application of Axial Flux PM Machines'. *Applied Thermal Engineering*, Vol. 130, 1520-1529.

Award

- Won 'The Best Poster – as voted by the symposium delegates' during *Faculty of Engineering, Environment and Computing Postgraduate Research Symposium, Coventry University* on 29th March 2017.

ACKNOWLEDGEMENTS

Verily in the creation of the heavens and the earth, and the alternation of night and day - there are indeed signs for men of understanding; Men who remember Allah, standing, sitting, and lying down on their sides, and contemplate the creation of the heavens and the earth (with the thought) "Our Lord! Not for nothing have You created (all) this. Glory to You! Give us salvation from the suffering of the Fire." - (Quran 3:190-191)

Praise be to Allah and His Messengers for the mercy and the strength through which I never dreamed that someone who used to have difficulties in his academic study and a miserable life could be at this level. My achievement today would not have materialised without all the great people that surround me. Therefore, I would like to express my gratitude to my supervisory team: Dr Kostas Gyftakis, for his valuable guidance in understanding electrical machines and friendly discussions; Mr Remus Cirstea for abundant help with flow physics and the software; Mr Mike Dickison and Professor Mike Blundell for constantly believing in me. Also, thanks to Dr Alex Pedcenko for kind responses to my query regarding high performance computing (HPC).

I would like to thank YASA Motors Ltd. for their generous funding, Dr Tim Woolmer, the founder, for his deep insight in helping me to understand the machine's challenges and for warm discussions about my life. Also, thanks go to Chris McCaw, David Mackenzie, Alexander Schnitzler and Tom Hillman for discussions regarding the design idea, limitations, the machine experimental and sensors calibration.

Special thanks go to my parents for their love and emotional support; my wife, Siew Yan for being supportive all the time; my children, Affan, Ansar and Asnaa for being understanding of being away from me and my ex-wife, Hasliza for patiently looking after them.

Finally, thanks go to all my colleagues and friends who shared the joys and tears together along the way.

TABLE OF CONTENTS

LIST OF FIGURES

LIST OF TABLES

NOMENCLATURE

Acronyms

1D	One-Dimensional
2D	Two-Dimensional
3D	Three-Dimensional
AFIR	Axial Flux Internal Rotor
AFIS	Axial Flux Internal Stator
AFPM	Axial Flux Permanent Magnet
BCs	Boundary Conditions
CFD	Computational Fluid Dynamics
CHT	Conjugate Heat Transfer
CO2	Carbon Dioxide
CPI	Cooling Performance Index
DSSR	Double Stator Single Rotor
EU	European Union
EV	Electric Vehicle
FE	Finite Element
FEA	Finite Element Analysis
HEV	Hybrid Electric Vehicle
HPC	High Performance Computing
IC code	Methods of cooling Code
LP	Lumped Parameter
MMF	Magnetic Motive Force
MRF	Moving Reference Frame
MSMR	Multi Stator Multi Rotor
NN	North-North
NOx	Nitrogen Oxide gasses
NS	North-South
OEM	Original Equipment Manufacturer
PM	Permanent Magnet
RANS	Reynolds-Averaged Navier-Stokes
RCPI	Rotor Cooling Performance Index
SIMPLE	Semi-Implicit Method for Pressure Linked Equations
SSDR	Single Stator Double Rotor
SSSR	Single Stator Single Rotor
SST	Shear-Stress Transport
TEFC	Totally Enclosed Fan Cooled
UK	United Kingdom
V&V	Verification and Validation
YASA	Yokeless and Segmented Armature

Latin Symbols

$\boldsymbol{A}$	Frontal area
$\boldsymbol{A_h}$	Heated area
$\boldsymbol{a}$	Length
$\boldsymbol{B}$	Magnetic flux density
$\boldsymbol{b}$	Width
$\boldsymbol{C_d}$	Drag coefficient
$\boldsymbol{C_f}$	Skin friction
$\boldsymbol{\overline{C_f}}$	Skin friction coefficient
$\boldsymbol{Cm_R}$	Moment coefficient of rotor
$\boldsymbol{C_p}$	Specific heat
$\boldsymbol{C_\mu}$	Coefficient of turbulent viscosity
$\boldsymbol{D_\omega}$	Cross-derivative
$\boldsymbol{d_h}$	Hydraulic diameter
$\boldsymbol{E}$	Total energy
$\boldsymbol{E_t}$	Turbulent wall function coefficient
$\boldsymbol{F_d}$	Drag force
$\boldsymbol{F_g}$	Geometrical factor
$\boldsymbol{f}$	Elliptic relaxation function
$\boldsymbol{f_c}$	Curvature correction factor
$\boldsymbol{f_r}$	Roughness function
$\boldsymbol{G}$	Gap ratio
$\boldsymbol{G_b}$	Generation of buoyancy production
$\boldsymbol{G_k}$	Generation of turbulence kinetic energy
$\boldsymbol{G_\omega}$	Generation of turbulence specific dissipation
$\boldsymbol{g}$	Total gap distance
$\mathbf{g}$	Gravitational vector
$\boldsymbol{g_n}$	Gravity
$\boldsymbol{H}$	Magnetic field strength
$\boldsymbol{H_t}$	Total enthalpy
$\boldsymbol{h}$	Enthalpy
$\boldsymbol{h_c}$	Convective heat transfer coefficient
$\boldsymbol{i}$	Electrical current
$\boldsymbol{k}$	Thermal conductivity
$\boldsymbol{k_e}$	Turbulent kinetic energy
$\boldsymbol{L}$	Characteristic length
$\boldsymbol{L_t}$	Turbulent length scale
$\boldsymbol{M}$	Molecular weight
$\boldsymbol{Ma}$	Mach number
$\boldsymbol{\dot{m}}$	Mass flow rate
$\boldsymbol{Nu}$	Nusselt number
$\boldsymbol{P}$	Machine power
$\boldsymbol{P_c}$	Magnet's permeance coefficient

P_{mech}	Mechanical power
Pr	Prandtl number
p_{abs}	Absolute pressure
p_{in}	Inlet pressure
p_{out}	Outlet pressure
p_{ref}	Reference pressure
p_{static}	Static pressure
∇p	Pressure gradient
q	Convective heat transfer or heat convection
$q"$	Heat flux
$q_s"$	Local surface heat flux
R	Specific gas constant
R_r	Rotor outer radius
R_t	Thermal resistance
R_u	Universal gas constant
Re	Reynolds number
Re_θ	Local Reynolds number
Re_ϕ	Rotational Reynolds number
r	Rotor radius
r_m	Mean annulus radius
$\mathbf{r}$	Position vector
S	Strain tensor
S_k	Source terms input by user
S_ϵ	Source terms input by user
T	Temperature
Ta	Taylor Number
T_{in}	Inlet temperature
T_{out}	Outlet temperature
T_{ref}	Characteristic or reference temperature
T_{rotor}	Rotor temperature
T_s	Surface temperature
T_{sensor}	Actual temperature data
T_t	Reynolds stress tensor
T_{ts}	Turbulent time scale
T_q	Torque
$T_{(r,z)}$	Actual local temperature
$T_{(r,z)max}$	Maximum local temperature
$\Delta T^*_{(r,z)}$	Non-dimensional temperature
∇T	Temperature gradient
t	Time
t_R	Rotor thickness
u	Fluid velocity
$\mathbf{u}_p$	Convection velocity

u^+	Non-dimensional velocity
u^*	Friction velocity near to the wall
$\overline{u}$	Mean velocity
V	Velocity
V_{output}	Voltage output
$\overline{v^2}$	Normal stress function or velocity scale
W	Losses
$\mathbf{W}$	Rotation rate tensor
w	Specific work
y	Distance to the nearest wall or of first cell thickness
y^+	Non-dimensional wall distance
z	z direction position
z^*	Local z direction positioning

Greek Symbols

α	Thermal diffusivity
β	Coefficient of thermal expansion
γ_{eff}	Effective intermittency
ϵ	Turbulent dissipation rate
ϵ_0	Ambient turbulence
λ	Second viscosity coefficient
μ	Dynamic viscosity
μ_t	Turbulent viscosity
ν	Kinematic viscosity
ρ	Density
σ_t	Turbulent Prandtl number
τ_w	Wall shear stress
$\boldsymbol{\phi}$	Viscous dissipation
Ω_{cr}	Critical angular velocity
ω	Rotational speed or angular velocity
ω_p	Angular velocity of MRF

Chapter 1

Introduction

1.0 Introduction

This thesis introduces a novel cooling strategy for Axial Flux Permanent Magnet (AFPM) in particular the Yokeless And Segmented Armature (YASA) machine. As other type or topology of electric machine, YASA machine also faces with its own thermal challenges that limit its efficiency, reliability and performance. Current YASA machine design has served well in automotive industry with its primary stator cooling, yet its full potential on continuous performance still limited. Therefore, this thesis proposed a novel concept of cooling as a secondary cooling method by rotor cooling technique to unlock the full potential of the machine without any modification on its electromagnetic component.

1.1 Electrical Machines and their Thermal Challenges

Over the last decades, fossil fuels have been the main resource for global energy supplies and 60% of the world's energy consumption is from fossil fuel production. However, the toxic chemical substances from the combustion or burning of fossil fuels lead to environmental degradation. With population and economic growth, the scale of the current environmental damage is at an alarming rate (Omer 2008).

Due to this consideration of the environmental impact, the development of sustainable energy resources such as wind, tidal and hydroelectric power

generation has become a vital part of government policy. An increasing number of countries and governments try to tighten the rules and regulations in the allowable amount of toxic emissions produced when fossil fuels are consumed. For the automotive industry, this has put great pressure on car manufacturers, especially with the recent United Kingdom (UK) investigation report that road traffic contributes about 60% of the country's Nitrogen Oxide gasses, NOx (Figure 1-1).

In McKinsey and Company's reports (2014), it is stated that car OEMs have to cut down approximately 30% of their Carbon Dioxide (CO2) emissions in order to meet the European Union's (EU) emission target by 2020 (Figure 1-2). The European Commission has set a strategy to reduce transportation emissions through low-emission mobility by increasing engine efficiency and venturing in alternative energy for transportation, leading towards zero-emission vehicles (European Commission 2016). Therefore, major automotive manufacturers have started to improve the powertrain of their new products towards electrification, as the solution for minimising the impact on the environment and reducing emissions.

Figure 1-1: Percentage of NOx in the UK (Department for the Environment, Food and Rural Affairs and the Department for Transport 2017).

Figure 1-2: Targeted CO2 emissions reduction of main OEMs by 2020 (McKinsey and Company 2014).

In recent years, electrified vehicles have become the new trend in the automotive sector, shifting away from the traditional powertrain and internal combustion engine market. The number of electric vehicles (EV) and hybrid electric vehicles (HEV) grows significantly because of changes in government policies and the increase in consumer demand. In addition, the availability and increasing number of charging infrastructures in urban areas play a significant role in this market penetration. To meet the high demand of the market, most of original equipment manufacturers (OEM) invest heavily in research and development in the areas of electric motors, power electronics and energy storage. Some of the concerns in these major changes are to improve the performance of electric motors, produce suitable power electronics systems and invent an expansion of energy storage capacity to make electric vehicles more reliable and suitable for this transformation of the automotive world.

Since Davenport patented the first radial flux electric machine in 1837, numerous research works and the advancement in knowledge of electric machines have quickly pushed this technology to its maturity level (Gieras et al. 2008). An electric machine has an advantage when it is adopted as a

vehicle powertrain, as it acts as a motor when it converts electrical energy into mechanical energy and switches its role to a generator during deceleration or braking, by converting the mechanical motion back into electrical energy for energy recovery. Nowadays, several types of electric machines are employed in EV/HEV which include the induction machine, the switched reluctance and the permanent magnet machine (Neudorfer et al. 2017; Dorrell et al. 2014). The selection of an electric machine type depends on the requirements, cost and performance of the intended application (Benlamine et al. 2014; Sarlioglu et al. 2015). Regardless of the type of machine configuration, the most important constraint for an electric machine is the over temperature operational. According to Wildi (2006), operating an electrical machine at 10°C above its allowable operating temperature may reduce its machine life by half.

This general constraint becomes a major challenge in vehicle applications where the machine is placed inside a confined space under the vehicle hood, which has low air circulation. This confined space will possibly accumulate the heat from other systems such as the internal combustion engine, heat exchanger and control system that could quickly raise the temperature of the electric machine (Gregorcic et al. 2017). The combination of external heat sources and the machine's internal heat generation may lead to machine overheat and fatigue failure. Specifically, the machine's temperature has a great impact on its efficiency, reliability and performance. Therefore, an effective cooling system for an electric machine is essential to ensure its continuous operation within its design intentions for automotive traction applications (Herbst et al. 2009).

1.1.1 Machine Efficiency Issues

Electric machine efficiency is defined as the ratio between the output power and the input power. When a machine operates as a motor, its efficiency is measured by the ratio of mechanical output over its input electrical power.

Either maximising the mechanical power output or minimising the electrical power input enables the improvement of the electric motor's efficiency.

The mechanical power P_{mech} of an electrical machine is derived by the torque T_q times the angular rotational speed ω, in rad/s (Eq. 1-1).

$$P_{mech} = T_q \omega \quad \textbf{(Eq. 1-1)}$$

The amount of torque that a machine can deliver relies on the produced magnetic flux density. In most electric machines, the magnetic field is formed by the use of current-carrying windings. Therefore, it is a common practice in electric machine design to increase the total magnetic field using a greater number of turns and a higher current value when trying to increase the magnetic flux density (Hughes 2006).

However, the increase in the number of turns and the flow of current eventually increase electrical losses and lead to high winding temperatures. Copper losses in the winding are the main contributor to machine losses for most electric motors and their electrical resistivity increases as the temperature is raised (Tong 2014). This means that the proposed flux improvement method with a higher number of turns and a higher current can only be achieved simultaneously with good thermal management and an effective cooling strategy in order to maintain or increase the machine's efficiency.

1.1.2 Reliability Issues

Machine reliability is closely related to the insulation material's lifetime and the machine's operating conditions. The term insulation includes the impregnation, the slot liner, the bobbin, the lamination coating layers and the most critical component: the coating layer of the conductor. Any damage to the coated layer will reduce the inter-turn resistivity and the occurrence of current leakage will be highly possible.

The purpose of the insulation layer on the conductor is to allow the conductor to be wound turn by turn, without causing electrical short circuits. The insulation layer, sometimes called the enamel, is classified based on its insulation grade, operating temperature range and dielectric breakdown voltage. The insulation layer material is usually polymer-based, which is a dielectric and low thermal conductivity material. The material properties such as the dielectric and mechanical strength of this type of material are time and temperature dependant. The material degrades with time and loses its insulation capability when the temperature is above the permissible range, in which the deterioration is related to time and temperature (Fitzgerald et al. 2003).

The combination of other factors such as vibration and electrical stress may accelerate the deterioration and shorten the lifetime of the insulation (Sumislawska et al. 2016; Gyftakis et al. 2016; Mayoux 2000). The slow orientation and the structure will change after several thermal cycles and repetitive temperature variations will reduce the mechanical strength of the material. Subsequently, this insulation layer becomes brittle. Voids and micro-cracks can then form in the insulation causing machine failure before the end of its expected lifetime, thus reducing its reliability. In order to avoid overheating, either the amount of power drawn from a machine has to be limited, or a better cooling mechanism has to be added to manage the operating temperature.

1.1.3 Performance Issues (Permanent Magnet Demagnetisation)

Apart from machine efficiency and reliability, performance is another issue related to the operating temperature of the permanent magnet (PM) machine. Operating with an excessive temperature will lead to PM demagnetisation. The demagnetisation is due to a high temperature weakening the magnetic strength of the machine (Zhang et al. 2012), thus reducing its performance. To have an in-depth understanding of demagnetisation, it is necessary to first look at the hysteresis loop of the PM material. The hysteresis loop represents

the magnetic flux in the magnet during magnetising and demagnetising. There are four quadrants: firstly, magnetisation until the saturation of the magnet, secondly, demagnetisation in a reversed direction magnetic field in the second quadrant, thirdly magnetisation to saturation in the opposite direction followed fourthly by demagnetisation. The second quadrant is also called the demagnetisation curve.

Nowadays, Neodymium Iron Boron (NdFeB) is the most common magnetic material in PM machines. Figure 1-3 shows its B-H curve illustrating the relationship between the magnetic flux density B and the magnetic field strength H for the NdFeB material. The temperature increase produced by the machine's losses may provide a sufficient energy supply to cause magnetic dipole moment misalignment. Consequently, this reduces the resistance to demagnetisation and the coercive force drops significantly as the temperature increases.

Figure 1-3: Demagnetisation curve of NdFeB at different magnet temperatures (Gieras et al. 2008).

This demagnetisation could be reversible or irreversible, depending on the temperature that the magnet has experienced. If the magnet's temperature is below the maximum operating point, then the demagnetisation is reversible and the magnetic strength could be recovered to its original state once the

magnet is brought back to room temperature. However, if the magnet is operating above the designed maximum limit, then it will start losing some spontaneous magnetisation until it reaches its Curie temperature where all its magnetisation is lost. For irreversible demagnetisation, the amount of losses in the magnet will shift the operating point below the initial curve after it returns to room temperature. This means the magnet has become weaker and consequently the machine's performance will be reduced. Demagnetisation under a fixed load will cause a high current, thus accelerating the demagnetisation.

1.2 The Axial Flux Permanent Magnet (AFPM) Machine

The permanent magnet (PM) machine is a popular machine type for automotive traction applications due to its high power density. For the Axial Flux Permanent Magnet (AFPM), the term 'axial' refers to the direction of the magnetic field across the air gap. Compared to its sibling, the Radial Flux PM machine, the AFPM machine is less likely to be used in the automotive industry due to manufacturing difficulties and high production costs. However, the advantages of the Axial Flux Permanent Magnet machine are its compact configuration, packaging size and its high power and torque delivery, so the development of this machine has been accelerated for automotive applications.

There are several AFPM machine topologies regarding the machine design configuration, as shown in Figure 1-4. The machine topology determines the performance of the motor and there are advantages and disadvantages for each topology.

Figure 1-4: Different types of AFPM machine (Kahourzade et al. 2014).

As an example, the topology of the Double Stator Single Rotor (DSSR) (Figure 1-5c) has an axial force that is more balanced compared to the Single Stator Single Rotor (SSSR) machine (Figure 1-5a). The SSSR machine consists of a single stator and rotor. This topology may produce a strong magnetic force that causes an unbalanced axial force leading to the distortion of the machine structure. To overcome this problem, Chan (1987) recommended a sandwich structure such as the DSSR or Single Stator Double Rotor (SSDR), where the rotor disc is placed between two stators (Figure 1-5c) or the stator is placed between two rotors (Figure 1-5b). Additionally, Multi Stator Multi Rotor (MSMR) configuration has also being introduced (Figure 1-5d). Other methods of improvement like increasing the rotor thickness and complex bearing arrangement have also been suggested by Parviainen (2005) and Kahourzade et al. (2014).

Of all the various topologies, the AFPM shares a common magnetic flux travel path that can be classified as North-North (NN) Torus-S and North-South (NS) Torus-S. Both machine types have a NdFeB PM on the rotors and wound winding on the stator core. The main differences between the NN Torus S and the NS Torus S machines are the arrangement of the permanent magnet on the rotor disc, the winding layout and the thickness of the stator iron core.

Figure 1-5: Types of AFPM machine (a) SSSR; (b) SSDR (c) DSSR (d) MSMR (Parviainen 2005).

As shown in Figure 1-6a, the NN Torus S drives the magnetic flux from the N pole permanent magnet into the stator core and travels circumferentially to the stator (the red dashed line), before passing through the air gap to the S pole permanent magnet on the same rotor disc. For the NS Torus S machine (Figure 1-6b), the flux from the N pole permanent magnet enters axially to the stator core, passing through the second air gap and the S pole permanent magnet before entering the opposing rotating rotor disc and closing the magnetic circuit.

Figure 1-6: Mechanical structure and magnetic circuit of (a) the NN Torus S and (b) the NS Torus S (Kahourzade et al. 2014).

Compared to the NS torus S machine, the NN machine requires a thick stator core to create a main circumferential path for the flux from both rotors. For the NS machine, the circumferential flux path is in the rotor disc and the stator core is unnecessary. Thus, the NN machine has much greater hysteresis or eddy current losses. However, the short back-to-back wrap end winding in the NN machine has shorter end winding and consequently has lower copper losses and a greater torque density than the lengthy lap winding of the NS Torus machine.

1.3 The Yokeless and Segmented Armature (YASA) machine

The Yokeless and Segmented Armature (YASA) machine is a new topology of axial flux permanent magnet motor that combines both designs of the NN Torus-S and the NS Torus-S AFPM machines (Woolmer and McCulloch 2006). The YASA machine employs the topology of the NS torus S machines, but with no stator core, a greater filling factor and short end winding (Figure 1-7). The first YASA machine was designed in 2006 for Morgan LIFEcar project (Woolmer 2009). It is a coreless stator AFPM machine with low core losses (Figure 1-8). The first invention was a 204mm diameter compact machine weighing only 20kg but able to deliver a peak power and torque of 45kW and 120Nm respectively.

Woolmer and McCulloch (2007) reported that compared to other AFPM machines, this new topology had 50% less iron in the stator but produced 20% more torque density. The other advantages of this machine design can be summarised in four points: shorter end winding (high torque density), a high winding fill factor, improved phase independence and a light stator core (Sergeant et al. 2014) A similar concept was employed and further developments were made to this machine to MW-scale for power generation applications (Sook and McCulloch 2014).

Figure 1-7: Derivation from the NS Torus S machine to the YASA machine (Woolmer 2009) .

Figure 1-8: The Yokeless and Segmented Armature (YASA) motor structure (Woolmer and McCulloch 2007)

This machine is light in weight and its pancake design means that less volume and space are taken up, compared to the same power and torque range of radial flux electric machines. The drawback of the YASA machine is that this topology has a high manufacturing cost due to its manufacturing complexity and unique stator structure. However, the manufacturing cost is not an issue because the target user of YASA machine usually could tolerate with this cost as most user comes from the high performance car manufacturer. Additionally, as this machine is a newly introduced one, there is still limited understanding in the area of diagnosis and prognosis of its health monitoring. Therefore, this is the area where the machine manufacturer is also invested in research.

After several years of continuous development, a series of YASA machines are available on the market with variations in size and power such as YASA-400 and YASA-750. Their performance is tabulated in Table 1-1 (YASA Motors Ltd. 2017). Both machines have a great amount of peak power yet are limited in their continuous power delivery. This is because the cooling strategy has remained the main issue in order to boost the machine's continuous performance.

The YASA machine mainly targets the automotive traction application market, ranging from hybrid vehicles for commuting purposes, to high performance vehicles such as the Koenigsegg Regera (Koenigsegg 2017) and motorsports such as e0PP03 and eO100 (Drive eO 2016). These applications require peak performance for acceleration and overtaking along with continuous performance for endurance and non-stop usage. Therefore, with an extensive range of traction requirements from low to high torque and a wider speed range, additional thermal management for this machine becomes critical and a novel cooling method is desired.

Table 1-1: Comparison of available YASA machines, where S is denoted as Standard or Sealed (YASA Motors Ltd., 2017).

1.3.1 Challenges

The main cooling system of the YASA machine depends on the circulation of oil in the stator. The coolant is pumped into the stator at a high flow rate and the specified design flow path within the stator allows the coolant to flow evenly and removes heat from the stator directly (Camilleri et al. 2012). This direct cooling method is sufficient to remove a significant amount of heat from the stator and this cooling method for the YASA machine will be further discussed in Chapter 2.0.

The YASA machine is a fully enclosed system with rotors at the both ends of the shaft situated in two independent confined spaces. With no active or passive cooling in the rotor cavity, the rotor assembly that includes the NdFeB magnets and the steel rotor relies on heat conduction in between them, while depending on heat convection from the rotating flow of air in order to transfer the heat to the machine's cover. This restrains the maximum potential of the machine as a limited amount of heat can be rejected from the rotor assembly.

The main challenge is to remove sufficient heat from the magnet and the rotor, as both components will affect the machine's efficiency, reliability and performance. The main heat source for the rotor assembly is the losses from the segmented surface mounted magnet and the rotor laminates. In addition, to enhance the machine's performance, the air gap is designed to be less than 1mm between the stator and the magnet. Even though the rotating flat rotor disc may act as a flow stirrer and circulate the air around, this tight air gap may not allow the air to flow smoothly and the local heat concentration may lead to uneven rotor and magnet temperature distributions. Furthermore, without any inlet and outlet flow, the excessive heat trapped in the compact space of air may rapidly raise the magnet's temperature.

As mentioned beforehand, the magnetic properties of the permanent magnet are sensitive to temperature and the motor has to operate below the maximum magnet temperature to avoid any demagnetisation. Thus, the

design of the flat rotor may be the best in electromagnetic terms, but acts as a poor heat exchanger in dispersing the heat without in-depth flow studies. Therefore, the possibility of the magnet overheating still remains as a question and the potential of this technology is still not fully explored due to the limitations of the operating conditions.

1.4 Aim and Objective

The aim of this doctoral project is to propose a new cooling system for the AFPM machine, as a secondary thermal management by the rotor cooling technique. This novel rotor cooling methodology will be explored by a Computational Fluid Dynamics (CFD) based design that should improve the machine's continuous performance with compact packaging (to minimise axial length) as its key priority.

The objectives of the research are as follows:

- Develop an understanding of the flow characteristic and heat transfer in the machine components, particularly the rotor assembly.
- Identify suitable CFD rotating flow models and compare the numerical predictions with experimental results for verification and validation.
- Investigate the heat path and the barriers in the rotor system using the numerical analysis of an existing machine (sealed machine).
- Explore a potential rotor design for a rotor cooling technique.
- Investigate suitable inlet/outlet arrangements for the machine as secondary cooling with the losses values from higher continuous performance.

1.5 Outline of the Thesis

The outline of this thesis is described below and can be summarised by the flow chart in Figure 1-9.

Chapter 2: A literature review of research works carried out by others in the area of electric machine losses, thermal management, cooling methods,

methodologies for thermal analysis and studies of the flow characteristics and heat transfer within the air gap.

Chapter 3: This covers the theoretical part of the CFD which includes the fundamental flow equation for the turbulence and rotational motion model. The steps of the CFD simulation process and model accuracy are also discussed in this chapter.

Chapter 4: This chapter focuses on the verification and validation of the CFD model developed for the present research in order to establish the credibility of the selected numerical model. This includes the mesh convergence study, the turbulence model accuracy and the rotational region sensitivity; before the flow and thermal validations were conducted.

Chapter 5: Using the established CFD model setup in Chapter 4, the sealed YASA machine is investigated to understand its thermal mechanism. A validation of this sealed YASA machine is included to have confidence in the results produced.

Chapter 6: This chapter is dedicated to the exploration of the active flow promoter in the machine's current topology. An in-depth study of the fan type defines the suitable rotor geometry, utilising the CFD simulation-based design.

Chapter 7: The study continues with an investigation of several inlet and outlet configurations as a passive flow promoter. This chapter focuses on the introduction of cooling air into the machine. The flow features and characteristics of various inlet/outlet combination designs will be discussed in detail. The chapter ends with a validation of the combination design to prove that the CFD based design has credible results.

Chapter 8: This presents a summary of the work done and possible future work based on this research.

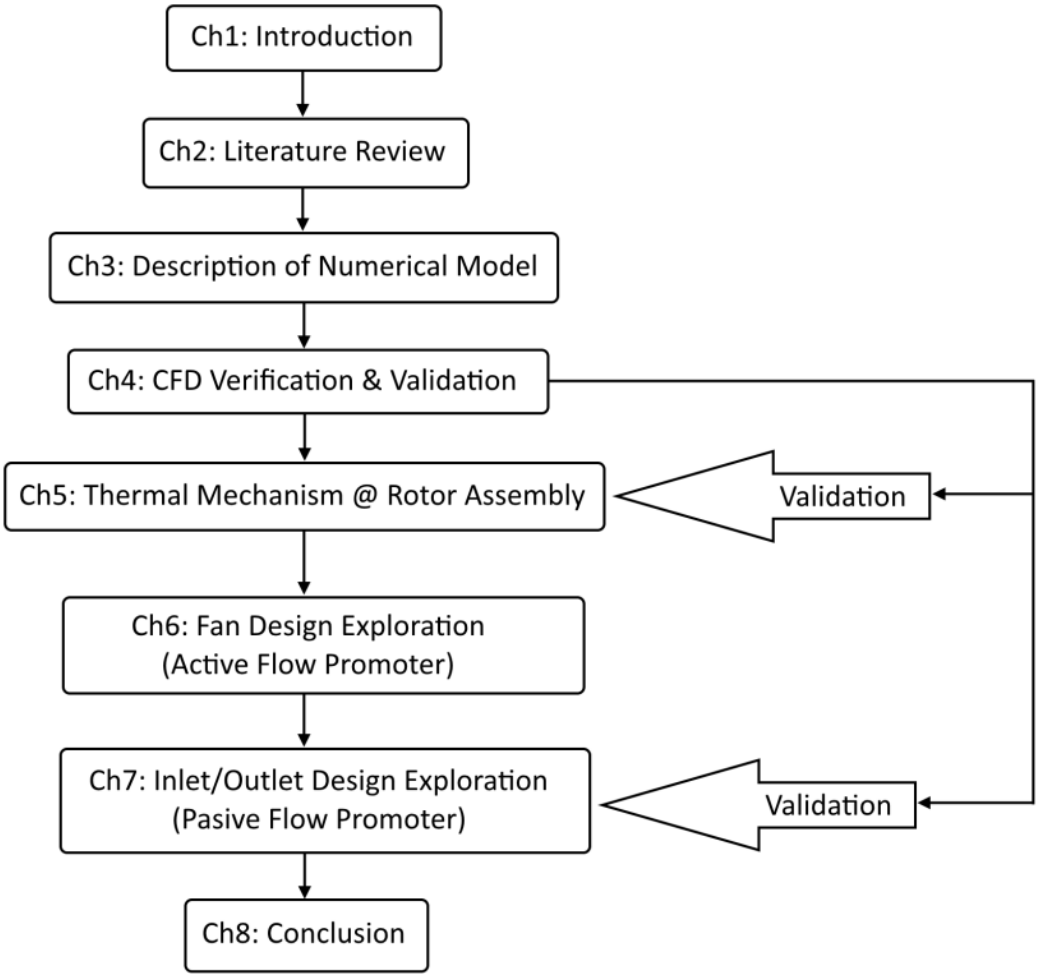

Figure 1-9: Thesis outline flow chart.

Chapter 2

Literature Review

2.0 Literature Review

In this chapter, the author tries to fulfil the objectives of “Develop an understanding of the flow characteristic and heat transfer in the machine components, particularly the rotor assembly” by severe literature review. A step back was taken by understanding the heat source of electrical machine that derived from its losses when converting from one source energy into another form of energy.

Next, the thermal analysis methodology of an axial flux or disc-type electrical machine was reviewed in detail based on past work to find the best suitable method to be adopted in this work. The literature review then continues with looking at available cooling method applied in electric machine and includes the current cooling method of YASA machine. This followed by a review on the flow and heat transfer of disc type machine, which will give most influence in understanding the cooling characteristic of this study.

2.1 Electric machine losses

The identification of losses in an electrical machine and a fundamental understanding of the heat source are essential before exploring the possible cooling methods. The heat generated in the electric motor is mainly caused by power losses during energy conversion (electrical to mechanical and vice-

versa) which manifest in the system as heat and dissipate to the surroundings. Consequently, this raises the internal temperature of the motor and increases the temperature of the components in the system. Without understanding thermal generation and proper thermal management, overheating could occur which may lead to catastrophic failure. Overheating in an electric machine can lead to several problems such as the degradation of the insulation material, increased copper resistance, magnet demagnetisation, which reduces the magnetic properties of the PM and affects the lubrication of the motor bearings (Tong 2014).

Chong et al. (2011) specified that the operational temperature of an electric motor is a balance between the heat generation and heat removal rates. Therefore, to increase a machine's efficiency, reliability and performance; good thermal management is required in order to cope with higher heat generation. This is because the heat generation increases parallel to the increase in the motor's performance.

Electrical machine losses or power losses can be divided into two groups: load and no-load losses. In the work of Benhaddadi et al. (2011), (Figure 2-1), 35% of the losses in an electric machine is from the stator winding, following by rotor and magnetic losses, where each section contributes 20% of the total power losses. Other losses such as stray losses and mechanical losses contribute 15% and 10% of the total losses in the machine, respectively. This shows that electric resistance in the winding (copper losses), either from the stator or the rotor, is the main contributor to the machine's total losses.

Figure 2-1: Percentage of losses in the electric motor (Benhaddadi et al. 2011)

2.1.1 Copper losses

The resistive winding loss depends on the current supply and translates into the motor torque. With an increase in the motor torque, the amount of current through the winding is higher which means the resistive loss is greater. This is true for low speed applications as the torque demand is high. However, as the motor spins faster, the torque requirement is lessened and the resistivity generated by the magnetic and windage starts to dominate.

2.1.2 Eddy-current losses and magnetic hysteresis losses

Eddy-current and magnetic hysteresis losses are related to changes in the magnetic flux and the magnetic field. To understand magnetic hysteresis losses, it is important to know the magnetisation hysteresis loop of the PM. Magnetic flux density (B) has a non-linear relationship with the magnetic field strength (H) of the PM, as shown in Figure 2-2a.

This loop shows the phenomena of the residual magnetisation and the coercivity of the PM. With an increase in temperature, the kinetic energy of the molecules will increase and cause the misalignment of the molecules' domain (Moosavi et al. 2015). Subsequently, it changes the shape of the magnet's hysteresis loop (Figure 2-2b) and as it is further exposed to high

temperatures, the permanent magnet loses its ability. This is called demagnetisation.

Figure 2-2: (a) Magnetisation hysteresis loop of the PM and (b) changes of operating point with the increase of temperature (Moosavi et al. 2015)

The magnet's permeance coefficient (P_c) is a measure of the demagnetisation of the magnet. This coefficient is usually greater than one for healthy magnetic material. If the P_c value is less than one, this means that the operation point is closer to the knee point, which will lead to irreversible demagnetisation. The reason why temperature has a great impact on the magnetisation of the PM is because an increase in temperature will shifts the operating point. If the operating point falls into the region around the knee point, irreversible flux loss will occur. The irreversible demagnetisation of the PM can cause the degradation of motor performance, thus leading to motor failure (Moosavi et al. 2015).

2.1.3 Mechanical losses

In an electric motor, the rotational movement and contact between the components also generate losses from friction and air resistance. The amount of these losses and the heat generated depends on the rotational speed of the machine. These mechanical friction losses include bearing losses, sealing losses and brush losses.

Another contribution from mechanical losses is windage loss. This loss is associated with the main moving part of the electric motor (the rotor

assembly) that causes disturbance and air resistance. In the work of Albert et al. (2011), the source of machine windage losses was found to be generated by the slot opening and the space of the Magnetic Motive Force (MMF) harmonic. This loss can be identified by predicting the drag of the rotated rotor assembly at a specific rotational speed, utilising analytical model for simplified model or CFD modelling for complex geometry.

2.1.4 Other losses

For conductor winding, skin and proximity effects are other frequency dependent coupling resistance losses that need to be taken into account. The skin and proximity effects are affected either by the diameter of the winding or the thickness of the square winding.

2.2 Thermal analysis methodologies

The thermal analysis of an electrical machine is usually performed by dimensional simulation at the design stage. Understanding the thermal performance of a particular electric machine design allows a suitable cooling strategy to be implemented if applicable (Sahin 2001a). Various thermal modelling methods have been developed and can be categorised into analytical methods, numerical methods or a combination of both. These modelling approaches are now favoured compared to the experimental approach, as the designer can make fast virtual design changes. Yet an experimental method will be performed for validation, that is usually used to evaluate the selected cooling strategy for the fabricated prototype machine, and is not limited to understanding the thermal behaviour (Sahin and Vandenput 2003; Scowby et al. 2004; Marignetti et al. 2008).

This section describes the literature of these thermal modelling methods specifically related to axial flux or disc-type machine applications.

2.2.1 Analytical methods

The Lumped Parameter (LP) thermal modelling technique is the most prominent analytical method that includes the geometrical of the electrical machine. This method represents the electric machine components by an equivalent thermal circuit, which may also include material, mechanical, electromagnetic and fluid domains. This simplification of heat transfer problems allows LP thermal modelling to solve different load cycles in fast computational times, either in steady state or in transient thermal solutions. In steady state simulation, LP thermal modelling relies on the input thermal resistance, heat transfer coefficients and heat sources connected together to represent the lumped components of the electrical machine. On the other hand, transient simulation considers the component's internal energy changes over time (Mahmoudi et al. 2013).

Mellor et al. (1991) conducted one of the early applications of LP thermal modelling for predicting the temperature of a radial flux electrical machine. These models were built for 75kW and 5.5kW of Totally Enclosed Fan Cooled (TEFC) induction motors and the results of the transient solutions were accurate with greater than 80% accuracy when compared to the experimental results. One year after its first introduction, the LP thermal model was applied to the disc-type machine by Spooner and Chalmers (1992), as shown in Figure 2-3 for an engine-driven generator application. The authors conducted an experiment with a dummy generator to obtain the thermal resistance of heat conduction for solid components and convection heat transfer for solid to fluid contact. These were input to their LP thermal model. However, the surface heat transfer coefficient used in the model was assumed to be at 150W/m^2.K. Additionally, the flow characteristics were also measured such as the air pressure difference and air mass flow rate between the inlet and outlet. The thermal model did predict well when compared with the measured data, with less than 10% error for some particular cases, while they argued that there was a potential flaw in the experiment, thus the

thermal model's temperature was under predicted. Perhaps the authors' assumption of the surface heat transfer coefficient may have led to this issue.

Figure 2-3: Thermal model of a TORUS machine (Spooner and Chalmers 1992)

.

Sahin et al. (2001b) conducted another example of LP thermal modelling for an electric vehicle application on an AFPM machine with DSSR topology. The model was assumed to be symmetric and a scaled quarter domain was made. The thermal model shown in Figure 2-4 was built based on the manufactured prototype including the cooling water channel. The machine's dimension, material properties and thermal parameters were used respectively to the build prototype. The results of the LP thermal model were then compared to the experimental data which was gathered by multiple thermocouples attached inside the prototype machine. The thermal model of the high speed water-cooled AFPM machine at 16,000rpm with a 30kW rating showed sufficient thermal information on the actual machine's thermal behaviour, yet had no more than 12ºC in-between the measured temperature and developed thermal model for AFPM machine in the study. Sahin (2001a) also made a comment in his thesis that the convection resistance of the surface-to-air interface is dependent on the heat transfer coefficient value, which is considerably crucial for accurate thermal modelling.

Figure 2-4: Lumped parameter thermal model of a quarter domain DSSR AFPM (Sahin 2001a) .

Based on the work of Spooner and Chalmers (1992) and Sahin (2001a), this analytical approach of predicting the thermal performance of an electric machine was strongly depends on the convection heat transfer input. Therefore, the convective heat transfer coefficient needs to be based either on previous experiments, CFD simplification results or empirical correlations (Chong 2015).

Parviainen (2005) studied the thermal performance of a high-speed AFPM machine of the DSSR type. The LP thermal models include an internal forced air-cooled structure (Parviainen et al. 2004a). In separate literature, Parviainen et al. (2004b) included water-cooling to cool the machine's bearings. The computed and measured results showed good agreement with 10% of error where the authors mentioned that the thermal resistances were adjusted according to the experimental results, due to the difficulty in estimating the contact thermal resistance. Fakhfakh et al. (2008) also used this analytical method to predict the thermal performance of an AFPM machine with two-cooling systems for EV traction application. The findings suggest that the water-cooling performed better than the air-cooling.

Erik et al. (2005) investigated the thermal behaviour and the cooling system for the stator of an AFPM machine designed for the generator of a heavy goods hybrid vehicle. The computational model shown in Figure 2-5 includes both the radial and axial heat flow by dividing the geometry into rectangular pieces. Good correspondence was found between the LP predicted results and the measured experimental data as shown in Figure 2-5b.

Figure 2-5: (a) Lumped parameter thermal model of a generator of a heavy goods hybrid vehicle and (b)comparative results of measured and predicted temperature (Erik et al. 2005).

Scowby et al. (2004) investigated a high powered AFPM machine for a hybrid vehicle of 300kW with a throughflow ventilated cooling strategy combining a one-dimensional (1D) empirical fluid flow model into the thermal model. A fan feature of a radial blade was incorporated in the hub to promote the flow. The flow model produced a reasonable agreement with the experimental measurement results. In addition, the authors also included a heat pipe as an alternative means to remove the heat. A similar approach was found in the work of Wang et al. (2005), where the LP thermal model was solved with the combination of a fluid flow model to create a thermofluid model for a typical AFPM machine. The fluid flow model was built based on empirical correlations from the various literatures to predict the surface convective heat transfer coefficients that would take into account the effect of pressure

development and pressure losses. This is due to the flow features of the flow recirculation, expansion and flow induced by the protruding surface mounted magnet. However, the fluid flow model did not include the effect of rotational motion and this may jeopardise the accuracy of the predicted results.

Vilar et al. (2005) constructed a single sided AFPM motor to gather the conduction, natural convection and thermal capacitance parameters for their LP thermal model. The LP thermal model was then validated with an experimental of a worst-case scenario where the rotor is in a stationary condition. The thermal model of the machine rated at 1kw at 3000rpm managed to predict the temperature well on the rotor, stator and frame, with a slight difference in the thermal development of the copper wire. Another simplified work utilising the LP thermal model was presented in Martin's (2007) work for a direct drive application. A 1D thermal model was used with a fixed convective heat transfer coefficient value from the experimental.

A series of extensive work presented by Lim et al. (2008) and Lim et al. (2010) not only compared and validated the thermal modelling, but also proved and proposed this method as an alternative to CFD simulations. A two-dimensional (2D) LP thermal circuit was used to simplify the AFPM generator of three pole pairs including the centrifugal cooling airflow. The LP thermal model was constructed by connecting the thermal generator component and internal cooling airflow, where the convection thermal resistances were calculated by the fluid flow circuit and interacted with the heat modelling in the radial and axial directions. The predicted temperature results were compared with the CFD simulations and experimental testing for validation and reasonable correlations were established. The fast solution of the LP was reliable in predicting the thermal of the selected machine, yet it can be questioned as to whether the fluid flow circuit can only solve the flow properties in lumped without taking the flow features into account. Howey (2010) made a bold statement suggesting that the LP of an airflow model for an AFPM machine needs to consider the complexity of the flow features, as the flow has a direct influence specifically on the stator heat transfer.

Camilleri et al. (2012a) presented a preliminary thermal analysis focused on the limitations of air-cooled AFPM motors for urban mobility purposes. Two LP thermal models of different topologies were studied, namely the axial flux internal rotor (AFIR) and the axial flux internal stator (AFIS) topology. The selected topologies were considered to be adapted for in-wheel applications and the corresponding schematic and LP is illustrated in Figure 2-6. In the findings, both topologies suffered from thermal limitations and a single in-wheel motor of both designs was not feasible for vehicle use implementation. The AFIR topology is predicted to perform well at a low speed with a traction power between 3.75kW to 5kW, which is proposed to be used on 3 or 4 wheels. On the other hand, the AFIS topology favours a high speed, as the cooling performance is dependent on a machine speed with a traction power up to 7.5kW and should be distributed on 2 wheels, if adapted to urban mobility usage. Additionally, this paper has presented an in-depth definition to calculate the heat transfer coefficients for all regions of the machines.

Figure 2-6: Schematic and simple 1D thermal network of (a) the AFIR type motor and (b) the AFIS motor (Camilleri et al. 2012a).

Ferreira and Costa (2012) created a LP thermal model for an AFPM at a steady state with a recursive electromagnetic design. The losses were

calculated iteratively, while the other parameters and heat transfer coefficients were assumed from the literature. An experimental testing was also conducted with five PT-100 temperature sensors for validation purposes and the results are promising.

The LP thermal model proposed by Rostami et al. (2013) coupled the electromagnetic model and the LP thermal model iteratively for a 5kW and 350rpm AFPM generator in a steady state solution. Figure 2-7 shows the thermal circuit and the proposed design procedure to predict the temperature of a DSSR configuration. The input heat transfer coefficients were calculated empirically based on the local Reynolds number and the corresponding Taylor and Nusselt numbers. Close agreement was recorded when compared with the measured temperature at seven components with a maximum temperature difference of 4ºC. Additionally, a sensitivity analysis was conducted with different air-gaps, different end-caps, variation of the emissivity of the frame surface and different machine loads and speeds (3.5kW and 250rpm). The proposed LP thermal model provides accurate temperature prediction.

Figure 2-7: (a) The equivalent thermal model and (b) the design procedure proposed by Rostami et al. (2013).

Vainel et al. (2013) investigated an example of a three-dimensional (3D) LP thermal model; a Kaman type fractional-slot concentrated-winding AFPM machine with tooth-wound coils. The 3D LP thermal model was constructed to evaluate three different variants of the rotor disc design of a DSSR configuration to find the best solution for minimum induced losses. Half the machine was modelled at its symmetry axis and the complex design was simplified by a cubiodal element, as shown in Figure 2-8. The simulations were conducted in steady state and in transient conditions. An additional flow model was included to calculate the flow performance such as pressure drops and fluid flow rates. The losses values from Giulii Capponni's et al. (2012) experiment were used, while the convective heat transfer coefficients were calculated using Howey's et al. (2011) publication. The simulations showed a good agreement with the experimental results, proving the effectiveness of the 3D LP thermal model with a maximum 6% and 10% of error for steady state and transient solutions respectively.

Figure 2-8: (a) A machine's cross section with red arrows for conduction and blue arrows for convection and (b) cuboidal element of the components (Vainel et al. 2013).

2.2.1.1 Summary of LP thermal model

It can be summarised (Table 2-1) that the analytical method of LP thermal modelling provides a fast solution with the capability to simulate the machine's temperature during steady state and transient conditions. However, based on their recorded drawback, the prediction accuracy is strongly dependent on the input correlations used such as thermal resistance, convective heat transfer coefficients and airflow characteristics (Howey 2010). Additionally, this method has another weakness because it only represents the component in lumped instead of machine actual geometry. Therefore, the thermal problem neglects the thermal distribution between the contact surfaces, especially on the solid-fluid interaction (Mahmoudi et al. 2013; Chong 2015). Thus, the numerical method is increasingly applied to understand the thermal performance and cooling effectiveness of an electrical machine.

Table 2-1: Summarised of the previous work using LP thermal modelling method

Authors	Methods	Advantages	Drawback
Mellor et al. (1991)	LP	The early applications of LP thermal modelling for predicting the temperature of a radial flux electrical machine with greater than 80% accuracy.	-
Spooner and Chalmers (1992)	LP	Early applications of LP thermal modelling for predicting the temperature of disc-type (axial flux) electrical machine. The thermal resistance, flow characteristics and convection heat transfer are obtained by experimental.	The surface heat transfer coefficient used in the model was assumed. Author argued that there was a potential flaw in the experiment, thus the thermal model's temperature was under predicted.

Sahin (2001a) and Sahin et al. (2001b)	1D LP	LP thermal modelling for an electric vehicle application on an AFPM machine with DSSR topology. It was simplification from the complex machine's dimension.	The results produce no more than 12ºC in-between the measured temperature and developed thermal model for AFPM machine. Author comment that the convection resistance of the surface-to-air interface is dependent on the heat transfer coefficient value, therefore need to be accurately assume.
Parviainen et al. 2004a, Parviainen et al. (2004b) and Parviainen (2005)	LP + forced air-cooled structure	Study of the thermal performance of a high-speed AFPM machine of the DSSR type. The LP thermal models include an internal forced air-cooled structure. Also included water-cooling to cool the machine's bearings in separate literature.	The authors mentioned that the thermal resistances were adjusted according to the experimental results, due to the difficulty in estimating the contact thermal resistance.
Fakhfakh et al. (2008)	LP + cooling systems	Predict the thermal performance of an AFPM machine with two-cooling systems for EV traction application.	-
Erik et al. (2005)	1D LP + stator cooling system	Investigated the thermal behaviour and the cooling system for the stator of an AFPM machine including both the radial and axial heat flow	-
Scowby et al. (2004)	1D LP + ventilated cooling	Investigated a high powered AFPM machine for a hybrid vehicle with a throughflow ventilated cooling by combining a one-dimensional (1D) empirical fluid flow model.	The fluid flow model did not include the effect of rotational motion and this may jeopardise the accuracy of the predicted results.
Wang et al. (2005)	LP + Fluid flow model	The LP thermal model was solved with the combination of a fluid flow model to create a thermofluid model	

Vilar et al. (2005)	1D LP	Simplified work of LP thermal model of a single sided AFPM motor on a worst-case scenario where the rotor is in a stationary condition.	-
Martin's (2007)	1D LP	1D thermal model with a fixed convective heat transfer coefficient value from the experimental.	-
Lim et al. (2008) and Lim et al. (2010)	2D LP + centrifugal cooling airflow	Compared and validated the 2D thermal modelling including the centrifugal cooling airflow. The convection thermal resistances were calculated by the fluid flow circuit and interacted with the heat modelling in the radial and axial directions.	It is questioned as to whether the fluid flow circuit can only solve the flow properties in lumped without taking the flow features into account.
Camilleri et al. (2012a)	LP	Two LP thermal models of different topologies were studied, namely the axial flux internal rotor (AFIR) and the axial flux internal stator (AFIS) topology for in-wheel applications.	This paper has presented an in-depth definition to calculate the heat transfer coefficients for all regions of the machines.
Ferreira and Costa (2012)	LP + electromagnetic	A LP thermal model for an AFPM at a steady state with a recursive electromagnetic design. The losses were calculated iteratively.	Heat transfer coefficients were assumed from the literature.
Rostami et al. (2013)	LP + electromagnetic model	Coupled the electromagnetic model and the LP thermal model iteratively of a DSSR configuration. The input heat transfer coefficients were calculated empirically	Complex thermal model and design procedure.
Vainel et al. (2013)	3D LP	3D LP thermal model of concentrated-winding AFPM by cuboidal element of the components. The losses values from Giulii Capponni's et al. (2012) experiment were used, while the convective heat transfer coefficients were calculated using Howey's et al. (2011) publication.	-

2.2.2 Numerical methods (FEA and CFD Model)

Numerical methods increase the prediction's accuracy by taking the geometry of the machine into the solution, thus it favourable to be used in a more complex machine design. The machine's geometrical representation will be discretised into a smaller spatial resolution to make it possible for the problem to be solved by the finite element or the finite volume method. Having a higher spatial resolution, numerical methods allow for a better understanding of the thermal distributions and the effectiveness of selected cooling mechanisms that are lacking in LP predictions. Two common tools for machine designers for thermal analysis by numerical methods are Finite Element Analysis (FEA) and Computational Fluid Dynamics (CFD).

Thermal modelling via FEA offers a prediction of the conductive heat transfer. For example, Wahsh et al. (2016) used FEA to analyse the temperature distribution by the effect of the speed variation of an AFPM machine. The geometry was simplified, wherein only 1/16 was modelled. To reduce the computational requirements, further simplifications were made by modelling the windings as a bulk solid and ignoring the effect of epoxy on the end windings. Two different machine speeds were chosen: 1000rpm and 7000rpm with natural air convection at a 30ºC ambient temperature. The input losses were taken from their previous work (Shazly et al. 2014) . The results showed that the overall temperature of the component was dependent on the rotational speed, where at 7000rpm multiple hotspots could be observed on the stator and the magnet's temperature increased significantly. However, these findings are good just for predictions, as no experimental comparison was conducted.

Another example of thermal analysis using FEA was performed by Wang et al. (2017) for an AFPM machine of DSSR configuration. Interestingly, the magnet was modelled by a rectangular combination instead of single magnet domain. It is claimed that the cogging torque can be reduced by having multiple segments of a magnet instead of a single block. In their study, the

LP thermal network was used to initially understand the average components' temperatures, which were then compared with the FEA simulation for a detailed temperature distribution. Figure 2-9 shows the temperature distribution produced by FEA. The results of FEA and LP have a maximum of 3% difference.

Figure 2-9: Temperature distribution of AFPM using FEA (Wang et al. 2017) .

Both examples of FEA thermal analysis were not experimentally validated, yet they are still useful as they give an understanding of the heat concentration inside an AFPM machine, particularly on the permanent magnet and the windings. FEA thermal analysis is usually performed in combination with other numerical methods to reduce the dependency on empirical assumptions. This is further discussed in Section 2.2.3.

On the other hand, CFD simulations give a better understanding of the flow characteristics, as convective heat transfer is influenced by the fluid flow rate, flow features, velocity field, pressure development and drop. Sequence work by Airoldi et al. (2008) demonstrated the use of 3D CFD to obtain the heat transfer coefficient and understanding of the machine's interior flow physics. The heat source was set at 1000W/m^2 at the stator wall and an inlet air temperature of 300K was defined. Utilising Reynolds Average Navier Stokes (RANS) equation and the realizable k-e turbulence model, the CFD simulation was solved in 18 hours by 4 processors. Experimental validation

was included and a good correlation between the CFD and the experimental was found to be limited at 1500rpm. Variations of the running clearance (rotor-stator air-gap) had no effect on the generated mass flow rate, however the stator heat transfer coefficient changed, with the highest recorded at the lowest running clearance. Similarly, the stator heat transfer coefficient rose linearly as the machine speed was increased. In Airoldi et al. (2009) the CFD simulation was repeated with different machine geometry to identify the temperature distribution and the heat transfer coefficient on the stator wall and the results are shown in Figure 2-10. Additionally, the Nusselt number was calculated based on the CFD results for further reference.

Figure 2-10: The CFD contour plots of (a) the stator temperature in K and (b) the stator heat transfer coefficient in W/m^2.K (Airoldi et al. 2009).

Lim et al. (2011) validated their CFD modelling with Airoldi (2010) experiment, specifically for the heat transfer coefficient prediction of the throughflow ventilated AFPM machine. The evaluated CFD results were made by disregarding the effects of natural convection, thus the stator surface heat transfer coefficients have 4% to 8% of error overall, with CFD simulations that are under the prediction of the local stator surface Nusselt numbers (between 7% to 61% of error). Nevertheless, further experiments with mixed convection (natural and forced) were conducted and the prediction results were improved.

It can be summarised that both FEA and CFD are great tools for the thermal analysis of an electric machine. However, these tools require huge computational time and costs when dealing with transient simulation.

2.2.3 The Hybrid method

The combination of multiple methods of thermal analysis may require less empirical input and be capable of providing accurate predictions. This hybrid method can be a combination of analytical and numerical methods or a combination of multiple numerical methods.

The combination of analytical and numerical methods was demonstrated by Hey et al. (2010). They developed a hybrid thermal model for predicting the temperature distribution of an AFPM machine. The CFD code was used to provide the average values of the convective heat transfer coefficient (particularly at the solid-fluid interface) and be as the input to the LP thermal model. The transient solution predicted well when compared to the experimental and it improved significantly when the Monte Carlo method was adopted. Figure 2-11 describes the optimisation flow process of their Monte Carlo method.

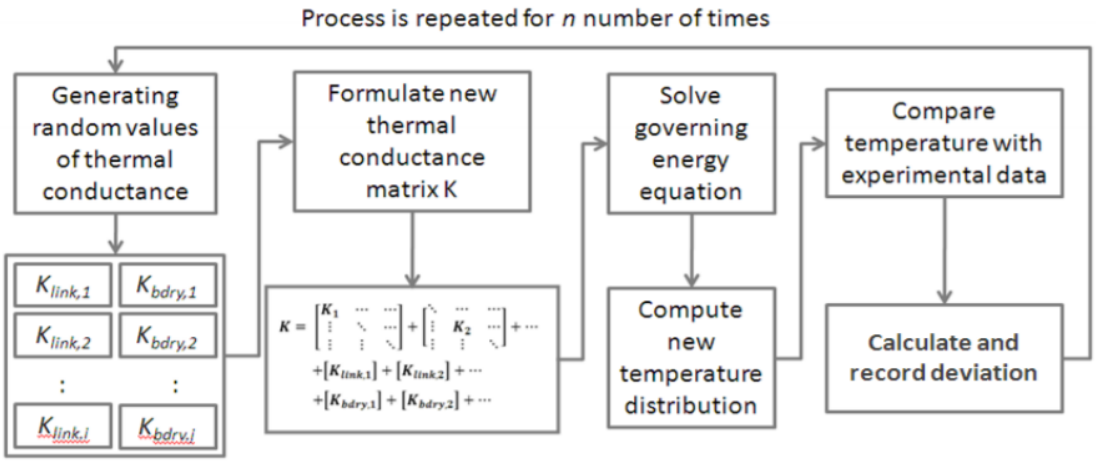

Figure 2-11: The Monte Carlo method adapted by Hey et al. (2010).

Marignetti et al. (2008) made an example of a hybrid method coupling the FEA electromagnetic thermal and fluid-dynamical FE for an AFPM

synchronous machine with forced air convection. The FEA electromagnetic thermal was used to obtain the variables and parameters including the losses, then solved by the fluid-dynamical model for the machine's temperature field. The FEA simulations managed to predict the trend of temperature growth as the current increase had as yet lacked accuracy, yet it is reasonable due to the assumption of heat generated by the stator and windings, only without including the rotor.

In summary, the hybrid method can provide a high level of accuracy as the weakness of each method can be counter effective i.e. the dependency of empirical input for analytical methods and the high computational requirements for numerical methods.

2.3 Cooling methods of electric machines

Common electric motors may have one or more adapted cooling systems. These can be identified from the methods of cooling (IC code) on the electric motor's tag or provided by the manufacturer. The IC code is the index of cooling that includes the classification of the cooling/ventilation methods and contains information such as the primary and secondary coolant type of the chosen cooling methods. The cooling method of an electrical machine can be either direct or indirect or a combination of both. The selected cooling method is chosen to control the machine's temperature based on the consideration of several factors such as the operating conditions and the temperature limit of the insulation material, machine power losses etc.

In general, there are two different designs of electric motor that reflect the machine's cooling system: an open or fully enclosed system. Electric motors with an open type system require less attention to the cooling design because external fresh air can be freely driven to its interior. However, for applications with hazardous or contaminated environments, the electric motor requires a fully enclosed casing and heat removal becomes a challenge. This is because there is a limited heat exchange between the inner and outer thermal flow. The heat transfer can only take place through the medium with

an exterior flow (ventilation through the casing) and the circulation of the internal flow within the enclosed space.

In recent years, the thermal management of electric motors has received great attention and other cooling methods (evaporative cooling, cold plate, oil-spray, etc.) have been further explored and investigated. Gieras (2008) summarised the advantages and disadvantages of different types of cooling systems as displayed in Figure 2-12. Gieras (2008) stated that the common practise to remove heat from the system is through fins around the frame and additional heat sinks. However, this approach increases the weight and size of an electric machine. Among these cooling methods (Figure 2-12), the most effective is direct liquid cooling (stator cooling) followed by oil-spray cooling for the rotor winding. Simons (1996) compile list of coolant types and the heat transfer coefficient used for direct liquid cooling of the microelectronic components as shown in Figure 2-13. An advanced cooling method utilising nitrogen has also been tested for its suitability for electric motor applications by Chen et al. (2012), Sugimoto et al. (2008) and Sivasubramanian et al. (2008).

Figure 2-12: Summary of the different cooling systems for electric machines (Gieras 2008).

Figure 2-13: Different coolant types for the direct liquid cooling of microelectronics (Simons 1996).

Cold plate is another heat dissipation method to cool an electric machine, especially for megawatt-sized generators. The high thermal conductivity of the cold plate between the pole core and the winding creates a passageway or heat path for the cooling medium to enter the system and carry the heat away from the generator. After passing through the heat exchanger, the coolant returns to the cold plate passage and the loop continues. Figure 2-14 shows the location of the cold plate passageway in the stator investigated by Gieras (2008).

Figure 2-14: Cold plate placed between the pole and winding (Gieras 2008).

Li et al. (2009) combined two cooling techniques in their study of an electric motor: oil-spray and evaporative. It was found that the spray and evaporative cooling systems are very effective in heat removal and only 1/10 of the total amount of coolant is required for immerse evaporative cooling. The coolant was first sprayed onto the end winding, creating a thin liquid film on the surface. After absorbing sufficient latent heat, the thin liquid film on the surface started to evaporate and the vapour would then be condensed by the heat sink. This technique was also reported and implemented for a 1.5kW heat source and a 1kW/m^2 heat flux (Xia 2002). In comparison to other cooling methods, oil-spray and evaporative cooling are more sustainable for rapid heat removal.

Also, in some applications, duo-cooling methods were used for fully enclosed motors by a heat exchanger of either air-to-air, water-to-air or liquid-to-air, which have separate air cooling circuits in machines predominantly manufactured by General Electric and ATB Morley (GE Global Research n.d; GE Power Conversion n.d; GE Transporation n.d; ATB Morley 2002).

2.3.1 Fans and CFD in electric machine cooling

One of the classic cooling methods is by uses a fan either to circulate the airflow within an open type machine or to surround the machine's casing for a fully enclosed machine. This approach improves the heat rejection as a fan promotes fluid motion thus changing the mode of convective heat transfer from natural to forced convection. The cooling fan can be driven by the machine itself or have a separate individual drive mechanism. For a fan driven by the machine, the cooling fan is mounted on the shaft of the non-drive end side and rotates in proportion to the machine's speed.

The use of a fan for the cooling mechanism of an electrical machine needs to be predicted during the design stage in order to have optimum heat control. However, the measurement of the rotating flow is complex and high cost, thus most machine designers have a tendency to utilise a commercial CFD software package in order to understand the flow behaviour that reflects the

cooling performance. As an example of flow visualisation extracted from CFD models, Figure 2-15 illustrates the velocity vector of an attached impeller in the motor, where the air velocity gradient along the curvature of the blade (especially at the leading and trailing edges) was studied (Li 2010). This help in understanding the cooling fluid direction thus design changes can be made accordingly.

Figure 2-15: Velocity profile of the impeller (Li 2010).

CFD modelling can also aid in identifying the cooling energy losses (slot, impeller, outlet and gap losses) specific to the machine design because the solution includes complex geometrical representation. Figure 2-16a and Figure 2-16b illustrate the difference in velocity vectors of an axial fan and a centrifugal fan respectively (Chang et al. 2010). With CFD simulation, this will help find the best solution for a cooling strategy by choosing the optimal design with low cooling energy losses.

Additionally, flow characteristics such as entering, separation, circulation, attachment and exiting the machine can be observed through CFD simulation. This gives CFD simulation an advantage in studying flow phenomena that is hard to be seen through an experiment. As an example, the flow circulation in the air-gap as shown in Figure 2-17 illustrates that the flow pattern changes by the size of the gap (Kim et al. 2009). Consequently, the experimental approach is still obligatory in order to validate the simulation result quantitatively.

Figure 2-16: Velocity vector of a) the axial fan b) the centrifugal fan (Chang et al. 2010).

Figure 2-17: Velocity profile within the air gap (Kim et al. 2009).

2.3.2 Cooling methods of YASA machines

Early YASA machines did not have any specific cooling strategy as the focus was given to the development and improvisation of the machine's electromagnetics. Yet the machine's performance was limited because there is an interlink between thermo and electromagnetic performance (Liwei et al. 2008; Ruoho et al. 2010). Due to this reason, Camilleri et al. (2012b) introduced direct liquid cooling to the machine's stator to regulate the temperature that rises due to the stator losses. The adaptation for liquid cooling from the standard design was easily adopted as the YASA stator has individual stator poles and does not have a yoke. Sealing both ends of the stator creates a spilt region between the rotor and the stator, thus allowing the liquid to flow and be contained within the specific region of the stator. The

experimental test was conducted on a 50kW YASA 750 machine to investigate the temperature profile of the pole piece over the various coolant flow conditions. The results showed the variance temperature on the radial and circumferential direction. Additionally, the authors have compared this with their early low-resolution LP thermal model and the assumption results were not realistic. Therefore, they developed another LP model that included a separate copper layer calculation into the model and the results were improved.

Since then, this cooling method has been adapted for every manufactured YASA machine and soon the industrial needs demanded that the machine be at an even higher performance. What was left were the losses from the rotor and the magnets that limited the machine's performance, thus another novel cooling strategy needed to be incorporated into the machine's design.

Vansompel (2010) in his PhD thesis has suggested forced air cooling by adding radial ribs that look like a fan's features, as shown in Figure 2-18. This concept is taken from the centrifugal fan or blower design to stirrer the interior air. As the machine rotates, the fan creates a pressure difference between the centre and the outer radial thus promoting the air to move around and absorbing the heat from the rotor and the magnets. The forced air not only cools the rotor and magnets, but is also blown towards the end windings of the stator tooth coils, yet no clear exit path was defined. Vansompel (2010) suggested that the air is then recalculated between the stator and the rotor within the machine's interior. The interior air circulation may transfer the internal heat to the machine's casing and then transfer the heat by natural convection to the surroundings. Figure 2-19 shows the assembly of the machine concept with a fan on the rotor and without the rotor, to show the airflow path on the edge of the stator and its return to the inner of the rotor.

Figure 2-18: Ribs on the rotor for the forced air-cooling of a YASA machine (Vansompel, 2010).

Figure 2-19: Proposed forced air-cooling for the rotor and stator of a YASA machine (Vansompel, 2010).

This interesting cooling concept by Vansompel (2010) needs to be further investigated in order to understand the usability of adding a fan to the YASA machine as a cooling strategy. The flow and heat transfer performance can be analysed by CFD, yet the flow structure of a rotating disc and its relation to better convective heat transfer is required to be comprehended beforehand.

2.4 Flow and heat transfer of a disc type machine

The automotive sector targets electric machines that are compact, lightweight and of a high power-density, thus the AFPM machine is one of the best

candidates for use. The AFPM machine, also known as a disc type machine such as the YASA machine, meets these criteria, yet better thermal management could further increase its performance. In order to improve its cooling performance, the internal flow structure and the heat transfer mechanism need to be understood.

For a disc type machine like the YASA motor, the airflow characteristic around the rotating rotor has a significant impact on the heat transfer and the tight air gap (~1mm), such as the stator-rotor air gap and rotor-cover air gap. Thus, the knowledge of the flow characteristic for a high-speed rotating disc is essential and crucial for design purposes.

Fundamentally, a free flow-rotating disc stirs the air on its axial direction to the centre of the disc and the centrifugal force causes the air at the centre to move outward radially, as shown in Figure 2-20. The disc's rotating motion creates a pressure gradient and velocity difference along its radius. The tangential air velocity at the disc is increased radially toward the edge, while the radial velocity of the air increases as it gets closer to the rotating disc.

Figure 2-20: Radial velocity profile of the free flow rotating disc (Howey et al. 2012).

On the other hand, when a rotating disc is sealed and enclosed with another adjacent stationary wall, the flow structure changes slightly. This is because the tight air gap restrains the motion, thus a flow circulation moving from the centre to the outer disc radius is formed, as illustrated in Figure 2-21. There is a series of research works on this subject of rotating flow characteristics and air gap convection (Elena and Schiestal 1996; Yuan et al. 2003; Schouveiler et al. 2001; Beretta and Malfa 2003). However, only a few studies were focused on disc type electric machine applications (Howey et al. 2011 and 2012).

Figure 2-21: Flow circulating within the enclosed air gap (Elena and Schiestel 1996).

2.4.1 Rotational effects of the rotor disc

As shown in Figure 2-20, the axial and tangential velocity profile of a free flow disc is in the function of the axial and radial distance. In the comprehensive report from the Engineering Sciences Data Unit (IHS ESDU 2010), the flow region can be in laminar or turbulence flow and can be defined by the local rotational Reynolds number. However, the flow that is closer to the rotating axes tends to be laminar in characteristic. Apart from the free disc, this report also provides an overview of the rotating disc, cylinder and cavities.

A fully enclosed rotating disc configuration studied by Elena and Schiestel (1996) reported that the flow within the stator-rotor air gap is radially restricted. This is displayed in the radial velocity profile in Figure 2-22a with no radial motion, but with a constant tangential velocity profile and in Figure 2-22b within the flow regime.

Figure 2-22: (a) Radial velocity profile and (b) tangential velocity profile between the stator and the rotor air gap (Elena and Schiestel 1996) .

When an inlet and outlet are introduced to the fully enclosed rotating disc, the streamline profile varies depending on the arrangement of the inlet and outlet, including the flow mass flow rate as illustrated in Figure 2-23. These flow patterns can be described by the Batchelor model and the Stewartson model specifically for the rotor-stator air gap flow. The Batchelor model assumed that the angular velocity of the core fluid in the air gap is at the point between the rotating disk and the stator, while the Stewartson model assumed that the air gap flow is the so called 'free disc' flow and there is no core rotation. In easier terms, Batchelor model assumed the air gap between rotor-stator is narrow while Stewartson model assumed large air gap.

Interestingly, both models are slightly contrary to each other in presenting the velocity profile in Figure 2-24. In Bachelor's flow model, it is observed that there are two boundary layers occurring on the rotor and stator, while the Stewartson model assumes that the tangential velocity of the flow outside the rotor boundary layers tends to be zero (Figure 2-24d). However, both models are accepted as they were tested under different speed conditions (IHS ESDU 2010).

The Batchelor-Stewartson model described previously is used specifically for the flow characteristic within the stator-rotor air gap in an axial direction. On the other hand, the flow characteristic on the radial of a disc flow has a different manner. The air gap between two concentric cylinders will form a

Couette flow in close proximity to the stator-rotor air gap. A Couette flow is used to describe a flow that is dominated by a viscous effect (laminar). When the Couette flow becomes unstable, a toroidal vortex could be formed between the two cylinders.

Figure 2-23: Streamline profile of the laminar flow with different inlet flow directions (Howey et al. 2012).

Figure 2-24: The Batchelor and Stewartson flow pattern (IHS ESDU 2010).

Taylor studied this instability criterion and found that the flow rotates at a critical angular velocity and subsequently introduces secondary flow vortices

in the annular gap axially (Childs 2011). The instability of the flow depends on the balance between the radial force and the radial pressure gradient. Any small disturbance in the flow will cause it to change its pattern. It can also become unstable when the radiant pressure gradient and viscous force are unable to balance this force in the flow (Childs 2011). The Taylor number is a dimensionless number that is used for indicating the stability and flow criterion in Couette flow and this number includes the geometry factor of the cylinders and the rotating speed. It represents the rotational centrifugal force over the fluid viscosity. Therefore, as the Taylor number exceeds the critical value of $Ta = 41.9$, the flow becomes unstable (for a narrow gap). The Taylor number is useful to the machine designer because it either helps to avoid the Taylor vortex flow or it can be used to understand the flow for chemical applications (IHS ESDU 2010).

Figure 2-25: The Taylor vortex between two concentric cylinders (Childs 2011)

.

2.4.2 Convective heat transfer of the rotor-stator air gap

Understanding the heat convection in the narrow air gap of the rotor-stator plays a significant role in managing the temperature of the permanent magnet (PM). Howey et al. (2011) has carried out multiple intensive studies on the convective heat transfer for AFPMs. One of his works employs CFD modelling to predict the rotor-stator heat transfer by a selection of turbulence models and the results were compared with experiment results. It is observed

that the fluid temperature increases along the radius as the centrifugal force causes the flow to pump out through the slot of the magnets. However, the presented work claimed that the CFD approach has difficulty in predicting the heat transfer accurately near to the flow transition regime and the edges of the rotor.

In another extensive work, Rasekh (2015 and 2017) concludes that the main parameters that influence the heat transfer of the stator-rotor air gap are the rotational Reynolds number, the gap size ratio, the magnet angle ratio and the magnet thickness ratio. The work also mentions that it is difficult to attach a fan to an AFPM machine due to its tight space. However, it is claimed that the magnet itself can act as a fan for an AFPM that has a surface mounted PM. Thus, the magnet thickness has a significant impact on the overall heat transfer (Rasekh 2017).

2.5 Summary of literature review

In this chapter, a detailed review on fundamental heat source of electric machine losses, thermal analysis methodologies, cooling methods of an electric machine and finally the flow and heat transfer of a disc rotor were conducted. The losses value either sources from electrical or mechanical will be used as a input to the selected thermal analysis methodology.

Based on multiple example of lumped parameter (LP) thermal model presented here, it was found that the methodology is robust and has low requirement in computation time. However, it has two major drawback when applied to the axial flux permanent magnet machine where the first one is the thermal model requires accurate convective heat transfer coefficient either from experimental, CFD analysis or empirical correlations (Chong 2015). Based on the work of Spooner and Chalmers (1992) and Sahin (2001a), this analytical approach of predicting the thermal performance of an electric machine was strongly depends on the convection heat transfer input. Secondly, the thermal model could not include the actual rotational flow generated from the rotating rotor disc. Howey (2010) made a bold statement

suggesting that the LP of an airflow model for an AFPM machine needs to consider the complexity of the flow features, as the flow has a direct influence specifically on the stator heat transfer. On the other hand, numerical methods such as FEA and CFD offer high accuracy due to higher spatial resolution yet has a disadvantage of computational time.

Numerical methods allows accurate prediction of the electric machine temperature profile that is known to be difficult to be achieved by using LP thermal model. Howey (2010) also added that the LP thermal model highly relying on the input correlations such as thermal contact resistances, convective heat transfer coefficients and air flow model. Therefore, in this work, Computational Fluid Dynamics (CFD) is chosen to be the thermal analysis methodologies as it offers detail perspective in temperature distribution thus appropriate cooling mechanism can be propose appropriately.

Chapter 3

Computational Fluid Dynamics

3.0 Computational Fluid Dynamics

In this work, the thermal behaviour of the AFPM machine is modelled numerically using Computational Fluid Dynamics (CFD) software. The current chapter presents the governing equation of the fluid flow including the energy equation and turbulence modelling. The approach to numerically represent the rotation of the rotor components is also explained with regard to the Moving Reference Frame (MRF) approach implemented in the STAR-CCM+ v11.04 software. Additionally, the CFD modelling accuracy is briefly described. All theories presented here refer to the STAR-CCM+ user guide (2016) and the CFD textbooks of Anderson (1995), Vergteeg and Malalasakera (1995), Tu et al. (2008) and Hughes and Brighton (1999).

3.1 Governing equations

The root of fluid dynamics is based on the basic principles of mass conservative, Newton's second law and energy conservation. These principles are derived into the fundamental governing equation by the partial differential equation of the transport equations for the CFD formulation. Table 3-1 shows the relation between basic principles and the fluid dynamic's fundamental equation in CFD. In STAR-CCM+, this set of equations is

implemented via the finite volume method to a discretisation of the geometrical problem of the rotor cooling for the AFPM machine by dividing the flow domain into infinitesimally small control volumes called mesh/grids. This then allows a numerical conversion of the transport equations presented in a partial differential equation form into a system of linear algebraic equations that are able to calculate iteratively.

Table 3-1: Principle of physic derivation towards the fluid dynamics fundamental (Ransau 2011).

3.1.1 The Continuity Equation

3.1.1.1 Mass conservation

Mass conservation obeys the rule where the rate of change of mass in a control volume is equivalent to the mass flux that travels across a surface. The conservation of mass in Eulerian terms, can be presented by:

$$\frac{\partial \rho}{\partial t} + \nabla \cdot (\rho \, \mathbf{V}) = 0 \qquad \textbf{(Eq. 3-1)}$$

where $\mathbf{V}$, is the fluid velocity at any point in the fixed space. A steady flow will have $\partial \rho / \partial t = 0$ and an incompressible flow which has constant density allows further simplification as:

$$\nabla \cdot \mathbf{V} = 0 \qquad \textbf{(Eq. 3-2)}$$

The mass conservation can be expressed in the Cartesian coordinate system by the local velocity components of x, y, and z, hence it becomes:

$$\frac{\partial \rho}{\partial t} + \left[\frac{\partial(\rho u)}{\partial x} + \frac{\partial(\rho v)}{\partial x} + \frac{\partial(\rho w)}{\partial z}\right] = 0 \qquad \textbf{(Eq. 3-3)}$$

3.1.2 Navier-Stokes equations

The conservation of momentum can be described by the Navier-Stokes equations derived from Newton's second law for a two-dimensional viscous Newtonian fluid (for ease of understanding) as below, where ν is the kinematic viscosity, which is $\nu = \mu/\rho$:

$$\underbrace{\frac{\partial u}{\partial t}}_{\text{Local acceleration}} + \underbrace{u\frac{\partial u}{\partial x} + v\frac{\partial u}{\partial y}}_{\text{Advection term}} = \underbrace{-\frac{1}{\rho}\frac{\partial p}{\partial x}}_{\text{Pressure gradient}} + \underbrace{\nu\frac{\partial^2 u}{\partial x^2} + \nu\frac{\partial^2 u}{\partial y^2}}_{\text{Diffusion term}} \qquad \textbf{(Eq. 3-4)}$$

In Cartesian coordinate system of the three-dimensional velocity components as below where the S_M is the momentum source vectors corresponded to each coordinates:

- x-momentum

$$\rho\frac{Du}{Dt} = \frac{\partial(-p + \tau_{xx})}{\partial x} + \frac{\partial \tau_{yx}}{\partial y} + \frac{\partial \tau_{zx}}{\partial z} + S_{Mx} \qquad \textbf{(Eq. 3-5)}$$

- y-momentum

$$\rho\frac{Dv}{Dt} = \frac{\partial \tau_{xy}}{\partial x} + \frac{\partial(-p + \tau_{yy})}{\partial y} + \frac{\partial \tau_{zx}}{\partial z} + S_{My}$$

- z-momentum

$$\rho\frac{Dv}{Dt} = \frac{\partial \tau_{xz}}{\partial x} + \frac{\partial \tau_{yz}}{\partial y} + \frac{\partial(-p + \tau_{zz})}{\partial z} + S_{Mz}$$

3.1.3 The energy equation

The energy equation is derived from the first law of thermodynamics and the conservation of energy can be expressed for a two-dimensional (for ease of understanding) as:

$$\underbrace{\frac{DT}{Dt}}_{\text{Thermal change}} + \underbrace{u\frac{\partial T}{\partial x} + v\frac{\partial T}{\partial y}}_{\text{Thermal advection}} = \underbrace{\frac{\mathrm{k}}{\rho \mathrm{C_p}}\frac{\partial^2 T}{\partial x^2} + \frac{\mathrm{k}}{\rho \mathrm{C_p}}\frac{\partial^2 T}{\partial y^2}}_{\text{Thermal diffusion}} \quad \textbf{(Eq. 3-6)}$$

The rate of change of energy in the Cartesian frame is:

$$\rho\frac{DE}{Dt}\Delta x\Delta y\Delta z \quad \textbf{(Eq. 3-7)}$$

3.1.4 The segregated fluid flow model

The segregated flow model is used to model the rotor cooling for the AFPM machine because the flow problem in this study was considered as an incompressible flow. This is based on the expected velocity value that is not high enough to cause any changes to the fluid density. The segregated flow model is suitable for incompressible flow cases where the flow condition is equal or below a Mach number of 0.3 ($Ma \leq 0.3$). This model uses a predictor-corrector approach to link the continuity and momentum equations meaning it solves each component sequentially, hence this model is named segregated. The pressure and velocity functions are calculated iteratively and combined using the Semi-Implicit Method for Pressure Linked Equations *(SIMPLE)* algorithm, thus it runs faster compared to the couple flow model for an incompressible flow condition (Vergeeg and Malalasakera 1995). Figure 3-1 describes the sequence of *SIMPLE* algorithm steps for each solution update.

Figure 3-1: The SIMPLE algorithm steps (Vergeeg and Malalasakera 1995).

3.1.5 The equation of state: constant density model and ideal gas model

The segregated flow model (discussed in 3.1.4) is a pressure based model which is rooted in the constant density flows/model. The constant density model depends on two additional sub-solvers, namely the velocity solver and the pressure solver while assuming that the density is constant and unchanged throughout the continuum. On the other hand, the ideal gas model uses the ideal gas law to express the value of density with regard to temperature and pressure.

The density of the ideal gas model is calculated by:

$$\rho = \frac{p_{abs}}{RT} \quad \textbf{(Eq. 3-8)}$$

The p_{abs} is the absolute pressure calculated by $p_{abs} = p_{static} + p_{ref}$, where p_{static} is the static pressure and p_{ref} is the reference pressure. The R is the specific gas constant given by $R = R_u/M$ where R_u is the universal gas constant at 8314.4621J/kmol.K and M is the molecular weight.

Most of the work performed here, involves the constant density model as it is faster to converge especially at the initial stage, where the focus is on the flow characteristic and the energy equation is not included. This will reduce the computational time and produce faster simulation results because the air density is assumed to be invariant in the continuum (STAR-CCM+ 2016). This selection is only used in the simulation that focuses on the flow condition and did not include any thermal variation. However, in the subsequent phase of the study, the ideal gas model was chosen and the energy equation was included to analyse the thermal performance of the rotor cooling approach.

3.1.6 Buoyancy and gravity

Most of the work in this thesis did not include the buoyancy effect into the simulations. This is because in force convection, the effect of buoyancy is negligible. However, the buoyancy and gravity is included in the work of Section 5.4 where conjugate heat transfer is used to evaluate the heat transfer from the machine's cover to the surrounding air.

3.2 Heat transfer

The temperature differences between media allow the energy to transit from hot to cold. CFD allows the solving of multiple thermofluid problems involving heat conduction, convection and radiation phenomena. It is favourable for the thermal analysis of electrical machines mainly because of these capabilities. The thermodynamics analysis in an electrical machine is usually focused on the forced heat convection and heat conduction while assuming that the

effect of the radiation is infinitesimally small and often neglected (Pyrhonen et al. 2008; Chirila et al. 2011).

Heat conduction occurs in all forms of matter including solids and fluids (liquids and gases). Heat conduction in a solid is greater due to the closer location of adjacent atoms allowing for the better transmission of molecule vibrations and the diffusion of free electrons. In fluids, it is weaker due to the large spatial distances between the atoms. Heat conduction uses Fourier's law and can be presented in differential form as:

$$q" = -k\nabla T \qquad \textbf{(Eq. 3-9)}$$

where $q"$ is the local heat flux vector, k is the thermal conductivity and ∇T is the temperature gradient. The simulation of thermal analysis in an electrical machine includes this heat transfer mode to determine the heat flux from one medium to another, particularly where lamination and bonding agents are applied in a machine design that is known to have poor thermal conductivity and may limit the heat transfer capability.

Heat convection is usually employed in the simulation of an engineering application involving a cooling analysis. This mode of heat transfer is highly dependent on the movement of the fluid because the energy transfer is due to diffusion and advection. In the thermal analysis of an electrical machine, the convection is often referred to as forced heat convection as the fluid is stirred by the rotational motion of the rotor. Convective heat transfer can be presented as:

$$q_s" = h_c(T_s - T_{ref}) \qquad \textbf{(Eq. 3-10)}$$

where $q_s"$ is the local surface heat flux, h_c is the local convective heat transfer coefficient, T_s is the surface temperature and T_{ref} is a characteristic temperature of fluid moving on the surface. The expression based on Newton's law of cooling has a liner relationship, although in reality it is nonlinear because the flow conditions can differ on the surface associated

with the local control volume and time. Moreover, most CFD software allows the heat transfer model to be included separately from the fluid flow model in order to solve the multi-physics problems based on the intended application.

3.2.1 Fluid Energy Modelling: segregated fluid temperature

The segregated fluid temperature was selected to model the convection of the cooling fluid in order to include heat transfer in the simulation. This model solves the energy equation using the temperature variables, then converts it into enthalpy using the equation of state. The total energy E can be expressed as the following equation:

$$E = H_t - \frac{p}{\rho} \quad \textbf{(Eq. 3-11)}$$

where H_t is the total enthalpy is given by:

$$H_t = h + \frac{|v|^2}{2} \quad \textbf{(Eq. 3-12)}$$

and the enthalpy h can be calculated by the specific heat C_p and the changes of temperature ΔT as:

$$h = C_p \, \Delta T \quad \textbf{(Eq. 3-13)}$$

Adding the segregated fluid temperature to the simulation allows the temperature variables to be inputted to the boundary conditions that need to be specified. This can be in the form of:

- Temperature
    - Static temperature on a specific wall (in ºC or K).
- Thermal energy generation
    - Heat flux - Thermal energy per unit area on a specific wall (in W/m^2).
    - Volumetric heat - Thermal energy per unit volume of a medium (in W/m^3).

- Specific heat - Thermal energy per unit weight of a medium (in W/kg).

- Heat source
  - Simply the energy amount produced by a medium (in W).

In this study, the temperature variables are inputted to the boundary conditions using either static temperature for simplicity or a heat source for an accurate prediction of the losses produced from the components.

3.2.1.1 Heat source – via FEA

The input heat source values in this work were based on electromagnetic Finite Element Analysis (FEA) simulations on particular continuous performance namely 50kW and 150kW. Detailed description of this input heat source by FEA is described in Section 5.1. The values were inputted in the simulation on *'Energy Source Option'* for corresponded components that are magnets and rotor losses.

3.2.2 The dimensionless parameters

3.2.2.1 The Reynolds number

The Reynolds number Re represents the flow characteristic which is defined as the ratio of the inertia force over the viscous force and can be expressed as:

$$Re = \frac{\rho V L}{\mu} = \frac{\rho V d_h}{\mu} \quad \textbf{(Eq. 3-14)}$$

where ρ is the fluid density, V is velocity, L is the characteristic length of the domain or d_h is the hydraulic diameter and μ is the dynamic viscosity. The Reynolds number of the ducting in this study is calculated using the hydraulic diameter for the inlet rectangular tube d_h by Eq. 3-17. However, the local Reynolds number of the rotating rotor disc Re_θ is represented by Eq. 3-16.

$$d_h = \frac{2ab}{(a+b)} \quad \textbf{(Eq. 3-15)}$$

$$Re_\theta = \frac{\omega \cdot r^2}{\nu} \quad \textbf{(Eq. 3-16)}$$

where a and b are the length and width respectively, ω is the rotor angular velocity, r is the local rotor radius and ν is the kinematic viscosity of the bulk air.

The flow regime for the rotor cooling application can be considered based on the study of Gregory et al. (1955), as tabulated in Table 3-2.

Table 3-2: Flow regime given by Gregory, Stuart and Walker (1955).

3.2.2.2 The Nusselt number

The Nusselt number is a dimensionless parameter that is commonly associated with convective heat transfer problems. It is the ratio of heat convection over heat conduction normal to the boundary. It has a close relation to the Reynolds number and Prandtl number by multiplying the convective heat transfer coefficient h_c with the characteristic length scale L over the thermal conductivity k, as:

$$Nu = \frac{h_c L}{k} \quad \textbf{(Eq. 3-17)}$$

3.2.2.3 Prandtl number

The ratio between the molecular diffusivity of momentum (kinematic viscosity) over the molecular diffusivity of heat is presented by the Prandtl number and is defined as:

$$Pr = \frac{\nu}{\alpha} = \frac{\mu C_p}{k} \quad \textbf{(Eq. 3-18)}$$

where α is the thermal diffusivity. In a heat transfer study, the dimensionless Prandtl number measures the growth of velocity and the thermal boundary layers and can determine the thermal conductivity of gasses.

3.3 Turbulence modelling

A domain with an obstruction causes a fluctuation of the velocity field in three dimensional spaces and generates turbulence. Even with a flat plate, as the flow travels along the surface, it changes from laminar to turbulent. The transition of the flow and the location of the transition point can be determined using the Reynolds number. Turbulence occurs when the momentum of the fluid becomes high enough to overcome its viscous damping. Chen and Jaw (1998) stated that this irregularity phenomenon can be predicted by a mathematical model, due to the inherently non-linear Navier-Stoke equations when the Reynolds number is above the critical value.

Modelling turbulence behaviour accurately in instantaneous conditions is very expensive computationally. Therefore, time-average results are usually preferred. This approach reduces the computational cost by removing the small scale of turbulence (which is not resolved) and making an approximate assumption of the values based on the pressure field and the local velocity based on the Navier-Stoke equations. The Reynolds stress tensor is introduced in the Navier-Stoke equations to include the momentum transport equation in the calculation, hence becoming Reynolds-Averaged Navier-Stokes (RANS) equations. The Reynolds stress tensor is defined as:

$$T_t \equiv -\rho\overline{v'v'} = -\rho\begin{bmatrix}\overline{u'u'} & \overline{u'v'} & \overline{u'w'}\\ \overline{u'v'} & \overline{v'v'} & \overline{v'w'}\\ \overline{u'w'} & \overline{v'w'} & \overline{w'w'}\end{bmatrix} \quad \textbf{(Eq. 3-19)}$$

STAR-CCM+ provides two approaches to model the Reynolds stress tensor T_t in terms of the mean flow quantities either by the Eddy viscosity models or the Reynolds stress transport models (STAR-CCM+ 2016). The Eddy viscosity models use Boussinesq approximation to relate the Reynolds stress

tensor T_t with the strain tensor S, the turbulent viscosity μ_t and the turbulent kinetic energy k_e. It is then derived in an additional transport equation for scalar quantities by the turbulence model. The Boussinesq approximation is presented as:

$$T_t = 2\mu_t\, S - \frac{2}{3}(\mu_t \nabla \cdot \mathrm{v} + \rho \mathrm{k_e})\mathrm{I} \qquad \textbf{(Eq. 3-20)}$$

$$S = \frac{1}{2}(\nabla \mathrm{v} + \nabla \mathrm{v}^T) \qquad \textbf{(Eq. 3-21)}$$

None of the available turbulence models is universal. Each model has been designed to suit specific applications and flow conditions. For this reason, the validation and verification of a selected turbulence model is required in order to represent the actual physical characteristics. STAR-CCM+ offers multiple turbulence models to be selected from one-equation, two-equation, nonlinear eddy viscosity models and Reynolds Stress Models (RSM). The applications of four major turbulence models available in STAR-CCM+ are described briefly in Table 3-3.

Table 3-3: Turbulence models available in STAR-CCM+ v11.04 with their recommended applications (STAR-CCM+ 2016).

Turbulence Model	**Application**
Spalart-Allmaras models	Suitable where flows near the boundary layer are attached and mild separation occurs. Not suitable for flow dominated by free-shear layers, complex recirculation or natural convection.
k-ε models	Suitable for complex flows of industrial-type applications especially for planar shear layers problems with a small pressure gradient. Not suitable for high pressure gradient flow conditions.

k-ω models	Suitable for internal flow with a high pressure gradient, separated flow and jets flow. Produces an unsteady iteration and takes a longer time for the solution to converge in some cases.
Reynolds stress transport models	Suitable for a strong anisotropic flow such as cyclone separator yet is computationally expensive.

Apart from these four main classes of turbulence models, STAR-CCM+ also provides further advanced derivations of turbulence models to be selected. In this study, the complex flow of the rotor cooling technique for the AFPM machine was predicted with multiple turbulence models to assess and seek a suitable modelling approach that will provide results close to the experimental data. The chosen turbulence models are namely:

- k-ε: Realizable k-ε models (see Section 3.3.1),
- k-ω: Shear-Stress Transport (SST) (see Section 3.3.2), and
- v^2f models (see Section 3.3.3).

3.3.1 The Realizable k-ε turbulence model

The Realizable k-ε turbulence model was developed by Shih et al. (1994) and is an improvement on the standard k-ε. This turbulence model has improved the predictions for the spreading rate of both the planar and round jets by introducing a new transport equation for the turbulent dissipation rate ϵ. Also, the turbulent viscosity μ_t has a new formulation which contains the coefficient of the turbulent viscosity C_μ, thus the model is able to accurately predict rotational flow, separation, recirculation and flow near the boundary layers under strong adverse pressure gradients (STAR-CCM+ 2016).

The transport equations for the standard k-ε model were modified for the Realizable k-ε model and are presented in Eq. 3-24 and Eq. 3-25. The new formulation includes a curvature correction factor f_c in the turbulence kinetic

energy and turbulent dissipation rate prediction as follows (STAR-CCM+ 2016):

$$\frac{\partial}{\partial t}\int_V \rho k_e \, dV + \int_A \rho k_e \left(\mathbf{v} - \mathbf{v}_g\right) \cdot d\mathbf{a} \qquad \textbf{(Eq. 3-22)}$$

$$= \int_A \left[\mu + \frac{\mu_t}{\sigma_k}\right] \nabla k_e \cdot d\mathbf{a} + \int_V \left[f_c \, G_k + G_b - \rho\left((\varepsilon - \epsilon_0) + \Upsilon_M\right) + S_k\right] dV$$

$$\frac{\partial}{\partial t}\int_V \rho\epsilon \, dV + \int_A \rho\epsilon \left(\mathbf{v} - \mathbf{v}_g\right) \cdot d\mathbf{a} \qquad \textbf{(Eq. 3-23)}$$

$$= \int_A [\mu + \frac{\mu_t}{\sigma_k}] \nabla\epsilon \cdot d\mathbf{a}$$

$$+ \int_V \left[f_c C_{\epsilon_1} S\epsilon + \frac{\epsilon}{k_e}\left(C_{\epsilon_1} C_{\epsilon_3} G_b\right) - \frac{\epsilon}{k_e + \sqrt{v\epsilon}} C_{\epsilon_2} \rho(\epsilon - \epsilon_0) + S_\epsilon\right] dV$$

where G_k is the generation of turbulence kinetic energy due to mean velocity gradients, G_b is the generation of the buoyancy production term, S_k and S_ϵ are the source terms input by the user, while ϵ_0 is the ambient turbulence value in the source terms that responds to the turbulence decay.

The turbulence kinetic energy production of G_k has remained the same as in the standard k-ε model (Eq. 3-24), where $\nabla \cdot \mathbf{v}$ is the velocity divergence and S is the modulus of mean strain rate tensor:

$$G_k = \mu_t S^2 - \frac{2}{3}\rho k \nabla \cdot \mathbf{v} - \frac{2}{3}\mu_t (\nabla \cdot \mathbf{v})^2 \qquad \textbf{(Eq. 3-24)}$$

$$S = |\mathbf{S}| = \sqrt{2\mathbf{S}:\mathbf{S}^T} = \sqrt{2\mathbf{S}:\mathbf{S}} \qquad \textbf{(Eq. 3-25)}$$

$$\mathbf{S} = \frac{1}{2}(\nabla\mathbf{v} + \nabla\mathbf{v}^T) \qquad \textbf{(Eq. 3-26)}$$

If the buoyancy effect is included, the buoyancy production term G_b is defined equivalent to standard k-ε as:

$$G_b = \beta \frac{\mu_t}{\sigma_t} (\nabla T \cdot \mathbf{g}) \quad \textbf{(Eq. 3-27)}$$

where β is the coefficient of thermal expansion using the Boussinesq approximation for constant density flows, ∇T is the temperature gradient vector, $\mathbf{g}$ is the gravitational vector and σ_t is the turbulent Prandtl number.

STAR-CCM+ computes the coefficient $C_{\epsilon 3}$ by Eq. 3-30 or else it can be specified as a constant as in Eq. 3-31:

$$C_{\epsilon 3} = \tanh \frac{|\mathbf{v}_b|}{|\mathbf{u}_b|} \quad \textbf{(Eq. 3-28)}$$

$$C_{\epsilon 3} = \begin{cases} 1 & for\ G_b \geq 0 \\ 0 & for\ G_b < 0 \end{cases} \quad \textbf{(Eq. 3-29)}$$

The Realizable k-ε has also introduced a new formulation for the coefficient of turbulent viscosity C_μ , rather than a constant value as in standard k-ε. The turbulent viscosity μ_t includes C_μ and is presented as:

$$\mu_t = \rho\, C_\mu \frac{{k_e}^2}{\epsilon} \quad \textbf{(Eq. 3-30)}$$

$$C_\mu = \frac{1}{A_0 + A_s\, U^{(*)} \frac{k_e}{\epsilon}} \quad \textbf{(Eq. 3-31)}$$

$$U^{(*)} = \sqrt{\mathbf{S}:\mathbf{S} - \mathbf{W}:\mathbf{W}} \quad \textbf{(Eq. 3-32)}$$

where $\mathbf{S}$ and $\mathbf{W}$ are the strain rate tensor and rotation rate tensor respectively as in Eq, 3-28. The coefficients related to the turbulent viscosity calculation are as below, with the mean strain rate tensor S equal to Eq. 3-27:

$$A_s = \sqrt{6} \cos \phi$$
$$\phi = \frac{1}{3} \mathrm{acos}\left(\sqrt{6}\, W\right) \quad \textbf{(Eq. 3-33)}$$

$$W = \frac{S_{ij}\, S_{jk}\, S_{ki}}{\sqrt{S_{ij}\, S_{ij}^3}}$$

$$A_0 = 4.0$$

Other coefficients involved in this turbulence model are:

$$C_{\epsilon 1} = \max\left(0.43, \frac{\eta}{5+\eta}\right)$$

$$\eta = \frac{Sk}{\epsilon} \qquad \textbf{(Eq. 3-34)}$$

$$C_{\epsilon 2} = 1.9\,, \qquad \sigma_k = 1.0, \qquad \sigma_\epsilon = 1.2$$

3.3.2 The Shear-Stress Transport (SST) k-ω turbulence model

To improve the k-ω turbulence model's capability, Menter (1993) introduced the k-ω SST model by combining k-ω with the robustness of the k-ε model. This turbulence model provides better predictions of the amount of flow separation at adverse or high pressure gradients. This increase in prediction accuracy is from the presence of shear-stress transport (SST) in the eddy-viscosity formulation and the better-developed prediction in the near-wall region.

The k-ω SST model switches between the k-ω and k-ε turbulence models within the domain to bring out the best of both functions. k-ω SST employs k-ω at the near wall region while k-ε is used in the free-stream and the far field region. The formulations of the k-ω SST model are presented below based on STAR-CCM+ (2016).

$$\frac{\partial}{\partial t}\int_V \rho k_e \; dV + \int_A \rho k_e \left(\mathbf{v} - \mathbf{v}_g\right) \cdot d\mathbf{a} \qquad \textbf{(Eq. 3-35)}$$

$$= \int_A \left(\mu + \sigma_k \mu_t\right) \nabla k_e \; \cdot d\mathbf{a} + \int_V \left(\gamma_{eff} G_k - \gamma' \rho \beta^* f_{\beta^*} (\omega k - \omega_0 k_0) + S_k\right) \; dV$$

$$\frac{\partial}{\partial t}\int_V \rho\omega \; dV + \int_A \rho\omega \left(\mathbf{v} - \mathbf{v}_g\right) \cdot d\mathbf{a} \qquad \textbf{(Eq. 3-36)}$$

$$= \int_A (\mu + \sigma_\omega \mu_t) \nabla\omega \cdot d\mathbf{a} + \int_V \left(G_\omega - \rho\beta f_\beta(\omega^2 - \omega_0^2) + D_\omega + S_\omega\right) dV$$

where G_k is the generation of turbulence kinetic energy due to the mean velocity gradients, G_ω is the generation of the turbulence specific dissipation rate ω and S_k and S_ϵ are the source terms input by the user. The ϵ_0 is the ambient turbulence value in the source terms that responds to the turbulence decay.

In addition to the standard k-ω turbulence model, the γ_{eff} is the effective intermittency provided by the Gamma ReTheta Transition model and the γ' expressed as Eq. 3-39 below.

$$\gamma' = \min\left[\max\left(\gamma_{eff}, 0.1\right), 1\right] \qquad \textbf{(Eq. 3-37)}$$

The turbulent kinetic energy production of G_k has remained the same as the standard k-ε model (Eq. 3-24). However, the production of the turbulence specific dissipation rate G_ω is changed and defined as:

$$G_\omega = \rho\gamma\left[\left(s^2 - \frac{2}{3}(\nabla \cdot \mathbf{v})^2\right) - \frac{2}{3}\omega\nabla \cdot \mathbf{v}\right] \qquad \textbf{(Eq. 3-38)}$$

where γ is a blended coefficient and the modulus of the mean strain rate tensor S as in Eq. 3-28.

The cross-derivative term D_ω is defined as:

$$D_\omega = 2(1 - F_1)\rho\sigma_{\omega 2}\frac{1}{\omega}\nabla k_e \cdot \nabla\omega \qquad \textbf{(Eq. 3-39)}$$

The turbulent viscosity μ_t is defined as:

$$\mu_t = \rho k T_t \qquad \textbf{(Eq. 3-40)}$$

where T_{ts} is the turbulent time scale based on Durbin's Realizability constraint as:

$$T = \begin{cases} \min\left(\frac{\alpha^*}{\omega}, \frac{a_1}{SF_2}\right) & without\ realizable\ scale \\ \min\left(\frac{1}{\max\left(\frac{\omega}{\alpha^*}, \frac{SF_2}{a_1}\right)}, \frac{C_T}{\sqrt{3}S}\right) & with\ realizable\ scale \end{cases} \quad \textbf{(Eq. 3-41)}$$

The blending functions F_1 and F_2 are given by:

$$F_1 = \begin{cases} \tanh(\arg_1 4) & without\ the\ \gamma - Re_\theta\ model \\ \max\left(\tanh\left(\arg_1 4\right), \exp\left[-\left(\frac{Re_T}{120}\right)^8\right]\right) & without\ the\ \gamma - Re_\theta\ model \end{cases} \quad \textbf{(Eq. 3-42)}$$

where

$$\arg_1 = mi(\max\left(\frac{\sqrt{k}}{0.09\omega y}, \frac{500v}{y^2\omega}\right), \frac{2k_e}{y^2 CD_{k\omega}} \quad \textbf{(Eq. 3-43)}$$

and

$$CD_{k\omega} = \max\left(\frac{1}{\omega}\nabla k \cdot \nabla\omega, 10^{-20}\right) \quad \textbf{(Eq. 3-44)}$$

while

$$F_2 = \tanh(\arg_2 2) \quad \textbf{(Eq. 3-45)}$$

where

$$\arg_2 = \max\left(\frac{2\sqrt{k}}{\beta^*\omega y}, \frac{500v}{y^2\omega}\right) \quad \textbf{(Eq. 3-46)}$$

and y is the distance to the nearest wall. Other coefficients involved in this model are given below:

$$a_1 = 0.31 \quad \textbf{(Eq. 3-47)}$$

$$\phi = F_1\phi_1 + (1 - F_1)\phi_2 \qquad \textbf{(Eq. 3-48)}$$

where the coefficients of set ϕ_1 are:

$$\beta_1 = 0.075\ , \qquad \sigma_{k1} = 0.85\ , \qquad \sigma_{\omega 1} = 0.5$$
$$\kappa = 0.41\ , \qquad \gamma_1 = \frac{\beta_1}{\beta^*} - \sigma_{\omega 1}\frac{\kappa^2}{\sqrt{\beta^*}} \qquad \textbf{(Eq. 3-49)}$$

and the coefficients of set ϕ_2 are:

$$\beta_2 = 0.0828\ , \qquad \sigma_{k2} = 1.0\ , \qquad \sigma_{\omega 2} = 0.856$$
$$\kappa = 0.41\ , \qquad \gamma_2 = \frac{\beta_2}{\beta^*} - \sigma_{\omega 2}\frac{\kappa^2}{\sqrt{\beta^*}} \qquad \textbf{(Eq. 3-50)}$$

Both sets of ϕ_1 and ϕ_2 share the same coefficient value as:

$$\beta^* = 0.09\ , \qquad \alpha^* = 1 \qquad \textbf{(Eq. 3-51)}$$

3.3.3 The v^2f turbulence model

The final selection of turbulence model involved in this study is the v^2f k-ε model which was generally proposed for low-Reynolds number applications. This turbulent model includes two additional turbulence quantities in addition to k and ϵ of the standard k-ε model. These two additional quantities are the normal stress function (also known as the velocity scale) $\overline{v^2}$ and the elliptic relaxation function f to improve the prediction of flows dominated by separation, especially near-wall turbulence effects. The formulation of the v^2f k-ε model is presented as:

$$\frac{\partial}{\partial t}\int_V \rho k_e\ dV + \int_A \rho k_e\left(\mathbf{v} - \mathbf{v}_g\right)\cdot d\mathbf{a} \qquad \textbf{(Eq. 3-52)}$$
$$= \int_A \left[\mu\ + \frac{\mu_t}{\sigma_k}\right]\nabla k_e\ \cdot d\mathbf{a} + \int_V \left[\ G_k\ + G_b - \rho\big((\varepsilon - \epsilon_0) + \ \Upsilon_M\big) + S_k\right]\ dV$$

$$\frac{\partial}{\partial t}\int_V \rho\epsilon \; dV + \int_A \rho\epsilon \left(\mathbf{v} - \mathbf{v}_g\right)\cdot d\mathbf{a} \tag{Eq. 3-53}$$

$$= \int_A \left[\mu + \frac{\mu_t}{\sigma_k}\right]\nabla\epsilon \cdot d\mathbf{a} + \int_V \left[\rho C_{\epsilon_1}\left(1 + a\sqrt{\frac{k}{\overline{v^2}}}\right)\frac{G_k}{T} - \rho C_{\epsilon 2}(\epsilon - \epsilon_0)\frac{\epsilon}{k} + S_\epsilon\right] dV$$

$$\frac{\partial}{\partial t}\int_V \rho\overline{v^2} \; dV + \int_A \rho\overline{v^2} \left(\mathbf{v} - \mathbf{v}_g\right)\cdot d\mathbf{a} \tag{Eq. 3-54}$$

$$= \int_A \left[\mu + \frac{\mu_t}{\sigma_k}\right]\nabla\overline{v^2} \cdot d\mathbf{a} + \int_V \left[\rho \, min\left\{k_e f, -\frac{1}{T}[(C_1 - 6)\overline{v^2} - \frac{2k}{3}(C_1 - 1)C_2 G_k\right\} - \frac{6\rho\overline{v^2}\epsilon}{k} + S_{\overline{v^2}}\right] dV$$

$$\int_A L^2\nabla f \cdot d\mathbf{a} + \int_V \left[-f + \frac{1}{T}(C_1 - 1)\left(\frac{2}{3} - \frac{\overline{v^2}}{k}\right) + \frac{C_2 C_{\mu_{\overline{v^2}}}\overline{v^2}\mathbf{S}^2}{\epsilon} + \frac{5\overline{v^2}}{k_e T} + S_f\right] dV = 0 \tag{Eq. 3-55}$$

where G_k is the generation of turbulence kinetic energy due to the mean velocity gradients, G_b is the generation of the buoyancy production term, S_k, S_ϵ, $S_{\overline{v^2}}$ and S_f are the source terms input by the user and ϵ_0 is the ambient turbulence value in the source terms that responds to the turbulence decay. The generation of turbulence kinetic energy G_k and the generation of the buoyancy production term G_b is presented in Eq. 3-26 and Eq 3-29

respectively. This turbulence model computes the turbulent viscosity μ_t differently in relation to its own definition of the turbulent time scale T_{ts} as:

$$\mu_t = \rho\, T \min\left(C_{\mu_{std}} k, C_{\mu_{v^2}} v^2\right) \quad \textbf{(Eq. 3-56)}$$

$$T = \begin{cases} \max\left(\dfrac{k_e}{\epsilon}, C_t\sqrt{\dfrac{v}{\epsilon}}\right) & without\ realizable\ scale \\ \max\left(min\left(\dfrac{k}{\epsilon}, \dfrac{\alpha k}{\sqrt{3}C_{\mu_{v^2}}\overline{v^2}\mathbf{S}^2}\right), C_t\sqrt{\dfrac{v}{\epsilon}}\right) & with\ realizable\ scale \end{cases} \quad \textbf{(Eq. 3-57)}$$

The turbulent length scale L_t is:

$$L_t = C_L \max\left(min\left(\frac{{k_e}^{3/2}}{\epsilon}, \frac{{k_e}^{3/2}}{\sqrt{3}C_{\mu_{v^2}}\overline{v^2}\mathbf{S}^2}\right), C_\eta\left(\frac{v^3}{\epsilon}\right)^{\frac{1}{4}}\right) \quad \textbf{(Eq. 3-58)}$$

Other coefficients involved in this turbulence model are:

$$a = 0.045, \quad \alpha = 0.6, \quad C_{\epsilon 1} = 1.4,, \quad C_{\epsilon 2} = 1.9$$

$$C_{\mu_{std}} = 0.09, \quad C_{\mu_{v^2}} = 0.22, \quad \sigma_k = 1.0 \quad \sigma_\epsilon = 1.3 \quad \textbf{(Eq. 3-59)}$$

$$C_1 = 1.4, \quad C_2 = 0.3, \quad C_\eta = 70.0, \quad C_t = 6.0, \quad C_L = 0.23$$

3.3.4 The non-dimensional wall distance, y^+

The non-dimensional wall distance y^+ is used to determine an estimated value of the first cell thickness y. The estimation of y from the target y^+ value can be done by using the formulae below:

$$y^+ = \frac{yu^*}{v} \quad ; \quad u_\tau \approx \sqrt{\frac{\bar{\tau}_w}{\rho}} \quad \textbf{(Eq. 3-60)}$$

Where $y^+$is the dimensionless wall distance, y is the first cell distance to the wall, u^* is the friction velocity near to the wall, v is the kinematic viscosity of air, ρ is the air density and τ_w is the wall shear stress that is related to the skin friction C_f, in relation to the velocity component u, as follows:

$$\overline{C_f} = \frac{\bar{\tau}_w}{\rho u^2/2} \quad \textbf{(Eq. 3-61)}$$

The skin friction coefficient $\overline{C_f}$ for the pipe flow application can be estimated by Eq. 3-64 while for the rotating rotor application, the local Reynolds number Re_θ can be represented by Eq. 3-18.

$$\frac{\overline{C_f}}{2} = \frac{0.039}{Re_D^{1/5}} \quad \textbf{(Eq. 3-62)}$$

3.3.5 Near wall treatment

The turbulent flow near a flat wall can be divided into four regimes. The velocity is equal to zero at a wall with a no-slip condition. As the fluid volume moves away from the wall, the velocity is increased linearly and this region is called the viscous/laminar sublayer. Above this, a region called the buffer layer is formed where the flow now begins to transition from laminar to turbulent flow. The viscous sublayer and the buffer layer are within the log-law region where it is 100 times the wall distance before reaching a free-stream region. This log-law region is dominated by the turbulent flow with the average flow velocity related to the log of the wall distance. Figure 3-2 shows the graphical explanation of these four flow regions.

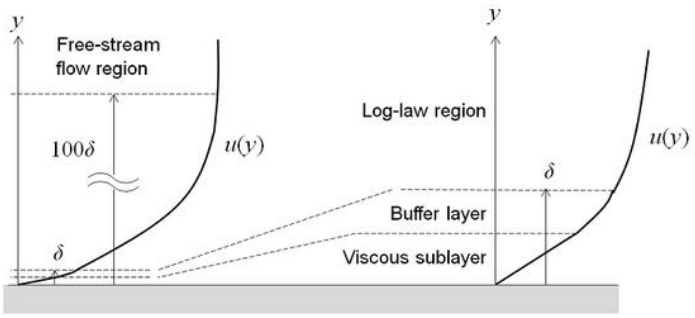

Figure 3-2: Regimes of turbulent flow (Frei 2013).

Based on this theory, a mathematical assumption was made to model the flow regime of the viscous sublayer and the buffer layer as 'near wall treatment' or 'wall functions'. Figure 3-3 shows the region and the effect of

the velocity profile by the computed flow field using the wall functions method. The assumption allows a faster prediction instead of resolving this region explicitly, which is computationally expensive. In the RANS model, a non-zero fluid velocity is used to compute this near wall flow region with the relation to the higher flow region based on a selected wall treatment type.

Figure 3-3: Wall functions assumption (Frei 2013).

Three types of wall treatment are available, while the wall treatment options in STAR-CCM+ are shown in Table 3-4. STAR-CCM+ computes the wall treatment based on the selected turbulence model by performing the following functions:

- Specifies the friction velocity u^* as the reference,
- Computes a value of turbulent production G_k as in Eq 3-24,
- For the turbulent model based on k-ε (Realizable k-ε and v^2f).
    - Computes a value of turbulent dissipation ϵ based on Eq. 3-23.
- For the turbulent model based on k-ω (SST).
    - Computes a value of specific dissipation ω based on Eq. 3-36.

Table 3-4: Wall treatment options and their definitions available in STAR-CCM+ (STAR-CCM+ 2016).

Wall Treatment Options	Definitions
High-y+ Wall Treatment	Traditional wall function approach by placing the near-wall cell centroid of the control volume in the log-law region. This requires the first cell to be between $30 \leq y^+ \leq 100$.
Low-y+ Wall Treatment	For low-Re applications, this wall treatment assumes that the mesh resolves the viscous sublayer and has adequate cells within the boundary layer. A typical first cell is $y^+ \approx 1$.
All-y+ Wall Treatment	Based on both the above approaches, this wall treatment is a treatment hybrid that shifts between the high-y+ and low-y+ wall function calculations to give accurate results.
Two-Layer All y+ Wall Treatment (only for K-ε models)	Identical to the All-y+ Wall Treatment, but includes the wall boundary condition for ϵ.

The friction velocity u^* can be calculated referring to the wall law and the dimensionless numbers are expressed as below in relation to the y^+ in Eq. 3-63:

$$u^+ = \frac{\bar{u}}{u^*} \quad \textbf{(Eq. 3-63)}$$

where u^+ is the non-dimensional velocity and $\bar{u}$ is the mean velocity parallel to the wall. The relationship between the non-dimensional velocity u^+ and the non-dimensional wall distance y^+ is presented in Figure 3-4 where:

- For a viscous sublayer of $y^+ < 5$:

$$u^+ = y^+ \quad \textbf{(Eq. 3-64)}$$

- For a log-law layer of $y^+ > 30$:

$$u^+ = \frac{1}{K}\ln\left(E' y^+\right) \quad \textbf{(Eq. 3-65)}$$

$$E' = \frac{E_t}{f_r} \quad \textbf{(Eq. 3-66)}$$

The constant value $K = 0.42$, the turbulent wall function coefficient $E_t = 9.0$ and the roughness function $f_r = 1$, for a smooth wall set by default.

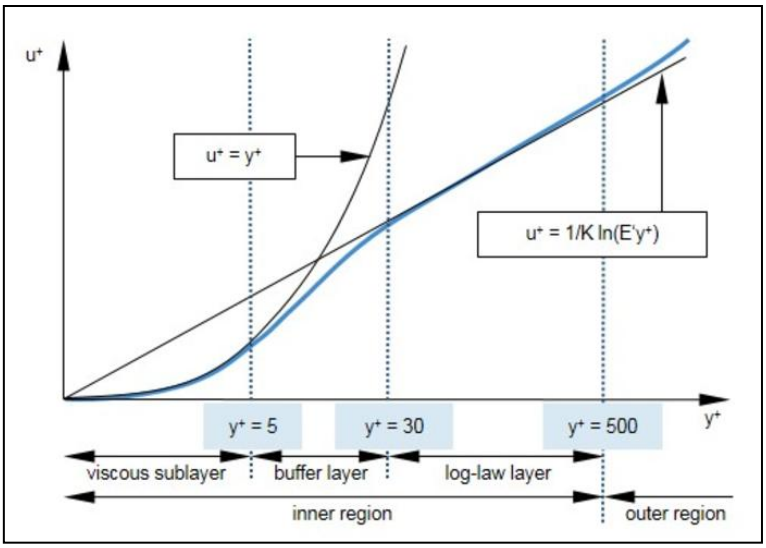

Figure 3-4: The relationship of non-dimensional velocity u^+ as a function of y^+ (STAR-CCM+ 2016).

3.4 Rotational modelling

In CFD, the rotational motion of a physical component can be modelled in several ways, where the motion is defined as the movement or the changes in the location relative to the frame of reference. This is useful for the thermal analysis of electrical machines because the rotational motion of the rotor influences the interior air of the machine. The various categories of modelling the rotational motion via CFD are:

1. Rotational interface
    a. The rotational body is represented by a domain or a wall instead of an actual CAD representation.
    b. This domain is set with specific rotating parameters equivalent to the rotational body, e.g. fan curves.
2. Moving Reference Frame (MRF)
    a. MRF is used to mimic the rotational motion of fluid without moving the mesh explicitly.
    b. This modelling approach allows rotational study to be conducted in a steady state solution without the high computational costs of unsteady/transient simulation.
3. Mesh displacement in real time (also known as sliding-mesh)
    a. The geometrical model represented by the mesh is moved explicitly with an actual displacement of mesh vertices around a specified axis.
    b. This method works only with transient analysis.

Figure 3-5 explains the types of available rotational motion modelling with their brief advantages and disadvantages. In this study, the MRF approach is selected to model the rotational motion of the rotor assembly because it has acceptable fidelity with fair computational costs. Mlinaric and Sebben (2008) recommended the MRF model to be used in simulating the rotation of spoked rims for simplicity, as it can be as good as a sliding mesh (unsteady or transient) simulation. Transient simulation of a wheel-rotating model by Modlinger et al (2008) shows that the complex flow field can be captured in detail, yet questioning the computational cost. Landstrom et at (2010) performed a comparative study between MRF and transient sliding mesh simulations and suggest that the MRF approach should be taken as a best practise when it comes to cost effectiveness and accuracy.

The rotor assembly has surface mounted magnets and a disc rotor in Chapter 5.0 while in the advanced study in Chapter 6.0; a fan design is attached to promote the rotor cooling technique into the system.

Figure 3-5: Types of rotational motion modelling (Siemans PLM Software 2015).

3.4.1 The Moving Reference Frame (MRF) model

The Moving Reference Frame (MRF) is a model that represents the rotational region as a rotating body with respect to the reference frame. This model assumes that the angular velocity is constant (as it is solved in a steady state condition) and the mesh is fixed and rigid. The rotational domain of MRF is calculated by modifying the conservative law where the fictitious centrifugal force is included in the domain and the fluid behaviour is altered along the rotating region. Theoretically, no explicit rotor/fan geometry is required when using the MRF function, but only the rotational domain in cylindrical form that covers the volume of the rotating body. This produces low fidelity at a lower computational cost. However, the rotor cooling technique proposed in this work consists of various fan blade types that have individual curvature profiles, therefore the CAD model has to be included in the rotating motion domain. With the CAD model included, the simulation will include the solid void of the rotor when deriving the rotating force and other variables, thus the accuracy of the model is improved and will produce a result that has characteristics based on the fan blade design.

The formulation of MRF refers to the continuity equation of the incompressible Navier-Stokes equation presented in Eq. 3-4 with the absolute velocity formulation as:

$$\frac{\partial \mathbf{V}}{\partial t} + \frac{d\boldsymbol{\omega}_p}{dt} \times \mathbf{r} + \nabla \cdot \left(\mathbf{u}_p \otimes \mathbf{V}\right) + \boldsymbol{\omega}_p \times \mathbf{V} = -\nabla\left(\frac{\mathrm{p}}{\rho}\right) + \nu \nabla \cdot \nabla \mathbf{V} \qquad \textbf{(Eq. 3-67)}$$

where $\boldsymbol{\omega}_p$ is the angular velocity of MRF, $\mathbf{r}$ is the position vector from the origin of MRF, $\mathbf{u}_p$ is the convection velocity relative to the MRF and the fluid velocity $\mathbf{V}$ has become the absolute velocity.

3.5 Convergence criterion

In this doctoral project, all excises has varied objective yet shared similar convergence criterion that was set to 1×10^{-4} apart from the iteration value base on the intended objective. Convergence criterion can be the temperature variables, flow variables such as mass flow rate and pressure or the windage losses. On the other hand, the iteration value on most of the work is set at 10,000 iterations while 20,000 iterations applied on the conjugate heat transfer (CHT) study which known to take more simulation time due to solving heat transfer without flow condition.

3.6 CFD modelling accuracy (uncertainty and error)

The numerical solution of CFD modelling may differ from the exact value of actual physics due to uncertainty and error. Based on the AIAA Guideline (1998), the definition of the uncertainty is the potential deficiency in the numerical modelling due to a lack of knowledge in the actual physics problem. The definition of an error is a recognisable deficiency in the numerical modelling of a known assumption and is not due to a lack of knowledge, Errors are a recognisable deficiency and can be classified as acknowledged and unacknowledged errors. Table 3-5 summarises the errors in CFD modelling.

Table 3-5: Type of systematic errors (NASA 2008).

Error		Error Cause
Acknowledged Error	Physical and geometrical modelling errors	The difference in value between the actual flow condition and the mathematical prediction. A major cause is often the simplification of actual geometries or assumptions of boundary conditions. It requires experimental data to evaluate.
	Discretisation errors	The difference between the original exact solution and the exact solution of a different discretisation level of the same equation. This is due to limitations in the computational elements of a domain. Multiple sets of discretisation schemes or levels can be made to evaluate. Further discussion in Section 0
	Round-off (machine) errors	Hardware limitations in handling floating point numbers. Running higher bits (64bits) and higher precision codes will reduce this error.
	Iteration (convergence) errors	The difference between an iterative solution and an exact solution related to the quality of the numerical solution.
Unacknowledged Error	Computer programming (software) error	Bugs and mistakes in code may reduce the accuracy of the prediction. A responsible software developer should fully test and remove any error before releasing their software to the market.
	Usage errors	Usage errors can be introduced at any stage of the CFD process by a user. Usually these

		errors are shown as modelling and discretisation errors. These errors can be minimised by proper training and experience.

To reduce the potential of errors in the solution, this thesis will cover the major work of the verification and validation in the initial stages of Chapter 4.0. This work conducts several tests including the mesh sensitivity study, the turbulence model accuracy and the rotational region size sensitivity to attain the acknowledged geometrical modelling errors and discretisation errors. In the end, the compilation of the reliable method and setup will be compared with the experimental results.

3.7 Chapter summary

This chapter described all governing equation and the fundamental CFD that are used in this project. The steady state CFD simulation of modelling the rotational flow has been explained in the Moving Reference Frame (MRF) section. Also included the description regarding uncertainty and error where CFD modelling may differ from the exact value of actual physics.

Chapter 4

CFD Model Verification and Validation

4.0 CFD model verification and validation

The verification and validation (V&V) processes are usually performed at the first stage of any numerical analysis such as a Computational Fluid Dynamics (CFD) study in order to establish the credibility of the simulation results. A well-known definition of verification and validation was made by Roache (1998) and the AIAA Standards Guide (2002), where verification is a process of finding the best mathematical set in solving an engineering problem and validation compares the accuracy of the mathematical model representation with the real world result.

In this chapter, these crucial procedures will verify the accuracy of the CFD simulation using STAR-CCM+ v11.04. At the end of this section, the CFD results will be validated with the experimental results to prove their suitability and build confidence in the methodology for further in-depth simulation design based studies. Part of this chapter's work has been published by Fawzal et al. (2016 and 2017).

4.1 CFD modelling

The three-dimensional (3D) rotor cavity of the YASA P400 S machine (YASA Motor Ltd. 2017) has been taken as the initial model. This sealed machine geometry displayed in Figure 4-1 was modified to include a fan with a backward-inclined aerofoil blade design on the steel rotor of its one side. The idea is to introduce a cooling channel from the centre of the machine which would allow an inflow driven by the rotational motion of the fan and exit through a single outlet port on the radial of the machine. Figure 4-2 shows the machine's topology with the proposed rotor cooling modification. During the operation, the rotating rotor and the fan blades will drive cold air into the centre of the system, disperse it into its surroundings and remove the heat. This means that the attached fan blades will act as an active flow promoter and a heat exchanger at the same time. It is expected that the cold air would be drawn in and would remove the heat from the rotor. With a colder rotor temperature, the heat from the magnet eventually should conduct through the solid rotor and reduce its temperature.

Figure 4-1: The YASA P400 S (sealed) machine.

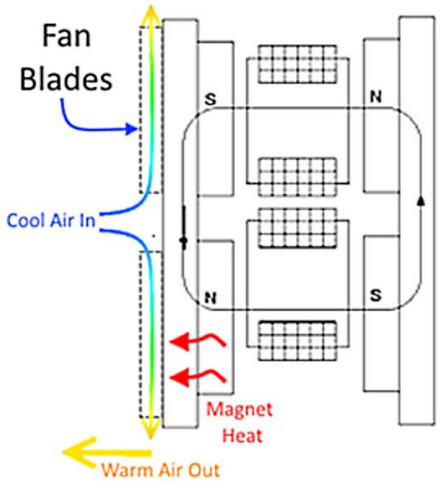

Figure 4-2: The YASA machine topology with single side rotor cooling.

4.1.1 Geometrical setup

Figure 4-3 shows the geometrical setup based on the idea of the proposed rotor cooling method previously described in the section 4.1. A complete cavity domain of the machine's non-drive-end was modelled because of the non-symmetrical position of the inlet and the outlet ducting. The air cavity within the rotor assembly was extracted and split into two segments namely the fluid domain (in blue) and the rotational domain (in red). The decision of the rotational region placement was made based on the best practice guidelines from the software supplier where the region to region interface is near to the rotating parts (STAR-CCM+ 2016). The rotational region of this initial study was made on the surrounding fan geometry and the magnet's array, which cover 50% of the rotor's air cavity volume. The geometry of the CFD modelling also includes the ducting, which is required for conducting future experimental testing. This is to ensure a similarity condition between CFD and the experimental testing. As the machine needs to be in a compact form, the inflow duct at its centre has been diverted to the side and an outlet duct is included (Figure 4-3). The addition of an extension to the inlet and outlet will benefit the simulation by ensuring that the flow is fully developed before it enters or exits the system. In addition, this approach helps in stabilising the outflow as it avoids the flow recirculation on the outlet

boundary wall, which can give negative impact to the simulation's results, causing residual divergence or bad mass balance between the inlet and the outlet. Therefore, the inlet and outlet duct has being extended by 150mm with additional frictionless ducting during the CFD modelling to aid the simulation's convergence with a slip-condition, without causing any pressure drop from the extension.

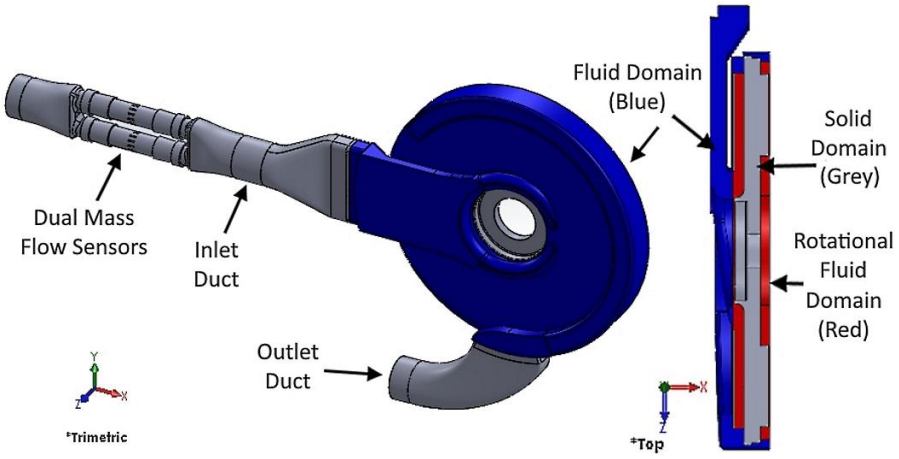

Figure 4-3: Geometrical setup of the CFD modelling.

The modification of the rotor was made by having a fan design as an integrated part of the rotor assembly. Figure 4-4 shows the comparison between the original sealed rotor and the rotor of the proposed rotor cooling technique. The front face of the sealed rotor has a rib feature to increase the rotor's rigidity. This rib feature was removed and replaced with fan features, as shown in Figure 4-5. The fan's blade features have been enclosed by a thin disc on its front face with an opening at the centre. This approach was made in order to avoid cooling air spillage; hence, the fan blade features are not seen in Figure 4-4. A backward-inclined aerofoil blade design was chosen at this stage as it was expected to suit the application compared to other blade designs. The effect of the blade design selection will be further investigated in Chapter 6.0.

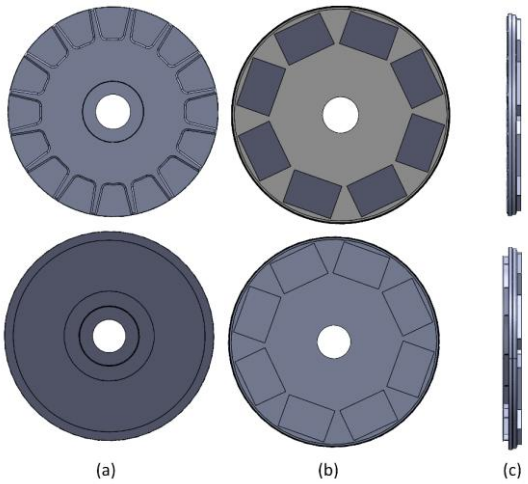

Figure 4-4: The sealed machine's rotor assembly (above) and proposed rotor cooling assembly (below) of the front view (a), rear view (b) and side view (c).

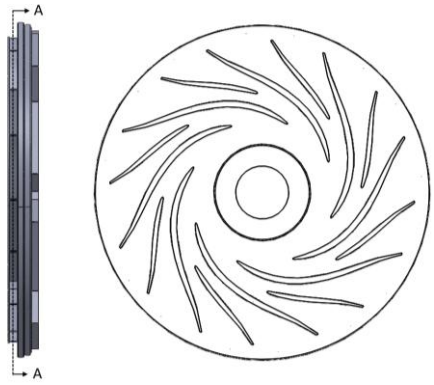

Figure 4-5: Section view of the rotor of the proposed rotor cooling.

4.2 The mesh sensitivity study

The independency of a numerical simulation such as the CFD needs to be assessed in order to reduce the uncertainty of the predicted results. The mesh/grid sensitivity or the mesh/grid independence study are the terms that describe the process of evaluating the effect of mesh size variation and quantify the simulation's accuracy (Roy 2003). This study should take place at the beginning of the V&V process in order to find the suitable discretisation resolution that produces an independent result for the mesh size.

The grid convergence index developed by Roache (1998) is not considered due to the complexity of the design and the mesh setup in this study. The

grid convergence index requires a constant grid spacing to calculate the order of the grid convergence, which in this study is inconsistent due to the variance of the fluid domain spacing (0.55mm-10.5mm), therefore it is not suitable. However, the judgement of the independency was made by the rate changes on each mesh level for the flow and thermal characteristics.

4.2.1 Meshing setup

The automated mesh generation in STAR-CCM+ was selected to produce an unstructured polyhedral volume mesh. The polyhedral mesh combines the benefit of automated mesh creation on complex mesh generation of tetrahedral mesh and accurate solution of hexahedral mesh (STAR-CCM+ 2016). These were achieved because the polyhedral mesh of STAR-CCM+ is based on the automated tetrahedral mesh that gives fast mesh creation but also has many neighbouring cells compared to the tetrahedral mesh, therefore the approximation on the gradients and local flow distribution has high accuracy (Peric and Ferguson 2005).

Five mesh levels were generated from the values tabulated in Table 4-1 and Table 4-2. Due to the complexity of the geometrical model, the low y^+ approach was selected to resolve the viscous sublayer in the near wall region (STAR-CCM+ 2016) and has being discussed in the previous section 3.3.5. Therefore, the prism layer was set with a target dimensionless wall distance y^+ ranging from 5 to ~1 for coarse mesh to finer mesh, respectively in order to have sufficient fine mesh near to the wall. The target y^+ is calculated by Eq. 3-60, with the local Reynolds number Re_θ of 3.73e^5 calculated by Eq. 3-16.

The improvement of the y^+ value on each increment of mesh level was made in an iterative manner because the actual y^+ value is dependent on the flow solution. Therefore, the target y^+ value of the medium mesh was calculated based on the post-processing of the actual y^+ value of the coarse mesh and the process is then repeated until the appropriate target y^+ value is achieved.

A custom mesh setup was made for several parts in the CFD model as tabulated in Table 4-2. Mainly, this additional refinement was made for the tight clearance within the machine. The machine's rotor outer diameter is 252.7mm and the clearance in the system is presented below by the gap ratio $G = s/R_r$: the magnet-to-stator is 0.00791, the rotor-to-stator is 0.04907, and the rotor-to-cover is 0.01187.

Figure 4-6 shows the generated mesh based on the mesh setup of Table 4-1 and Table 4-2. The generated mesh of the finer level and finest level are almost identical due to their similar refinement value. For a better visualisation, the cross section of fine mesh level is illustrated in Figure 4-7, where a conformal mesh can be observed in between the static fluid region and the rotational region. The prism layers wrap surrounds all the walls and the first cell of the unstructured polyhedral seems to be large at this mesh level. It is expected that these sudden changes of mesh size may affect the result. Therefore, further refinement levels of the finer and the finest mesh level were generated.

Table 4-1: Default Mesh Setup

Mesh Level	Base Size (mm)	Minimum	Prism Layer		
			No. of Layers	Stretching	Thickness (mm)
Coarse	5	25%	4	1.3	2
Medium	4	15%	6	1.2	1.75
Fine	3	12%	7	1.1	1.5
Finer	2	10%	8	1	1.25
Finest	1.25	10%	9		

Table 4-2: Custom Mesh Setup

Refine Magnet Face				Refine Thin Wall				Refine Rotational Region		Refine Vanes and Magnet			Mesh Cell Count
Target	Prism Stretch	Prism Thickness (mm)	Minimum (mm)	Target (mm)	Prism Stretch	Prism Thickness (mm)	Minimum (mm)	Target (mm)	Prism Thickness (mm)	Target (mm)	Minimum (mm)	Surface Curvature	
2.5	1	0.2	1	3.5	1.1	0.3	1.75	3	1.5	5	0.175	50	1,939,164
2			0.5	3			1.5	2	1.25	4	0.15		5,141,052
1.75			0.25	2.75			1	1.5	1	3	0.1375		9,842,908
1.5			0.1	2.5			0.5	1		2.5	0.125		14,641,274
				-						-	0.1		16,734,277

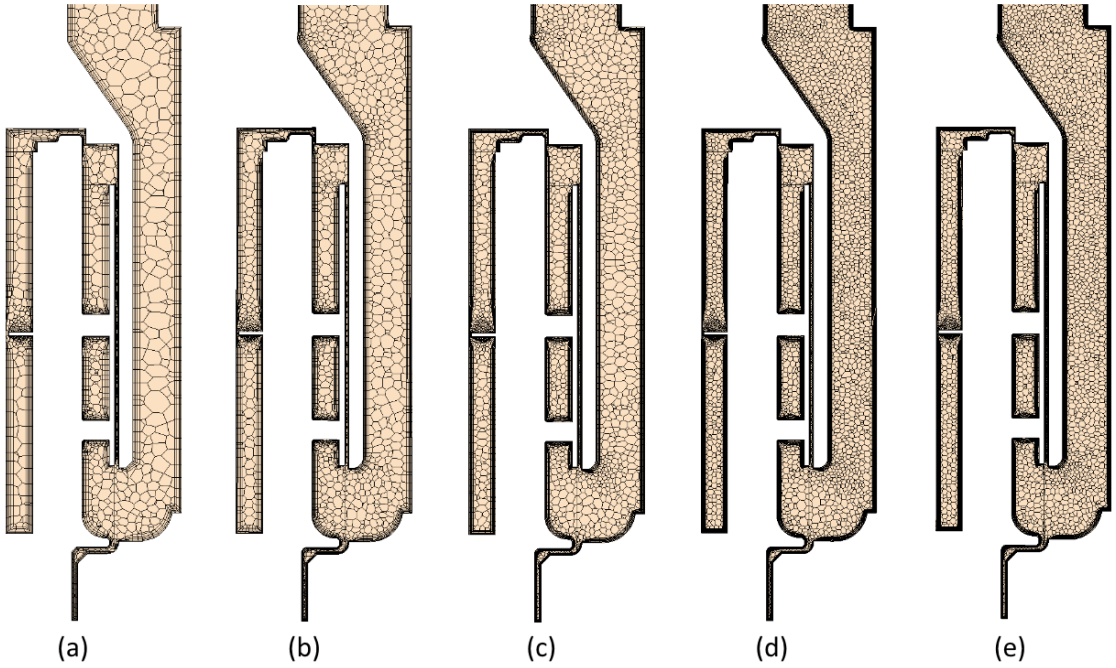

Figure 4-6: Cross section side view of all selected mesh levels; (a) coarse mesh, (b) medium mesh, (c) fine mesh, (d) finer mesh and (e) finest mesh.

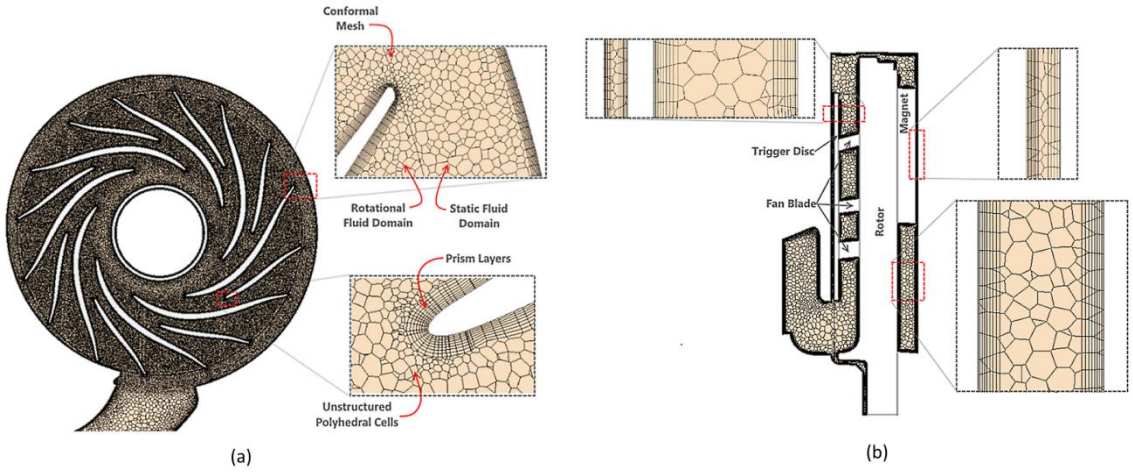

Figure 4-7: (a) Cross section front view and (b) cross section side view of the fine mesh.

4.2.1.1 Boundary conditions

The boundary conditions for the mesh sensitivity study were specified as follows:

1. *Inlet*: Stagnation inlet, total inlet pressure p_{in} = 0Pa, total inlet temperature T_{in} = 26.85°C (300K), turbulence intensity of 0.01 and turbulent viscosity ratio of 10.
    a. The stagnation inlet boundary condition that allows the fan features on the rotor to drive the air inside the machine naturally (without any force inflow boundary condition) where the flow is at rest. It is also referred as far field or opening boundary condition in some literature or software.
    b. The total inlet temperature is set based on the initial assumption of the inlet temperature where the experimental test was conducted with the same inlet temperature value.
    c. The values of the turbulence intensity and turbulent viscosity ratio were set based on the minimum recommended value (STAR-CCM+ 2016). These values assume that the upstream flow is under-developed (thus the *Imaginary ducting* is included*).* The simulation has been repeated with higher values yet there is no difference in the result product. Furthermore, the turbulence parameters have been plot and show that the system turbulence parameters are higher than the specified values. Therefore the assumed value is adapted because the finding of a correct turbulence quantities value is difficult (STAR-CCM+ 2016) particularly in a complex case.
2. *Outlet*: Pressure outlet p_{out}= 0Pa and opening outlet temperature, T_{out} = default.
    a. The opening outlet temperature was set to default as this will allow the outlet temperature to vary and not being constrained to any specific value.

3. *Magnets and Rotor (including fan blade)*: No-slip condition rotating wall, rotational rate, $\omega = rpm * 2\pi/60$ and T_{rotor} = 80°C (353.15K).
    a. The decision for this static temperature was based on the maximum allowable rotor and magnet temperature set by the machine's manufacturer at full load operation. The machine's manufacturer has used this value as a temperature cut-off, meaning that if the rotor temperature exceeds this value, the machine will stop in order to protect the machine from overheat that could lead into catastrophic failure. This fixed temperature value will be further discussed in Chapter 6.0.
4. *Stator wall*: Static temperature of 60°C (333.15K) and no-slip condition wall.
    a. This value is taken from the experiment where the stator wall has an average 60°C.
5. *Cover walls*: adiabatic no-slip condition wall.
6. *Ducting walls*: adiabatic no-slip condition wall.
7. *Imaginary ducting*: adiabatic slip condition wall.
    a. This imaginary wall is added to aid the simulation's convergence with a slip-condition, without causing any pressure drop from the extension.

The cover and ducting walls are assumed as adiabatic walls to simulate the worst case for cooling in which there is no heat transfer occurring through these walls.

Other relevant configurations of this mesh sensitivity study are presented in Table 4-3 and the air properties are listed in Table 4-4. The choice of the SST k-ω turbulence model in this exercise was investigated and discussed in Section 4.4.

Table 4-3: CFD model configuration for the mesh sensitivity study.

Simulation type:	Steady State Simulation
Equation of state:	Constant density
Turbulence model:	SST K-Ω
Wall treatment:	All y^+ wall treatment

Table 4-4: Material properties of air.

Properties	Unit	Value
Dynamic viscosity	Pa.s	1.8551×10^{-5}
Molecular weight	kg/mol	28.9664
Specific heat	J/kg.K	1003.62
Thermal conductivity	W/m.K	2.6031×10^{-2}
Turbulent Prandtl number		0.9

A machine rotational speed of 3000rpm was selected for this mesh sensitivity study to reduce the risk of the prediction within the laminar-turbulent transition flow regime. It is expected that this transition flow regime will occur at lower rotational speed, in which below 2000rpm and further discussion can be found in the Section 4.4.

The stopping criterion was set to a maximum number of steps at 10000 iterations, while checking the convergence of the residual plots. Additionally, the inlet mass flow and the outlet temperature were observed to ensure the convergence of the physics.

4.2.2 Results

The mesh sensitivity of this study can be seen by plotting the flow characteristics and the thermal characteristics of each mesh level. The mass flow rate in Figure 4-8 shows a fluctuation in the results as the mesh level

increases. As expected, the values of mass flow rate (either at the inlet or at the outlet) and the total pressure rise become more accurate as the grid is refined because the spatial resolution and the temporal discretisation errors are reduced. The biggest change in value only occurs between the coarse and medium mesh levels. This is because the medium mesh has five time more cells compared to the coarse mesh (Table 4-1 and Table 4-2). However, the fluctuation of the mass flow produced on each mesh level above the coarse mesh is small, with a standard deviation of 8.6868×10^{-5}kg/s (or equivalent to 4.4015L/min). The average difference between the inlet and the outlet mass flow rate is 0.79%, which shows that the continuity equation works well in predicting the mass flow rate, especially for the finer and finest mesh levels where the difference is only 0.27% and 0.22% respectively. The total pressure rise shows an improvement in the prediction as the cell count gets higher.

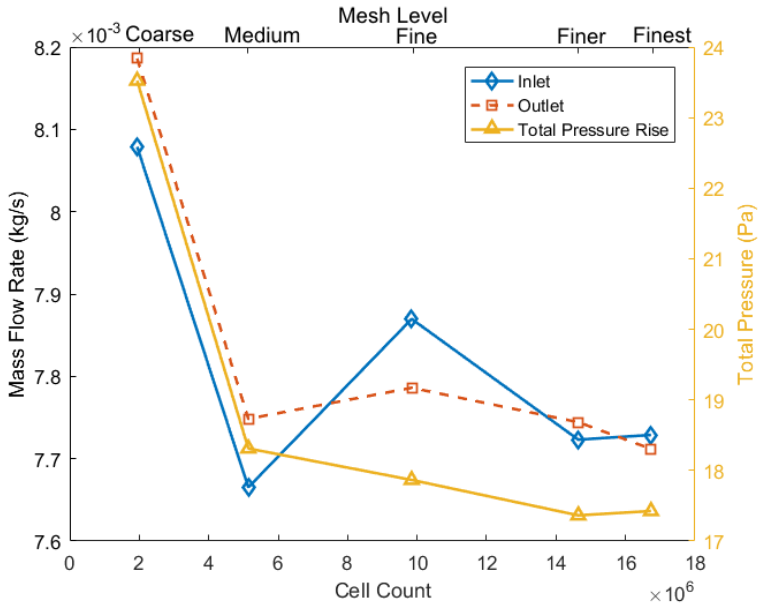

Figure 4-8: Flow characteristic of the mesh sensitivity study

Similarly, the thermal characteristic in Figure 4-9 shows the results of the air outlet temperature and air system temperature, which do not change significantly above 5 million cells (medium mesh level). The temperature

changes above the coarse mesh level are only within 1°C difference and are insignificant.

In a common case, the computational time is increased as the cell count increases at almost exponential progression rate when using the same number of processors. However, the solver time in this study increases linearly as the cell count increases as shown in Figure 4-10. This unique relationship has been shown in many occurrences when conducting CFD simulation using STAR-CCM+ because the parallel computing code of the software has an optimum number of mesh counts for the amount of processors (Siemans PLM Software 2017). In this study, the number of processors has been set to 12 for all mesh levels. On the lower cell count (i.e. coarse level), the software was wasting some precious computational time by dividing the workload and communicating between the processors. While on the higher cell count (i.e. finest level), the software was fully utilised its parallel computing capability thus linear progression rate can be seen between 1.9million cells and 16.7million cells. Various study cases have shown a similar trend as presented in Siemans PLM Software 2017.

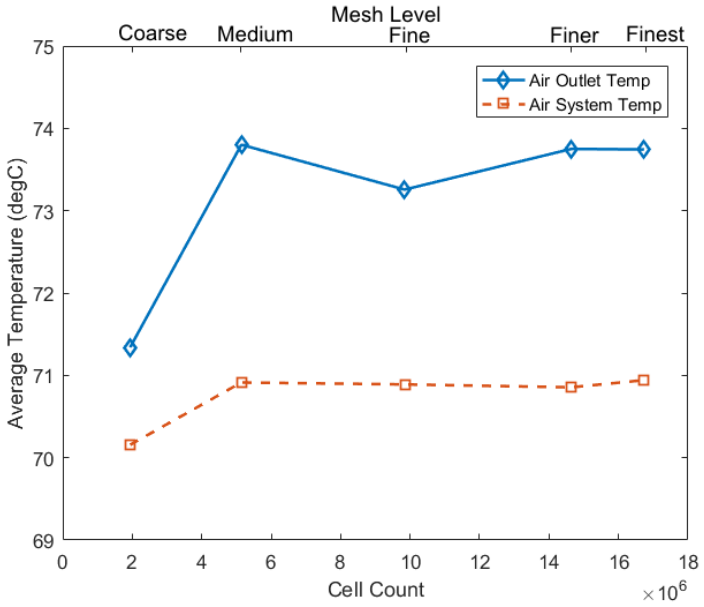

Figure 4-9: Thermal characteristic of the mesh sensitivity study

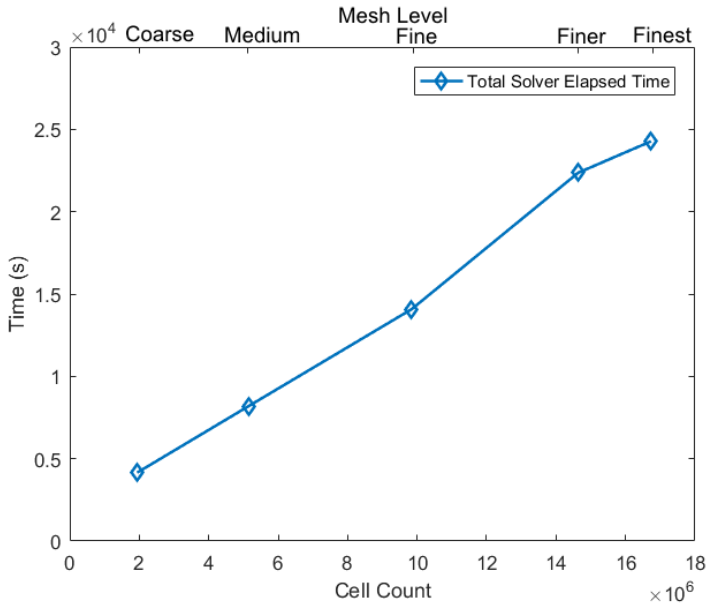

Figure 4-10: Solver time of the mesh sensitivity study

Based on these results, it is appropriate to consider that the finer mesh of 14.6 million cells is the brake-even point between accurate solution and computational time. Further simulations will be used the mesh default (Table 4-1) and custom refinement mesh setup (Table 4-2) of the finer mesh as it is most suitable for this study and it produces reliable results within an acceptable solving time.

4.3 The experimental method

The objective of these experiments is to measure the flow and temperature the prototype YASA machine for CFD validation purposes. The prototype YASA machine is a single stator dual rotor (SSDR) AFPM machine and has a single rotor cooling on the non-drive end (named vented rotor) and a sealed rotor on the drive end (named non-vented rotor).

The measurements were conducted separately. For the flow measurement, the focus given on the mass flow rate generation on the vented rotor while the temperature measurement, the focus was given on the temperature of the vented rotor and the non-vented rotor.

4.3.1 Flow measurement

The flow measurement was carried out on the prototype YASA machine identical to the design used in the CFD modelling. The machine was installed on the rig with a Remy 115S dynamometer to spin the machine without any load (mechanical or electrical) in order to assess the generated mass flow rate of the prototype YASA machine's vented rotor. Figure 4-11 shows the experimental setup where the prototype machine is driven by the computer-controlled dynamometer.

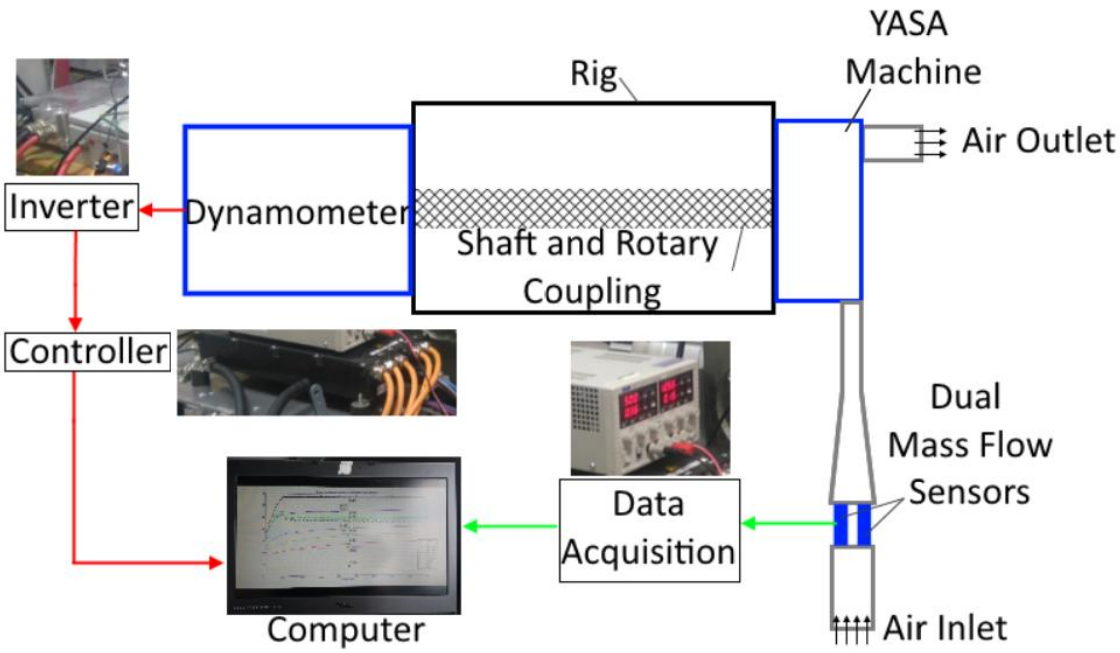

Figure 4-11: The experimental setup for flow measurement.

A dual POSiFA PMF4104V mass flow sensor was equipped on the inlet of the machine. The mass flow sensor ducting has a straight pipe section length of five times of the sensor diameter before and after the mass flow meter to ensure that the reading is based on a fully developed and undisturbed airflow for accuracy as shown in Figure 4-12. These mass flow sensors featured temperature compensation for the accuracy of the measurements that allow for flow data correction if there is a gradient on the air inlet temperature (POSiFA, 2017). Also, these calibrated sensors have a linearise output from 1V to 5V and the actual mass flow rate can be calculated based on (Eq. 4-1).

$$\dot{m}_{actual} = \left[\frac{V_{out} - 1V}{4V}\right] \times \dot{m}_{fullscale} \quad \textbf{(Eq. 4-1)}$$

Where the $\dot{m}_{fullscale}$ is the maximum capability of the sensor to measure the flow rate. The calibration was conducted by YASA Ltd. and has been reviewed by the author, yet could not be presented here due to the confidentiality. The calibration includes the sensor, the data acquisition and computer for data logging shows 5% of accuracy. However, the selected instrumentation has a limitation of measuring the mass flow rate up to 0.011842kg/s (600L/min). A preliminary CFD simulation was conducted to access this instrumentation limitation and it was found that the flow limit would be reached at around 4000rpm with the backward-curved fan design on the vented rotor.

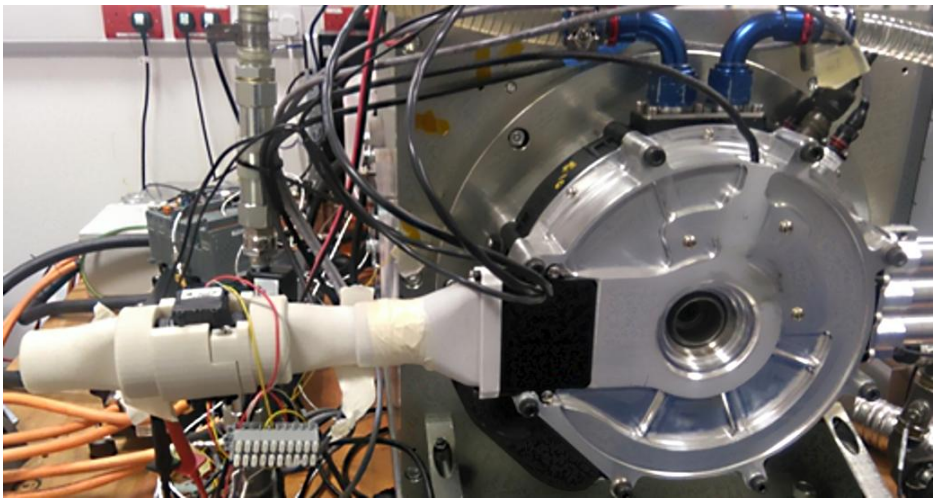

Figure 4-12: The experimental rig with the airflow-measuring nozzle and sensor installed.

Although it is expected that the mass flow sensor will reach its limits in terms of measuring the flow around 4000rpm based on the preliminary CFD simulation, the initial experimental was conducted from 1000rpm to 8000rpm to validate this assumption with two modes:

- Ramp up: The machine start from stand still (0rpm) and ramp up with a rate of 10rpm/sec until 8000rpm

- Ramp down: The machine will reduce its speed from 8000rpm to 0rpm by a rate of 100rpm/sec.

4.3.1.1 Mass flow sensor position (at the inlet versus at the outlet)

Figure 4-13(a) shows the experimental mass flow rate data collected at the inlet with smooth linear progression during ramp up and oscillating output on ramp down. The result agrees with the simple CFD simulation's prediction where the mass flow measurement reached its limit near at 4000rpm and flattens out. Although the sensors are able to record up to 0.012236kg/s (620L/min), the measurement is only reliable to 0.011842kg/s (600L/min) according to its specification. Therefore, further data measurements were only taken up to this specified limit. Additionally, the experiment was continued by changing the location of the mass flow sensors assembly to the outlet port and letting the inlet be an opening vent. The result of the outlet measurement in Figure 4-13(b) showed an increase of 2.79% over the inlet measurement although it was expected to produce the same amount of mass flow rate.

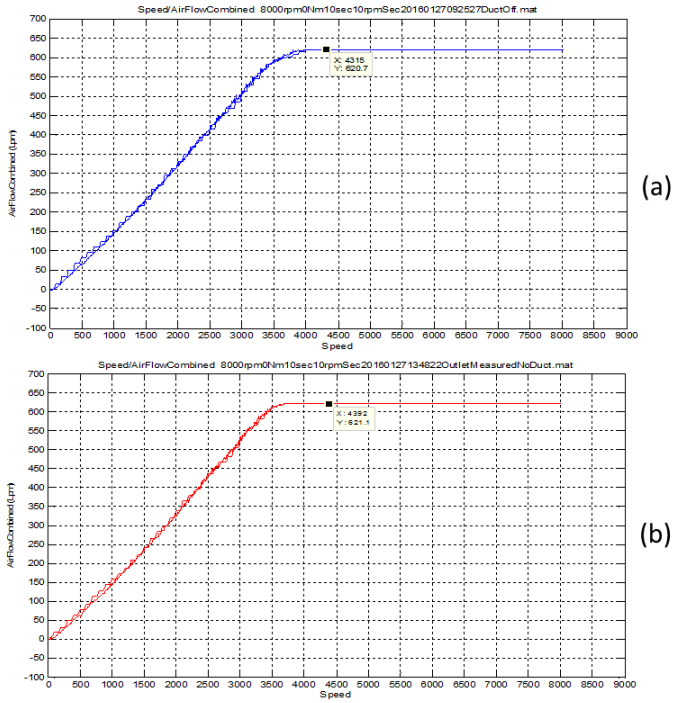

Figure 4-13: (a) Inlet and (b) outlet mass flow rate.

Based on this measurement, the error analysis was conducted by analysing the standard deviations of the mass flow rate on each rotational speed and then calculate the standard error. Figure 4-14 presented the mass flow rate standard error where most error occurs at 3000rpm to 3600rpm. The main reasons for this error can be understood by looking at the flow features when the mass flow sensors assembly change their position between the inlet and the outlet by CFD simulation.

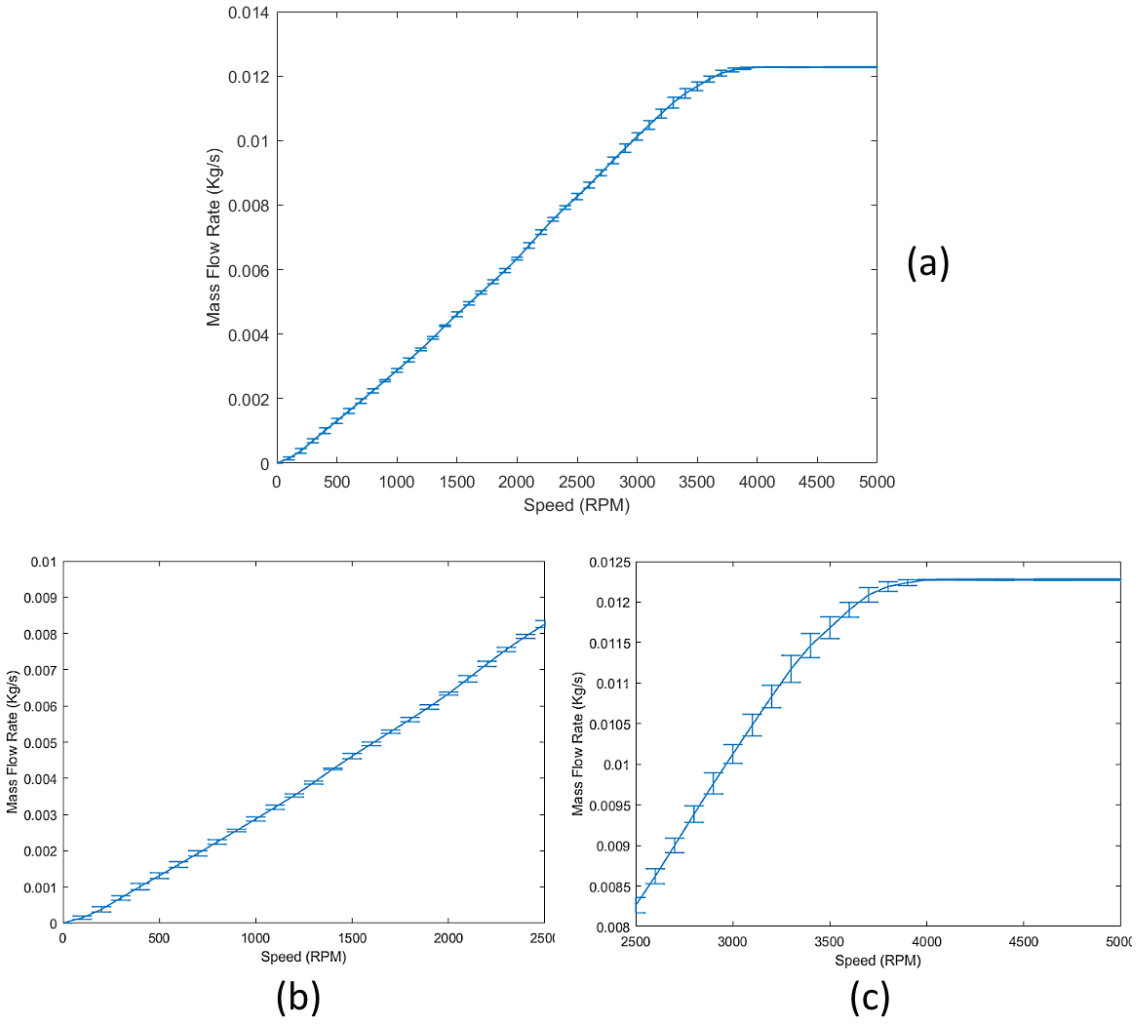

Figure 4-14: The mass flow rate standard error based on the inlet and the outlet measurements of (a) 0-5000rpm, (b) zoom in 0-2500rpm) and (c) zoom in 2500-5000rpm.

Figure 4-15 presents the cross section vector plot and the velocity profile from the red dash line near to the outlet port. The velocity profile Figure 4-15(a) suggests that there is a flow circulation at the centre of the outlet duct when the mass flow sensors assembly was placed on the inlet. This occurrence is due to the sudden pressure change between the air inside the short outlet duct and the ambient pressure. However, when the mass flow sensors assembly is moved to the outlet, it stabilises and straightens the flow due to the additional ducting length as shown in Figure 4-15(b). Therefore, having the mass flow sensors assembly on the outlet port helps the machine to have better flow because the additional ducting eliminates sudden pressure changes that could create flow circulation and straighten the flow, thus increasing its mass flow slightly.

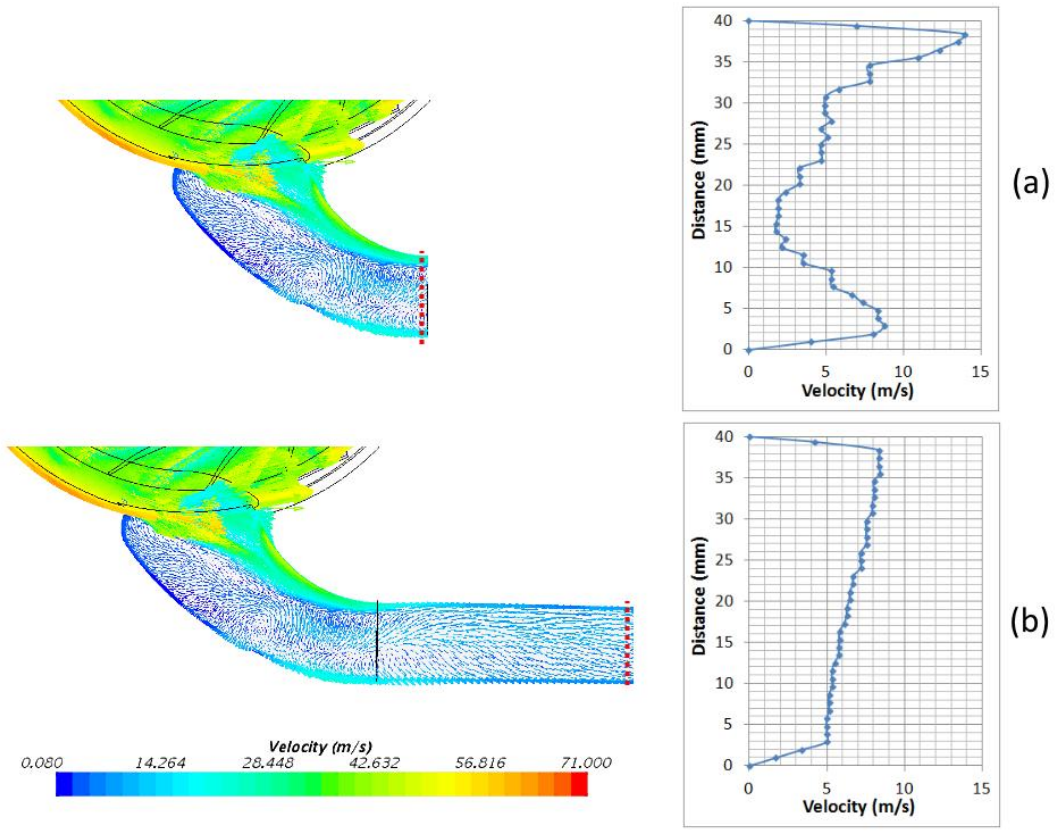

Figure 4-15: Vector plot (left) and velocity profile (right) at the outlet (a) and extended outlet (b) at 3500rpm.

4.3.1.2 Flow measurement for CFD validation

The flow measurement for CFD validation was conducted with a rotational speed up to 3500rpm. This decision is made based on previous result where the sensors will reached its measuring limit of 0.011842kg/s at 4000rpm. The test cycle will have a ramp up rate of 10rpm/sec.

For validation purposes, the flow measurement will have the mass flow assembly mounted on the inlet due to these reasons:

- The sensor has a maximum temperature compensation at 50°C.
    - It is expected in the future to re-run the test with load conditions and the air outlet temperature may exceed this temperature limit.
- Only small differences can be observed when changing the location of the measurement.
    - 2.79% increase when measuring from the outlet.

The complete assembly of this future production machine will be equipped with a mesh-filter at the outlet to prevent contamination from entering the system due to the back-pressure effect. The mesh-filter is made of stainless steel SS304 with an aperture of 1.8mm. To ensure that the mesh-filter did not cause huge airflow restriction, a small sized wire of 30 SWG (Standard Wire Gauge) is selected that results to 72% free area for the air to pass through.

It is expected that this mesh-filter may restrain the flow, thus the data was recorded on the scenarios of including and excluding this mesh-filter on the outlet port in Figure 4-16. Both scenarios show a linear progression and as expected, the mass flow rate of the machine with the mesh-filter is lower than the test without the mesh-filter on the outlet, as the filter restrains the outflow slightly. This result will be used for validating the CFD flow result.

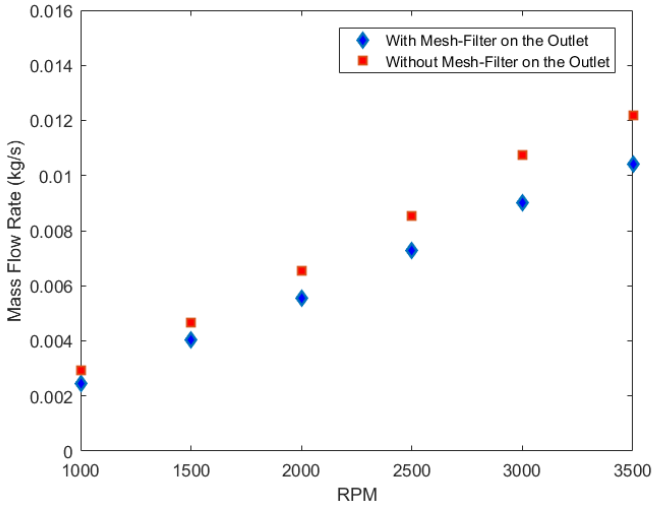

Figure 4-16: Mass flow rate measurement of the prototype YASA machine with and without the mesh-filter on the outlet port.

4.3.2 Temperature measurement

The setup for the temperature measurement is similar to the previous flow measurement. However, the 150kW prototype machine is now subjected to mechanical and electrical loads that are computer controlled as shown in Figure 4-17. The machine is coupled with a Remy 115S dynamometer and controlled by a Sevcon Gen4Size10 AC motor controller and a Rinehart PM250 power propulsion inverter that were designed specifically for high performance automotive traction applications. The stator cooling system is included to regulate the stator temperature. Details on the stator cooling system will not be included here as it is not the purpose of this study. Various researchers have conducted extensive studies on the YASA's stator cooling namely Camilleri et al. 2012, Camilleri et al. 2015 and Vansompel et al. 2017. An adiabatic close ambient box encloses the YASA machine to constrain the heat of the machine from dispersing to the test room. This is simulated near to the actual machine application where it will be placed under a car engine hood with limited space for the machine temperature to disperse to its surrounding. Figure 4-18 shows the experimental rig with all its mechanical and electrical connections including coolant pipes for stator cooling without the close ambient box.

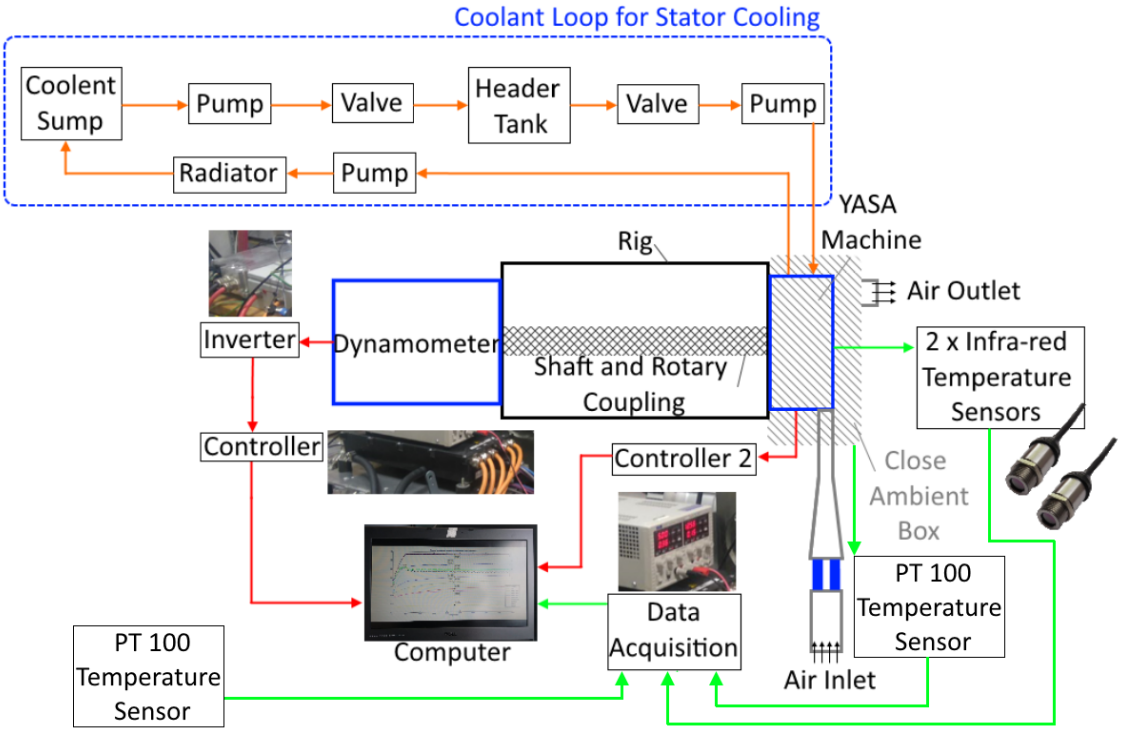

Figure 4-17: The experimental setup for temperature measurement.

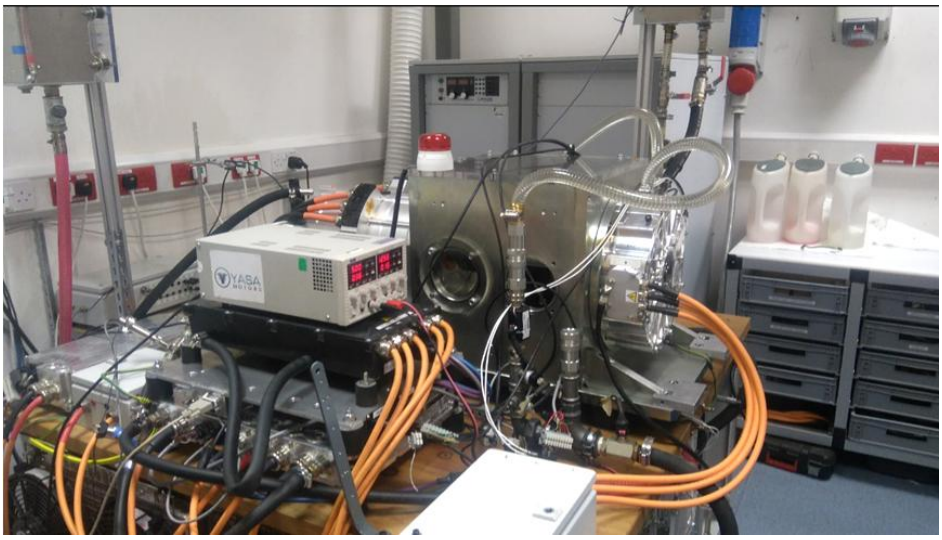

Figure 4-18: The experimental rig for temperature measurement.

4.3.2.1 Temperature sensors

The temperature measurements were collected at four locations: two for air temperature and other two for the machine's rotor. The air temperature was measured by PT100 sensor that one is placed inside the close ambient box

and the other within the test room to measure the ambient air (Figure 4-17). The sensor for the machine's rotor temperature measurements is used to measure the non-vented rotor and the vented rotor, as shown in Figure 4-19. Although the most critical component in this prototype machine is the permanent magnets, it is not possible to measure its temperature due to the compact space to mount the sensor because the prototype machine was designed to be as close as possible to the engineering end-product which has complexity and compactness. Therefore, the rotor temperature is collected due to this limitation.

All temperature measurements will be used for the CFD validation. On the other hand, the temperature measurement from the rotor is also used as a temperature signal for the machine's cut-off state to protect the machine from overheating and thermal stress. Again, the magnet, as the critical component is sensitive to overheating. The NdFeB N00H series magnets have a temperature threshold of 100°C and a maximum magnet service temperature at 120°C (Eclipse Magnetics 2014). Therefore, the machine's manufacturer has set the rotor's temperature threshold at 80°C to reduce the risk of overheating that can lead to catastrophic failure. A KIR4 series infra-red temperature sensor was mounted on the radial of machine aligned to the outer edge of the rotor (Figure 4-19).

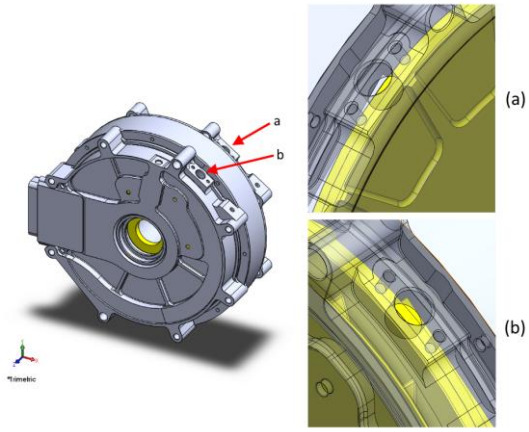

Figure 4-19: Temperature measurement locations for (a) a non-vented rotor and (b) a vented rotor.

This non-contact sensor is design for motorsports applications and has a 0 °C to 200 °C temperature range (KA Sensors 2015). The actual temperature data T_{sensor} can be calculated based on Eq 4-2 from the output V_{output} of 0.5V to 5V after calibration that has 3.7% accuracy.

$$T_{sensor} = 79.3V_{output} - 89 \quad \textbf{(Eq. 4-2)}$$

4.3.2.2 Experimental procedure

In the flow measurement, the prototype machine is driven by the computer-controlled dynamometer without any applied load. However, for the temperature measurement, the prototype machine is driven by itself while current is injected in the stator of the machine and induces the magnetic field that reacts with the PM, thus the machine spins. Additionally, the computer-controlled dynamometer is adding a mechanical load to the prototype machine at 150kW. Because the machine is now subjected to electrical and mechanical loads, the losses from converting electrical energy to mechanical energy is manifested as heat on the magnets and the rotors and this becomes the thermal boundary conditions of this experimental.

Moreover, a limited thermal scenario was performed because any operating condition above the specified temperature threshold of 80°C may cause overheating that could lead to catastrophic machine failure. Therefore, the experiment for the temperature measurement is conducted on this scenario of:

- 2000rpm up to temperature threshold of 80°C.
- 4000rpm until the temperature reaches the steady state condition.

The reason of the limited scenarios which were performed on this prototype machine is because any operation above the manufacturer temperature threshold standard (80°C) will damage the machine. Due to the high manufacturing cost of the prototype, the experiment cannot withstand the motor operation at every single rotational speed (e.g. 2000rpm) until it reaches its steady state condition and then replace the machine with a new

one to conduct a test on different rotational speed (e.g. 4000rpm). So, this is a limited scenario.

The first temperature measurement at 2000rpm was collected after several heat cycles. Figure 4-20 shows that the measurement was stopped, although none of the rotor's temperatures were stabilised due to the non-vented rotor having reached its temperature threshold of 80^{o}C. If the machine did not have the temperature cut-off feature, the temperature will rise gradually until the steady state, yet it will damage the machine due to overheating.

The machine was then left to cool down for several minutes before the temperature measurement at 4000rpm was conducted. This second and final measurement was conducted with the machine's over temperature cut-off turned off to allow for a continuous operation even at higher rotor temperatures. Figure 4-21 shows the recorded temperature data for 4000rpm for the non-vented and vented rotor above their threshold limit together with the air ambient and air close box temperatures. The ambient air temperature was constant, meaning that the cooling air entering the machine is constant while the air close box temperature increases gradually and similarly to the growth of non-vented and vented rotor's temperature. The machine was classified as 'thermal damaged' after the experiment due to the excessive temperatures on the rotor assembly and was disassembled for inspection.

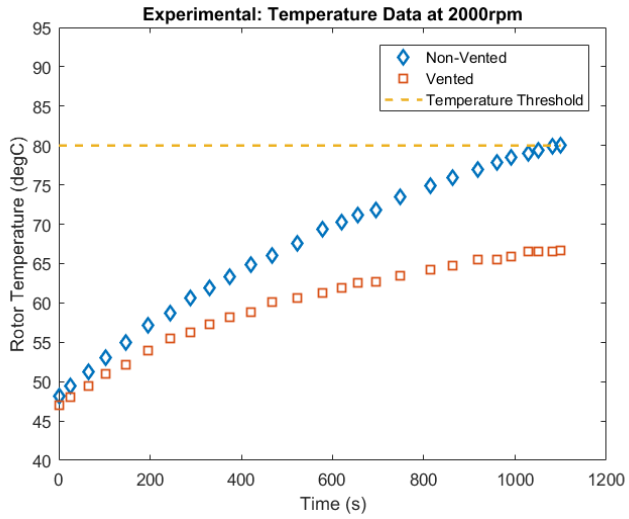

Figure 4-20: Temperature measurements at 2000rpm on non-vented and vented rotors.

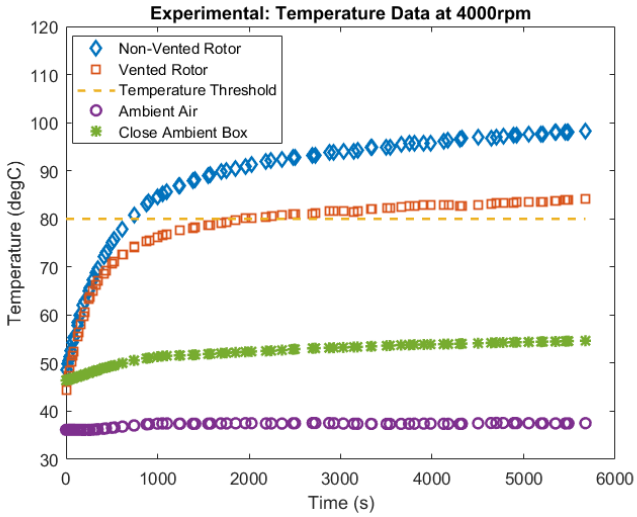

Figure 4-21: Temperature measurements at 4000rpm on non-vented and vented rotors.

4.4 Turbulence model accuracy

Three selections of turbulence models were selected to verify and validate their suitability for predicting the flow of the proposed rotor cooling technique. The chosen turbulence models are as follows:

1. The Shear-Stress Transport (SST) k-ω model (Menter 1993),

2. The Realizable k-ε model (Shih et al. 1994),
3. The v2-f model, (Durbin 1995 and 1996; Lien et al. 1998; Davidson et al. 2003).

The tested flow measurement from 0rpm to 3500rpm is expected to include the flow regime of laminar, transition from laminar to turbulent and turbulent flow. Therefore, the additional turbulence model of the SST k-ω with a transition model of Gamma ReTheta (Menter et al. 2004; Langtry 2006; Langtry et al. 2015) was included to evaluate if any potential improvement could be made by adding a transition model to the turbulence model.

Figure 4-22 shows the mass flow rate of the various turbulence models compared to experimental results from the flow experimental in Section 4.3.1. In general, all the turbulence models under-predicted the actual mass flow rate with insignificant differences between the models. However, all the selected turbulence models produced parallel trends to the experimental with the mesh-filter on the outlet, although this equipment was not included in the simulation.

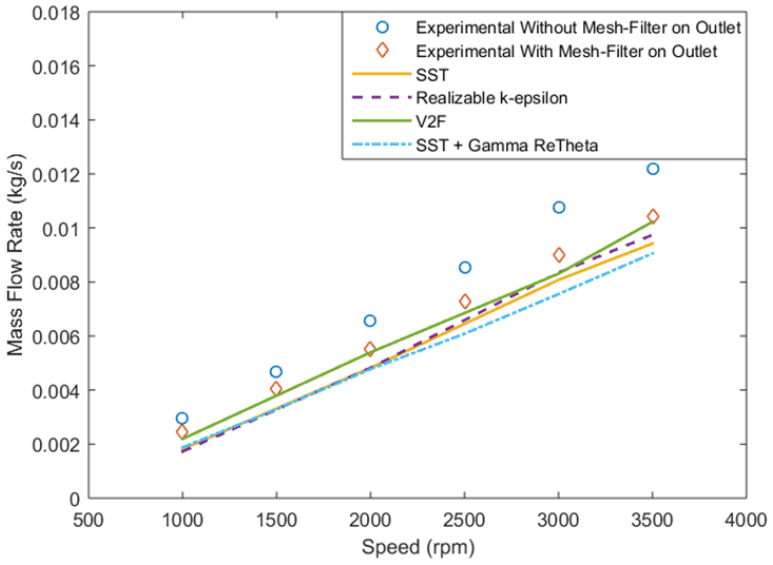

Figure 4-22: Various turbulence models' mass flow rate over experimental.

The simulations of the SST k-ω and Realizable k-ε give a similar mass flow rate, while the advancement of the v2-f turbulence model improves the

prediction of the experimental by including a mesh-filter on the outlet, due to having an additional curvature correction compared to the other two-equation models. This improvement of the v2-f is derived from the standard k-ε model but has three transport equations (namely turbulence kinetic energy, turbulence dissipation and the normal velocity squared) and the elliptic relaxation equation, which solves the Reynolds stress in the near wall region. On the other hand, the two-equation models such as the SST k-ω and the Realizable k-ε used the law of the wall at the solid boundaries and the velocity boundary condition at the location away from the solid boundaries. Interestingly, the SST k-ω with an additional transition model of Gamma ReTheta did not improve the CFD results and produced poorer result above 2000rpm. This additional transition model required an assumption of free-stream edges (the position where the boundary layer end above the wall), which in this study was assumed to be 1.5mm above the wall, as the generic prism layer maximum thickness is 1.25mm from the wall. A proper calibration on Gamma ReTheta constant values is required to fully utilise this transition model's capability as an example performed by Malan, Suluksna and Juntasaro (2009).

The transition from laminar to fully developed flow for a rotating disc can be calculated based on the work of Gregory, Stuart and Walker (1955). Table 4-5 presents the equivalent speed of this machine with the transition flow and it ends at 1970rpm. Again, it can be observed that the SST k-ω with Gamma ReTheta results in Figure 4-22 diverted above this 2000rpm machine speed proving its unsuitability to perform on turbulence flow without proper calibration.

Table 4-5: Flow regime given by Gregory, Stuart and Walker (1955) with its equivalent speed for this machine.

Flow regime	Reynolds number	Equivalent speed
Transitional flow	$1.8 \times 10^5 < Re < 2.1 \times 10^5$	$1690rpm < n < 1970rpm$
Fully developed turbulent flow	$Re > 3 \times 10^5$	$n > 2810rpm$

Figure 4-23 shows that the results of all the selected CFD's turbulence models reduced as the rotational speed increased from 1000rpm to 3000rpm. This is because the RANS and the turbulence model is designed to predict the condition of the turbulent flow. The turbulence models SST k-ω and Realizable k-ε shared almost similar results, while the v2-f model provided the least amount of error at a low rotational speed of 1000rpm and did not give a significant improvement over the other turbulence models at 3000rpm. Moreover, the computational time of these turbulence models had a significant difference as shown in Table 4-6. Therefore, the SST k-ω turbulence model was selected for the advanced simulation based on this evidence, the similarity of predicting the mass flow rate and the significance of the computational time.

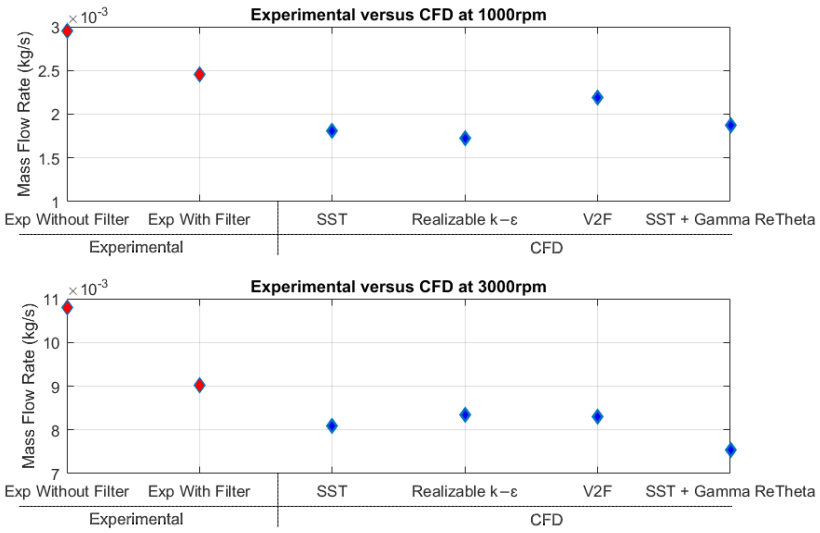

Figure 4-23: CFD turbulence models over experimental data.

Table 4-6: Total Solver Elapsed Time for each turbulence model simulation

Turbulence Models	Total Solver Elapsed Time (HH:MM:SS)	Time Difference (HH:MM:SS)
SST k-ω	05:53:38	
Realizable k-ε	06:16:10	00:22:32
v2-f	06:44:41	00:51:03

4.5 The rotational region sensitivity study

The Moving Reference Frame (MRF) model was incorporated into the simulation in order to simulate the rotational motion of the rotor assembly in a steady state condition. This approach has intermediate fidelity and acceptable computational costs when compared to the unsteady/transient simulation of the rigid body motion model. Darvish and Frank (2012) stated that the MRF allows for a faster rotational flow simulation compared to a transient simulation. The MRF model applies a fictitious centrifugal force to its domain, which mimics the rotational motion implicitly. A detailed explanation of the MRF was discussed in Section 3.4.1. This section focuses on finding the effect of the rotational region sizing on producing the mass flow rate, as there is no available reference or guideline for this matter. Figure 4-24 presents the cross section domain of different rotational region sizes in order to assess their sensitivity as:

1. No-region: Figure 4-24(a)
    a. No explicit rotational region included.
    b. Also known as rotational interface.
2. Half-region: Figure 4-24(b)
    a. The rotational region covers the rotor assembly specifically on the fan blades and magnet's array.
    b. All initial simulations took this as an assumption based on the STAR-CCM+ tutorial guide of *Moving Reference Frame: Rotating Fan* (STAR-CCM+, 2016)

3. Full-region: Figure 4-24(c)
    a. The rotational region covers the whole area of the rotor assembly.

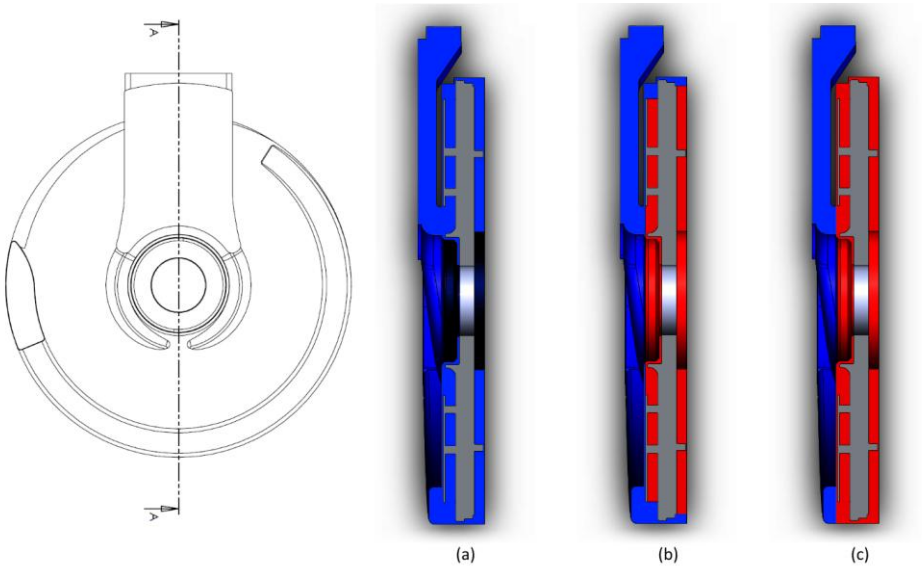

Figure 4-24: Cross-section of the rotor cooling indicates the fluid region (blue) and the rotational region (red) for (a) no-region, (b) half-region and (c) full-region.

The produced mass flow rate at 3000rpm of each scenario was recorded and compared with the experimental results. Figure 4-25 shows the effect of changing the size of the rotating region. The CFD prediction shows a positive trend of an increase in the accuracy while the size of the region increases. This is because the larger size of the rotational region, the larger size of cell count that has been assign with fictitious rotational motion, which then reflects to the greater mass flow rate produced. In this exercise, the full-region produces 10% and -7% differences when compared to the experimental without the mesh-filter and with the mesh filter respectively.

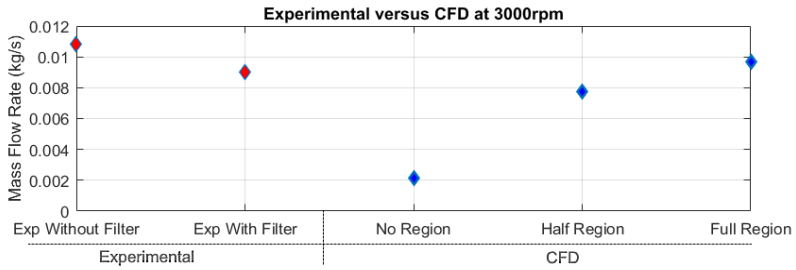

Figure 4-25: Comparison of CFD and experimental data of the rotational region sensitivity study at 3000rpm

4.6 CFD model validation

The final stage of this V&V procedure is to examine the performance of the numerical setup based on the previous exercises and to compare it with the experimental result. All the setup has remained the same with the decisions made from each preceding exercise as follows:

1. Mesh Sensitivity Study
    a. *Finer mesh* level is used.
2. Turbulence Model Accuracy
    a. *SST k-ω turbulence model* was selected.
3. Rotational Region Sensitivity Study
    a. *Half-region* and *full-region* were tested to evaluate the difference for the flow validation.

4.6.1 Flow validation

Two sets of simulation were made for the flow validation where the half-region and full-region of the rotational region were simulated from 1000rpm to 3500rpm at every 500rpm increment. The preliminary validation that used the half-region is named ‘early prediction’ whilst the full-region is named ‘improve prediction’.

Figure 4-26 compares the two sets of simulations with the experimental results:

- Early prediction: The first set of simulations was conducted with the half-rotational region that is used in the preliminary study (e.g. the mesh sensitivity study and the turbulence model accuracy). This was included in this flow validation section to show that the sensitivity study of the rotational region will give a major impact to the produced mass flow rate of the simulation.
- Improved prediction: The second set of simulations has similar setup to the early prediction except the fact that 100% of its air volume in the system cavity has been assigned as a full-rotational region.

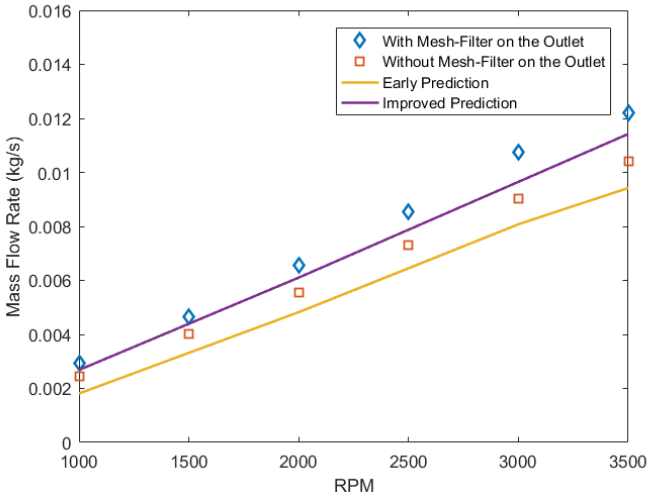

Figure 4-26: Comparison between improved and early CFD flow predictions over experimental

In Figure 4-26, both of these simulations: early prediction and improve prediction under-predict the actual mass flow rate and improve the prediction notably. The average margin of error reduces from 28% to 8% when compared to the experimental without the mesh-filter on the outlet. The assumption of full-region has most of the air cavity inside the machine as the rotational region increases the mass flow rate results, because a larger volume has been assigned to carry the rotational motion.

4.6.2 Temperature validation

During the temperature experiment, the prototype machine was subjected to 150kW load compared to its original design 50kW because we expected that the novel integrated rotor cooling will be able to handle such extreme increase of machine power. This however will lead to overheating of the sealed non-vented rotor (at drive end side) while more regulated temperature is expected on the vented rotor (at non-drive end side). The temperature measurement results in Figure 4-20 for 2000rpm and Figure 4-21 for 4000rpm show that, the vented rotor is colder as expected and it is maximum 13°C and 15°C when compared to the non-vented rotor respectively. Therefore, the temperature validation can only be performed at two rotational speeds due to the limited experimental test in section 4.3.2. The reasons for the limited experimental testing that can be performed are:

- Degradation of performance: The tested machine was considered as thermally damaged after the test as it was operating above the threshold temperature that may effect demagnetisation on the permanent magnet (PM). Testing the same machine with different rotational speed and load will give foul results as the machine will be performed as its intended design due to degradation of its permeability and other non-metal materials.
- Safety: The temperature experiments may lead to catastrophic failure to the machine and cause destruction to its surrounding (sensors, instrumentation and equipment). Therefore, it needs to be conducted with special care and require high supervision.
- Manufacturing cost: Building a new machine for measuring the temperature for a single rotational speed is not cost effective. The manufacturing cost for this prototype is expensive and a refurbished one from the thermally damaged machine will not performed similar to the new one.

The simulations were conducted with boundary conditions similar to the experimental test with an energy equation of segregated fluid temperature being included. The losses input on the magnets and the rotor were inserted based on the finite element analysis for a maximum torque of 376Nm. The input losses value is presented in Table 4-7 for this selected rotational speed.

Table 4-7: The speed, torque, magnet losses and rotor losses of a YASA machine produced by FEA for a single sided rotor.

Speed (rpm)	Peak Torque (Nm)	Magnet Losses (W)	Rotor Losses (W)
2000	376.0	13.25	67.07
4000	373.3	51.57	122.05

Table 4-8 lists the material properties for the magnet and the rotor for the simulation. In reality, the magnet was fixed to the rotor by adhesive bonding which is not included in this simulation, due to the difficulty in the mesh generation of this adhesive thin layer. In this simulation, it was assumed that the magnets have a direct contact to the rotor which in reality does not happen. The simplification of having a direct contact between the magnets and the rotor will have slightly lower magnet temperature because the adhesive layer has lower thermal conductivity and will act as thermal barrier. Therefore, this approach is expected to increase the heat transfer via conduction by excluding the thin adhesive layer that may act as a thermal barrier. Detailed analysis of the effect of adding the thin adhesive layer into the simulation is discussed in Chapter 5.0.

Table 4-8: Material properties of the magnet and the rotor.

Material	Magnet (NdFeB)	Rotor (Steel)
Density (kg/m^3)	7500	7840
Specific heat (J/kg.k)	440	490
Thermal conductivity (W/m.K)	9	48

The experimental testing was conducted at two rotational speeds, namely 2000rpm and 4000rpm. The first run at 2000rpm was stopped as soon as the non-vented rotor reached its threshold temperature of 80°C. The machine cut-off was deactivated to allow the final run of 4000rpm to be able to pass beyond the threshold temperature. The final run at 4000rpm was conducted until both the non-vented and vented rotors achieved their stabilised temperature. The thermal condition is considered as steady state because the temperature has only been creeping as much as 3.1°C for 1 hour and only 1.2 °C for the last 30mins. Figure 4-21 shows that this increase in rotors temperature is parallel with the increase of close ambient box temperature.

A steady state CFD simulations for temperature validation were run at these rotational speeds of 2000rpm and 4000rpm. Although the 2000rpm experimental did not reach its thermal steady state condition, the temperature validation was made between the forecasted temperature based on the short data and compared with the steady state CFD simulations. This assumption of using forecast is reliable because:

- The vented (solid line) and non-vented rotor (dash line) temperatures share a similar trend for 2000rpm and 4000rpm as shown in Figure 4-27. The temperature difference (delta temperature) between the 2000rpm and 4000rpm of each rotor is almost constant above 500sec.
- Forecast was made by using sigmoid function (von Seggern 2007) This function have S-shaped curve that suits the trend of the temperature growth in the temperature measurement where the temperature growth is sharply up to 1000sec, gradually increases between 1000sec to 2000sec, then steadily grows above 2000sec.

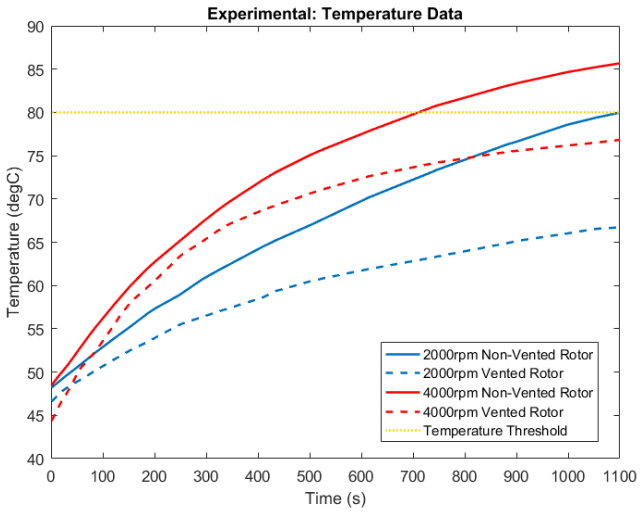

Figure 4-27: Vented and non-vented rotor temperatures of 2000rpm and 4000rpm

Additionally, it is not practical to build another prototype machine to perform a single rotational speed test as discussed previously due to safety and manufacturing cost. On the other hand, performing the CFD validation with transient simulation is also not feasible because:

- The focus of this work is on steady state simulation and all of the work in this project is using steady state simulation.
- Validation by steady state CFD simulation of rotor cooling technique for an axial flux permanent magnet machine is novel. Limited reference is available on steady state let alone for transient simulation.
- Performing transient simulation will lead to greater uncertainty that needs to be verified.
- Performing transient simulation requires high computational cost and time because the moving part will be explicitly rotated at the designated rotational speed.

Therefore, the vented rotor temperature measurement of 2000rpm was forecast with reference to the regression in Eq. 4-3. The forecasted trend was added to the graph plotted in Figure 4-28. The forecast of 2000rpm was

decided to be stopped at 6000s as the vented rotor's temperature was only creeping up 0.5°C between its final 500s and insignificant.

$$T_{Vented} = 81.17 + \frac{(-34.55)}{\left(1 + \left(\frac{t}{779.55}\right)^{0.97}\right)} \quad \textbf{(Eq. 4-3)}$$

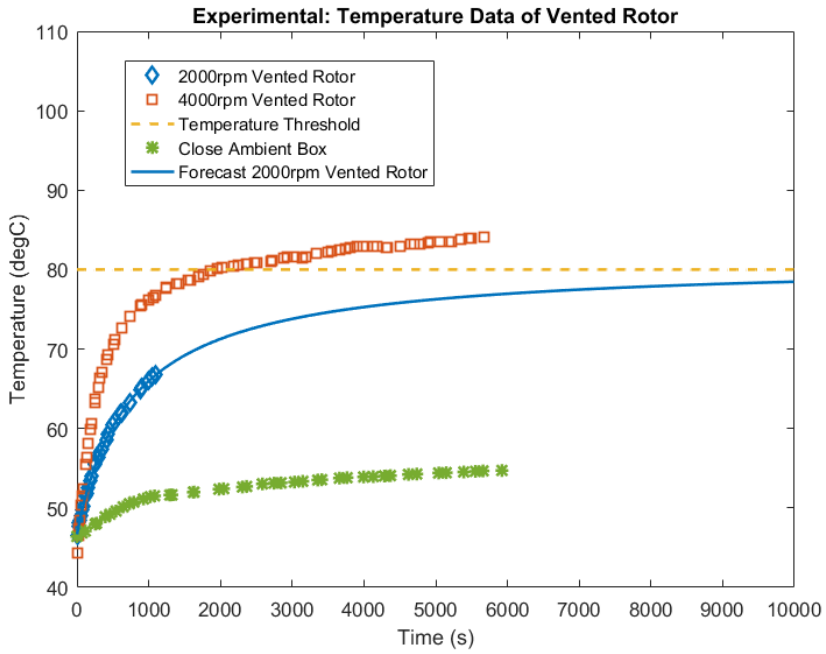

Figure 4-28: Forecast trends of rotor's temperature at 2000rpm

The temperature value of the vented rotor forecast result at 2000rpm and the measurement data at 4000rpm were collected. Table 4-9 tabulated the comparison between the CFD simulation and the experimental results for validation purpose. The CFD simulations at both rotational speeds managed to get a decent prediction with a percentage of error of 0.87% and 0.96% (calculated in Kelvin) for 2000rpm and 4000rpm respectively. The percentage of error is calculated in Kelvin when compared to the temperature results because it is the 'true' temperature value. The term 'true' temperature value is because the absolute zero temperature is equal to zero Kelvin and not zero degree Celsius. Therefore, the percentage of error is small (less than 1%) although the temperature difference is 3°C.

$$\% \text{ Error} = \frac{\left(T_{Experiment} + 273.15\right) - \left(T_{CFD} + 273.15\right)}{\left(T_{Experiment} + 273.15\right)} \times 100 \quad \textbf{(Eq. 4-4)}$$

Table 4-9: The vented rotor's temperature validation

RPM	Exp	Forecast	CFD	ΔT	%
	°C	°C	°C	°C	Error
2000		76.75	73.72	3.04	0.87%
4000	83.97		80.56	3.41	0.96%

4.7 Chapter summary

The verification and validation of the rotor cooling technique has been established in this chapter. Various exercises were performed in order to have credibility for the results produced by the CFD modelling. Without these essential steps, it would be very difficult to achieve confidence (Milnes et al. 2008). In this study, it can be summarised that:

1. Mesh sensitivity study shows the finer mesh level gives reliable results.
2. All turbulence models perform reasonably well.
3. The flow validation shows that the accuracy of the CFD modelling is increased by assuming the whole of the rotor's air cavity in the machine as a rotational domain.
4. Finally, the CFD model manages to predict the vented rotor temperature very close to the experimental data.
5. This should provide evidence that the chosen CFD modelling setup and boundary condition is reliable to be used in further CFD design based studies.

Chapter 5

Thermal Modelling of the Sealed Rotor

5.0 Thermal modelling of the sealed rotor

It is important to understand the thermal mechanism of the sealed machine before the exploration of the rotor cooling technique. This step assesses the temperature development within the rotor cavity without any intervention of cooling air. The strategy here is to investigate the thermal effect of all the components of the rotor's assembly (rotor, magnets, adhesive, air and cover), thus a better solution can be made via design exploration for the rotor cooling technique.

Two types of thermal assumption were considered in this work with their advantages and disadvantages, as listed below:

1. Fixed temperature
    a. The specific heated wall is assumed to have a certain amount of temperature usually based on the target operating thermal or the temperature threshold.

b. This is the easiest form of thermal assumption that allows the evaluation of the air's effectiveness to attract the heat from the solid.
c. It is the fastest and lowest computational cost solution as the solid domain is not required during the simulation.
d. The heat distribution within the solid could not be assessed due to the lack of the solid domain.

2. Losses density based on losses simulation
    a. The specific solid volume is input with its losses value produced by finite element analysis (FEA) simulation.
    b. It is the most accurate assumption as it may represent the realistic thermal production of the magnet and rotor by the losses.
    c. This is the most expensive assumption in terms of skills and computational time, as it requires another set of tools to estimate the losses within the system.

5.1 Losses in the YASA machine's rotor assembly

In this study, the focus was given to the losses values of the magnet and the rotor, which occur within the rotor assembly. To identify the losses on the rotor assembly, an electromagnetic Finite Element Analysis (FEA) is applied simulating the motor at specific operating conditions based on the machine design, intended machine performance (e.g. continuous power) and input power. As discussed previously in Section 2.1, the interaction of the magnetic field between the rotor magnets and the rotating field created by the stator windings creates losses in the machine, which manifest as heat. The most accurate way to attain these losses is by using FEA, for example in the work of Wahsh et al. 2016, which took the losses of Shazly et al. 2014 as an input, and Wang et al. 2017.

The FEA simulations applied for the losses identification of this YASA machine, are based on the work of Woolmer 2009 (PhD thesis). The losses

are calculated via FEA for a sealed YASA machine and then modified to in-cooperate the rotor cooling technique. The FEA model is then validated with experiment data. These losses then become the main heat source for the CFD modelling. Even though FEA analysis was not part of the scope of this study, however, some fundamental understanding of the losses is essential as the basis of the electric machine operation is electromagnetic by nature.

The losses in the AFPM machine can be subdivided into two parts; rotor and stator (Chapter 2). Rotor losses are composed of eddy losses (load and no load) and iron losses. For AFPM, rotor's losses in the electric machine are calculated using the following equations. The magnet's losses were calculated by the non-linear equations Eq. 5-1 and Eq. 5-2 and the rotor losses W were calculated by Eq. 5-3.

$$W_{NonLoad,Eddy} = k_{NonLoad,Eddy} \cdot \omega^2 \quad \textbf{(Eq. 5-1)}$$

$$W_{Load,Eddy} = k_{Load,Eddy} \cdot i^a \cdot \omega^2 \quad \textbf{(Eq. 5-2)}$$

$$W_{Rotor,Load} = k_{Rotor,Load} \cdot i^b \cdot \omega^c \quad \textbf{(Eq. 5-3)}$$

where i is the current, ω is the rotational speed and $k_{NonLoad,Eddy}$, $k_{Load,Eddy}$, $k_{Rotor,Load}$, a,b,c are the constant values that have been validated between the FEA and the experimental yet could not be included here due to confidentiality. The FEA model with custom constant values has 4% of error compared to the experimental results.

The sealed YASA machine tested in this chapter has a 50kW continuous power rating. Additionally, for an advanced design, the losses value was calculated with 150kW power ratings. Nevertheless, each study may use different thermal assumptions and different machine power ratings. The losses will be mentioned in regard to the objective of the exercises and studies.

The methodology conducted in this chapter, can be extended into other thermal modelling for any electrical machine. The losses input need to be

corresponding to the electrical machine type, topology, geometry and design while it is suggested to gain the losses values from Lumped Parameter (LP) modelling or FEA modelling that have been validated.

5.2 CFD model of the sealed machine

Figure 5-1 illustrates the three-dimensional (3D) YASA sealed machine where the cross-section view shows the fluid rotational region in red and the solid domain of the rotor and magnets in grey. The rotor has circular array rib features to add strength to support the centrifugal force produced by the surface mounted magnet on the other side of its face, as shown in Figure 5-2. This feature is placed at r/R of 0.68. The size of the rotor's outer diameter is 252.7mm and the clearances of the system are presented by the gap ratio $G = s/R_r$: the magnet-to-stator is 0.00791, the rotor-to-stator is 0.04907, the rotor-to-cover is 0.03957 at inner (r/R <0.68) and 0.05303 towards the rotor's outer edge.

All setups including mesh, setup and boundary conditions are the same as the setup of the verification and validation presented in Chapter 4.0, unless otherwise specified. The material properties used in this study are tabulated in Table 4-8 with adhesive material properties added to the list.

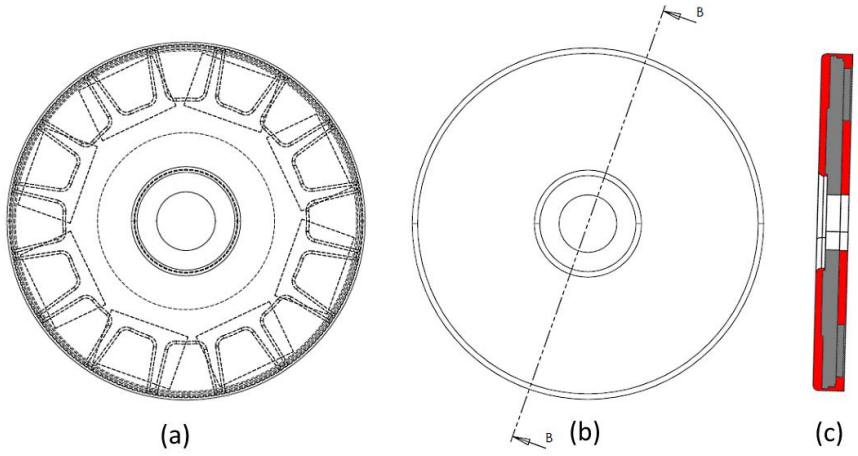

Figure 5-1: Single side of the YASA sealed machine's rotor cavity of (a) the front view with hidden line visible, (b) the front view and (c) the b-b cross-section view.

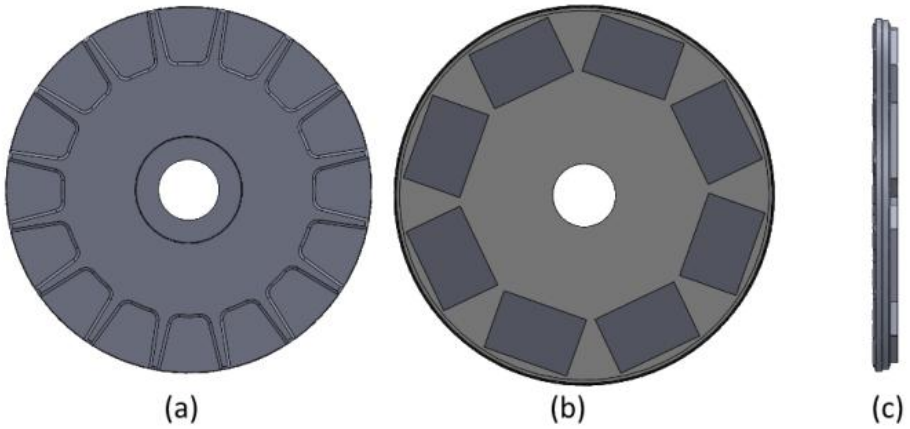

Figure 5-2: The sealed machine's rotor assembly of front view (a), rear view (b) and side view (c).

Table 5-1: The material properties.

Material	**Magnet**	**Rotor**	**Adhesive**	**Air**
	NdFeB	**Steel**	**2273D**	
Density (kg/m^3)	7500	7840	1200	
Specific heat (J/kg.K)	440	490	1000	1003.62
Thermal conductivity (W/m.K)	9	48	0.19	2.60×10^{-2}
Dynamic viscosity (Pa.s)				1.85×10^{-5}
Molecular weight (kg/mol)				28.96
Turbulent Prandtl number				0.9

5.2.1 Full geometry versus partial 1/8 simulation

Given that the sealed machine has symmetrical geometry, the 3D CFD model was simplified into a partial pie-cut geometry instead of a full circular geometrical domain (named "partial 1/8" from now on). However, this may jeopardise the accuracy of the prediction if the uncertainty is unknown. Therefore, the first step is to conduct a study that identifies the results variation between full geometry and partial 1/8 simulation. Figure 5-3 shows

the slice of partial 1/8 from the full geometry. The term '*slice'* indicates that the partial 1/8 simulation took a small, however symmetrical, piece out of the the full geometry.

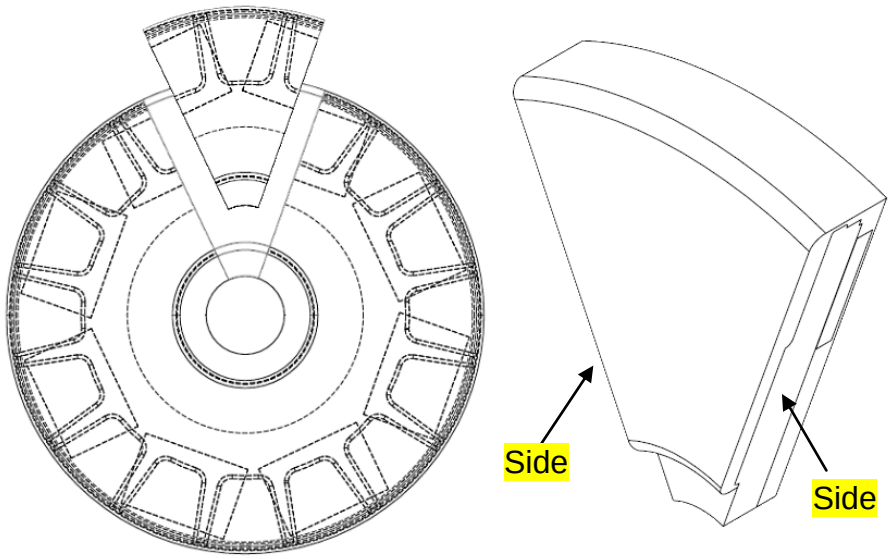

Figure 5-3: Full geometry (left) and the slice of partial 1/8 geometry (right) including new sides surfaces.

The boundary conditions (BCs) of the full geometry have remained the same as the V&V procedure while the partial 1/8 geometry has to be adapted by implementing periodic boundaries on its sides (see Figure 5-3) for all the components. The sides are now newly introduced flat surfaces that present themselves as the geometry has been cut through. A periodic boundary is used to match any two unattached surfaces to allow conformal mesh generation, thus it is able to transfer parameters and functions from one surface to another (STAR-CCM+ 2016). For this case, a rotational periodic contact is used in the partial 1/8 model. The cover and stator wall were set to 60°C following the machine manufacturer's standard test assumption (Yasa Motors Ltd. 2017). The magnets are assumed to have a fixed losses density of 100W (of full geometry) for simplicity. The simulations were set at 2000rpm, 4000rpm, 6000rpm and 8000rpm.

The average temperatures of the magnets, rotor and interior air were collected and Figure 5-4 plots the differences between these two approaches. All the components demonstrated a similar trend with average differences of 1.62%, 0.39%, 0.01% and 0.35% at 2000rpm, 4000rpm, 6000rpm and 8000rpm respectively.

Additionally, the computational time has reduced significantly, as provided in Table 5-2. Both simulations were conducted with the same number of processors (12 processors) and it is expected that the computational time of partial 1/8 simulation should reduce nearly $1/8^{th}$ of the full geometry. However, this is not the case because the STARCCM+ automatic mesh generation has created a mesh refinement on the periodic boundaries in order to achieve conformal mesh in between the sides surfaces. As a result, the partial 1/8 CFD model has only managed to reduce the cell count by half when compared to the full geometry of the CFD model. Therefore, the computational time has been reduced but not proportionally to the size reduction of the geometry.

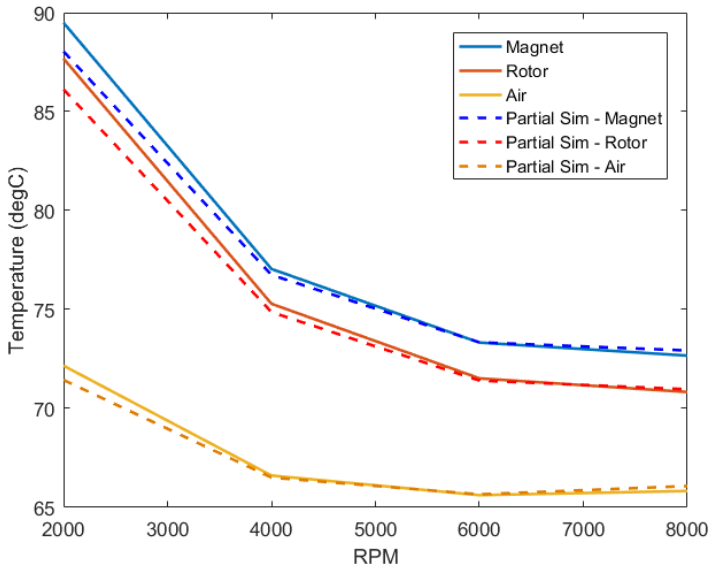

Figure 5-4: Average volume temperature between full geometry and partial 1/8 simulations.

Table 5-2: Total Solver Elapsed Time for each turbulence model simulation

CFD Models	Cell Count	Total Solver Elapsed Time (HH:MM:SS)	Time Difference (HH:MM:SS)
Full Geometry	7,694,217	03:10:32	01:08:34
Partial 1/8	3,710,560	02:01:57	

5.3 Effect of the adhesive layer

The initial study of this sealed rotor shows a considerable difference in the computational time between the full geometry and the partial 1/8 simulations, while both produced almost similar temperature results. So, the partial 1/8 simulation was considered in this section, where the additional component of an adhesive layer was included. The surface mounted magnets were held together on the steel rotor by a strong adhesive that has a low thermal conductivity. Therefore in this section, the thermal changes across the solid components will be evaluated where this thin adhesive layer may cause a bottle-neck or chocking effect on the temperature flow. Figure 5-5 shows the location of this 0.2mm adhesive layer which requires fine mesh, thus it may increase the computational time of the partial simulation, yet within the tolerable extended period.

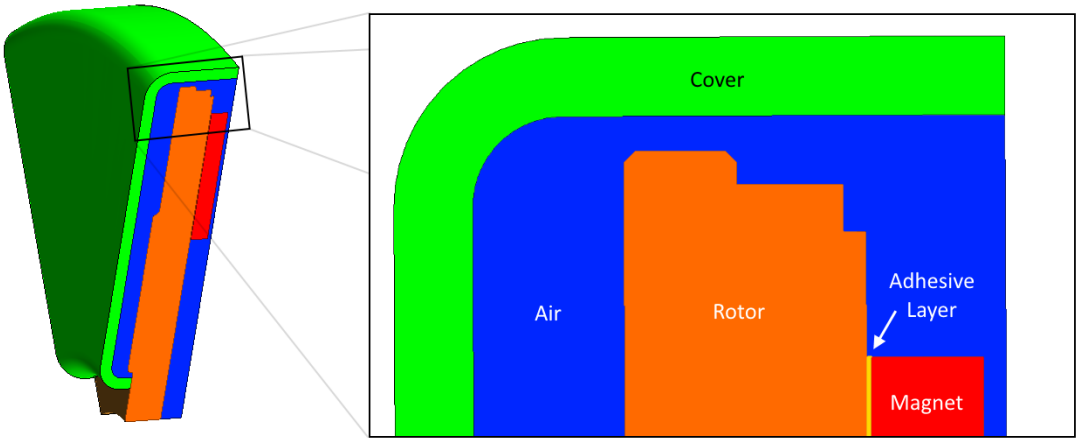

Figure 5-5: Partial 1/8 CFD model with material labels.

The input losses for the magnets and the rotor were based on the FEA simulation of a 50kW machine that produced a healthy torque of 125Nm up

to 4000rpm before drop down at a higher rotational speed. As mentioned beforehand, FEA analysis was not in the scope of this study, also due to the confidentiality the detail of the FEA was not enclosed in here and only the results are used.

The magnet losses increased as the rotational speed increased although the rotor losses only increased until 4000rpm and started to decrease as the machine ran faster. The torque-speed curve with the losses is presented in Figure 5-6. The cover and the stator walls were set at a static temperature of 60°C. The maximum steps were set to be 10,000 iterations to allow reliable results with close monitoring of the average volume temperature as shown in Figure 5-7.

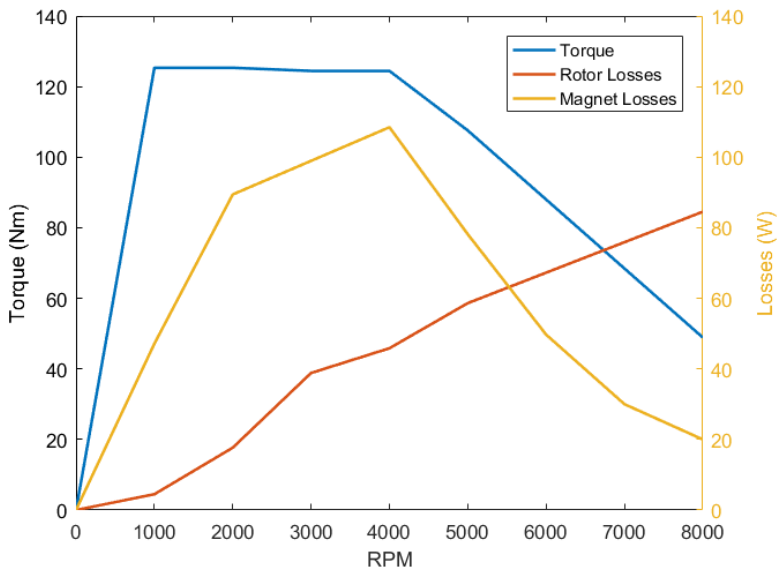

Figure 5-6: Torque-speed curve and the losses of 50kW (continuous power) for the sealed machine.

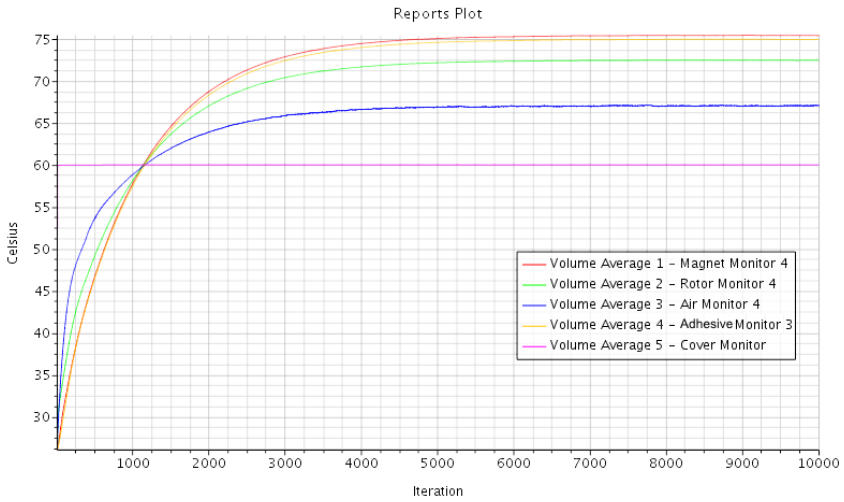

Figure 5-7: The average volume temperate plot over iteration for 4000rpm.

Figure 5-8 shows the average volume temperature of the magnets, rotor, adhesive and interior air between the simulations of the with adhesive layer and the without adhesive layer. The percentage error was calculated in Kelvin because the absolute zero temperature is measured by Kelvin rather than in degrees Celsius. The percentage error of the temperature can be calculated by Eq. 4-4. Therefore, the error in temperature is usually presented in small values although the difference is obvious (i.e. 1% of error is a result from a temperature difference of 3.5 $^{\circ}$C). Also, as these values are expected to be small, both simulations of the with adhesive layer and the without the adhesive layer were performed using the same mesh in order to eliminate the uncertainty of meshing error. The adhesive layer of 0.2mm was assumed to be part of the magnet on the without the adhesive layer simulations.

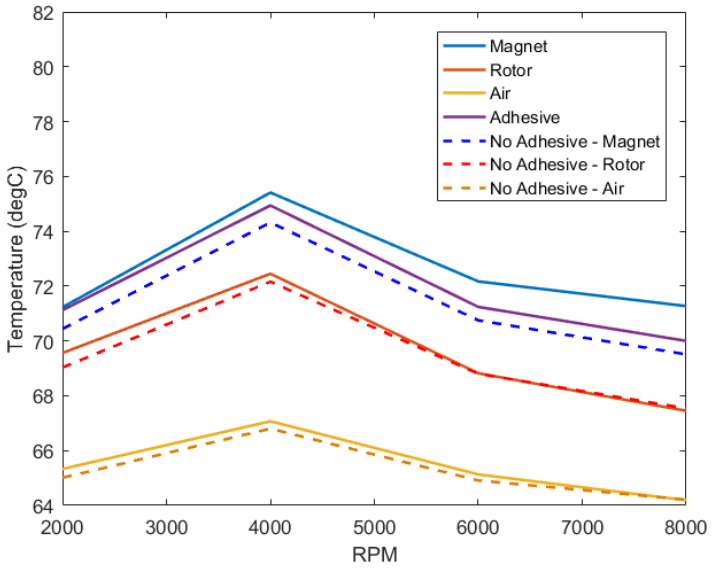

Figure 5-8: The average volume temperature with and without an adhesive layer for the 50kW sealed machine.

In here, the magnet temperature with the adhesive is higher than the simulation without the adhesive at all rotational speeds. At a lower speed, the difference is 0.23% and the gap increases at a higher speed up to 0.51% at 8000rpm. However, the rotor and the interior air temperature only shows major differences at a lower speed with 0.16% for the rotor and 0.10% for the air, providing similar data as the rotational speed increases.

The bottle-neck or chocking effect of the adhesive layer on the temperature flow can be better visualised by the non-dimensional temperature profile at r/R 0.79, which flows from stator-air-magnet-adhesive-rotor-air-cover. Figure 5-9 shows the set of results overlaid between 'with and without' adhesive simulations for every tested rotational speed. In these figures, the normalised axial direction is represented by z^* in Eq. 5-4:

$$z^* = \frac{z}{g} \qquad \textbf{(Eq. 5-4)}$$

where z is z coordinate and g is the gap ratio, and the non-dimensional temperature is defined by $\Delta T^*_{(r,z)}$ in Eq. 5-5:

$$\Delta T^*_{(r,z)} = \frac{T_{(r,z)} - T_{ref}}{T_{(r,z)max} - T_{ref}} \quad \textbf{(Eq. 5-5)}$$

where $T_{(r,z)}$ is the local temperature, $T_{(r,z)max}$ is the maximum temperature and T_{ref} is the reference temperature. The stator surface is located at z^*= 0 and the cover surface is located at z^*= 1.

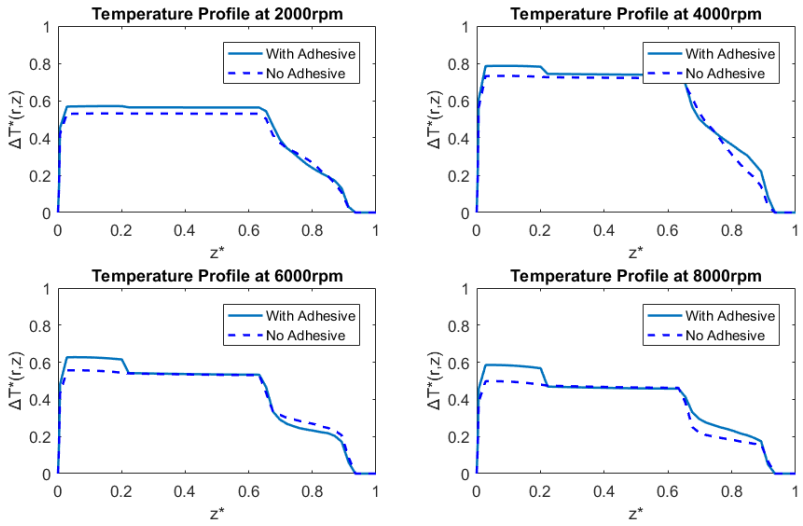

Figure 5-9: Non-dimensional temperature profile comparison between with and without an adhesive layer for the 50kW sealed machine at r/R 0.79.

Having the adhesive, the heat from the magnet is blocked from flowing through the steel rotor, thus the temperature of the magnet rises at all rotational speeds with an obvious difference in temperature above 4000rpm. The low thermal conductivity of the adhesive creates a maximum difference of 8.8% between the magnet and the rotor at 8000rpm.

5.4 The machine cover's conjugate heat transfer (CHT)

The study using the partial 1/8 CFD model was extended by adding an air domain to the exterior of the machine in order to evaluate the Conjugate Heat Transfer (CHT) from the machine's cover to the exterior air. This exercise is useful in order to assess the effect of using a static temperature on the cover which was previously set at 60°C, based on the machine manufacturer's

standard test assumption. This time, the CFD simulations include the buoyancy and gravity effect as the CHT at the outer layer of the cover will be via natural convection. The illustration in Figure 5-10 shows the CFD model for this CHT study, which has included an air domain extension of 150mm to the z direction. The simulated machine has included an aluminium cover and an adhesive layer for comparison purposes. The material properties of the added cover are tabulated in Table 5-3.

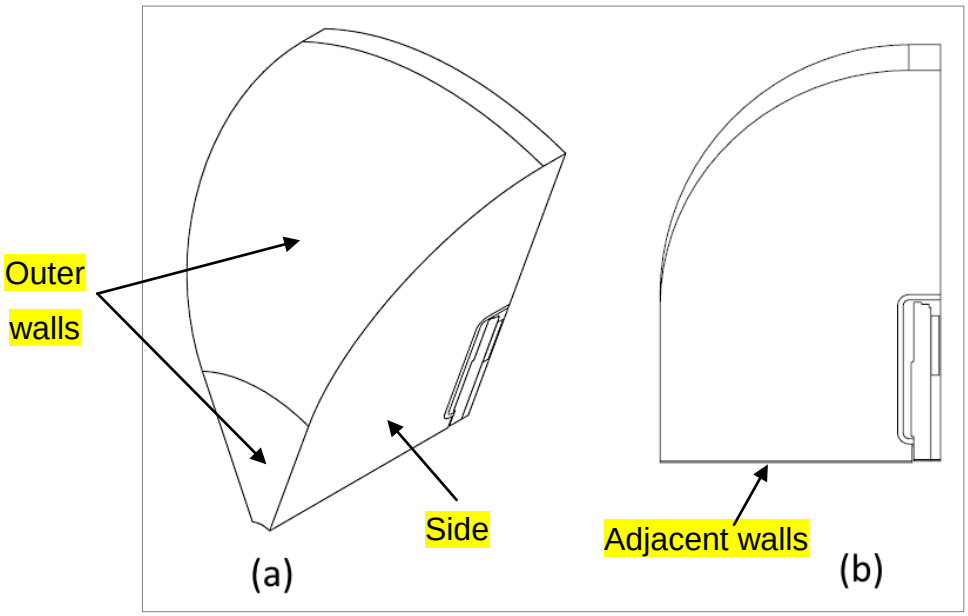

Figure 5-10: Additional air domain of 150mm in the z direction for conjugate heat transfer simulation.

Table 5-3: The material properties.

Material	**Cover**
	Aluminium
Density (kg/m^3)	2702
Specific heat (J/kg.k)	903
Thermal conductivity (W/m.K)	237

The side of the air exterior has periodic boundary conditions, the adjacent walls are adiabatic walls while the exterior wall was set as a free stream boundary condition. A free stream boundary represents these outer walls without any constrain and its flow variables are determined by Riemann invariants (STAR-CCM+ 2016). Although this BCs is usually used in external aerodynamic simulations, it can be exploited for this CHT simulation with no flow variables inserted, but only the static temperature of the environmental air at 25°C. The simulation was set to run longer iterations of 20,000 to allow convergence of the temperature variables with a convergence criterion of 1×10^{-4} that is applied across this doctoral project (see Section 3.6).

Two sets of scenarios were conducted where the initial CHT simulation was subjected to the losses of over performance in order to validate the capability of the CFD software. Later, the CFD simulation was tested again with its actual performance losses.

5.4.1 The sealed machine's over performance (temperature validation)

This initial exercise of CHT heat transfer is conducted by using the losses of the 150kW machine which was tested experimentally in Chapter 4.0. Previously, the experimental of the temperature measurement was conducted on the machine that has single rotor cooling (vented rotor) on the non-drive-end side and a sealed rotor (non-vented rotor) on the drive-end side. The non-vented rotor in the previous experimental has an identical geometry with the sealed rotor of this study. Therefore, it is only possible to conduct temperature validation at specific rotational speeds equivalent to the experimental test of 4000rpm. The forecasting method that was implemented in the Section 4.6.2, was not suitable for this case because there is no appropriate mathematical expression or regression that can suit the short experimental temperature data and reach a steady state condition for the 2000rpm. Therefore, it was not implemented in this case.

Table 5-4 presents the temperature validation result where the CHT simulations managed to predict close to the forecast and the experimental results, with an error of 0.2% (calculated in Kelvin) for the 4000rpm. The slight difference in temperature is may be because in the experiment, the cover of the drive-end side was mounted onto the steel rig and its contact surface may provide heat conduction through the solid, while almost eliminating the possibility of CHT, due to the lack of air between the machine's cover and the rig. On the other hand, the machine's cover in this CHT simulation is fully exposed to the environmental air to allow heat convection.

Table 5-4: The non-vented rotor's temperature validation

RPM	Exp	CFD	ΔT	%
	°C	°C	°C	Error
4000	98.11	97.57	0.54	0.2%

5.4.2 The sealed machine's actual performance

The actual simulation of the CHT was computed by using the losses of the 50kW sealed machine, which is the actual machine performance. The input losses values for these simulations were based on earlier losses data presented in Figure 5-6. The results of Figure 5-11 present the average volume temperature of all the components for the CHT simulations comparing with the previous adhesive simulations that did not include the exterior air (Figure 5-8) where the machine cover temperature was fixed at 60°C. These data are called 'fixed cover temperature' in the Figure 5-11.

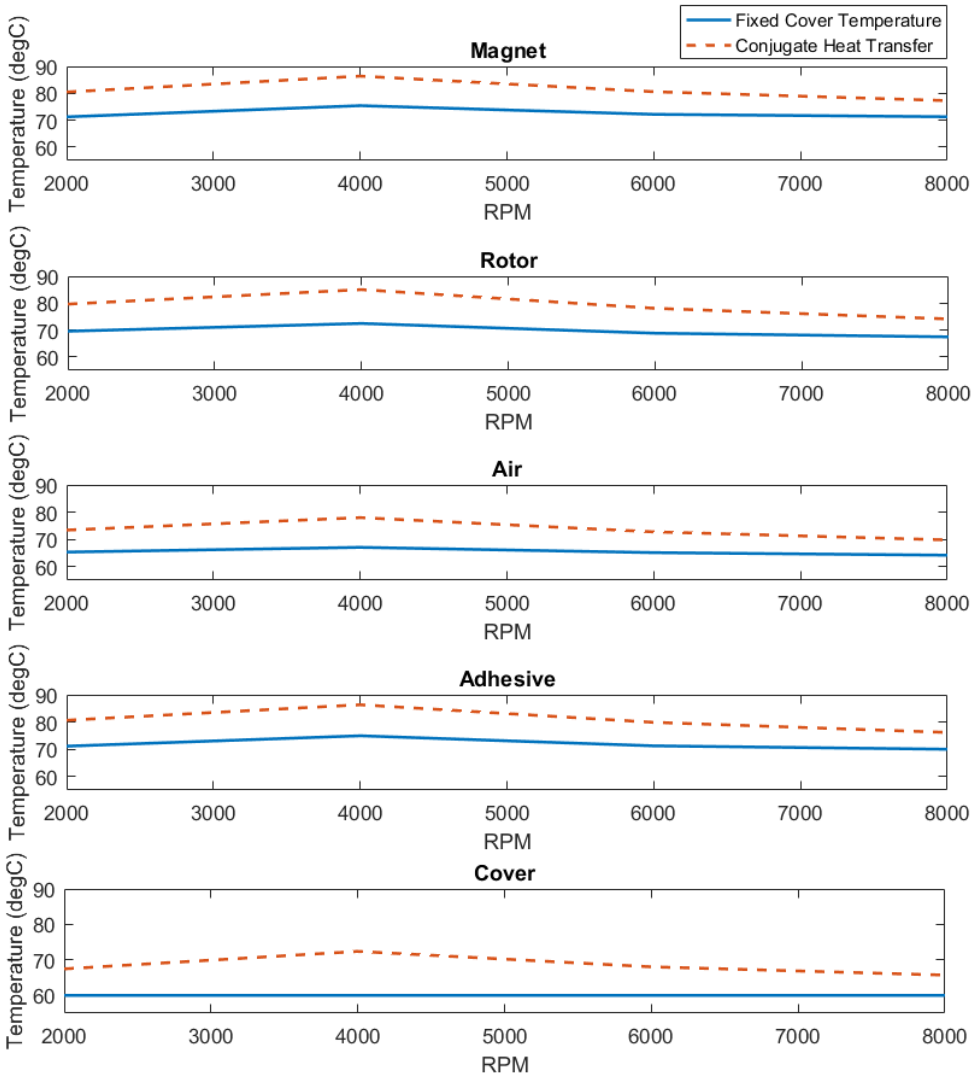

Figure 5-11: The average volume temperature with and without the exterior air for the conjugate heat transfer (CHT) of the 50kW sealed machine.

For comparison, all of the components in the sealed machine have a higher temperature value in the CHT simulations. This is because the cover temperature of the CHT simulations is always higher than the assumption made by the machine manufacturer of 60°C on the fixed cover temperature simulations. Initially in the fixed cover temperature simulations, the heat from the rotor and the magnet reach their equilibrium temperature at a lower temperature because the cover has a static temperature of 60°C. However, in CHT simulations, the cover did not have any constrain in terms of

temperature. This means that the heat from the internal components will transfer to the cover and this heat then transfer to exterior air naturally. The exterior air of CHT simulations did not have any flow condition that could promote the convective heat transfer between the cover and the exterior air. In the results, the cover has more temperature and at 4000rpm, the cover temperature of the CHT simulation is 12.4°C higher than the specified static temperature. The increase in the cover temperature leads to the raising of the rotor average temperature at 11.5°C and magnet at 8.7°C at 4000rpm.

Similarly, the same trend can be observed at 8000rpm, where the cover temperature of the CHT simulation is 5.7°C higher than the specified static temperature with the rotor average temperature of 9.5°C and magnet of 6.1°C. Therefore, the internal components of the sealed machine have a dependency on the temperature of the machine's cover. On the other hand, the internal air temperature did not show much difference between the CHT simulations and the fixed cover temperature simulations. This is because the air has low thermal conductivity at 2.60×10^{-2}W/m.K.

Additionally, Figure 5-12 shows the temperature contour plot at the cross section for all the rotational speeds. It is observed that, the temperature propagation to the air exterior is dependent on the internal heat. The high losses of the rotor and the magnet at 4000rpm show that the hottest internal component temperature is the larger air exterior area to the cover that has high temperature (see Figure 5-12c). On the other hand, the least losses values at 1000rpm in Figure 5-12a point at the smaller air exterior area to the cover that has high temperature.

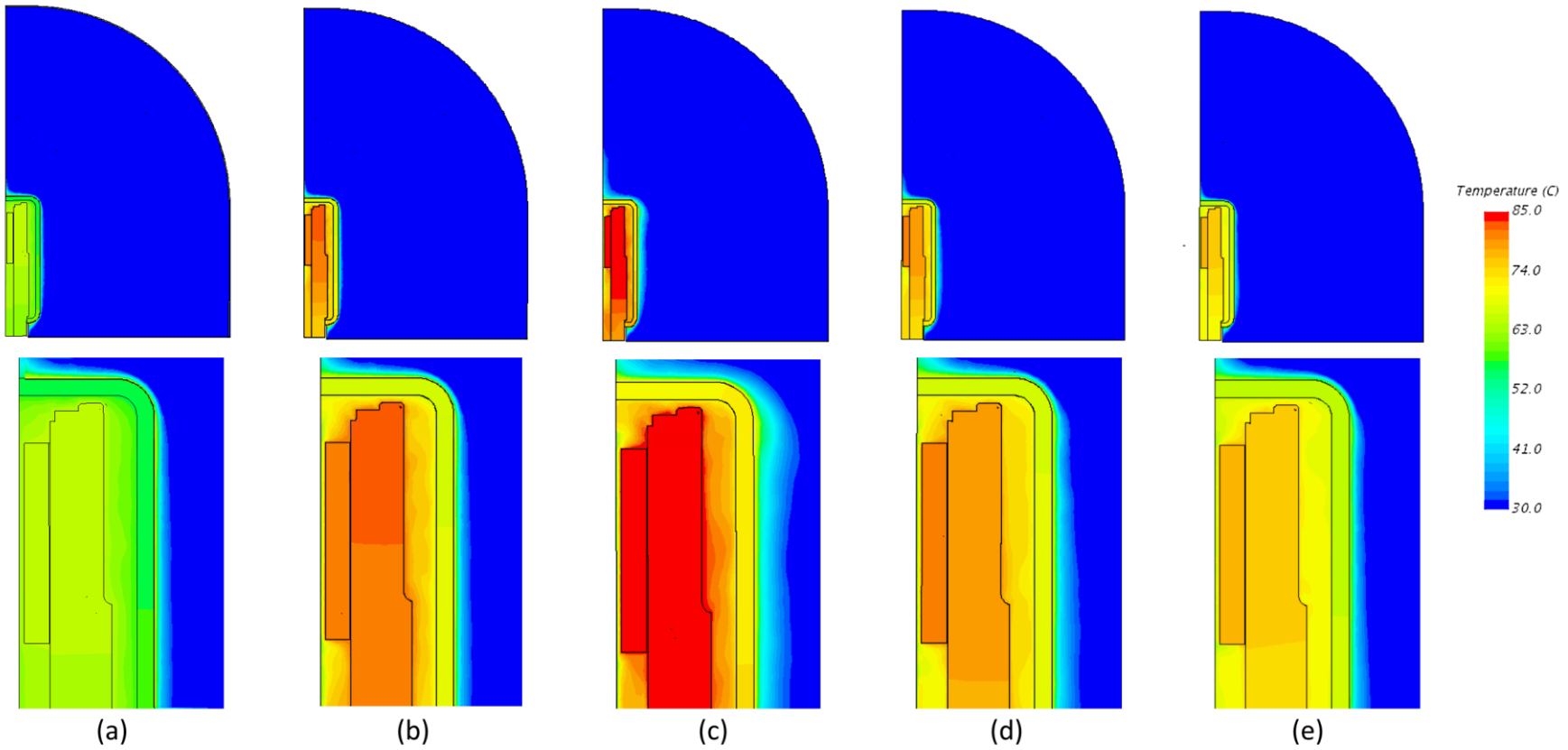

Figure 5-12: Contour plots of the conjugate heat transfer simulation at (a) 1000rpm, (b) 2000rpm, (c) 4000rpm, (d) 6000rpm and (e) 8000rpm.

5.5 The heat transfer coefficient and the thermal resistance

The heat transfer coefficient and the thermal resistance are the two parameters useful to the machine designer. Utilising validated CFD models, these parameters can increase the accuracy of analytical calculations such as the LP thermal model for simplification. This is important because the LP thermal model allows faster transient predictions than the CFD simulations. The heat transfer coefficient and the thermal resistance were calculated by Eq. 5-6 and Eq. 5-7 respectively.

$$h = \frac{q"}{\left(T_s - T_{ref}\right)} \quad \textbf{(Eq. 5-6)}$$

$$R_t = \frac{\left(T_s - T_{ref}\right)}{q"} = \frac{1}{h_c} \quad \textbf{(Eq. 5-7)}$$

where $q"$ is the wall heat flux, T_s is the surface temperature and T_{ref} is the reference temperature based on the local bulk temperature of the interior air.

Figure 5-13 and Table 5-5 present the average heat transfer coefficients and the average thermal resistance results of the solid and fluid domains. They are presented in detail for magnet-to-air interior, magnet-to-adhesive, rotor-to-adhesive, rotor-to-air interior, cover-to-air interior and cover-to-air exterior. The average heat transfer coefficient of rotor-to-air interior and cover-to-air interior increase linearly as the rotational speed increases. The magnet-to-air interior value also increases up to 4000rpm and is then flattened, as the heat is unable to transfer to the interior air as it spins too fast. On the other hand, the average heat transfer coefficient of the surface that has contact with the adhesive increases abruptly after 4000rpm because the losses values of the magnet and the rotor decrease. Finally, the cover-to-air exterior increases its heat rejection at a lower speed and changes its linear pattern as the cover has reached its optimal thermal conductivity.

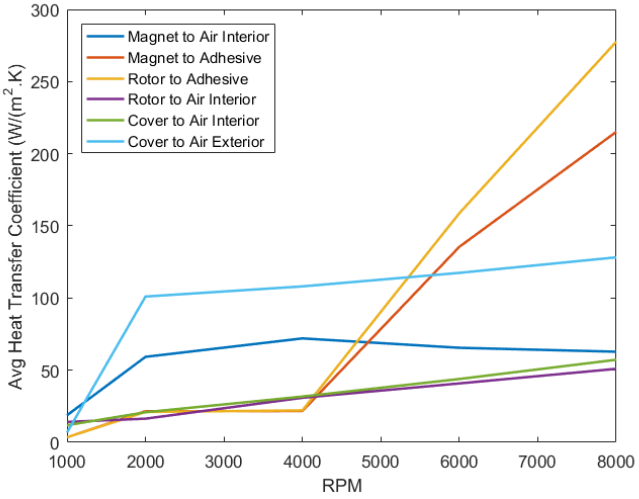

Figure 5-13: Average heat transfer coefficient of the sealed machine.

Table 5-5: Average thermal resistance of the sealed machine.

		Average thermal resistance, R_t (m^2.K/W)				
From	**To**	**1000**	**2000**	**4000**	**6000**	**8000**
Magnet	**Air Interior**	0.0533	0.0169	0.0139	0.0153	0.0159
	Adhesive	0.2880	0.0464	0.0461	0.0074	0.0046
Rotor	**Adhesive**	0.2889	0.0475	0.0452	0.0063	0.0036
	Air Interior	0.0707	0.0610	0.0324	0.0245	0.0196
Cover	**Air Interior**	0.0844	0.0479	0.0315	0.0228	0.0175
	Air Exterior	0.1476	0.0099	0.0093	0.0085	0.0078

5.6 The relationship between the rotor and the magnet temperature

The regression of the relationship between the rotor and the magnet temperature is presented in Table 5-6. There are approximately similar regressions of both static cover temperature and CHT simulations when

adding the adhesive. However, these relationships will be inaccurate for a rotor temperature above 90°C, thus the regression of the static cover temperature without adhesive simulation is advisable for high temperatures. These regressions are useful especially to AFPM manufacturers, as at the moment, the machine's temperature monitoring point is limited to the rotor temperature only.

Table 5-6: Relationship of the rotor and the magnet temperature.

Simulation	Scenario	Regression
Static Cover Temperature	Without adhesive	$T_{magnet} = 1.0463T_{rotor} - 1.1849$
	With adhesive	$T_{magnet} = 0.8414T_{rotor} + 14.404$
CHT	With adhesive	$T_{magnet} = 0.834T_{rotor} + 15.469$

5.7 Chapter summary

In this chapter, the thermal mechanism of the sealed machine has been extensively explored. A symmetrical geometry allows for the simplification of the CFD models where the partial 1/8 simulation produced similar results yet there is a significant decrease in the computational time as expected. The partial simulation allows extensive studies that would take days to complete if conducted in a full geometrical model. By slicing into 1/8 of its geometry, the adhesive layer was added and later the air exterior was included allowing the machine cover to disperse the heat by a conjugate heat transfer simulation.

Finally, the static temperature of machine manufacturer's standard test assumption at 60°C was a sensible approach yet it would be more precise if the machine's cover temperature was assumed to be 65°C across the rotational speed range.

The results and findings from this chapter will be used in the exploration of rotor cooling techniques for an AFPM machine.

Chapter 6

The Rotor Cooling Technique via Computational Fluid Dynamics

6.0 The rotor cooling technique via Computational Fluid Dynamics

This chapter focus on the execution of the rotor cooling technique in AFPM machines. Previously in Chapter 5.0, the thermal performance of a sealed YASA machine with a 50kW continuous power rating including the primary direct stator cooling was analysed. The results showed that the temperature of the magnets reached 85°C which is a suitable operating temperature, as it is below the generic temperature threshold of 100°C for NdFeB N00H series magnets (Eclipse Magnetics 2014). The optimal rated continuous power for YASA sealed machine was determined from the following considerations:

a. Permanent magnet thermal limit
b. Rotor thermal limit
c. Target product application
d. Reliability of other materials (e.g. seal, epoxy, adhesive) that could lead to deterioration and degradation due to high temperature
e. Cost of manufacturing

Therefore, the machine manufacturer has set 50kW as the optimum rated continuous power for their sealed machine. It is expected that by introducing the secondary cooling method, the machine will have better thermal management especially for the permanent magnets (PMs) that are surface mounted on the rotor. This better thermal management will not only serve as a reason to increase the machine's performance, but will also increase its reliability as it may reduce the potential of machine failure due over temperature that may lead to magnet demagnetisation and degradation.

This chapter begins with the establishment of a novel cooling performance index in order to assist in assessing the design changes for rotor cooling purposes. The introduced cooling performance index is then put into practice by analytical and computational fluid dynamics (CFD) results. Furthermore, multiple fan types from other engineering applications were attached to the rotor of the YASA machine. The evaluation was done on flow characteristics, power requirements and thermal characteristics; then assessed by the newly introduced cooling performance index. Part of the studies has been published in Fawzal et al (2016) and (2017).

6.1 The rotor cooling performance evaluation

6.1.1 The Cooling Performance Index (CPI)

The Cooling Performance Index (CPI) was initially introduced as the *Rotor Cooling Performance Index (RCPI)* by Fawzal et al. (2017), for the assessment of electrical machine cooling, specifically the AFPM's rotor cooling application. It is a dimensionless number that represent the ratio of the convective heat transfer of a design over its power consumption to drive the coolant air. It is expressed as:

$$CPI = \frac{Convective\ HT}{Windage\ Losses} = \frac{q}{W} \quad \textbf{(Eq. 6-1)}$$

$$W = T_q \omega \quad \textbf{(Eq. 6-2)}$$

where T_q is the torque required to spin the rotor at the specific rotational speed ω, in radians per second. The formula Eq. 6-1 will provide a number that will assist a designer to evaluate the cooling design, particularly when involved with design changes, comparisons or optimisation.

Furthermore, the formula can also be applied to other cooling applications with slight derivations to suit them, such as:

- Automotive/motorsports disc brake cooling
    - Using the same formula as Eq. 6-1.
- Heat exchanger (assessment of an external flow)

$$CPI = \frac{Convective\ HT}{Drag\ Power} = \frac{q}{F_d u} \quad \textbf{(Eq. 6-3)}$$

$$F_d = \frac{1}{2} C_d\, A\, \rho\, u^2 \quad \textbf{(Eq. 6-4)}$$

where F_d is the drag force, C_d is the drag coefficient, A is the frontal area and u is the external cooling flow velocity.

- Cooling system by pump or fan (assessment of an external or internal flow)
    - Such as electronic cooling, water jacket cooling, HVAC, refrigeration, air-conditioning etc.

$$CPI = \frac{Convective\ HT\ of\ Cooling\ System}{Pump\ Power\ Consumption} = \frac{q}{\dot{m}\, w} \quad \textbf{(Eq. 6-5)}$$

$$w = \frac{\Delta p}{\rho} \quad \textbf{(Eq. 6-6)}$$

where w is the specific work in Nm/kg or J/kg or m^2/s^2. In some of the applications, the convective heat transfer may be replaced with cooling power or cooling capacity where applicable.

Therefore, the initial name of this formula: the *Rotor Cooling Performance Index (RCPI)* may be viewed in a narrow perspective, hence the author altered its name to the Cooling Performance Index (CPI) to be more

appropriate and concise. This name change is based on the judgement that the application should be broad and not limited to the application of cooling an electrical machine. Rather, the use of this dimensionless number can be applied to any engineering field that requires a cooling assessment that has a relationship between the forced heat convection and the power to drive or generate the flow of the cooling fluid.

6.1.2 Heat convection

The general derivation of the convective heat transfer is expressed by the local surface heat flux q_s" as:

$$q_s" = h_c(T_s - T_{ref}) \quad \textbf{(Eq. 6-7)}$$

where h_c is the local convective heat transfer coefficient, T_s is the surface temperature and T_{ref} is a characteristic temperature of moving fluid on the surface.

From Eq. 6-7, the heat convection q can be calculated by:

$$q = \dot{m}\, C_p\, \Delta T = h_c A(\Delta T) \quad \textbf{(Eq. 6-8)}$$

where $\dot{m}$ is the mass flow rate, C_p is the coolant specific heat capacity and ΔT is the temperature difference between the surface and the reference temperature, h_c is the local convective heat transfer coefficient and A is the heated surface.

6.1.2.1 Heat convection prediction for AFPM machines

For rotating electrical machine applications, the prediction of the heat convection has been studied extensively and published by Howey, Childs and Holmes (2012). The specific formulation to calculate the local convective heat transfer coefficient h_c for the disc type machine or AFPM machine is extracted and presented in radial and axial convective heat transfer separately, as below:

Radial convective heat transfer

The radial convective heat transfer can be computed by calculating the critical angular velocity Ω_{cr}:

$$\Omega_{cr} = \frac{41.19v}{r_m^{0.5}\,(b-a)^{1.5}} \quad \textbf{(Eq. 6-9)}$$

where v is the kinematic viscosity of air and the mean annulus radius r_m is:

$$r_m = \frac{a+b}{2} \quad \textbf{(Eq. 6-10)}$$

Next, the Taylor Number Ta is calculated based on the mean annulus radius r_m:

$$Ta = \frac{\Omega\, r_m^{0.5}\,(b-a)^{1.5}}{v} \quad \textbf{(Eq. 6-11)}$$

If the Taylor Number Ta is higher than the critical Taylor Number $Ta_{m,cr} = 41.19$ value, then the Taylor vortices are formed with the radial of the machine. Where if it is less than the critical Taylor Number, the flow will remains as a Couette flow. The Taylor number and Taylor vortices have been discussed in detail in Section 2.4.1. To determine the type of flow regime, the geometrical factor F_g is calculated as:

$$F_g = \frac{\pi^2}{41.19\sqrt{S}} \cdot \left(1 - \frac{(b-a)}{2r_m}\right)^{-1} \quad \textbf{(Eq. 6-12)}$$

where S is calculated by:

$$S = 0.0571\left(1 - 0.652\frac{\left((b-a)/r_m\right)}{1-\left((b-a)/2r_m\right)}\right) + 0.00056\left(1 - 0.652\frac{\left((b-a)/r_m\right)}{1-\left((b-a)/2r_m\right)}\right)^{-1} \quad \textbf{(Eq. 6-13)}$$

The type of flow regime can be determined by the value of Ta^2/F_g^2 and compared with the correlations from Becker and Kaye (1962) and (1962). It is summarised in Table 6-1.

Table 6-1: Type of flow regime and its suitable Nusselt number formulation by Becker and Kaye (1962) and (1962).

Flow Regime	$\boldsymbol{Ta^2/F_g^2}$	**Nusselt Number Correlation**
Laminar flow	$1700 < {Ta^2}/{F_g^2} < 10^4$	$Nu = 0.128\left({Ta^2}/{F_g^2}\right)^{0.367}$
Turbulent flow	$10^4 < {Ta^2}/{F_g^2} < 10^7$	$Nu = 0.409\left({Ta^2}/{F_g^2}\right)^{0.241}$

Once the Nusselt Number has been calculated, the convective heat transfer coefficient h_c can be calculated by:

$$h_c = \frac{Nu \cdot k}{D_h} \quad \textbf{(Eq. 6-14)}$$

Axial convective heat transfer

The calculation of axial convective heat transfer is much simpler when the Local Reynolds number Re_θ is calculated first:

$$Re_\theta = \frac{\Omega \cdot R^2}{v} \quad \textbf{(Eq. 6-15)}$$

Then, the gap ratio G between the rotating component and the stationary component is worked out by:

$$G = g/R_r \quad \textbf{(Eq. 6-16)}$$

With these two equations, the type of flow regime can be determined by comparing the gap ratio G with the rotor heat transfer correlations from Boutarfa and Harmand (2005), as tabulated in Table 6-2.

Table 6-2: Rotor heat transfer correlations (Boutarfa & Harmand, 2005)

G	Flow Regime	Nusselt Number Correlation
0.01	Laminar flow	$Nu = 7.46Re_\theta^{0.32}$
0.02 - 0.06	Laminar flow	$Nu = 0.5\,(1 + 5.47 \times 10^{-4} e^{112G}) \cdot Re_\theta^{0.5}$
0.01	Turbulent flow	$Nu = 0.044Re_\theta^{0.75}$
0.02 - 0.06	Turbulent flow	$Nu = 0.033\,(12.57e^{-33.18G}) \cdot Re_\theta^{0.6+25G^{12/7}}$

6.1.3 Windage losses for disc-type machines

The windage losses in electrical machines are the mechanical losses due to the shear and pressure of a rotating component. The shear torque is a result of a rotating component trying against the surrounding fluid viscosity thus creating air friction, while the pressure torque is due to the pumping pressure created by a rotating component.

6.1.3.1 Windage losses prediction for AFPM machines

The specific formulation to calculate windage losses for a disc type machine or AFPM machine is extracted and presented in radial and axial windage losses separately, as below:

Radial windage losses

The radial windage losses can be computed by Childs' formulation (2011). For a rotating cylinder system, the moment coefficient of cylinder Cm_C is defined in Eq. 6-17. Note that an iterative solution is required to solve this equation due to the Cm_C on both sides of the equation. In general, an initial value of $Cm_C = 0.02$ is used and repeated until the solution is converged to three decimal places.

$$Cm_C = \left(\frac{1}{-0.8572 + 1.25\ln\left(Re_\phi \sqrt{Cm_C}\right)} \right)^2 \quad \textbf{(Eq. 6-17)}$$

While the rotational Reynolds number, Re_ϕ is calculated by:

$$Re_\phi = \frac{\rho \Omega r^2}{\mu} \quad \textbf{(Eq. 6-18)}$$

Then, the axial windage losses are calculated by Eq. 6-2 where the torque T_q is:

$$T_q = \frac{1}{2}\pi\rho\Omega^2 r^4 t_R \cdot Cm_C \quad \textbf{(Eq. 6-19)}$$

Axial windage losses

The axial windage losses can be computed by Childs' formulation (2011). For a rotating disc system, the moment coefficient of the rotor Cm_R is defined by the gap ratio G and the local rotational Reynolds number $Re_{\theta,}$ as below:

$$Cm_R = 0.040 G^{-0.167} Re_\theta^{-0.25} \quad \textbf{(Eq. 6-20)}$$

Then, the axial windage losses are calculated by (Eq. 6-2) where the torque T_q is:

$$T_q = 0.5\rho\Omega^2 R^5 Cm_R \quad \textbf{(Eq. 6-21)}$$

6.1.4 Comparison of analytical calculations and CFD

A comparative study was conducted to evaluate the results of the analytical and the CFD on the convective heat transfer and the windage losses. A simple disc was created based on the conceptual design illustrated in Figure 6-1. For simplicity, the tested geometry in this comparative study did not include the magnet and rotor-cover air gap and the design specification and properties are tabulated in Table 6-3 and Table 6-4.

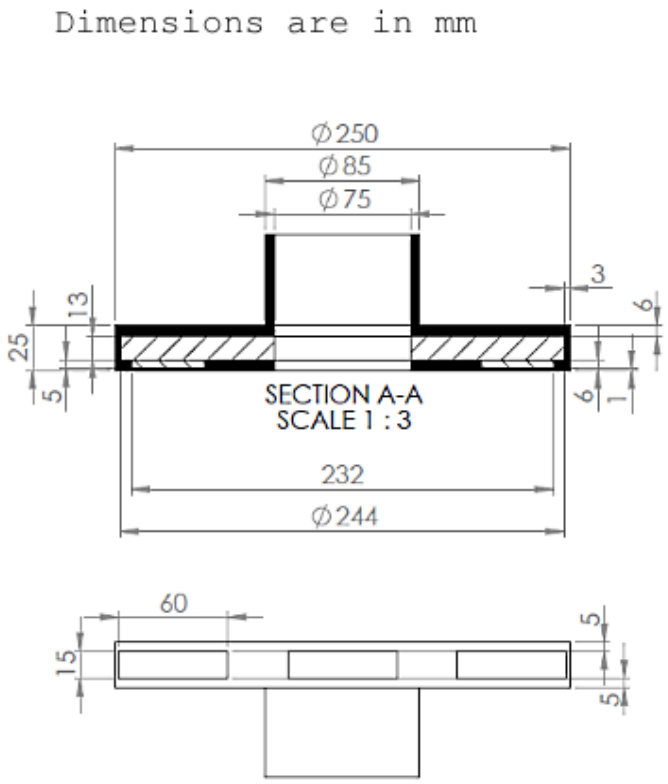

Figure 6-1: Conceptual design of the rotor cooling system.

Table 6-3: Design specifications.

Specifications	Unit	Value
Rotor diameter	mm	244
Rotational speed	rpm	4000
Radial air gap	mm	3
Axial air gap	mm	1
Rotor thickness	mm	13
Rotor temperature	°C	90
Stator temperature	°C	60

Table 6-4: Properties of air.

Properties	Unit	Value
Density	kg/m^3	1.067
Kinematic viscosity	m^2/s	2.00×10^{-5}
Specific heat	J/kg.K	997.85
Thermal conductivity	W/m.K	0.0285
Absolute viscosity	kg/m.s	2.00×10^{-5}

The analytical calculation of heat convection is calculated by Eq. 6-9 to Eq. 6-16 for the radial and axial convective heat transfer. The windage losses are calculated by Eq. 6-2 based on the torque values of Eq. 6-18 and Eq. 6-21. On the other hand, the CFD heat convection is calculated by the simulations' Nusselt number while the windage losses are computed by STAR-CCM+ (2016) as below:

$$T_{q\_CFD} = \sum_f \left[\boldsymbol{r}_f \times \left(\boldsymbol{f}_f^{pressure} + \boldsymbol{f}_f^{shear}\right)\right] \cdot \boldsymbol{a} \qquad \textbf{(Eq. 6-22)}$$

where $\boldsymbol{r}_f$ is the position of face f relative to the axis point of $\boldsymbol{x}_0$, $\boldsymbol{a}$ is the vector reflect to the axis point $\boldsymbol{x}_0$ for the moment calculation, $\boldsymbol{f}_f^{shear}$ and $\boldsymbol{f}_f^{pressure}$ are the shear and pressure force vectors. Again, the windage losses are mechanical losses due to the shear and pressure of a rotating component, where the shear force is a resistance of the rotation face against the surrounding fluid viscosity, while the pressure force is due to the pressure development by a rotating component. Therefore, the face f means the cell edges that form a conformal mesh face between the rotating components and the fluid.

The shear force vector is computed by:

$$\boldsymbol{f}_f^{shear} = -\boldsymbol{T}_f \cdot \boldsymbol{a}_f \qquad \textbf{(Eq. 6-23)}$$

where $\boldsymbol{T}_f$ is the stress tensor of face f and $\boldsymbol{a}_f$ is the face area vector.

And the pressure force vector is computed by:

$$\boldsymbol{f}_f^{pressure} = (p_f - p_{ref})\boldsymbol{a}_f \qquad \textbf{(Eq. 6-24)}$$

where p_f is the static pressure of face f and p_{ref} is the reference pressure.

Two different CFD models have been built for the purpose of comparing the analytical results with the CFD results, which are the following:

A. Radial CFD model
B. Axial CFD model

The models of convective heat transfer were built with a 1/8 or 45° section CFD model as shown in Figure 6-2 to reduce the computational requirements. This approach of simulating a symmetrical section of the full geometry has been verified and tested in Chapter 5, where only a minimal difference in the results was observed, while the computational time can be significantly reduced.

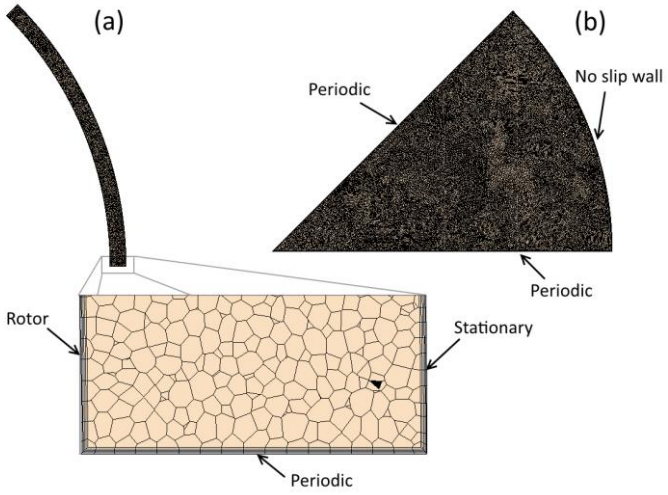

Figure 6-2: Examples of polyhedral mesh for (a) radial and (b) axial CFD models with wall boundary conditions.

The automated mesh generation of polyhedral volume mesh is used with low y^+ approach and the mesh setup is presented in Table 6-5. Figure 6-2 shows the example of the resulted mesh with some of the wall boundary conditions.

Table 6-5: Mesh setup for the comparative study

Base Size (mm)	Minimum	Prism Layer		
		No. Of Layers	Stretching	Thickness (mm)
0.5	10%	5	1.15	0.2

The k-ω SST turbulence model is chosen and the Moving Reference Frame (MRF) is included into the fluid domain to mimic the rotational motion without having to rotate the rotor surface explicitly. The energy equation is included to be computed and the temperature assumption in the design specifications (Table 6-3) is input into the respective walls. The CFD model was recreated again to have a complete circular form in order to compute the windage losses, yet the energy equation is turned off to save computational time.

The results of this comparative study for the convective heat transfer are presented in Figure 6-3 as well as the windage losses results in Figure 6-4. In general, the CFD results predicted the parameters well, close to the analytical calculation derived from the experimental correlations. The convective heat transfer has maximum 5% and 10% of error for radial and axial respectively at 2000rpm. While, the windage losses has maximum 20% and 9% of error for radial and axial respectively at 4000rpm. Although the maximum error of radial for the windage losses is 20%, it is reduced to 13% of error when viewed globally, which combines the radial and axial values.

These data sets are then combined and the Cooling Performance Index (CPI) is calculated and compared in Table 6-6. This comparative study shows that both methods of prediction are matched and can be used in the initial stages of design derivation. The analytical method has an advantage of fast calculation time, which is useful to understand the cooling performance of selected design specifications. Then later, the complex machine design can be evaluated by the CFD.

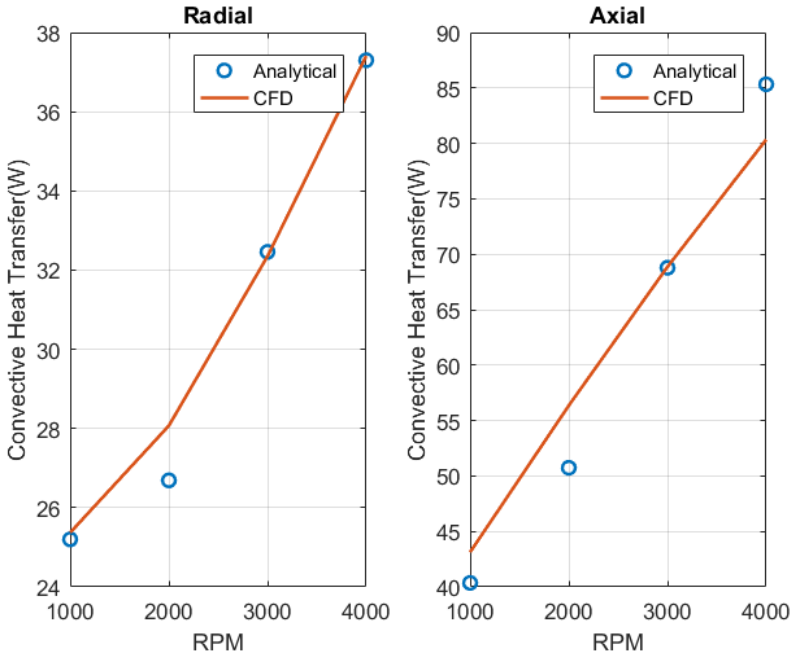

Figure 6-3: Radial and axial convective heat transfer of the analytical and the CFD.

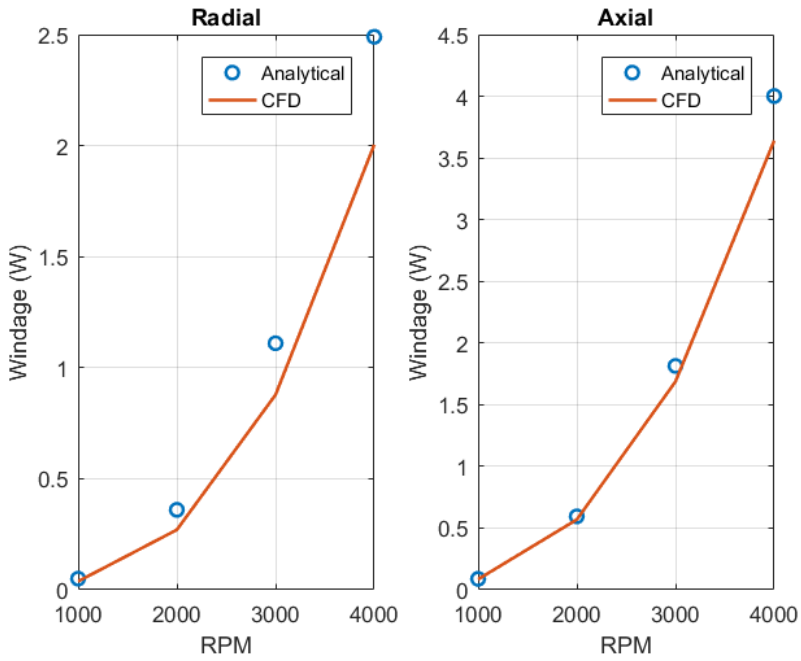

Figure 6-4: Radial and axial windage losses of the analytical and the CFD.

Table 6-6: Cooling Performance Index (CPI) of the analytical and the CFD.

rpm	Analytical			CFD			ΔCPI
	Convective HT, q (W)	Windage, W (W)	CPI, (W/W)	Convective HT, q (W)	Windage, W (W)	CPI, (W/W)	
1000	65.56	0.130	504.44	68.50	0.122	560.08	55.63
2000	77.43	0.829	93.32	84.43	0.839	100.58	7.26
3000	101.24	2.462	41.13	101.22	2.567	39.43	-1.69
4000	122.64	5.330	23.01	117.75	5.644	20.86	-2.14

6.2 Fan engineering

In general, a fan can be classified into two categories: the axial fan and the centrifugal fan. These categories are defined by the way the air passes through the fan impeller. The axial fan propels the air normal to its direction (axially) with a trace of swirl flow, once the air passes the rotating fan blades.

This type of fan is good for producing velocity and kinetic energy yet is limited in the generation of pressure and potential energy. In its counterparts, the air enters the centrifugal fan axially and changes direction as the air is pushed radially. The centrifugal fan produces good velocity and pressure development due to its centrifugal force.

From these two categories, the centrifugal fan is more suitable for the rotor cooling technique because:

- The AFPM machine's steel rotor comes in a solid disc form and cannot be replaced with impellers, instead an impeller's features can be added onto the rotor.
- The existing machines have a prominent primary stator cooling between the rotor's cavity so there is no need to have a cross-flow across the stator for cooling purposes.
- Centrifugal fans have an advantage of pressure development that is vital for electric vehicle (EV) or hybridisation applications. Having positive pressure will ensure that further added components such as inlet/outlet cooling ducting, air filters, etc. do not suffocate the machine.

6.2.1 Fan selection for the rotor cooling technique

The pumping and airflow drive by the fan is done by two important components: the impeller, as an active flow promoter and the casing, as a passive flow promoter. In this chapter, focus is given to assessing the suitable active flow promoter component that induces the airflow. The passive flow promoter is discussed in the next chapter (Chapter 7.0).

Centrifugal fans are available in various types and it is classified according to the fan blade configuration. These are forward curve, backward curve and radial blade. Each of these fan blade configurations produces different flow characteristics due to the way the blade design induces the airflow. Figure 6-5 shows the unique resultant velocity vector, R, by the fluid velocity of the

fan blade tip, v_2 and the centrifugal velocity, v_1 for all the fan blade configurations. Thus, each configuration has its own intended application reflecting its advantages and disadvantages. These are summarised in Table 6-7 from the Energy Efficiency Center (n.d.), Energy, Mines and Resources, Canada (n.d.) and the US Department of Energy (US DOE 1989).

Figure 6-5: Fan blade vector diagram (Twin City Fan Companies Ltd. 2000).

Table 6-7: Advantages and disadvantages of each fan type Energy Efficiency Center (n.d.), Energy, Mines and Resources, Canada (n.d.) and the US Department of Energy (US DOE 1989).

Fan type	Advantages	Disadvantages
Forward curve	• Produces high air volume per size ratio. • Lightweight and relatively small sized. • Low noise level. • Economical. • Not sensitive to clearance between the impeller and the opening inlet. • Suitable for small air handling equipment such as heating, ventilation, and air conditioning (HVAC).	• Easy to collect deposits due to its 'bucket' shaped impeller. • Only for handling clean air. • The power curve is increased steadily with the airflow. • Low energy efficiency (55-65%)

Backward curve	• Produces smoother constant air flow. • Backward curved fan can operate at the full range of speed, while the backward inclined fan has unstable flow conditions at lower speeds. • High energy efficiency (80-85%). • Suitable for forced draft applications.	• High noise level. • Not suitable for dirty air streams, the blades may be subject to erosion. • The aerofoil blade may create stall at certain speeds.
Radial	• Suitable for high static pressure and high temperature handling. • Simplest design. • Able to handle 'dirty' air streams. • High durability and easy to repair. • Optimised blade design can achieve up to 75% efficiency.	• Lower fan efficiency (60%) for un-optimised designs. • Only suitable for low to medium airflow rates.

6.2.2 Fan adaptation for the YASA machine

Similar to the initial concept of rotor cooling for the AFPM machine proposed by Vansompel (2010), the implementation of rotor cooling for the YASA machine was accomplished by attaching fan features to the machine's rotor and creating an inlet opening at the centre of the machine and a single radial opening outlet. This alters the current YASA machine topology with a single side rotor cooling, as shown in previous Figure 4-2.

Several fan designs were selected and tested by CFD to analyse their suitability for rotor cooling applications. The analysis will be viewed by the flow performance in order to ensure that there is sufficient mass flow rate and pressure development, fan power requirements as windage losses, thermal performance including the average heat transfer and finally, the Cooling Performance Index (CPI). Three fan designs from other engineering

applications were chosen and adapted for this objective. Figure 6-6 presents the selection of the fan blade design as:

- Backward curve
    - Taken from a force-draft blower application (Bloch and Soares 1998).
    - Known for its high energy efficiency design.
- Radial blade
    - Taken from typical fan engineering applications (Bloch and Soares 1998).
    - Known for its robust flow generator.
- Pillar blade
    - Taken from automotive disc brakes (Wallis et al. 2002).
    - Its applications mostly focus on heat dissipation.

Figure 6-6: The fan selection for the rotor cooling technique of (a) the backward-inclined aerofoil blade, (b) the radial aerofoil blade and (c) the tear drop pillar blade (Fawzal et al. 2017).

All three selected fan designs were integrated with aerofoil fan features that were not optimised. The machine cover design was also not optimised, but had a slight volute feature to increase the pressure development. Here, the focus was only given to a uni-directional design because the automotive application only requires limited counter-rotation (e.g. reverse) and only occurs at a slow speed. In rotating machinery, the term ‘uni-directional’ means that a machine has been designed to rotate at a single specific rotational direction. On the other hand, if the machine can rotate in both

directions, it is then called ‘bi-directional’. Additionally, all the tested fan blades are designed as enclosed impellers to avoid air spillage.

The geometrical setup for CFD simulations is carried forward from the verification and validation assessment in Section 4.1.1 and the geometrical setup shown in Figure 4-3. The geometrical setup also includes the inlet and outlet duct similar to the experimental test. The finer mesh level is used for the mesh generation setup and the boundary conditions are followed based on the verification and validation assessment.

6.3 Radial fan blade selection

The selection of 9, 13 and 17 numbered radial fan blades has been implemented.

There is no guideline in choosing the number of blades and in here, the selection was based on:

- Fan blade pass frequency (BPF) that the number of blade will produce. (Fu-An et al. 2011) (Jin 2017) (Parag Fan and Cooling System Ltd. n.d.).
    - Fewer blades usually have high amplitude with lower frequency which can be noisy.
    - Flow-induced vibration: The BPF may induce other component vibration such as machine cover/casing (Cai et al. 2012).
- Simplicity and complexity of design and manufacturing.

Moreover, it is observed that the selection of number of blades for a centrifugal fan or pump is varied and usually an odd number is dominant to be selected. For an example:

- Zhang and Jin 2011 tested six different fan blades of 5, 7, 9, 11, 13 and 15 blades.
- Gölcü et al. 2006 conducted an experiment on 5, 6 and 7 blades.
- Liu 2010 studied on 4, 5, 6, 7 blades.

Liu 2010 has also mentioned that the research on blade number is low and the influence has not beed understood completely.

The radial blade design on this study has a primary and secondary blade with an equal number as illustrated in Figure 6-7. The primary blade is dominant and used mainly to drive the air from the centre of the machine towards the radial outlet. The secondary blades (also known as splitter blades) are added to reduce the wake of the primary blade when it rotates, thus slightly lower fan power requirements or windage losses can be achieved. In the review of splitter blades by Patil and Todkar 2013, they conclude that by adding splitter blades to the fan design, it can improve fan performance by reducing clogging and reduce pressure fluctuation that lead to vibration and noise. In other perspective, the secondary blades (or splitter blades) reduce the wake region thus reduce the noise, drag and perhaps increase cooling properties due to having less flow disturbance.

The objective of this exercise is to evaluate the performance of selective number of blades for radial fan and it is expected that the higher number of fan blades will perform better in terms of flow, thermal and cooling performance.

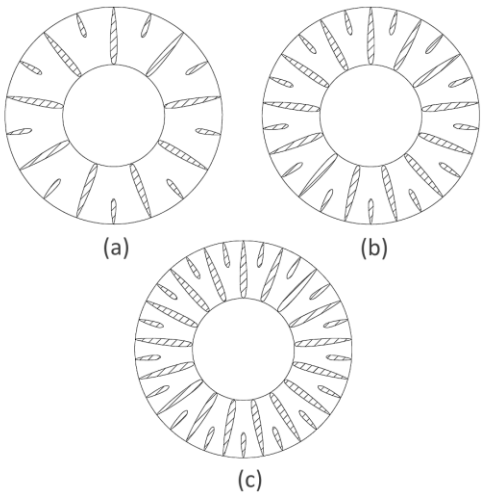

Figure 6-7: Radial fan blade selection of (a) 9 blades, (b) 13 blades and (c) 17 blades.

6.3.1 Radial fan blades results

In this assessment, the fan was rotated at 3000rpm and the static rotor and magnet temperature of 80°C is specified. The rotational speed of 3000rpm was chosen to ensure that the simulation was performed at a fully developed flow. Again, in Section 4.4, the flow has a transition between laminar flow to turbulence flow at 1970rpm and based on Gregory, Stuart and Walker (1955) correlation, fully developed flow can be achieved at 2810rpm. Also, the magnet was assumed to have a static temperature of 80°C based on the manufacturer temperature threshold that has been discussed in Chapter 5, for simplicity. Therefore, 3000rpm and 80°C are reasonable assumptions and have been used in this example. The machine's cover and the stator walls were set at 60°C as these assumptions had previously been validated in Chapter 4.0.

The flow characteristics in Figure 6-8 shows that the higher the number of fan blades, the better the performance. However, the performance may be limited to a certain number of blades where the flow performance will not be further increased due to the air gap between the blades being too small to drive the air, yet it is not included in this study. Furthermore, the average air temperature on the outlet and the rotating region shows that the 17 blades are able to remove draw out more air temperature compared to what is left inside the machine (Figure 6-9).

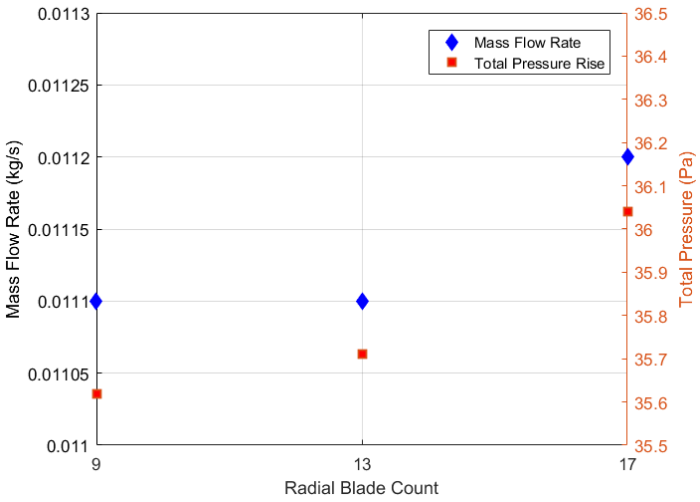

Figure 6-8: Flow characteristics of the radial fan blades assessment.

The positive performance of 17 radial blades has shown good windage losses in Figure 6-10a and a good performance in drawing out hot air. The average heat transfer coefficient of 17 radial blades marks the highest value. Figure 6-10b shows that the average heat transfer coefficient steadily increases as the blade number increases, similar to its flow performance. Finally, the cooling performance index (CPI) is computed and concludes that the 17 radial blades is the best among these tested radial blade designs in Figure 6-10c.

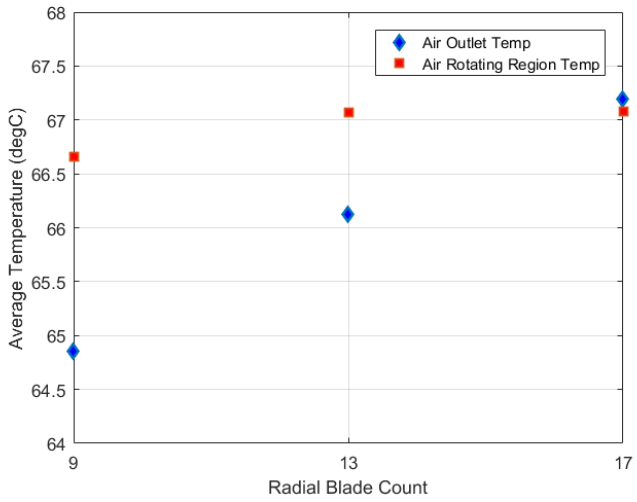

Figure 6-9: Average air temperature of the radial fan blades assessment.

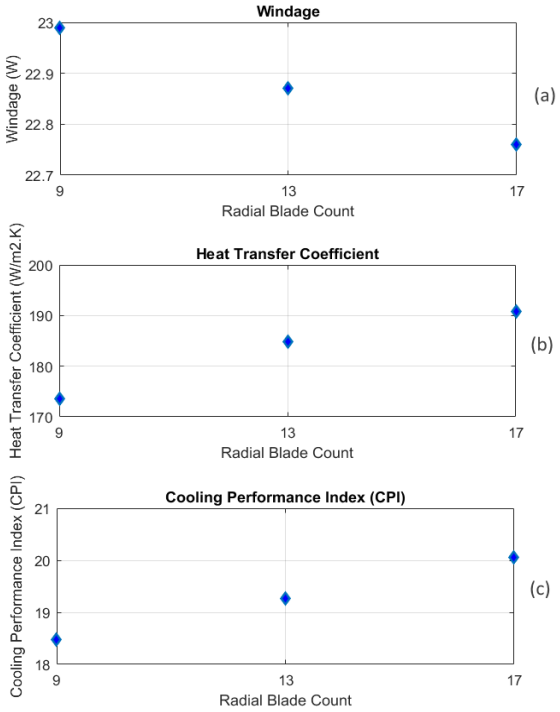

Figure 6-10: (a) the windage losses, (b) the average heat transfer coefficient and (c) the Cooling Performance Index (CPI) of the radial fan blades assessment.

6.4 Fan selection comparison

The fan selection comparison was conducted to assess their suitability for rotor cooling purposes as a secondary thermal management of AFPM machines. Three fan designs were selected and implemented into a YASA machine, as described in Section 6.2.2: namely backward curve, radial and pillar blades. The three fan blade designs are illustrated in Figure 6-6, having a varied number of blades:

- The backward curve fan has 8 primary and 8 secondary blades.
- The radial fan has 17 primary and 17 secondary blades as assessed in Section 6.3.1 and that showed good potential.
- The pillar fan has 26 radial arrays.

The test was conducted at 1000rpm to 3500rpm for every 500rpm increment. This uni-directional rotational speed range was chosen as suitable for the

intended automotive application. Additionally, this chosen speed range is also within the critical rotating speed at which the transition flow regime may occur, based on the findings from Gregory, Stuart and Walker (1955) of $1.8 \times 10^5 < Re < 2.1 \times 10^5$ with the equivalent speed for a YASA machine of $1690rpm < n < 1970rpm$. Therefore, a speed of 1500rpm and 2000rpm may be difficult for CFD to be able to predict well. However, the verification and validation in Chapter 4.0 has shown a positive outcome.

6.4.1 Flow characteristics: fan performance curves

The flow characteristic of each fan design is plotted by the mass flow rate produced, the generation of the pressure rise and the fan power requirement for the windage losses over the speed range. Figure 6-11 plots the mass flow rate and pressure rise where the radial blade dictates across the tested rotational speed compared to the other design. It was expected that, the radial blade outperforms the other blade design due to the straight blade arrangement in radial aerofoil able to swipe the flow from the centre to the radial effectively compared to the backward curved and the pillar blade. The pillar blade has fair flow performance and the backward curved fan showed the least performance. The flow performance of pillar blade comes second because the arrangement of each pillar is in straight sequence of which identical to the radial blade. However, it has less flow performance compared to the radial blade, as there is an air void between each pillar. Meanwhile, the backward curved fan gives the least performance due its blade design that has smooth flow transition from the inlet (centre) towards the radial.

On the other hand, it can be observed that the windage losses of the pillar blade required the most fan power and the least was backward curve, while the radial blade was placed in between the two designs (Figure 6-12). The reason is that the pillar blade has a multiple solid-air void that creates patches of wake region as the rotor and fan spins. Similarly, the radial blade has also a wake region due to the sharp angle of the blade. This wake or recirculation region causes drag to the fan thus its windage losses are high.

The backward curve however, has the least windage losses because the blade leading edge is tangential to the rotational motion and its profile is following the centrifugal flow direction.

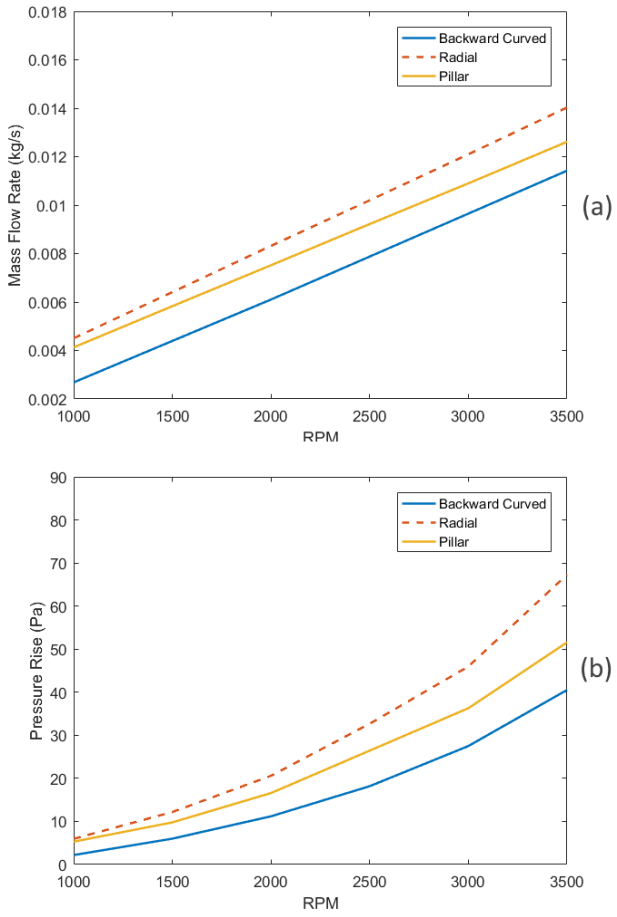

Figure 6-11: CFD fan characteristics of a) the mass flow rate and b) the pressure development of each fan design.

The fan performance curves can be generated by correlating the pressure rise of Figure 6-11b and the windage losses of Figure 6-12 with the mass flow rate data. Thus, the fan curve of each tested fan blade design is presented in Figure 6-13. The backward curve blade (Figure 6-13a) shows a fair amount of pressure development with reasonable windage losses across the production of the mass flow rate. The fan curve of the radial blade (Figure 6-13b) has higher pressure development in proportion to the increase of its windage losses, with a slightly higher mass flow rate production. However,

the pillar blade (Figure 6-13c) has a fair amount of pressure development yet the windage losses increase sharply over the mass flow rate.

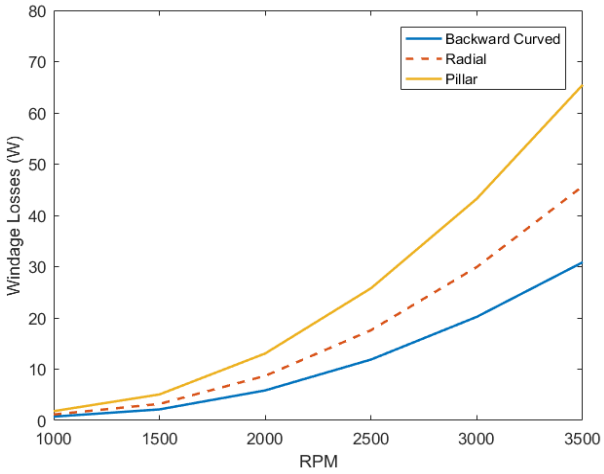

Figure 6-12: CFD windage losses of each fan design.

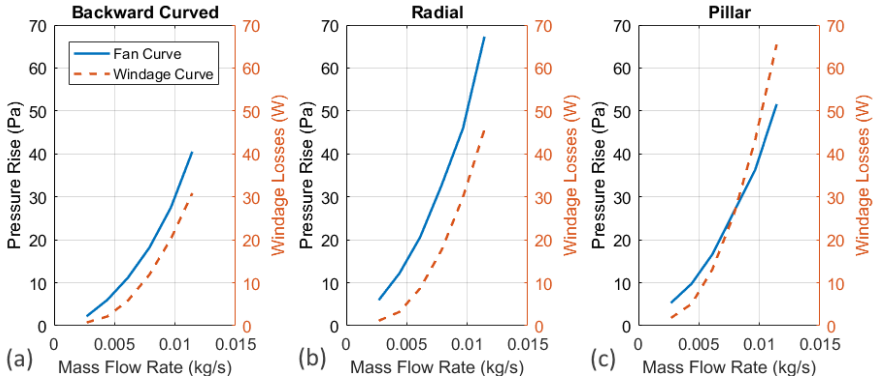

Figure 6-13: CFD fan curve with its windage losses of (a) the backward-inclined aerofoil blade, (b) the radial aerofoil blade and (c) the tear drop pillar blade.

6.4.2 Thermal characteristic

A static temperature of 80°C was set on the magnets and the rotor (including the fan blade features) in order to access the thermal characteristics. One of the unique features of this proposed rotor cooling method is that the fan not only works as flow driven, but also act as a heat exchanger at the same time.

The fan blade design is sliced with a section plane at Z+3mm above the heated rotor surface. The temperature of the air is plotted to analyse the temperature contour for each blade design. Figure 6-14a of the backward curve blade shows obvious hot air patches at 80°C near the blade's wake region. The flow circulation due to the blade's wake scoops the temperature efficiently and this hot air is flown to the radial space of the machine. This reveals the reason for the backward curve blade managing to produce the highest average air outlet temperature in Figure 6-15 and the average air temperature within the rotating region in Figure 6-16.

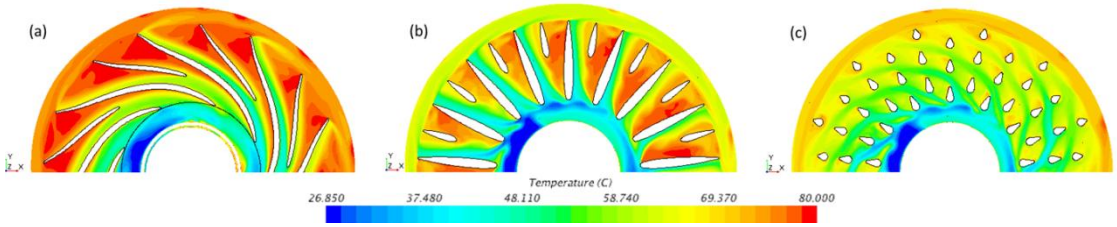

Figure 6-14: Contour plot of the air temperature at z +3mm from the heated rotor surface for 3500rpm of a) the backward curve blade, (b) the radial blade and (c) the pillar blade.

Equally, multiple hot air patches can be observed in the contour plot of the radial blade with slightly less efficiency (Figure 6-14b). However, the hot air remains in its location instead of being flown towards the radial space of the machine. As a result, the average air outlet temperature of the radial blade (Figure 6-15) is lower than its average air temperature within the rotating region in Figure 6-16. The radial blade design has also reached its steady state in driving the hot air to the outlet at 1500rpm.

On the other hand, it is interesting to see that there is no evidence of hot spots in the contour plot of the pillar blade (Figure 6-14c) although the design is intended mainly for the heat dissipation of automotive disc brake cooling. Nevertheless, this blade design manages to collect a higher air temperature at the radial space of the machine, thus its average air temperature in Figure 6-15 shows a fair amount of temperature rejected, while having the coolest average air temperature within the rotating region (Figure 6-16).

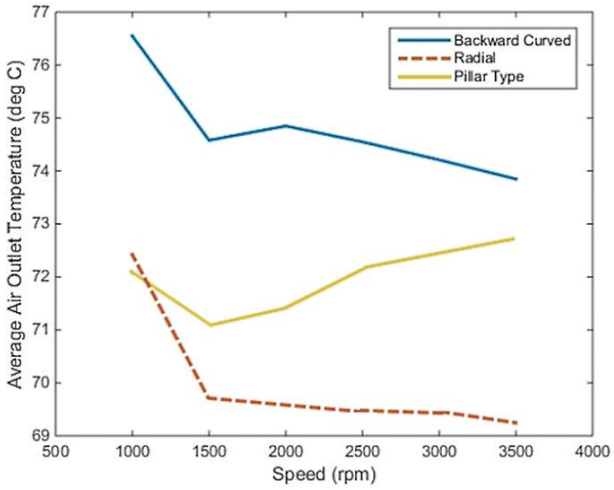

Figure 6-15: Average air outlet temperature of each fan design.

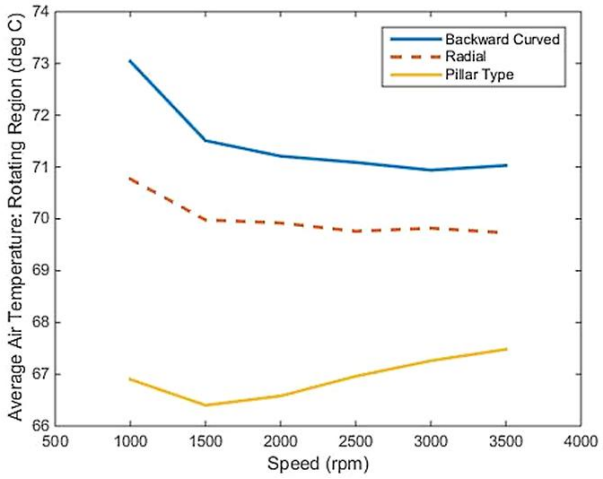

Figure 6-16: Average air temperature within the rotating region of each fan design.

The thermal characteristics of each fan blade design can be further analysed by the average heat transfer coefficient. The average heat transfer coefficient is calculated by referring to Eq 3-14 with the input data that has been collected so far as:

$$h_c = \frac{q"}{\Delta T} = \frac{\dot{m}\, C_p\, (T_{outlet} - T_{inlet})}{A_h\, (T_{rotor} - T_{system})} \qquad \textbf{(Eq. 6-25)}$$

where h_c is the average heat transfer coefficient, $q"$ is the surface heat flux, ΔT is the temperature difference, $\dot{m}$ is the mass flow rate generated by the

fan, C_p is the specific heat capacity of the air, A_h is the heated area of the rotor including the fan, T_{outlet} is the outlet temperature, T_{inlet} is the inlet temperature, T_{rotor} is the rotor temperature and T_{system} is the system temperature or air interior temperature.

Figure 6-17 shows the calculated average heat transfer coefficient, where the radial blade has the highest value and is closely matched by the backward curved blade. This matched performance between these two blade designs is because the radial blade has a better mass flow production, while the backward curved blade is able to dissipate more heat. Moreover, the pillar blade marked the lowest quality of the average heat transfer coefficient due to its average production of mass flow rate and its least average air temperature within the rotating region.

Optionally, the curve of this average heat transfer coefficient over the speed range can be expressed in regression form, as tabulated in Table 6-8 for LP thermal model usage.

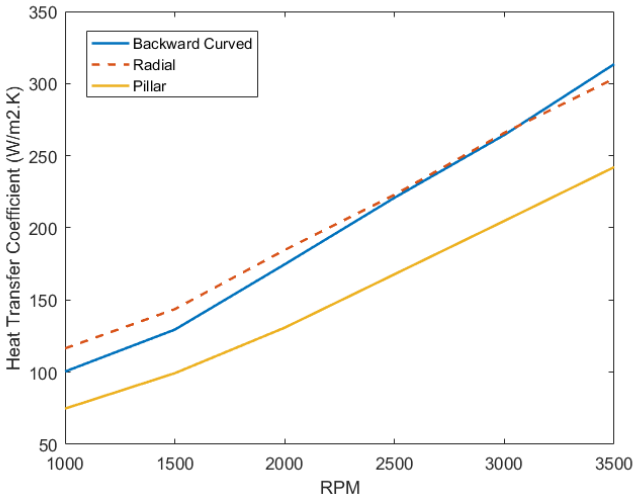

Figure 6-17: Average heat transfer coefficient by input fixed temperature.

Table 6-8: Regression of the average heat transfer coefficient.

Fan Blade Design	Regression
Backward-Inclined	$y = 7.83 \times 10^{-12}x^4 - 7.52 \times 10^{-8}x^3 + 2.63 \times 10^{-4}x^2 - 3.06 \times 10^{-1}x + 210.69$
Radial	$y = 2.14 \times 10^{-12}x^4 - 2.47 \times 10^{-8}x^3 + 1.02 \times 10^{-4}x^2 - 9.92 \times 10^{-2}x + 135.84$
Pillar Type	$y = 6.00 \times 10^{-13} - 9.13 \times 10^{-9}x^3 + 4.84 \times 10^{-5}x^2 - 3.40 \times 10^{-2}x + 68.86$

6.4.3 Rotor cooling performance index implementation

Finally, the cooling performance index (CPI) in Section 6.1.1 can be calculated to assist the selection of suitable design changes, particularly involving comparative design analysis. Figure 6-18 is plotted from Eq. 6-1 and shows that all the fan blade designs have a higher cooling performance at lower speeds and their performance declines as the rotational speed increases. This is due to the increase of windage losses exponentially to the speed, while the capability of air to dissipate the heat from the heated surface is stabilised.

Additionally, the result also shows that in this rotor cooling application, the backward curved has the best cooling performance at all ranges of tested speeds, followed closely by the radial speed with the pillar blade as the bottom performer.

Here, the CPI value helps in determining the best fan blade design for rotor cooling technique of YASA machine. One can see that although some of the fan designs have better flow performance (mass flow rate and pressure development), it does not mean that it is the best option for cooling purposes. This is because, in order to determine the best design for cooling, the factor of power consumption or requirement to drive or supply the coolant together

with its heat transfer capability need to be included. Therefore, the CPI shows the true picture of cooling design changes.

The CPI can be used in any cooling system design when the designer wants to assess the convective heat transfer over its power requirement to drive the coolant. As it has been derived earlier (in Section 6.1.1), the CPI can be used in the cooling assessment of the rotating flow (i.e. electrical machine, turbine, automotive disc brake), heat exchanger, and also other cooling system (i.e. electronic cooling, water jacket cooling, HVAC (heating, ventilation, and air conditioning), refrigeration, etc). However, the CPI may have limitations where the value differences between the designs can be insignificant if the design changes does not affected the power consumption. This needs to be greatly studied in order to fully understand its limitations.

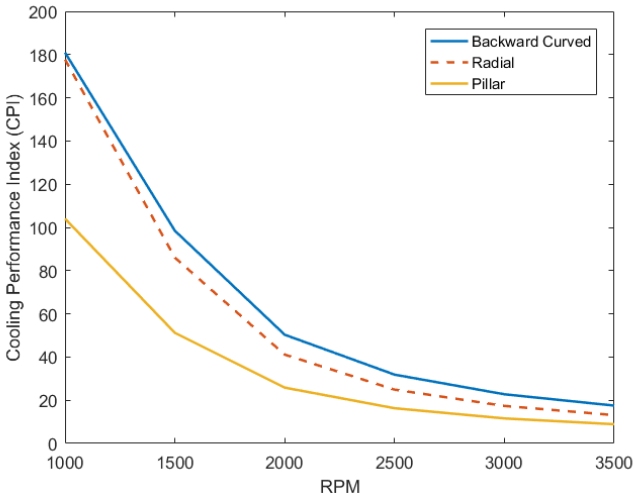

Figure 6-18: Cooling Performance Index (CPI) curves by input fixed temperature.

6.5 Chapter summary

The active flow promoter of an impeller from a centrifugal fan design was tested in this chapter. Multiple fan blade designs were evaluated by examining the flow characteristics, the thermal characteristics and the cooling performances. It can be summarised that:

1 A higher number of fan blades will produce a better flow and cooling performance, particularly for the radial blade design.
2 The backward curved design has the best cooling performance and is suitable for rotor cooling applications.
3 The radial blade has also shown good cooling performance with better mass flow and pressure development. However, the windage losses are higher than the backward curved fan.
4 The pillar blade surprisingly did not meet its expectation to dissipate heat as its intended application is automotive disc brake cooling. Therefore, this design is not suitable for rotor cooling applications.
5 A higher CPI number means a better cooling capability.

Additionally, this chapter also proposed a new cooling performance index (CPI) that evaluates the cooling capability over its power requirement. Both analytical and CFD provide similar predictions for convective heat transfer and windage losses. At a lower rotational speed, the CPI value between the analytical and the CFD have significant differences, yet the gap is narrow as the speed increases. Nevertheless, both approaches show a similar CPI trend.

Finally, the application of the proposed dimensionless number of the cooling performance index (CPI) may help machine designers to choose the best cooling design, as tested in this chapter.

Chapter 7

Inlet and Outlet Arrangement for the Rotor Cooling Technique

7.0 Inlet and outlet arrangement for the rotor cooling technique

The final step in this study is to explore the best arrangement for the inlet and the outlet ducting in order to cool both sides of the rotors, thus creating dual rotor cooling. Previously in Chapter 4.0, the temperature measurement of the machine with a single rotor cooling application showed that the vented and the non-vented rotor recorded a high temperature difference at 4000rpm. This difference in temperature may cause thermal distortion during a high and long continuous power application. Therefore, one of the possibilities to match the temperature difference is to allow forced air convection on the both sides of the rotors. Additionally, the design changes and modifications of the machine need to comply with compact packaging (to minimise the axial length) as a key priority, including the design's flow behaviour, windage losses and thermal characteristics. Part of these studies has been presented in Fawzal et al. (2018).

7.1 Inlet and outlet design exploration

The design exploration of the inlet and outlet arrangement begins with a simplification of the geometry taken from Chapter 6.0. In Chapter 6.0, the rotor cooling technique was implemented onto the machine by adopting the conventional centrifugal fan/blower/pump design that is proven to serve this purpose. However, this inlet/outlet arrangement acquires a large axial space that will result in a bulky machine if it is implemented on the both sides of the rotors.

7.1.1 Design

A step back to the inlet/outlet design was taken by creating multiple arrangements that may possibly be adapted to the machine, discarding its known negative effect on the centrifugal motion of the spinning rotor. Three designs have been proposed and tested, as illustrated in Figure 7-1. The three designs are:

1. Design 1 (Figure 7-1a) is a simple approach where the inlet and the outlet is introduced to the rotor cavity at the top and bottom respectively, just to establish a starting point.
2. Considering the force from the rotating motion of the rotor, Design 2 introduces the inlet and the outlet tangentially to the circular cavity design (Figure 7-1b).
3. Both Design 1 and the Design 2 are clearly not an ideal design, thus, the conventional centrifugal fan design is included in Design 3, where the incoming air is introduced from the centre of the rotor cavity and exits at one tangential outlet.

All three inlet/outlet arrangement designs can be combined into a modular design because they share the same rotor cavity geometry. This will not only save time during the geometry creation but also reduce the pre-processing time as this minimises the back and forth process of the geometrical conversion from CAD to CFD software. Having a modular geometry, the corresponding inlet/outlet arrangement design can be simply selected within

the CFD software to form the desirable design for a specific simulation. Once selected, the individual proposed designs of Design 1, Design 2 and Design 3 are represented in Figure 7-1 where it can be seen together with the excluded ducting in a grey colour. Also, the direction of inflow is shown by the blue arrow, while the red arrow indicates the outflow direction.

An eight circular array of a magnet is included on the rotor as a surface mounted magnet and the radial and axial air gap between magnet-to-stator, rotor-to-cover, etc. are similar to the actual machine design for a near-realistic approximation. The dimension of the modular geometry is detailed in Figure 7-2, where the solid machine cover is excluded and not modelled in the simulations.

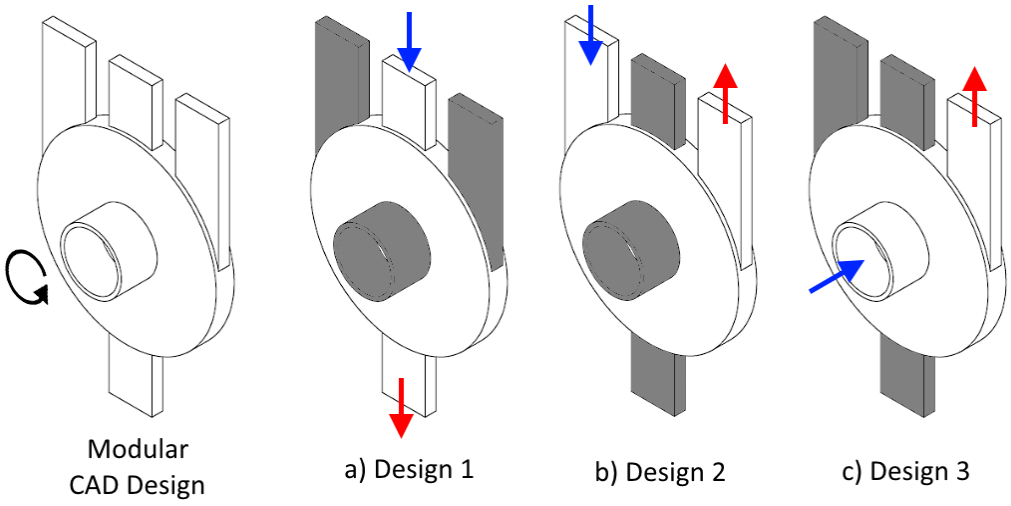

Figure 7-1: The modular CFD models of (a) Design 1 – inlet on top to outlet at the bottom, (b) Design 2 – tangential inlet-outlet and (c) Design 3 – conventional centrifugal fan arrangement.

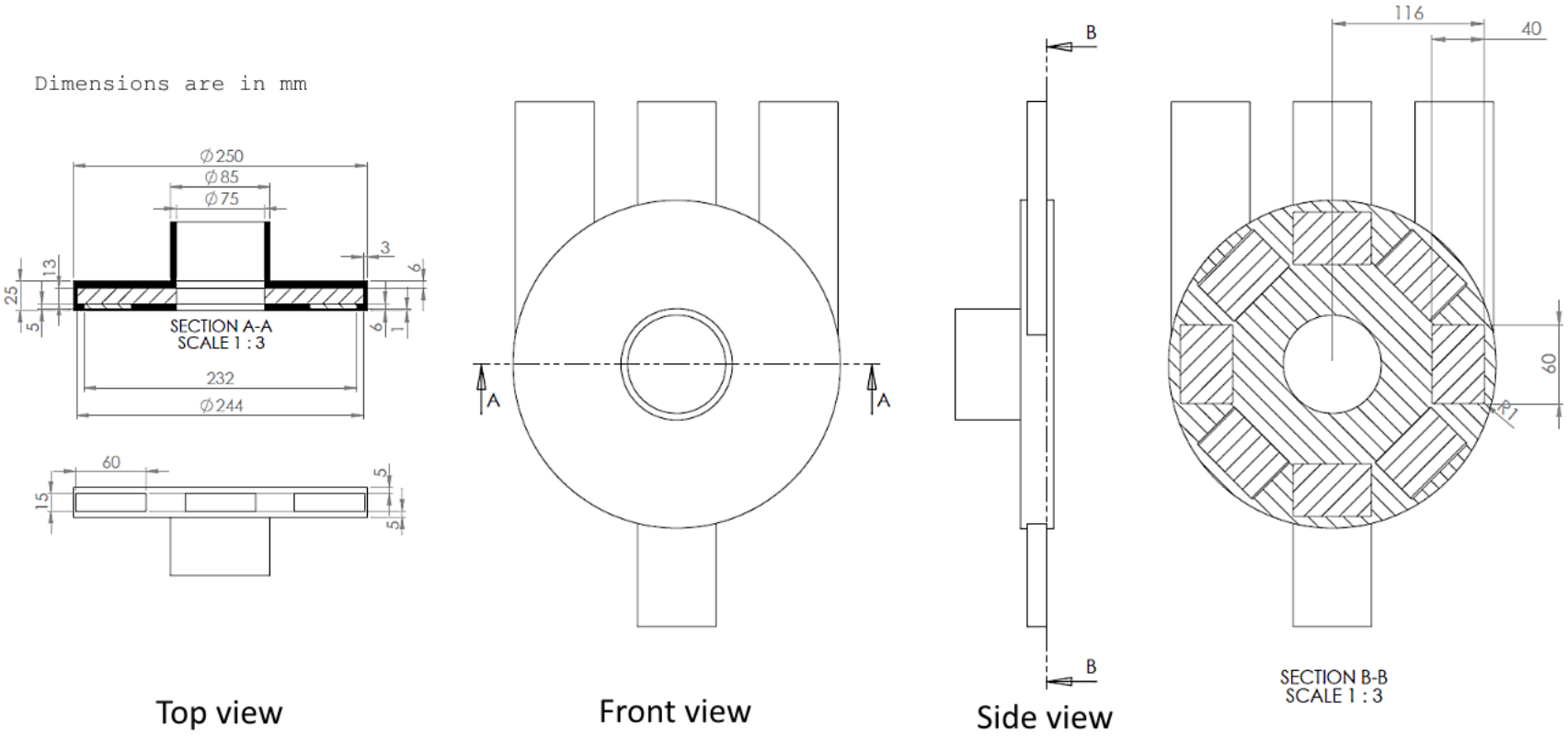

Figure 7-2: Detailed drawing of the 3-dimensional CFD model including section A-A and section B-B.

7.1.2 Setup

The selected designs were imported into the STAR-CCM+ v11.04 and all the merged surfaces were imprinted to achieve a conformal mesh between the ducting and the rotor cavity. The rotor cavity was set as the rotational region and this allows the Moving Reference Frame (MRF) to be implemented, which replicates the rotational motion of the rotor assembly.

The polyhedral cells with a prism layer were chosen to be the discretisation method from the automated mesh generation function, for a faster yet reliable mesh creation. The prism layer was input based on the calculated optimum first cell size y with the target dimensionless wall distance $y^+ \sim 1$ by Eq. 3-68, Eq. 3-69 and the specific local Reynolds number Re_θ of 5.96x10^5 is calculated by Eq. 3-24. The final mesh generation produced an average 2.3 million cell count for Design 1, Design 2 and Design 3.

The geometrical design of the rotor is assumed to be a flat disc where it is prone to divergence of iteration, especially at a low rotational speed. To eliminate this issue, the inlet was set to be as a mass flow inlet, based on the CFD data of the backward curved design presented in Fawzal, Cirstea, Gyftakis, Woolmer, Dickison, and Blundell: 'Fan performance analysis for rotor cooling of axial flux permanent magnet machines' (2017). The CFD mass flow rate data is generalised as Eq. 7-1 and was set as the inlet boundary condition of the simulation.

$$\dot{m} = 2.895 \times 10^{-6} * \left(\left(\frac{60}{2\pi}\right) \cdot \omega\right) - 1.018 \times 10^{-3} \quad \textbf{(Eq. 7-1)}$$

The heat generation from the rotor and the magnet losses were input to the volumetric solid region corresponding to the complex geometry of the machine that computed the losses via the Finite Element Analysis (FEA) of a dynamic electromagnetic. The setup of the transient FEA model has been presented in detail in Section 5.1 and for this exercise, the machine was set to 375Nm and spins from 1000rpm to 6000rpm. The developed losses from

the transient FEA model are shown in Figure 7-3. For simplicity, the air inlet and the cavity walls were set at 60ºC to simulate a harsh machine operating condition, while an adiabatic walls boundary was set at the ducting walls.

All other setups are similar and based on the lesson learned from the previous chapters, while in this exercise, the CFD simulation is performed from 1000rpm to 6000rpm for every 1000rpm.

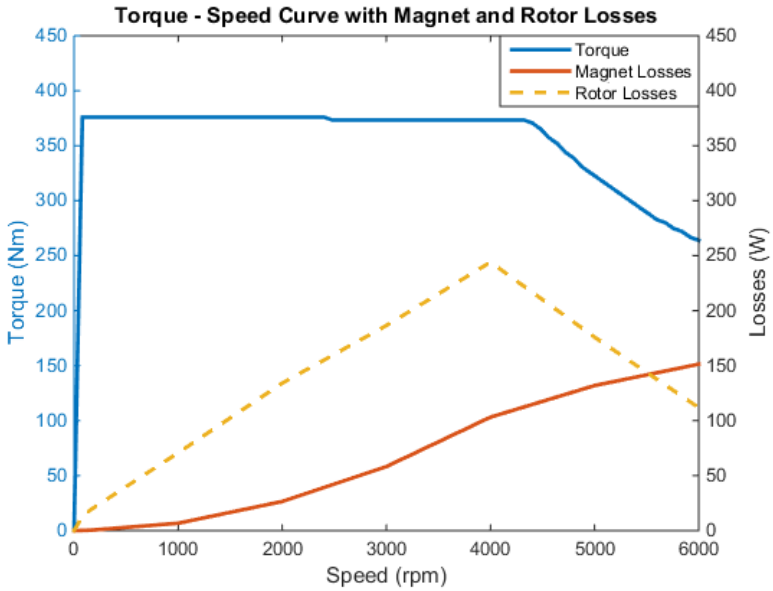

Figure 7-3: The torque, rotor losses and magnet losses of a 150kW YASA machine produced by transient FEA.

7.1.3 Flow performance and windage losses

The assessment of flow performance can only be evaluated by the pressure difference between the inlet and the outlet of each selected design, due to the mass flow rate being input to the inlet of the machine as a function of the rotational speed. In this exercise, the inlet was set under the ‘mass flow inlet’ boundary condition, where STAR-CCM+ will compute the velocity, static pressure and static temperature distributed over the inlet surface (STAR-CCM+ 2016), while the outlet was left to be equal to the ambient pressure. Therefore, higher pressure in between this port will reflect the pressure resistance created by the design. Figure 7-4 shows the results of the

pressure drop for all the designs where Design 1 has highest pressure drop followed by Design 2 and Design 3, as expected. It can be seen that Design 1 has a significant pressure drop growth rate due to the abrupt flow entry between the inlet duct and rotor cavity, thus minimising the suction capability when the inflow collides with the rotor assembly rotational flow.

Although the pressure drop shows clear differences between each inlet/outlet design, the windage losses required to spin the rotor assembly did not show much diversity. In Figure 7-5, Design 1 has the highest windage losses due to the designed inflow direction being unfavourable to the direction of the spinning rotor. Design 2 however, produced the least amount of windage as this design allows the inflow and outflow to be swept by the rotor's rotational motion.

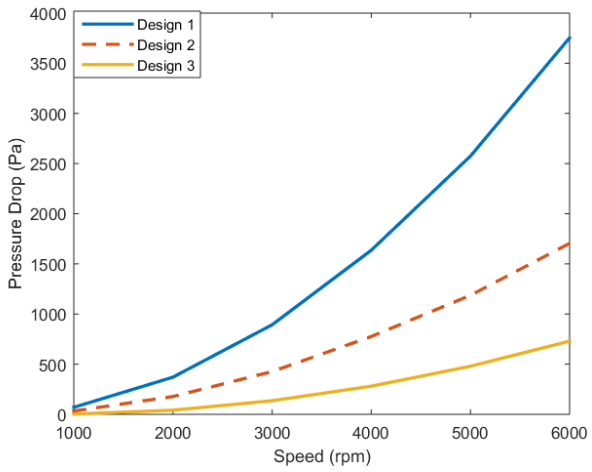

Figure 7-4: Pressure drop of the different inlet/outlet arrangement designs.

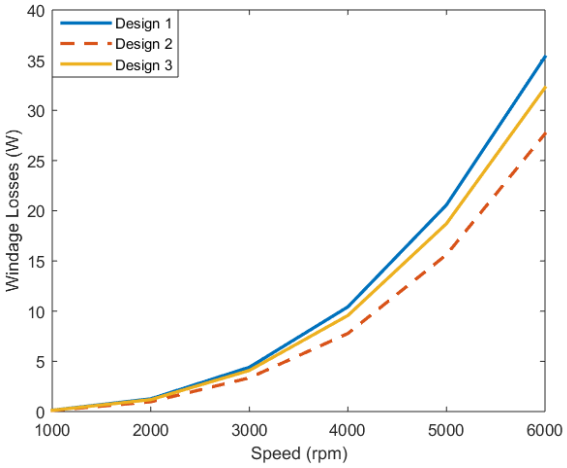

Figure 7-5: Windage losses of the different inlet/outlet arrangement designs.

7.1.4 Cooling performance

The cooling performance is assessed by examining the average air temperature at the outlet, the average air temperature within the rotational system and the average solid temperature. For better understanding, the average air temperature at the outlet and the average air temperature within the rotational system are plotted in the same graph, as shown in Figure 7-6. Surprisingly, Design 1 provides a close relationship between the air outlet and the system average temperature, while Design 2 has the most temperature difference of about 4ºC in between. On the other hand, Design 3 offers the best heat rejection, where its average outlet temperature is higher than the temperature remaining in the cavity system.

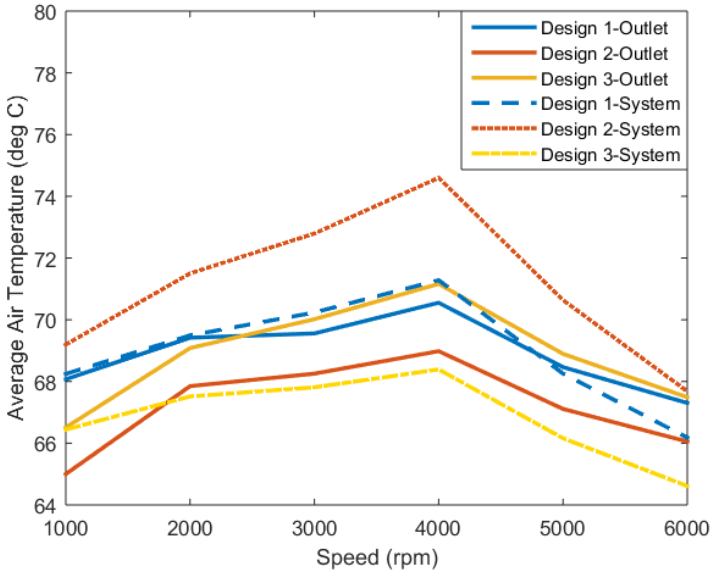

Figure 7-6: Average air temperature on the outlet and within the rotational system of the different inlet/outlet arrangement designs.

These thermal characteristic can be further understood by inspecting the speed of the flow inside the cavity. Figure 7-7 shows the coloured flow streamlines of velocity from 0m/s to 50m/s overlaid with the low velocity region in blue translucent patches for all the inlet/outlet arrangement designs. The ISO surface of the low velocity region is set at a fluid velocity of less than 10m/s. In Figure 7-7, Design 2's inflow accelerates as it enters the cavity and reduces its fluid velocity slightly, thus the low velocity region is small and placed in between the entry and exit ducting. This high air velocity escapes from the system without managing to absorb the heat, thus reflecting the high system average temperature compared to the air outlet temperature. The inflow fluid of Design 1 however, lost its velocity once it entered the cavity system and then took the exit. This created a larger low velocity region compared to Design 2. Unsurprisingly, Design 3's low velocity region has covered almost the whole cavity volume as the inflow direction was changed from a perpendicular linear to a centrifugal direction, thus managing to extract the most heat from the system and flush it to the outlet. The temperature contour of the solid component is illustrated in Figure 7-8. It can

be observed that, the colder rotor temperature was achieved in the low velocity region (blue translucent patches in Figure 7-7).

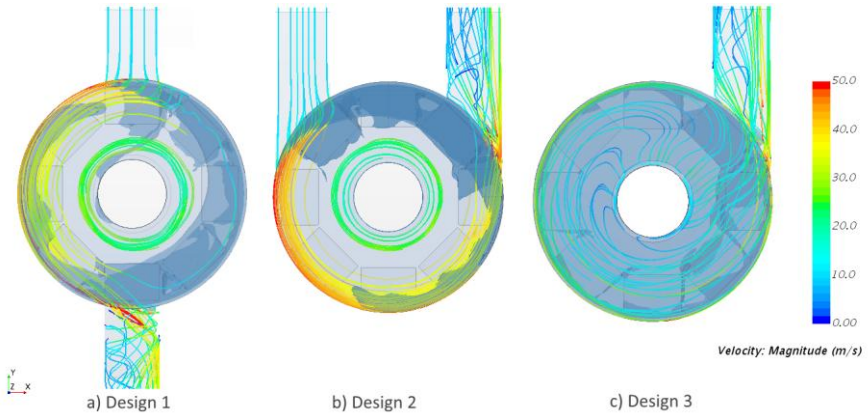

Figure 7-7: Flow streamlines of each design and their ISO surface of low velocity region (<10m/s) at 4000rpm in blue translucent patches.

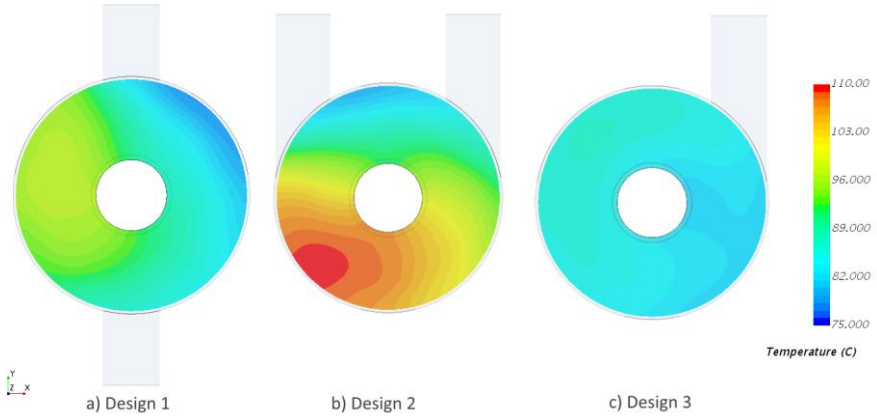

Figure 7-8: Temperature contour of the solid component at 4000rpm.

The average solid temperature plotted in Figure 7-9 shows the agreement where Design 2 has the highest solid temperature followed by Design 1 and Design 3. The peak temperature at 4000rpm for all the selected designs is due to the highest rotor losses value given in Figure 7-3. It is worth noting that Design 1 and Design 2 shared similar solid temperature characteristics where the rotor temperature was higher than the magnet temperature and only changed above 5000rpm as the magnet losses started to dominate. Conversely, Design 3 has different solid temperature characteristics compared to the radial entry of Design 1 and Design 2 in that its rotor

temperature is less than the magnet temperature, as the inflow air is directed to the rotor.

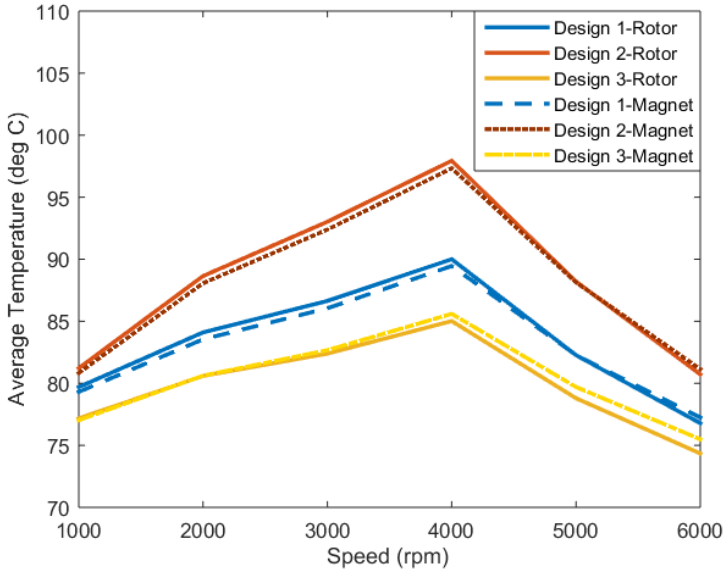

Figure 7-9: Average solid temperature of the rotor and the magnets of the different inlet/outlet arrangement designs.

Furthermore, the average heat transfer coefficient can be calculated by Eq. 6-25 using the results of Figure 7-6 and Figure 7-9 as an input. The calculated results produced are conservative; meaning that the results are cautiously moderated because the inflow has limited changes due to all the selected designs sharing the same mass flow rate that was specified at the inlet. The average heat transfer coefficient in Figure 7-10 shows that the conventional centrifugal fan of Design 3 has the best value followed by Design 1 and Design 2.

Finally, the cooling performance of these inlet/outlet arrangement designs is evaluated by the Cooling Performance Index (CPI) that was introduced and proposed in Chapter 6. The dimensionless number was calculated by Eq. 6-1 and Figure 7-11 plots the value from 1000rpm to 6000rpm. It can be seen that major cooling performance differences only occur at low rotational speeds and they start to share similar cooling performances at high rotational speeds. At slow speed (1000rpm), the Design 1 is 15% greater than the

Design 3 and the Design 2 is 7% lower than the Design 3. At high speed (6000rpm) the Design 1 and the Design 2 are characterised by 11% and 6% lower cooling performance respectively than the Design 3. This suggests that the changes of inlet/outlet design produce a convective heat transfer that is proportionate to the windage losses requirement.

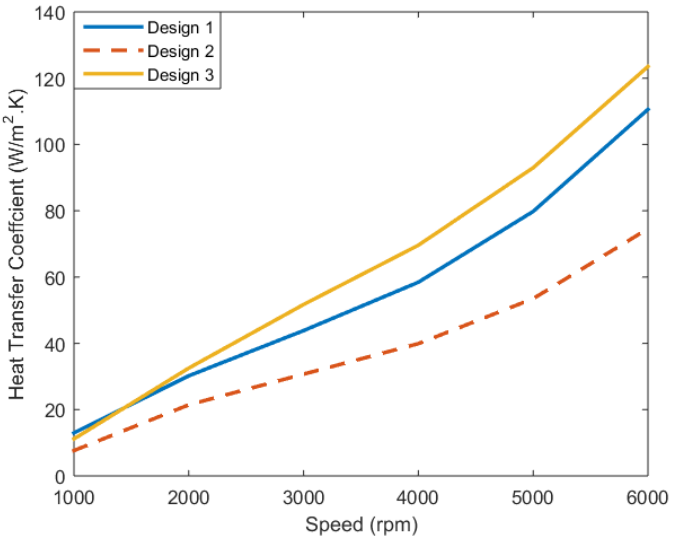

Figure 7-10: Average heat transfer coefficient of the different inlet/outlet arrangement designs.

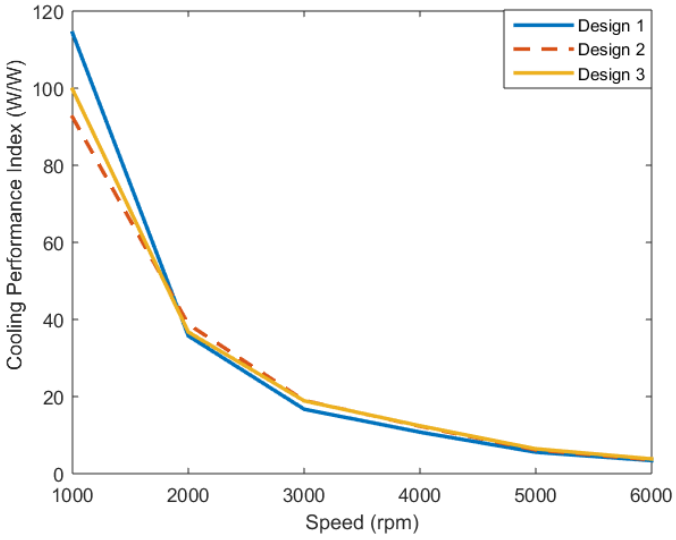

Figure 7-11: Cooling Performance Index (CPI) curves of the different inlet/outlet arrangement designs.

Table 7-1 below summarises the performance of the inlet and outlet design. For the pressure drop and the windage losses, the highest value means bad outcome as the inflow is restricted and high drag is produced. While, for heat transfer coefficient, and cooling performance index, the highest value means it is good.

Table 7-1: Summarise of the inlet and outlet design performance.

	Pressure Drop*	Windage Losses* (not significantly difference)	Heat Transfer Coefficient	Cooling Performance Index (CPI)
Design 1	Highest (bad)	Highest (bad)	Highest (good)	Lowest (bad)
Design 2	Fair	Lowest (good)	Lowest (bad)	Fair
Design 3	Lowest (good)	Fair	Fair	Highest (good)

7.2 Passive flow promoter improvement

The idea presented in Section 7.1 shows that the unconventional inlet/outlet arrangement has the potential to be used for rotor cooling purposes. Based on the CFD analysis, Design 3 performed the best in terms of flow and thermal performance as it is a conventional inlet/outlet arrangement and is known in the industry. The unconventional inlet/outlet arrangement of Design 2 also shows good potential due to less pressure resistance. On the other hand, although Design 1 provides good cooling by lowering the average solid temperature (Figure 7-9) and has a good average heat transfer coefficient (Figure 7-10), this design develops a great amount of pressure drop (Figure 7-4) that may lead to a choking effect, thus it has been neglected.

In this section, Design 2 (the inlet/outlet ducts are tangential to the circular rotor cavity) was chosen to be improvised. The overall geometry was the

same as tested in Section 7.1, yet this time, the inlet was set as the stagnation inlet boundary condition to let the rotor assembly (the rotor disc and its circular array of magnets) drive the air inward and no input mass flow rate was specified, as in the previous exercise. By doing so, the pressure difference from the inlet and outlet will be the pressure development or the pressure rise as the air is driven inward by the rotor assembly. Conversely, in the previous study, the inlet mass flow rate was specified and the pressure difference between the inlet and the outlet was the pressure drop.

The inlet and outlet ducts were extended with a 'virtual/imaginary duct' of 200mm and 300mm respectively. These frictionless ducts were set as wall slip boundary conditions, thus no pressure drop would be added by these extension ductings due to no shear stress occurring on its walls. This approach was taken to aid the convergence as the flow produced by the rotating rotor assembly is expected to be low and may produce reverse flow either at the inlet duct or more prominently at the outlet duct. The inlet boundary condition was set as the inlet mass flow for the first 200 iterations and later changed to the stagnation inlet boundary condition on the remaining 800 iterations to have a faster convergence. It is faster to achieve numerical convergence because this approach allows the air to be forced into its flow direction due to the input mass flow rate on the inlet, instead of letting the rotor assembly suck and blow the air by itself.

Apart from this modification, all other geometrical, meshing strategies and numerical setups were similar to the previous exercise. The rotor and magnets were input with their own losses based on the transient FEA model presented in Figure 7-3 at 4000rpm. All simulations were run at 4000rpm, because it produces the highest temperature due to the highest rotor losses and significant magnet losses values.

7.2.1 Rotor design: Flat disc versus ribs disc

The improvisation of the inlet/outlet arrangement based on Design 2 starts with adapting the rotor design from the YASA sealed machine (in Chapter 5)

into the design. The rotor of the YASA sealed machine has a ribs feature at the outer edge to increase the disc rigidity. This ribs feature may stir the flow and give a similar effect to a fan blade when compared to the flat disc. Therefore, it is most likely to produce better flow properties thus helping to slightly increase the force convective heat transfer. Figure 7-12 shows the difference between the flat disc and the ribs disc taken from the YASA sealed machine.

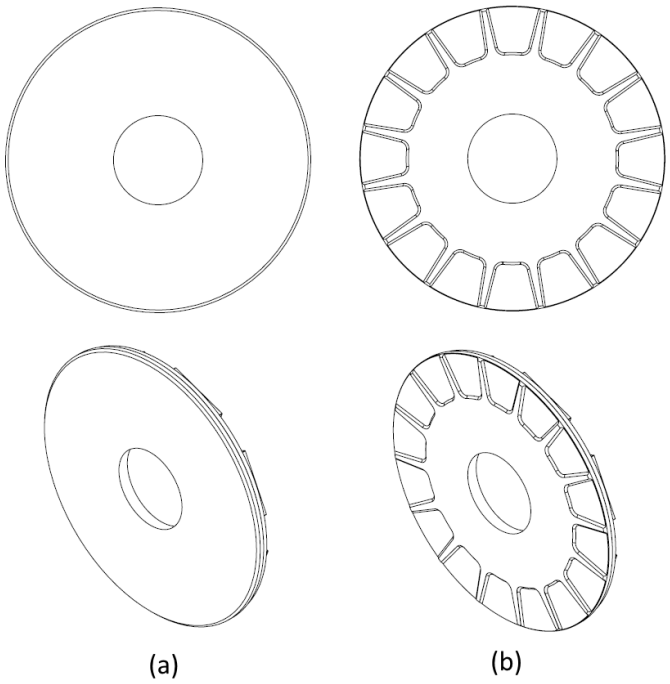

Figure 7-12: The front and isometric views of (a) the flat disc rotor and (b) the ribs disc.

The flow performance of adding ribs at the edge of the rotor disc improved as tabulated in Table 7-2. The mass flow rate presented in Table 7-2 is the mass flow produced by the rotational motion of the rotor disc and the circular magnet array, as no forced airflow on the inlet was specified. Therefore, the pressure produced by the system is a pressure rise. As the flow performance shows a positive improvement, the thermal performance also improves by producing a lower temperature with the ribs feature (Table 7-3). Additionally, the windage losses, the average heat transfer coefficient and the Cooling

Performance Index (CPI) were calculated and presented in Table 7-4. Adding the ribs feature on the rotor provides an additional 6 CPI number, thus shows that this approach (adding ribs on the edge of the rotor) is practical and suitable to be implemented on the prototype machine.

Table 7-2: Flow performance of flat versus ribs disc.

Design	**Mass flow rate**	**Pressure rise (Pa)**
Flat Rotor	77.7ltr/min (0.00153kg/s)	3.55
Ribs Rotor	104.1ltr/min (0.00205kg/s)	6.52
Ribs Rotor - Flat Rotor	+26.4ltr/min (+0.00052kg/s)	+2.96

Table 7-3: Thermal performance of flat versus ribs disc.

	Average Temperature			
Design	**Air Outlet (°C)**	**Air System (°C)**	**Magnets (°C)**	**Rotor (°C)**
Flat Rotor	75.45	84.17	108.72	108.88
Ribs Rotor	75.36	81.93	106.59	106.59
Ribs Rotor - Flat Rotor	-0.09	-2.24	-2.13	-2.17

Table 7-4: Windage losses and cooling performance of flat versus ribs disc.

Design	**Windage Losses (W)**	**Average HT Coefficient (W/m^2-K)**	**CPI (W/W)**
Flat Rotor	1.06	6.546	22.45
Ribs Rotor	1.12	8.641	28.38
Ribs Rotor - Flat Rotor	+0.06	+2.09	+5.93

7.2.2 Axial inlet/outlet duct positioning

Previously in the flat versus ribs disc rotor, the axial position of the inlet and outlet ducts is placed almost in the middle of the width of the circular rotor cavity (Z+ = 5mm). However, these openings for air to enter and exit from the cavity system were introduced directly on the edge of the rotor disc. Figure 7-13 illustrates the axial position of the inlet and outlet ducts on this DE side of the machine. Here, the focus was given to the parametric study of the positioning of the ducting axially, where the duct will be placed in various Z-direction locations to analyse the effect on the flow and the thermal performance. Figure 7-14 presents the location of the Z+ reference as a red dot and the direction the ducts will be moved from Z+ = 0mm (near to the machine's cover) to Z+ = 10mm (near to the stator) for every 2mm. The justification of choosing this increment of 2mm for the parametric study is because it is a sufficient resolution to represent the flow and thermal change over the ducts positioning. Therefore, the tested positions are, Z+ = 0mm, Z+ = 2mm, Z+ = 4mm, Z+ = 6mm, Z+ = 8mm and Z+ = 10mm including Z+ = 5mm from the previous exercise (the rotor with the ribs disc).

The geometrical setup was carried from the ribs feature's CAD, together with the meshing strategy and the numerical setups. The ducting was translated to an intended position as previously described. All the tested positions have the same rotor and magnets losses and spin at 4000rpm, to analyse the performance of the changes at the highest temperature produced, due to the highest rotor losses and significant magnet losses values.

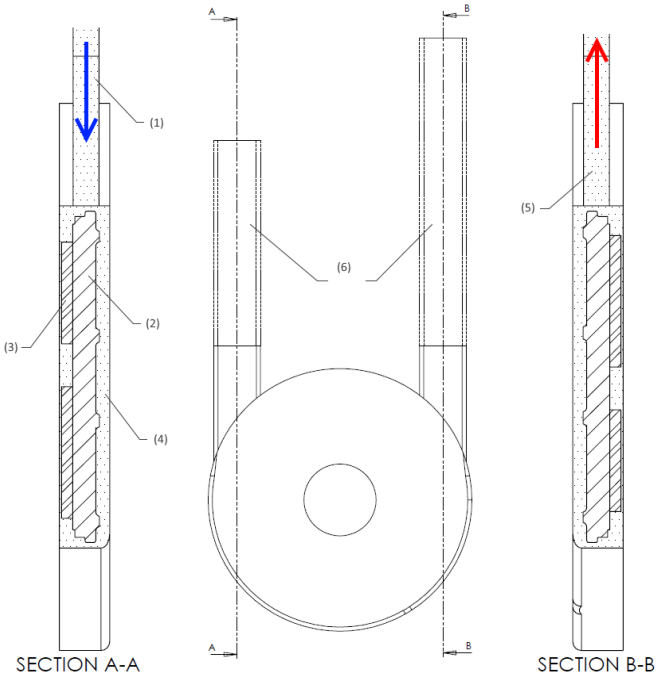

Figure 7-13: The cross section of the DE side with the inlet flow direction (blue arrow) and the outlet flow direction (red arrow) including (1) inlet duct, (2) rotor disc with ribs feature, (3) magnets, (4) cavity interior air, (5) outlet duct and (6) virtual duct with wall slip conditions.

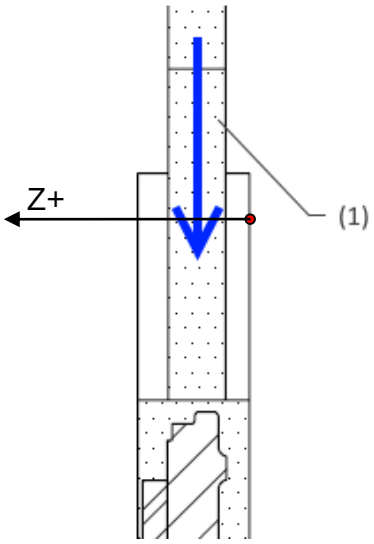

Figure 7-14: The axial or positive Z-direction with the red dot as a reference location or zero values of (1) the inlet duct.

Figure 7-15 shows the mass flow rate and pressure rise when the inlet and outlet duct are in varied positions from 0mm to 10mm from the reference location Z. It is observed that the mass flow rate produced is proportional to the pressure rise with Z = 2mm giving the best values and Z = 10mm the worst. The main difference between these two locations is that Z = 2mm introduces an opening near to the rotor ribs feature, while Z = 10mm introduces an opening at the back of the rotor normal to the magnet's array. To appreciate the difference in these locations, a velocity vector by line integral convolution was presented in Figure 7-17. The common velocity vector is displaying glyphs to represent the field vector. However, in this work, line integral convolution is used. Line integral convolution was introduced by Cabral and Leedom (1993) as another visualisation technique and was adopted in CFD to provide a detailed line view based on the velocity vector of a complex flow (STAR-CCM+ 2016). Therefore, one can see that the velocity vector has no arrowhead as common velocity vector; instead, all vectors are represented in series of lines. The line integral convolution shows that:

1. Z = 2mm
    a. The inflow was directed to the ribs feature and some was flown to the back of the rotor.
    b. The outflow has a circulation flow due to the differential speed and pressure between the air flow from the ribs feature and the magnets.
2. Z = 5mm
    a. The inflow was directed onto the rotor's edge and the flow split to the front and the back of the rotor.
    b. The outflow has a circulation flow due to the wake of the rotating rotor.
3. Z = 10mm

a. The inflow was directed to the back of the rotor and the inlet flow velocity was slightly reduced compared to the other axial positions.
b. The outflow has circulation flow, as the air did not uniformly escape from the system's cavity.

On the other hand, the windage losses in Figure 7-16 show that Z = 5mm, 6mm and 8mm have average windage losses, with 0mm as the best and 10mm as the worst.

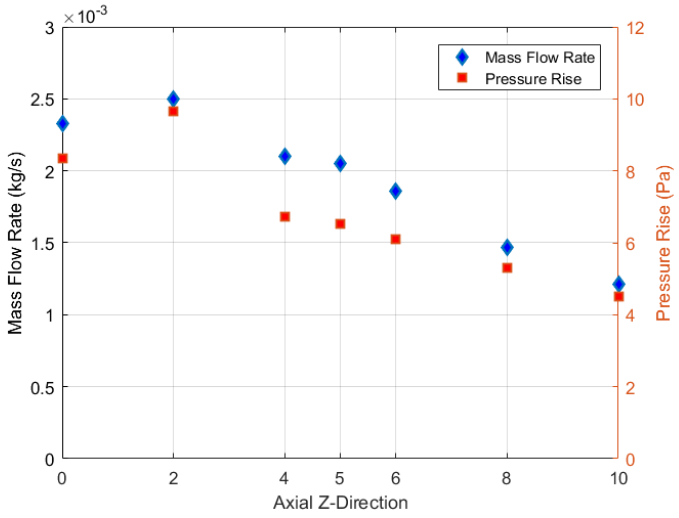

Figure 7-15: Mass flow rate and pressure rise of the axial duct positioning.

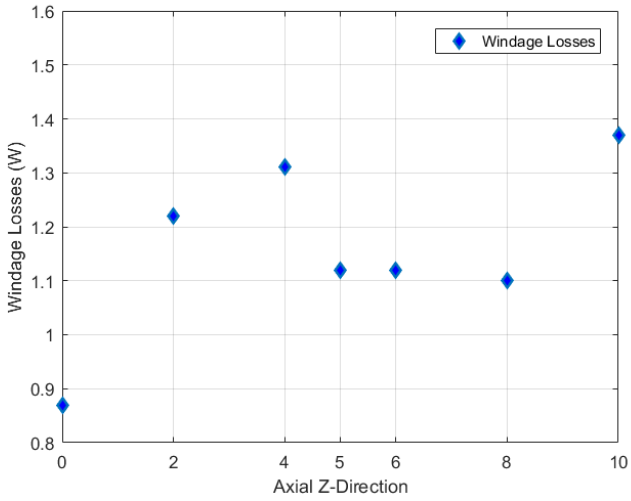

Figure 7-16: Windage losses of the axial duct positioning.

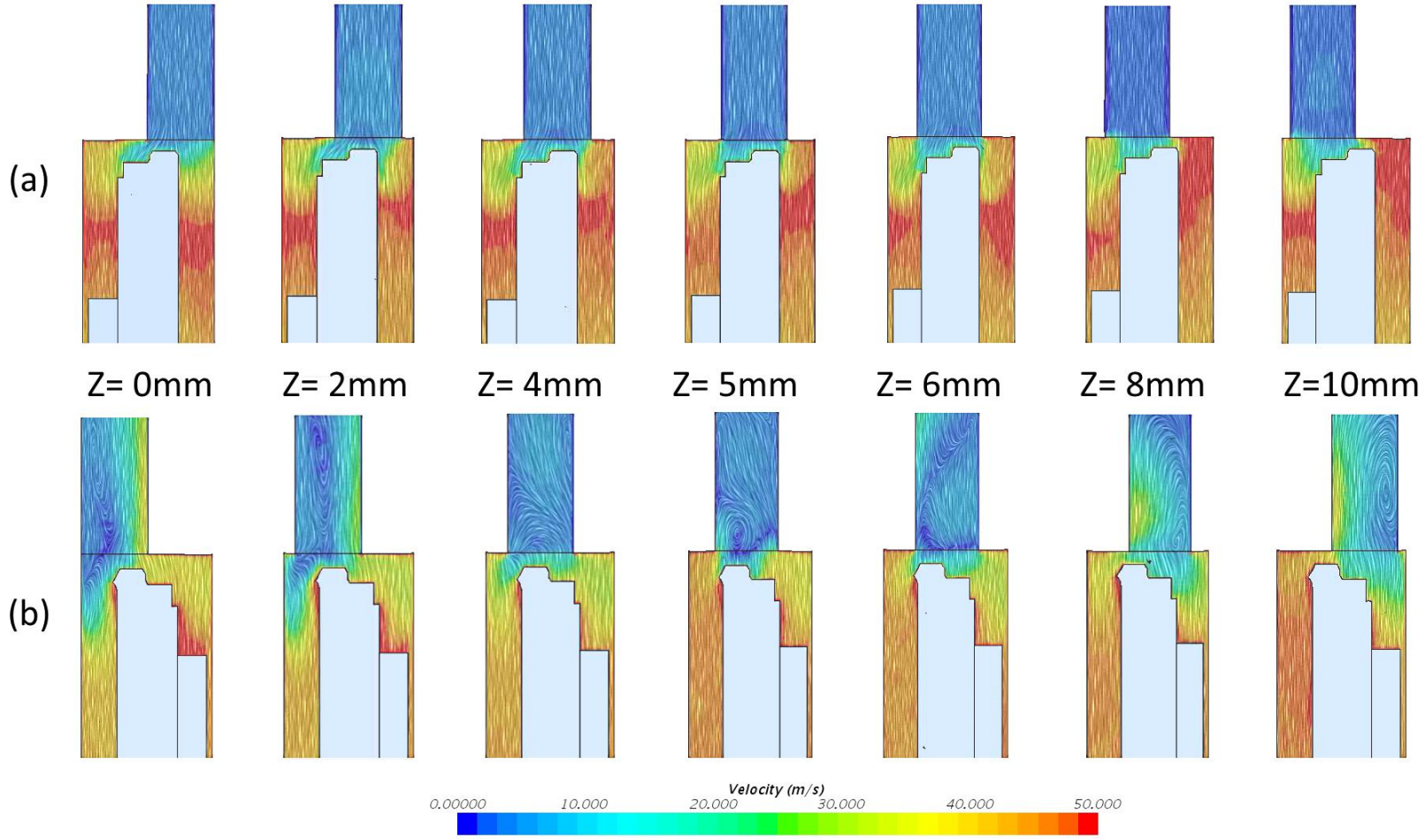

Figure 7-17: Velocity vector by the line integral convolution of (a) the inlet duct and (b) the outlet duct for 0mm to 10mm.

Although the flow performance shows a significant difference towards the variation of the axial inlet and the outlet positioning, the temperature of all tested positions in Figure 7-18 did not have any significant change between them. This is due to the low amount of mass flow entering the system, thus the temperatures produced are higher compared to those when there is a high mass flow rate specified on the inlet as in Section 7.1.

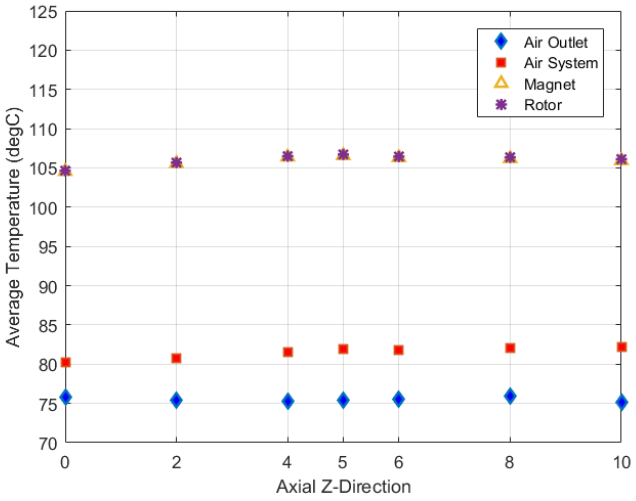

Figure 7-18: Average temperature of the air and the solid components of the axial duct positioning.

The average heat transfer coefficient and the Cooling Performance Index in Figure 7-19 show a similar trend where Z = 0mm provides the best value and Z = 10mm gives the worst value. Interestingly, Z = 5mm (which had been chosen since the beginning of this chapter) produced an average value of the average heat transfer coefficient and the cooling performance index.

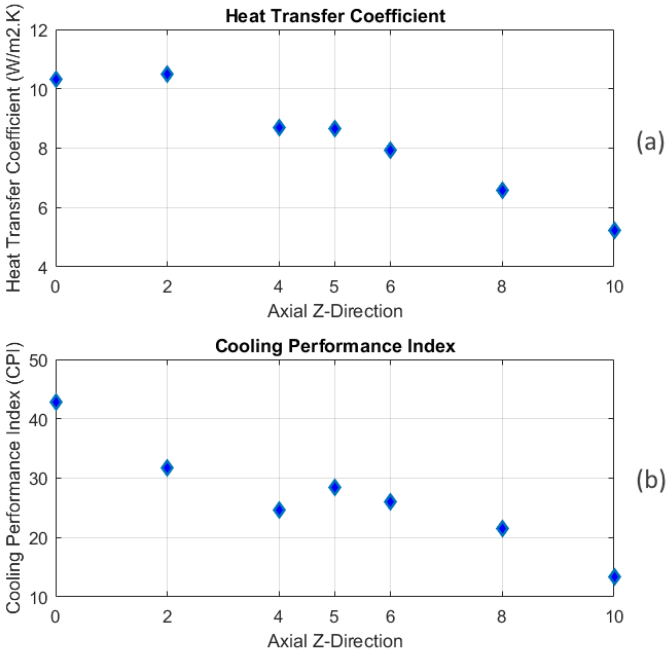

Figure 7-19: (a) Average heat transfer coefficient and (b) Cooling Performance Index (CPI) of the axial duct positioning.

7.2.3 Straight versus tilt ducting

Another parametric change that can be made to improve the flow on the ducting is the angle of the ducts. Figure 7-20a illustrates the flow direction of the inflow (blue arrow) and the outflow (red arrow) on the straight ducting that has been tested previously. For straight ducting, the inflow and outflow had to change their angle once entering the rotor cavity system tangentially therefore, a tilt ducting of 6^{o} was created to input this assumption into a test (Figure 7-20b). The angle of 6^{o} was chosen as the tangential angle between the end point of the inlet/outlet ducting and the circular rotor cavity. All other geometrical, meshing and numerical setups were left the same as in the previous exercises.

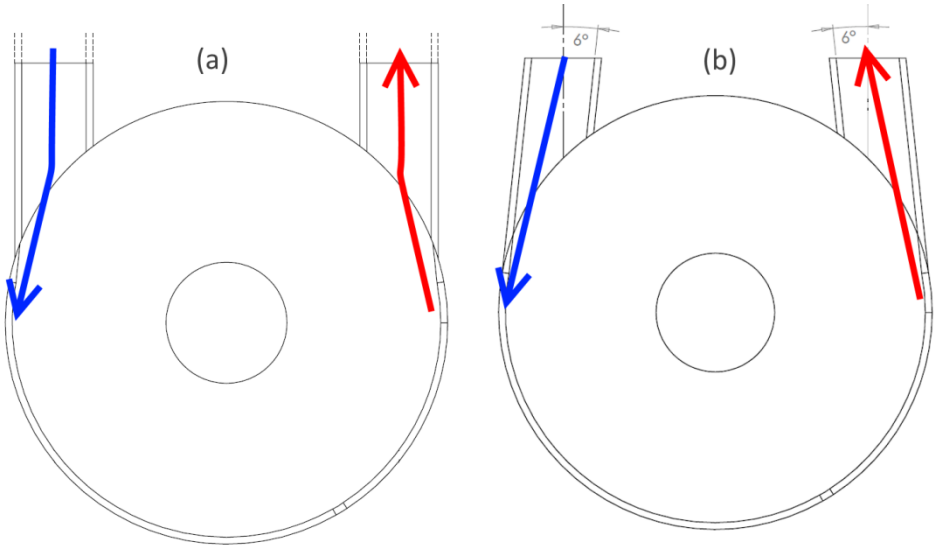

Figure 7-20: The expected inflow and outflow direction of (a) the straight ducting and (b) the tilt ducting.

The result of this tilt duct modification is compared with the straight ducting from the ribs rotor assessment in Section 7.2.1, where both shared the axial positioning at Z = 5mm. Table 7-5 tabulated the flow performance where the tilt duct improved the mass flow rate and the pressure rise. However, the thermal performance did not yet improve significantly, as shown in Table 7-6. The average heat transfer coefficient improved slightly by 2W/m^2-K, while this modification did not give a major increase of windage losses thus, the CPI number only changed by 0.6.

Table 7-5: Flow performance of straight versus tilt ducting.

Design	**Mass flow rate**	**Pressure rise (Pa)**
Straight Duct	104.1ltr/min (0.00205kg/s)	6.52
Tilt Duct	136.6ltr/min (0.00269kg/s)	11.14
Straight Duct - Tilt Duct	+32.5ltr/min (+0.00064kg/s)	+4.62

Table 7-6: Thermal performance of straight versus tilt ducting.

Design	Average Temperature			
	Air Outlet (°C)	**Air System (°C)**	**Magnets (°C)**	**Rotor (°C)**
Straight Duct	75.36	81.93	106.59	106.71
Tilt Duct	74.19	81.03	105.38	105.53
Straight Duct - Tilt Duct	-1.17	-0.90	-1.20	-1.18

Table 7-7: Windage losses and cooling performance of straight versus tilt ducting.

Design	Windage Losses (W)	Average HT Coefficient (W/m^2-K)	CPI (W/W)
Straight Duct	1.12	8.64	28.38
Tilt Duct	1.39	10.60	27.77
Straight Duct - Tilt Duct	+0.27	+1.96	-0.61

Apart from all the modifications and parametric studies tested above, it is observed that there is evidence of flow circulation on the outlet duct due to the changing flow pattern from rotational flow to directional flow. This flow circulation may limit the exiting outflow and the flow can be straightened by adding a guide vane (either single or multiple) if favoured by the machine designer to further increase the flow performance.

7.3 Design implementation: Dual rotor cooling

After the exploration of the design concept of a different inlet/outlet arrangement, if was found that Design 1 has produced the highest pressure drop, thus it was discarded. Therefore, Design 2 and Design 3 were chosen to be integrated into the YASA machine for the dual rotor cooling technique. Figure 7-21 illustrates the new YASA machine topology with dual rotor cooling. The idea is to allow cool air to be drawn in by the fan attached to the

non-drive end's (NDE) rotor and absorb the heat from the rotor via force convection. Later, the warm air is channelled to cool the drive end's (DE) rotor before exiting to the ambient.

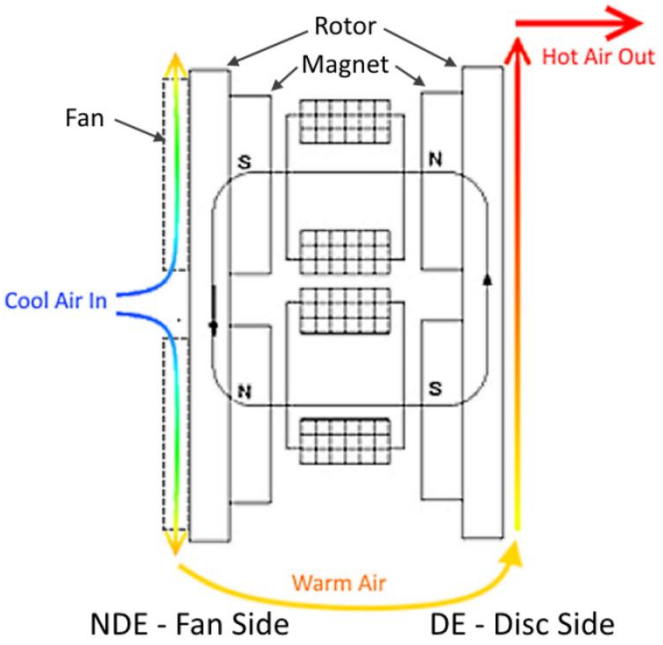

Figure 7-21: The new YASA machine topology including rotor cooling on both rotors.

The conceptual design in Figure 7-22 was built based on the proposed topology in Figure 7-21. The design implementations from the original YASA sealed machine design are:

a) Design 3 – The conventional inlet and outlet arrangement of the centrifugal fan design is adapted to the machine's non-drive-end (NDE) side. A backward curved fan design from Chapter 6.0 been attached to the rotor as an inflow drive mechanism. The outlet duct was channelled to the other side of the machine (DE side). This is named: 'NDE - Fan side'.
b) Design 2 – The unconventional inlet and outlet arrangement of the tangential duct is adapted on the machine's drive-end (DE) side. The

inlet was taken from the outlet of Design 3, NDE - Fan side. This is named: ‘DE - Disc side’.

The design implementation of Design 2 onto the conceptual design also included the findings from Section 7.2 where:

- The rotor has a ribs feature on its edge.
- Z = 5mm was considered as the axial positioning for both the inlet and outlet ducts due to its ease of design and manufacturing, such as mounting point, sealing, etc. Z = 5mm provided an average flow performance among all the tested positions.
- 6^{o} tilt ducting on both the inlet and outlet ducts increases the flow performance.

Although the proposed design implementation of Design 3 and Design 2 was not the best, it complied with compact packaging (to minimise the axial length) as the key priority. A transfer duct was designed to bridge the flow of the resulting warm air from the NDE fan side to the inlet port of DE disc side. The hot air is then released to the ambient through the outlet of the DE disc side. Figure 7-22 shows the conceptual design in a cyan colour for the ducting, dark blue for the fluid domain, red for the fluid rotational domain and yellow for the rotors. Note that the inlet ducting (in cyan) also includes a mass flow sensor for the experimental setup. In the CFD simulation, two parts are not included: the stator in a grey colour and the transparent covers.

The setup of the CFD simulations such as material properties, boundary conditions and losses input are similar to the previous exercise in this chapter except that the inlet air temperature is set at 26.85ºC (300K) for realistic operational temperature values instead of 60ºC for harsh conditions. Yet all the subjected walls were specified as 60ºC to simulate the condition when the machine is placed under the hood. Also, the thin layer of adhesive material between the magnet and the rotor was not included due to the complexity of the meshing resulting in a longer simulation time. This time, again to aid the convergence, the inlet and outlet ducts were extended by a

'virtual duct' of slip walls and the inlet boundary condition is set as the mass flow rate based on Eq. 7-1 for 200 iterations before changing to the stagnation inlet until the simulations converge. The steady state simulations were performed at 1000rpm to 6000rpm for every 1000rpm increment.

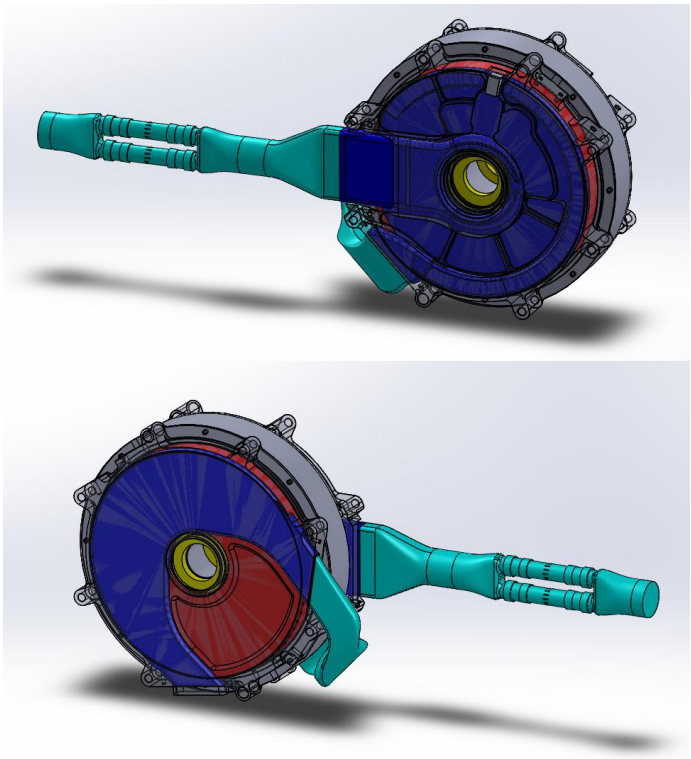

Figure 7-22: The YASA machine assembly integrated with Design 2 and Design 3's inlet and outlet arrangements including dual mass flow sensors on the inlet.

7.3.1 Experimental setup

Based on the conceptual design in Figure 7-22, a prototype has been built for flow validation purposes, as shown in Figure 7-23. The prototype has included a working rotor assembly including the magnet arrays attached to it on the both sides of the rotor. However, the stator was left blank without any workable component, yet all covers, seals and mountings were present to allow for the experimental data collection, specifically the mass flow rate. The mass flow rate data were collected by the dual PMF4104V mass flow sensors mounted on the inlet duct, as discussed previously. This prototype

machine was spun by a secondary motor from 1000rpm to 6000rpm and the data was collected at every 1000rpm. The rotational speed was held at every 1000rpm for some time to let the mass flow rate data stabilise before being collected.

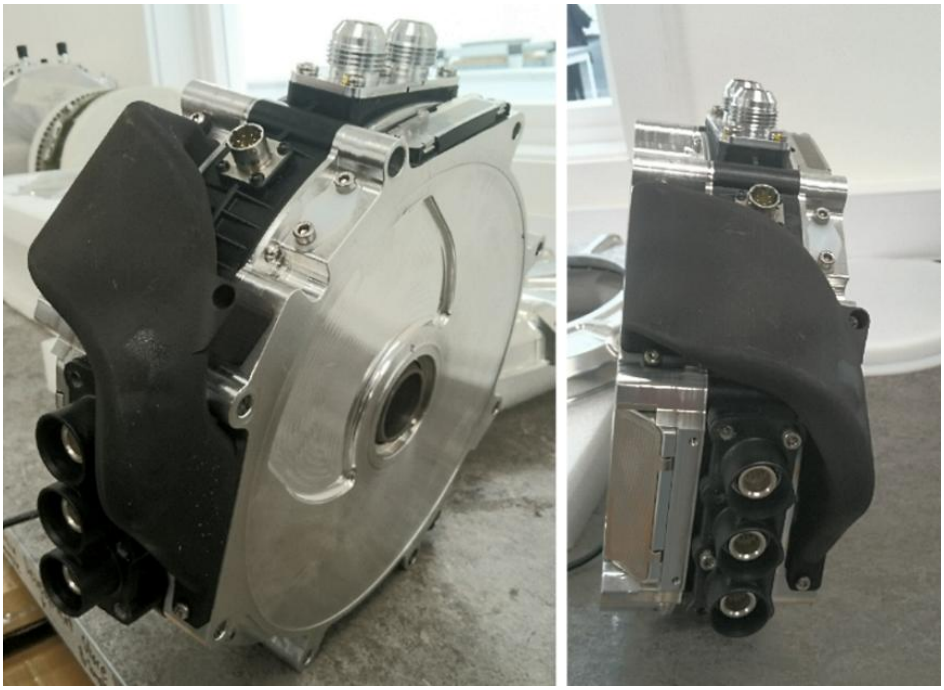

Figure 7-23: The prototype of the new YASA machine topology incorporated with dual rotor cooling via the air transfer duct.

7.3.2 Flow validation

Figure 7-24 presents the comparison of the mass flow rate between the experimental and the CFD simulations. The CFD modelling shows an accurate prediction at all rotational speed ranges. The improved accuracy of the CFD modelling was achieved because at the time, all the air cavity inside the machine was assumed to be a rotating fluid region, while the conservative fluid domain is assigned only to the ducting. This large rotating region of air volume produces a higher mass flow rate as the whole cavity is rotated by the MRF method, which has a fictitious rotating velocity.

Additionally, the pressure rise of the system is collected by CFD to assess if the proposed design implementation has caused a stalling effect. Table 7-8

shows that the system produced an adequate positive pressure across the rotating speed. However, further analysis is required if the machine is required to operate under 1000rpm for a long duration due to the lower pressure rise value.

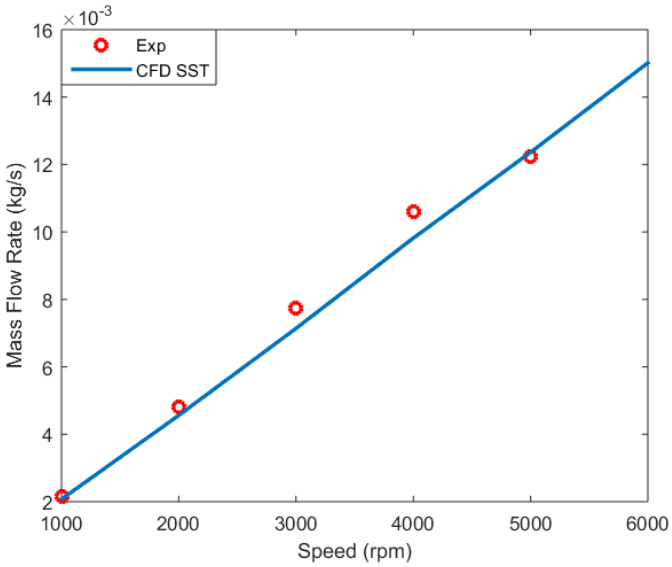

Figure 7-24: Comparison between the CFD and the experimental data of the mass flow rate.

Table 7-8: Pressure rise of the proposed dual rotor cooling via CFD.

Speed (rpm)	1000	2000	3000	4000	5000	6000
Pressure Rise (Pa)	7.98	20.24	49.44	99.46	153.37	229.66

7.3.3 CFD thermal analysis

The temperatures of the air and the solid components are extracted from the CFD simulations. The average air temperature at the outlet and the cavity system were compared in Figure 7-25. Most of the hot air is able to be flown out by the fan on the NDE fan side, thus its outlet temperatures are higher than the system's temperature. On the other hand, the outlet temperature of the DE disc side is similar to its system's temperature from 1000rpm to 4000rpm as the ribs feature is able to efficiently drive the hot air to the outlet. The rotor of the DE disc side of this prototype machine has ribs features that

disturb the airflow. This feature causes flow disturbance thus generating turbulence, as plotted in Figure 7-26b. Additionally, this design implementation has contrary findings due to this ribs feature where it is observed that there are greater low velocity patches inside the cavity systems (Figure 7-26b) compared to the initial study presented in Figure 7-7.

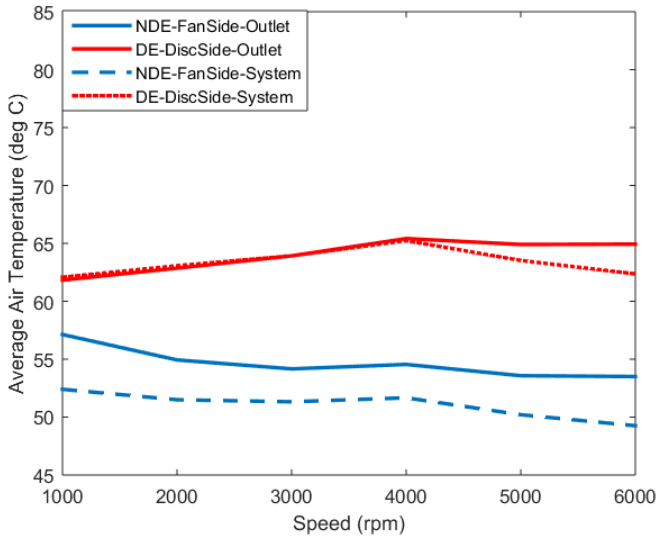

Figure 7-25: Average air temperature on the outlet and within the rotational system of the design implementation.

The solid component's temperature in Figure 7-27 shows that the rotor and magnet's temperature at the NDE fan side is lower compared to the DE - disc side, as expected. This is because the cold aid from the ambient is received on the fan side, which then channels its warm air to the other side. Consequently, a slightly higher temperature remains on the DE - disc side. Although the temperature of the DE - disc side is higher, the temperature remains within the specification, particularly the magnet temperature that has a generic temperature threshold of 100°C, as well as a maximum service temperature at 120°C for the NdFeB N00H series magnet (Eclipse Magnetics 2014).

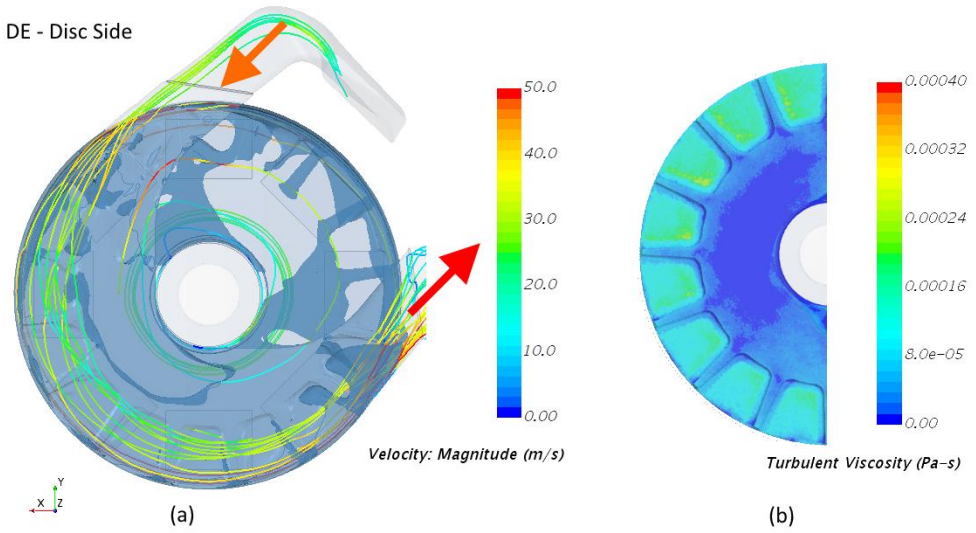

Figure 7-26: (a) Flow streamlines and ISO surface of the low velocity region (<10m/s) at 4000rpm of the DE – disc side. The arrows show the flow direction from the ducting. (b) The air turbulence viscosity on the rotor.

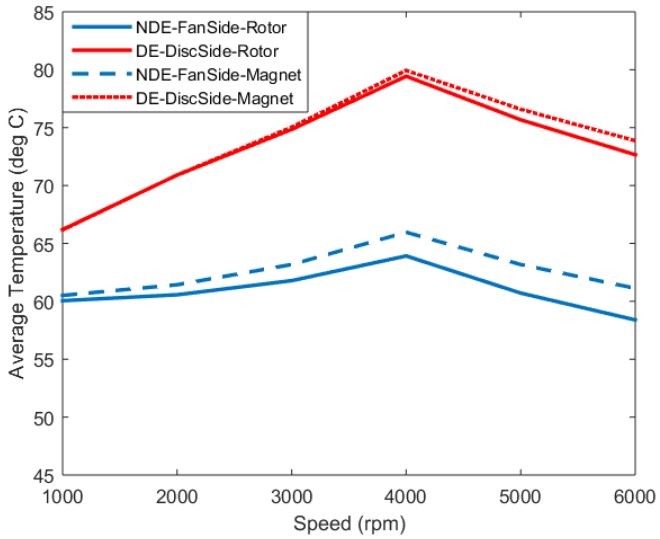

Figure 7-27: Average solid temperature of the rotor and the magnets of the design implementation.

7.3.4 Cooling performance

The windage losses of both rotors are presented in Figure 7-28, where the NDE fan side has the highest windage, as expected. This is due to the fan feature trying to scoop and force the air inside the system where it is blown to

the other side of the machine. Similarly, the NDE fan side has the highest average heat transfer coefficient compared to DE disc side due to the NDE fan feature stirring the airflow, thus more forced convective heat transfer occurs on the rotor surface (Figure 7-29). Additionally, the fan feature increases the rotor surface, thus the losses on the rotor can be separated in a slightly larger contact surface between the hot rotor and the cold air. The Cooling Performance Index (CPI) of the NDE fan side offers a high cooling index up until 3000rpm and shares a similar cooling performance once 4000rpm is reached and continues to behave similar to the DE disc side, as shown in Figure 7-30. This is due to the windage losses being dominated at a higher rpm range mainly above 4000rpm, while the convective heat transfer did not increase in a similar pattern.

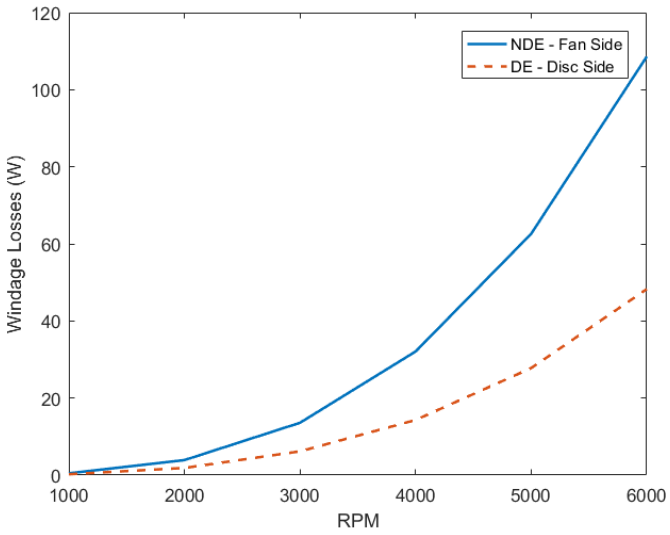

Figure 7-28: Windage losses of the design implementation.

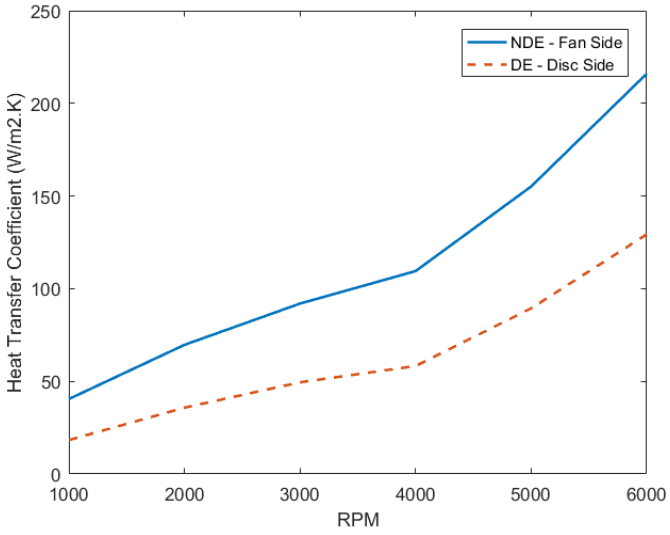

Figure 7-29: Average heat transfer coefficient of the design implementation.

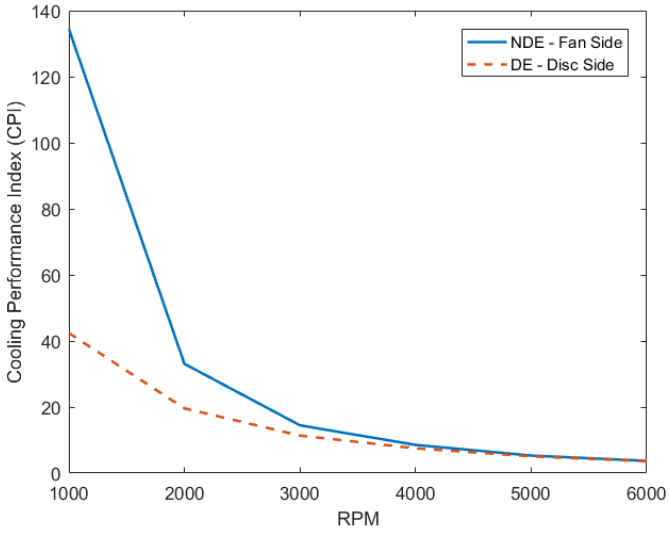

Figure 7-30: Cooling Performance Index (CPI) of the design implementation.

7.4 Chapter summary

In this chapter, a new design concept of dual rotor cooling for an AFPM machine was proposed by accessing multiple inlet and outlet arrangement methods for rotor cooling by CFD. Initially, three inlet and outlet arrangements were studied and analysed by creating a single modular design. This approach has reduced the pre-processing time and any machine

designer can adopt this methodology when dealing with CFD models that have basic geometrical similarities. The findings are:

- Design 1 – Produced the highest pressure drop due to the location of the air inlet straight top down to the cavity system. This creates sudden changes in the flow direction and the inward flow contradicts with the circular motion of the flow in the cavity system. Thus, this design was discarded.
- Design 2 – Produced an acceptable pressure drop with minimum thermal performance due to the inflow being accelerated once it enters the cavity system, thus it has a minimum low velocity region within. However, this design is expected to be improvised, due to its minimum axial thickness.
- Design 3 – Performed the best on thermal and cooling as it has a well-known centrifugal fan design. It was taken to be adapted into the conceptual machine, although it would drastically increase the axial thickness.

Design 2 was improvised to improve is properties as a passive flow promoter by analysing the effects of different rotor designs, axial inlet/outlet positioning and the angle of ducting. Later, Design 2 was implemented on the drive-end of the machine and Design 3 was adopted on the non-drive-end side to form a novel dual rotor cooling configuration, hence a new topology was created. The flow results from the CFD were validated and showed great correlation with the experimental data. The pressure rise of the new proposed machine showed positive pressure development without the stalling effect occurring.

Additionally, the thermal analysis shows an acceptable operating temperature of the rotor assembly specifically for the magnet temperature, when subjected to 150kW continuous power. This should increase the machine's reliability and efficiency when operating under a similar load as tested in this chapter. If the machine manufacturer wishes to further increase the continuous performance, both rotors' ends should be adopted as Design

3; the conventional centrifugal fan design for high flow and a better thermal and cooling performance.

It can also be concluded that the Cooling Performance Index (CPI) can be used to assess the suitability of design changes for improvisation or optimisation.

Chapter 8

8.0 Conclusion and Further Work

This chapter summarises and concludes the aim and objectives of the study given in Section 1.4. The first part serves the conclusion for each of the works done and is followed by the recommendations and discussion of potential further research.

8.1 Conclusion

This thesis has presented a novel secondary cooling method via rotor cooling technique for Axial Flux Permanent Magnet (AFPM) machines while the work focused in the Yokeless and Segmented Armature (YASA) type. It has been shown, that the rotor cooling technique is an ideal approach to increase the cooling capacity and this newly proposed thermal management allows for the performance of the machine to increase drastically. It is also expected that other major challenges related to thermal behaviour of an electrical machine are increased such as the machine's efficiency and reliability because the of additional effectiveness of the cooling strategy.

The work started with identifying the suitable numerical modelling of computational fluid dynamics (CFD) by verification and validation (V&V) over the experimental measurement of flow and temperature. Various exercises have been performed in Chapter 4 and the V&V process shows that CFD is

able to produce credible results when compared with the measurements, thus confidence is developed. The presented data served as evidence that the chosen CFD modelling setups were suitable for further CFD based design study.

Having established a credible numerical modelling, the current design of YASA sealed machine has been extensively studied with CFD. In Chapter 5, various exercises have also been conducted. Firstly, the full geometry was compared with partial 1/8 CFD modelling which produced similar results with a significant saving in computational time. This allows more complex and detail mesh to be included in the simulation, where the effect of the adhesive layer between the magnet and the rotor temperature is studied. In addition, the study of the heat transfer to the exterior air via the conjugate heat transfer was tested. Furthermore, over-performance condition (150kW) of YASA sealed machine was compared with experimental data and shows good correlations. The findings also include the relationship between the rotor and the magnet temperature that is useful for AFPM manufacturers to predict the magnet temperature based on the rotor data

The specific design of the cooling technique for an AFPM machine begins in Chapter 6 where various fan designs were examined with focus on its flow characteristic, thermal characteristic and cooling performance. The concept of attaching a fan feature to the rotor is valid and can be adopted as it is proven that it can dissipate the heat out from the rotor, thus it may cool the rotor and the magnets. To aid the evaluation of the cooling performance of each fan design, a novel cooling performance index (CPI) has been introduced. It was found that the CPI that was initially intended for the rotor cooling assessment can also be applied to other cooling applications and the formulation is presented. This dimensionless number shows that a higher CPI number indicates a better cooling capability.

Chapter 7 has presented the final design work of this thesis on implementing the conceptual dual rotor cooling of an AFPM. Firstly, several inlet/outlet

arrangement was built by a single modular design and the results shows that unconventional inlet/outlet arrangement can be adopted for the rotor cooling technique, although the arrangement may need extra flow on its inlet to perform well. Then the cooling performance index (CPI) was use to evaluate the suitability of design to be adopted. Finally, the conceptual dual rotor cooling of an AFPM was tested with high continuous performance of 150kW and shows a good correlation when compared with the measurement from the prototype machine.

This conceptual dual rotor cooling technique presents an alternative to the machine designer for AFPM machine topologies to increase their machines' performance. Although the manufacturing cost will increase due to additional component of the fan, the consequence of this novel secondary cooling method shows that with the same topology and existing interior components, the machine's performance can be drastically improved, which shows a significant potential to be adopted into traction application of automotive industry.

8.2 Specific Contribution of This Thesis

The author believes that this work has made several key contributions with an original outcome to the academic knowledge as listed below:

1. A steady state CFD modelling on analysing the thermal and cooling of YASA machine topology has been verified and validated with a measurement of the prototypes machine. The machine inflow and rotor temperature have been well predicted with an average 7.6% and 0.96% of error respectively.
2. The suitable analytical equations for prediction of convective heat transfer and windage losses have been compiled and compared with the CFD modelling results.
3. An analytical equation of the relationship between the rotor and the magnet temperature was presented. This helps the machine

manufacturer to predict the magnet temperature since the machine only monitors the rotor temperature due to sizing constrains.

4. A novel cooling strategy of the rotor for AFPM machine has been developed by introducing a fan on the rotor that becomes a flow driven mechanism and heat exchanger simultaneously. The work was analysed by CFD to evaluate its usability and appropriateness.
5. An extensive study including several fan designs took place, where the different designs were tested and several inlet and outlet design arrangements were conducted to find the best possible design for single and dual rotor cooling purposes.
6. In order to help in selecting the best design, a new dimensionless number named Cooling Performance Index (CPI) was introduced which assess the design cooling capacity over it power requirement.
7. The dual rotor cooling for YASA machine that was explored by CFD model has reviled that the flow prediction is accurate with an average 4.6% of error.

8.3 Further Work

Several ideas for further research to improve this study's rotor cooling technique are detailed in this section.

8.3.1 Bi-directional assessment

This study only assessed the effectiveness of the selected fan in a uni-directional motion due to limited operational on the reverse rotational direction. Yet, knowing the bi-directional cooling performance will provide a comprehensive understanding of the adapted rotor cooling technology and the machine may be applied to other applications that require bi-directional motion.

8.3.2 Dual rotor cooling

The dual rotor cooling performance can be further improved:

- Both rotors use Design 3 for the best cooling performance but this will increase the machine's axial thickness.
- Both rotors use Design 2 for the minimum increase of the machine's axial thickness but this requires further design exploration and improvisation for the ribs feature to work as a fan.

8.3.3 Transient modelling

The CFD simulations undertaken in this study were conducted in steady state simulation. It would be interesting to investigate the fan and cooling performance in transient conditions. Two areas can be considered which are:

- Low speed application – 0 to 1000rpm for a backward curve, as it is known to create a stall effect at a lower speed.
- Normal speed application – 1000rpm to 4000rpm where the flow and temperature are steadily increased.

The potential constraints of the transient modelling are the conformal mesh, which is crucial in meshing strategy, selecting time step and physical time step need to be carefully selected due to the speed changes. Therefore, the feasibility of running transient modelling of rotor cooling technique will highly dependent on the computational recourses and solution time.

8.3.4 Rotor cooling via air injection

Another potential method for a rotor cooling technique is to inject or spray cold air onto the rotor for a quick cooling solution. The cold air produced by a vortex air gun (e.g. https://www.vortec.com/cold-air-guns) used mainly in the manufacturing industry could be embedded in the machine cover. However, detailed analysis is required in order to eliminate the potential of thermal distortion due to the different rotor surface temperature.

8.3.5 Broader Cooling Performance Index (CPI) evaluation

A broader assessment of the Cooling Performance Index (CPI) is required, as this dimensionless number has the potential to be applied to other engineering applications. As listed in Chapter 6.0, this dimensionless number can be extrapolated to other cooling applications by assessing its cooling capacity over its cooling power requirement.

REFERENCES

Agrawal, K. (2007) *Industrial Power Engineering Handbook.* Boston: Butterworth-Heinemann.

AIAA Guideline (1998) *Guide for the Verification and Validation of Computational Fluid Dynamics Simulations*. AIAA G-077-1998.

AIAA Standards Guide (2002) *Guide for the Verification and Validation of Computational Fluid Dynamics Simulations*. AIAA G-077-1998(2002), s.l.: s.n.

Airoldi, G. (2010) *Numerical Investigation of Air Flow and Heat Transfer in Axial Flux Permanent Magnet Electrical Machine*. Unpublished PhD Thesis. Durham: Durham University School of Engineering and Computing Sciences.

Airoldi, G., Bumby, J., Dominy, C., Ingram, G., Lim, C., Mahkamov, K., et al. (2009) Air Flow and Heat Transfer Modeling of an Axial Flux Permanent Magnet Generator, *International Conference on Computer, Electrical and Systems Science Engineering, WASET.* Dubai, UAE, 4-6 February 2009.

Airoldi, G., Ingram, G., Mahkamov, K., Bumby, J., Dominy, R., Brown, N., et al. (2008) Computations on Heat Transfer in Axial Flux Permanent Magnet Machines, *2008 18th International Conference on Electrical Machines (ICEM).* Vilamoura, Portugal, 6-9 Sept. 2008.

Albert, L., Fornasiero, E., Bianchi, N. and Bolognani, S. (2011) 'Rotor Losses Measurement in an Axial Flux Permanent Magnet Machine'. *IEEE Transaction on Energy Conversion,* 26(2), 639-645.

Anderson, J. (1995) *Computational Fluid Dynamics: the Basic with Applications.* USA: McGraw-Hill Mechanical Engineering, McGraw-Hill Inc..

Anon. (2015) *Discovering Better Pumps Faster through Full-Fidelity CFD Simulations.* s.l.: s.n.

ATB Morley. (2002) *Mining Drive Motors.* [online] available from <www.morleymotors.com/Mining%20Drive.pdf> [30 July 2015].

Becker, K. and Kaye, J. (1962) 'Measurements of adiabatic flow in an annulus with an inner rotating cylinder'. *Trans. ASME, J. Heat Transf.,* 84, 97–105.

Becker, K. and Kaye, J. (1962) 'The influence of a radial temperature gradient on the instability of fluid flow in an annulus with an inner cylinder rotating'. *Trans. ASME, J. Heat Transf.,* 84, 106–110.

Benhaddadi, M., Olivier, G., Ibtiouen, R., Yelle, J., and Tremblay, J. (2011) *Electric Machines and Drives.* ISBN 978-953-307-548-8. US: InTech.

Benlamine, R., Dubas, F., Espanet, C., Randi, S. A., and Lhotellier, D. (2014) Design of an Axial-flux Interior Permanent-magnet Synchronous Motor for Automotive Application: Performance Comparison with Electric Motors used in EVs and HEVs. *Vehicle Power and Propulsion Conference (VPPC).* Coimbra, Portugal, IEEE.

Beretta, G. and Malfa, E. (2003) 'Flow and heat transfer in cavities between rotor and stator disks'. *International Journal of Heat and Mass Transfer,* 46, 2715-2726.

Bloch, H. and Soares, C. (1998) *Process Plant Machinery.* Boston: Butterworth-Heinemann.

Boutarfa, R. and Harmand, S. (2005) 'Local convective heat transfer for laminar and turbulent flow in a rotor–stator system'. *Exp. Fluids,* 38(2), 209–221.

Cabral, B. and Leedom, L. (1993) *Imaging Vector Fields Using Line Integral Convolution.* Anaheim, California, s.n., 263-270.

Cai, J., Qi, D. and Zhang, Y. (2012) "A Numerical Study Of The Blade Passing Frequency Noise Of A Centrifugal Fan". *Vibration, Acoustics And Wave Propagation, 12.*

Camilleri, R., Howey, D. and McCulloch, M. (2012a) Thermal Limitations in Air-cooled Axial Flux In-wheel Motors for Urban Mobility Vehicles: a Preliminary Analysis. *2012 Electrical Systems for Aircraft, Railway and Ship Propulsion (ESARS),* Bologna, Italy, 16-18 Oct. 2012, s.n., 1-8.

Camilleri, R., Woolmer, T. and Mcculloch, M. (2012b) Investigation into the Temperature Profile of a Liquid Cooled YASA© AFPM Machine. *6th IET International Conference on Power Electronics, Machines and Drives,* Bristol, IET, 1-8.

Camilleri, R., Howey, D.A. and Mcculloch, M. (2015) Predicting the Temperature and Flow Distribution in a Direct Oil-Cooled Electrical Machine with Segmented Stator. *IEEE Transactions of Industrial Electronics,* 63(1).

Chan, C. (1987) 'Axial field electrical machines-design and application'. *IEEE Transaction on Energy Conversion* 2(2), 294-300.

Chang, C., Kuo, Y., Wang, J. and Chen, S. (2010) 'Air cooling for a large scale motor'. *Applied Thermal Engineering,* 30, 1360-1368.

Chen, A. et al. (2012) 'Sub-Cooled liquid nitrogen test system for cooling HTS synchronous motor'. *IEEE Transactions on Applied Superconductivity,* 22(3).

Chen, C. and Jaw, S. (1998) *Fundamentals of Turbulence Modelling*. London, UK: Taylor and Francis.

Childs, P. (2011) *Rotating Flow.* Amsterdam: Elsevier. 81-125.

Chirila, A. I., Ghita, C., Craciunescu, A., Deaconu, I., Navrapescu, V., and Catrinoiu, M. (2011) 'Rotating Electric Machine Thermal Study'. *Renewable Energy and Power Quality Journal*, 1089-1093.

Chong, Y. (2015) *Thermal Analysis and Air Flow Modelling of Electrical Machines.* Unpublished PhD thesis. Edinburgh: The University of Edinburgh.

Chong, Y., Magahy, D., Chick, J., Mueller, M., Staton, D., and Mcdonald, A. (2011) Numerical Modelling of an Axial Flux Permanent Magnet Machine for Convection Heat Transfer. *IET Conference on Renewable Power Generation*, Edinburgh, IET, 1-6.

Darvish, M. and Frank, S. (2012) Towards the CFD Simulation of Sirocco Fans: From Selecting a Turbulence Model up to the Role of the Cell Shapes, *FAN2012: International Conference on Fan Noise, Technology and Numerical Methods*, Senlis, France, s.n., 1-12.

Davidson, L., Nielsen, P. and Sveningsson, A. (2003) Modifications of the V2 Model for Computing the Flow in a 3D Wall Jet, *Proceedings of the International Symposium on Turbulence, Heat and Mass Transfer 4,* Antalya, Turkey, s.n., 577-584.

Department for the Environment, Food and Rural Affairs and Department for Transport, (2017) *Technical Report.* [online] available from <https://www.gov.uk/government/uploads/system/uploads/attachment_data/file/632916/air-quality-plan-technical-report.pdf> [29 August 2017].

Dorrell, D., Parsa, L. and Boldea, I. (2014) 'Automotive electric motors, generators and actuator drive systems with reduced or no permanent magnets and innovative design concepts'. *IEEE Transactions on Industrial Electronics* 61(10), 5693-5695.

Drive eO (2016) *Drive eO Pikes Peak*. [online] available from <https://driveeo.com/pikes-peak/pp03/> [29 August 2017].

Durbin, P. (1995) 'Separated flow computations with the k-epsilon-v-squared model'. *AIAA Journal*, 33(4), 659-664.

Durbin, P. (1996) 'On the k-3 stagnation point anomaly'. *International Journal of Heat and Fluid Flow*, 17(1), 89-90.

Eclipse Magnetics (2014) *NdFeB Magnets / Neodymium Iron Boron Magnets Datasheet.* [online] available from

<http://www.eclipsemagnetics.com/media/wysiwyg/datasheets/magnet_materials_and_assemblies/ndfeb_neodymium_iron_boron-standard_ndfeb_range_datasheet_rev1.pdf> [29 August 2017].

Eclipse Magnetics (2014) *Rare Earth Neodymium NdFeB.* [online] available from <http://www.eclipsemagnetics.com/media/wysiwyg/datasheets/magnet_materials_and_assemblies/ndfeb_neodymium_iron_boron-standard_ndfeb_range_datasheet_rev1.pdf> [29 August 2017].

Elena, L. and Schiestel, R. (1996) 'Turbulence modeling of rotating confined flows'. *International Journal of Heat and Fluid Flow*, 17(3), 283-289.

Energy Efficiency Center (n.d.) *Efficient Fan Blades*. Oregon: Oregon State University.

Energy, Mines and Resources Canada (n.d.) *Energy Management Series 13: Fan and Pumps.* Ottawa: Business and Government Energy.

Erik, N., Sebastian, T., Alan, W., Peethamparam, A., and Michael, L. (2005) *Lumped Circuit Thermal Model of an Axial Flux Motor.* s.l.: s.n. [online] available from <https://www.researchgate.net/publication/268029676_Lumped_Circuit_Thermal_Model_of_an_Axial_Flux_Motor> [14 Febuary 2017].

European Commission (2016) *Reducing Emissions from Transport.* [online] available from <http://eur-lex.europa.eu/legal-content/en/TXT/?uri=CELEX:52016DC0501> [29 August 2017].

Fakhfakh, M., Kasem, M., Tounsi, S. and Neji, R. (2008) 'Thermal analysis of a permanent magnet synchronous motor for electric vehicles'. *Journal of Asian Electric Vehicles*, 6(2), 1145-1151.

Fawzal, A. S., Cirstea, R., Gyftakis, K., Woolmer, T. J., Dickison, M., & Blundell, M. (2016) The Fan Design Impact on the Rotor Cooling of Axial Flux

Permanent Magnet Machines. *2016 XXII International Conference on Electrical Machines (ICEM),* Lausanne, Switzerland, s.n., 2725-2731.

Fawzal, A. S., Cirstea, R., Gyftakis, K., Woolmer, T. J., Dickison, M., & Blundell, M. (2017) 'Fan performance analysis for rotor cooling of axial flux permanent magnet machines'. *IEEE Trans. Ind. Appl.,* 53(4), 3295-3304.

Fawzal, A. S., Cirstea, R., Woolmer, T. J., Dickison, M., Blundell, M., & Gyftakis, K. (2018) 'Air Inlet/Outlet Arrangement for Rotor Cooling Application of Axial Flux PM Machines'. *Applied Thermal Engineering,* 130, 1520-1529.

Ferreira, A. and Costa, A. (2012) Thermal Analysis of an Axial Flux Permanent Magnet Machine. *2012 XXth International Conference on Electrical Machines (ICEM),* Marseille, France, 2-5 Sept. 2012, s.n., 1482-1487.

Fitzgerald, A., Kingsley Jr, C. and Umans, S. (2003). *Electric Machinery*. 6th edn. New York: McGraw-Hill.

Frei, W. (2013) *Which Turbulence Model Should I Choose for My CFD Application? [*online] available from <http://www.comsol.com/blogs/which-turbulence-model-should-choose-cfd-application/> [20 July 2015].

Fu-An, L., Wang, X., Da-Tong, Q. and Jian-Cheng, C. (2011) "Study Of The Tonal Casing Noise Of A Centrifugal Fan At The Blade Passing Frequency". *Journal Of Low Frequency Noise, Vibration And Active Control, 30* (2), 89-105

GE Global Research (n.d.) *GE Scientists Successfully Test World-Class Traction Motor For Hybrid and Electric Vehicles.* [online] available from <http://www.geglobalresearch.com/news/press-releases/ge-scientists-successfully-test-world-class-traction-motor-for-hybrid-and-electric-vehicles> [30 July 2015].

GE Power Conversion (n.d.) *MV and HV Cage Induction Motors.* [online] available from <http://www.gepowerconversion.com/product-solutions/induction-motors/mv-hv-cage-induction-motors> [20 July 2015].

GE Trasportation (n.d.) *AC Drilling Motor Water Jacket (5GEB1150W)*. [online] available from <http://www.getransportation.com/drilling/water-cooled-motors> [20 July 2015].

Gieras, J. (2008) *Advancements of Electric Machines.* Bydgoszcz, Poland: Springer.

Gieras, J. F., Wang, R.J. and Kamper, M. (2008) *Axial Flux Permanent Magnet Brushless Machines.* s.l.:Springer.

Giulii Capponi, F., De Donato, G., Rivellini, G. and Caricchi, F. (2012) Fractional-slot Concentrated-winding Axial-flux Permanent-magnet Machine with Tooth-wound Coils. *2012 XXth International Conference on Electrical Machines (ICEM).* Marseille, France, 2-5 Sept. 2012, s.n.

Gölcü, M., Pancar, Y. and Sekmen, Y. (2006) "Energy Saving In A Deep Well Pump With Splitter Blade". *Energy Conversion And Management, 47* (5), 638-651

Gregorcic, G., Oberlechner, F. and Drage, P. (2017) Modeling and Control of Thermal Cycles in Vehicle Clectrification. *25th Mediterranean Conference on Control and Automation (MED).* Valletta, Malta, IEEE.

Gregory, N., Stuart, J. and Walker, W. (1955) 'On the Stability of Three-Dimensional Boundary Layers with Application to the Flow Due to a Rotating Disk'. *Philosophical Transactions of the Royal Society A: Mathematical, Physical and Engineering Sciences*, 248(943), 155-199.

Gyftakis, K. N. et al. (2016) 'Dielectric Characteristics of Electric Vehicle Traction Motor Winding Insulation under Thermal Ageing'. *IEEE Transactions on Industry Applications,* 1398-1404.

Herbst, J., Hahne, J., Jordan, H., Liu, H., Gattozzi, A., and Wu, B. (2009) Challenges in the Design of a 100 kW Induction Motor for a PHEV Application. *IEEE Conference Vehicle Power and Propulsion.* Miami, USA, IEEE.

Hey, J., Howey, D., Martinez-Botas, R. and Lamperth, M. (2010) 'Transient Thermal Modeling of an Axial Flux Permanent Magnet (AFPM) Machine Using a Hybrid Thermal Model'. *International Journal of Mechanical and Materials Engineering,* 4(11), 150-159.

Howey, D. (2010) *Thermal Design of Air-cooled Axial Flux Permanent Magnet Machines.* Unpublished PhD thesis. London: Imperial College London.

Howey, D., Childs, P. and Holmes, A. (2012) 'Air gap convection in rotating electrical machines'. *IEEE Transactions on Industrial Electronics,* 59(3), 1367-1375.

Howey, D., Holmes, A. and Pullen, K. (2011) 'Measurement and CFD prediction of heat transfer in air-cooled disc-type electrical machines'. *IEEE Transactions on Industry Applications*, 47(4), 1716-1723.

Hughes, A. (2006) *Electric Motors and Drives Fundamentals, Types and Applications.* Oxford, UK: Newnes.

Hughes, W. F. and Brighton, J. A. (1999) *Fluid Dynamics*. 3rd edn. USA: McGraw-Hill Companies, Inc..

IHS ESDU (2010) ESDU 07004: *Flow in Rotating Components - Discs, Cylinders and Cavities.* [online] available from <https://www.esdu.com/cgi-bin/ps.pl?sess=unlicensed_1180119101928bhxandt=docandp=esdu_07004a > [19 December 2017].

Jin, H. (2017) "Numerical And Experimental Research On Aerodynamic Noise Characteristics Of A Multi-Blade Centrifugal Fan". *Destech Transactions On Engineering And Technology Research (ICIA)*

KA Sensors (2015) *Infra-Red Sensors.* [online] available from <http://www.kasensors.com/sites/default/files/downloads/KIR4_Infra-Red_Temperature_Sensor_Datasheet_KIR4_0116.pdf> [29 August 2017].

Kahourzade, S., Mahmoudi, A., Hew, W. P. and Uddin, M. N. (2014) 'A comprehensive review of axial-flux permanent-magnet machines'. *Canadian Journal of Electrical and Computer Engineering,* 37(1), 19-33.

Kim, M., Lee, K. and Um, S. (2009) 'Numerical. Investigation and Optimization of the Thermal. Performance of a Brushless DC Motor'. *International Journal of Heat and Mass Transfer,* 52, 1589-1599.

Koenigsegg (2017) *The Regera - a New Era.* [online] available from <http://koenigsegg.com/regera/> [29 August 2017].

Langtry, R. B. (2006) *A Correlation-Based Transition Model Using Local Variables for Unstructured Parallelized CFD Codes.* Unpublished PhD thesis. Stuttgart: University of Stuttgart.

Langtry, R. B., Sengupta, K., Yeh, D. T. and Dorgan, A. J. (2015) Extending the Local γ-Re_(θ_T) Correlation based Transition Model for Crossflow Effects. *AIAA Fluid Dynamics Conference 2015.* Dallas, TX, USA., s.n.

Li, H. (2010) 'Cooling of a permanent magnet electric motor with a centrifugal impeller'. *International Journal of Heat and Mass Transfer*, Vol. 53, 797-810.

Li, Z., Fu, D., Guo, J., Gu, G., and Xiong, B. (2009) Study on Spraying Evaporative Cooling Technology for the Large Electrical Machine. *International Conference on Electrical Machines and Systems (ICEMS).* Tokyo, Japan.

Lien, F., Kalitzin, G. and Durbin, P. (1998) RANS Modeling for Compressible and Transitional Flows. *Center for Turbulence Research - Proceedings of the Summer Program*, s.l., s.n., 267-286.

Lim, C., Airoldi, G., Bumby, J., Dominy, R., and Ingrama, G. (2010) 'Experimental and CFD investigation of a lumped parameter thermal model of a single-sided, slotted axial flux generator'. *International Journal of Thermal Sciences*, 49(9), 1732-1741.

Lim, C., Airoldi, G., Dominy, R. and Mahkamov, K. (2011) 'Experimental validation of CFD modelling for heat transfer coefficient predictions in axial flux permanent magnet generators'. *International Journal of Thermal Sciences,* 50(12), 2451-2463.

Lim, C., Bumby, J., Dominy, R., Ingram, G., Mahkamov, K., Brown, N., et al. (2008) 2-d Lumped-Parameter Thermal Modelling of Axial Flux Permanent Magnet Generator. *18th International Conference on Electrical Machines, 2008, ICEM 2008.* Vilamoura, Portugal, 6-9 Sept. 2008.

Liu, H. (2010) "Effects Of Blade Number On Characteristics Of Centrifugal Pumps". *Chinese Journal Of Mechanical Engineering, 23* (06), 742

Liwei, S., Zijian, L., Jingyi, G., Qingchu, Z., and Fuping, W. (2008) Thermal Effect on Water Cooling Induction Motor's Performance used for HEV. *IEEE Vehicle Power and Propulsion Conference.* Harbin, China, 3-5 Sept. 2008, s.n.

Mahmoudi, A. et al. (2013) 'Design and prototyping of an optimised axial-flux permanent-magnet synchronous machine'. *IET Electr. Power Appl*., 7(5), 338-349.

Malan, P., Suluksna, K. and Juntasaro, E. (2009) Calibrating the Gamma-ReTheta Transition Model for Commercial CFD. *47th AIAA Aerospace Sciences Meeting.*

Marignetti, F., Colli, V. D. and Coia, Y. (2008) 'Design of Axial Flux PM Synchronous Machines Through 3-D Coupled Electromagnetic Thermal and Fluid-Dynamical Finite-Element Analysis'. *IEEE Transactions on Industrial Electronics,* 55(10), 3591-3601.

Martin, R. (2007) *Axial Flux Permanent Magnet Machines for Direct Drive Applications.* Unpublished PhD Thesis. Durham: Durham University.

Mayoux, C. (2000) 'Degradation of insulation materials under electrical stress'. *IEEE Transactions on Dielectrics and Electrical Insulation*, 7(5), 590-601.

McKinsey and Company (2014) *Electric vehicles in Europe: Gearing up for a New Phase?* [online] available from <http://www.mckinsey.com/netherlands/our-insights/electric-vehicles-in-europe-gearing-up-for-a-new-phase> [29 August 2017].

Mellor, P., Roberts, D. and Turner, D. (1991) 'Lumped parameter thermal model for electrical machines of TEFC design'. *IEEE Proceedings B - Electric Power Applications,* 138(5), 205-218.

Menter, F. R. (1993) 'Zonal Two Equation k-ω Turbulence Models for Aerodynamic Flows'. AIAA Paper 93-2906.

Menter, F. R., Langtry, R. B., Likki, S. R., Suzen, Y. B., Huang, P. G., and Volker, S. (2004) A Correlation-Based Transition Model Using Local Variables Part 1 --- Model Formulation. *Proc. ASME Turbo Expo.* Vienna, Austria.

Milnes, J., Drikakis, D., Malick, Z. and Shapiro, E. (2008) Advanced CFD Strategies for HyperVapotron Flows and Heat Transfer. *Proceedings for the IMechE Seminar, Computational Fluid Dynamics Validation – How much is enough?* London, UK.

Moosavi, S., Djerdir, A., Amirat, Y. and Khaburi, D. (2015) 'Demagnetization fault diagnosis in permanent magnet synchronous motors: A review of the state-of-the-art'. *Journal of Magnetism and Magnetic Material*, 391, 203-212.

NASA (2008) Uncertainty and Error in CFD Simulations. [online] available from <http://www.grc.nasa.gov/WWW/wind/valid/tutorial/errors.html> [20 July 2015].

Neudorfer, H., Wicker, N. and Binder, A. (2017) Comparison of Three Different Electric Powertrains for the use in Hybrid Electric Vehicles. *Power Electronics, Machines and Drives, 2008. PEMD 2008. 4th IET Conference.* York, UK, IET.

Omer, A. (2008) 'Energy, environment and sustainable development'. *Renewable and Sustainable Energy Reviews*, 12, 2265-2300.

Parag Fan and Cooling System Ltd. (n.d.) *Fan Noise and Vibration* [online] available from <http://paragfans.com/wp-content/uploads/2016/05/fan_noise__vibration.pdf> [17 July 2018]

Patil, P. and Todkar, R. (2013) "An Overview Of Effect Of Splitter Blades On Centrifugal Pump Performance". *International Journal Of Engineering Research and Technology (IJERT)* 2 (11), 2249-2252

Parviainen, A. (2005) *Design of Axial-Flux Permanent-Magnet Low-Speed Machines and Performance Comparison Between Radial-Flux and Axial-Flux Machines.* Unpublished PhD Thesis. Lappeenranta, Finland: Lappeenranta University of Technology.

Parviainen, A., Niemelä, M. and Pyrhönen, J. (2004a) 'Modeling Axial-flux Permanent-Magnet Machines'. *IEEE Transaction on Industry Applications*, 1333-1340.

Parviainen, A., Niemelä, M. and Pyrhönen, J. (2004b) Modeling Axial-flux PM Machines: Thermal Analysis. *In Proceedings of International Conference on Electrical Machines ICEM'04.* Cracow, Poland, 5-8 September 2004.

Peric, M. and Ferguson, S. (2005) *The Advantage Of Polyhedral Meshes* [online] Technical report. CD Adapco Group. available from <http://www.cd-adapco.com/news/24/TetsvPoly.htm> [8 July 2018]

Poncet, S., Chauve, M. and Schiestel, R. (2005) 'Batchelor versus Stewartson flow structures in a rotor-stator cavity with throughflow'. *American Institute of Physics, Physics of Fluids*, 17(7).

POSiFA (2017) PMF4000 Series. [online] available from <http://www.posifamicrosystems.com/pdf/2013-59-00-09-22__PMF4000-Data-Sheet---FINAL-v4.pdf> [29 August 2017].

Pyrhonen, J., Jokinen, T. and Hrabovcova, V. (2008) *Design of Rotating Electrical.* 1st edn. Chichester: John Wiley and Sons, Ltd..

Ransau, S. (2011) *Numerical Methods in Marine Hydrodynamics*. Unpublished lecture notes. Norwegian University of Science and Technology.

Rasekh, A., Sergeant P. and Vierendeels. J. (2015) 'Convective heat transfer prediction in disk-type electrical machines'. *Applied Thermal Engineering*, 91, 778-790.

Rasekh, A., Sergeant P. and Vierendeels. J. (2017) 'Fully predictive heat transfer coefficient modeling of an axial flux permanent magnet synchronous machine with geometrical parameters of the magnets'. Applied Thermal Engineering, Volume 110, 1343-1357.

Roache, P. J. (1998) *Verification and Validation in Computational Science and Engineering.* Albuquerque, N.M.: Hermosa Publishers.

Rostami, N. et al. (2013) 'Lumped-Parameter Thermal Model For Axial Flux Permanent Magnet Machines'. *IEEE Transactions On Magnetics*, 49(3), 1178-1184.

Roy, C. J. (2003) 'Grid Convergence Error Analysis for Mixed-Order Numerical Schemes'. *AIAA Journal*, 41(4), 595-604.

Ruoho, S., Kolehmainen, J., Ikaheimo, J. and Arkkio, A. (2010) 'Interdependence of Demagnetization, Loading, and Temperature Rise in a Permanent-Magnet Synchronous Motor'. *IEEE Transactions on Magnetics*, 46(3), 949-953.

Sahin, F. (2001a) *Design and Development of a High-speed Axial-flux Permanent-magnet Machine*. Unpublished PhD Thesis. Eindhoven: Technische Universiteit Eindhoven.

Sahin, F., Tuckey, A. and Vandenput, A. (2001b) Design, Development and Testing of a High-speed Axial-flux Permanent-magnet Machine. *Industry Applications Conference, 2001. Thirty-Sixth IAS Annual Meeting.* Chicago, IL, USA, 1640-1647.

Sahin, F. and Vandenput, A. (2003) 'Thermal modeling and testing of a high-speed axial-flux permanent-magnet machine'. *COMPEL: Int. J. Comput. Math. Elect. Elect. Eng.*, 22(4), 982-997.

Sarlioglu, B., Morris, C. T., Han, D. and Li, S. (2015) Benchmarking of Electric and Hybrid Vehicle Machines, Power Electronics and Batteries. *Intl Aegean Conference on Electrical Machines & Power Electronics (ACEMP),* Side, Turkey, IEEE.

Schouveiler, L., Gal, P. and Cauve, M. (2001) 'Instabilities of flow between a rotating and a stationary disk'. *Journal of Fluid Mech,* 443, 329-350.

Scowby, S., Dobson, R. and Kamper, M. (2004) 'Thermal modelling of an axial flux permanent magnet machine'. *Applied Thermal Engineering,* 20(2), 193-207.

Sergeant, P., Vansompel, H. and Dupre, L. (2014) Performance and Implementation Issues Considering the use of Thin Laminated Steel Sheets in Segmented Armature Axial-flux PM Machines. *International Conference on Electrical Machine (ICEM),* Berlin, Germany, s.n., 1363-1369.

Shazly, J., Wahsh, S. and Yassin, A. (2014) 'Thermal Analysis of Axial Flux Permanent Magnet Synchronous Motor using 3D Finite Elements'. *International Journal of Thermal Technologies*, 4(4).

Shih, T.-H., Liou, W., Shabbir, A., Yang, Z., and Zhu, J (1994) 'A New k-Eddy Viscosity Model for High Reynolds Number Turbulent Flows'. *NASA TM* 106721.

Siemens PLM Software (2017) *The Steve Portal. Spotlight On... Parallel Performance* [online] <Available from https://thesteveportal.plm.automation.siemens.com/articles/en_US/FAQ/Spotlight-on-Parallel-Performance> [29 August 2017].

Simons, R. (1996) 'Direct liquid immersion cooling for higher power density microelectronics'. *Electronic Cooling,* 2, 24-29.

Sivasubramanian, K., Laskaris, E., Lokhandwalla, M., Zhang, T., Bray, J., Gerstler, B., et al. (2008) Development of High Speed Multi-megawatt HTS Generator for Airborne Application Power and Energy Society General Meeting-conversion and Delivery of Electrical Energy in the 21st century. Pittsburgh,PA, s.n.

Sook, T. and McCulloch, M. (2014) 'Optimal Design Method for Large Scale YASA Machines'. *IEEE Transactions on Energy Conversion*, (99), 1-8.

Spooner, E. and Chalmers, B. (1992) 'TORUS: A slotless, toroidal-stator permanent-magnet generator'. *IEEE Proceedings B - Electric Power Applications,* 139(6), 497-506.

STAR-CCM+ (2016) STAR-CCM+ v11.04.010 Tutorial Guide. s.l.:s.n.

STAR-CCM+ (2016) STAR-CCM+ v11.04.010 User Guide. s.l.:s.n.

Sugimoto, H., Morishita, T., Tsuda, T., Takeda, T., Togawa, H., Oota, T., et al. (2008) Development and Test of an Axial Flux Type PM Synchronous Motor with Liquid Nitrogen Cooled HTS Armature Windings. s.l., *8th European Conference on Applied Superconductivity EUCAS 2007.*

Sumislawska, M., Gyftakis, K. N., Kavanagh, D. F., McCulloch, M. D., Burnham, K. J., and Howey, D. A. (2016) 'The impact of thermal degradation on properties of electrical machine winding insulation material'. *IEEE Transaction on Industry Applications,* 2951-2960.

Tong, W. (2014) *Mechanical Design of Electric Motors*. Abingdon, UK: CRC Press Taylor and Francis Group.

Tu, J., Yeoh, G. H. and Liu, C. (2008) Computational Fluid Dynamics: A Practical Approach. Oxford, UK: Butterworth-Heinemann.

Twin City Fan Companies Ltd. (2000) *Fan Engineering: Fan Performance Characteristics*, Minneapolis: Twin City Fan and Blower.

US Department of Energy (US DOE) (1989) *Improving Fan System Performance – a Sourcebook for Industry.* s.l.: Energy Efficiency and Renewable Energy.

Vainel, G., Staton, D., Giulii Capponi, F., De Donato, G., and Caricchi, F. (2013) Thermal Modelling of a Fractional-Slot Concentrated-Winding Kaman Type Axial-Flux Permanent-Magnet Machine. *2013 IEEE Energy Conversion Congress and Exposition.* Denver, CO, USA, 15-19 Sept. 2013,

Vansompel, H. (2010) *Design of an Energy Efficient Axial Flux Permanent Magnet Machine.* Unpublished PhD Thesis. Ghent: Ghent University.

Vansompel, H., Hemeida, A. and Sergeant, P. (2017) Stator Heat Extraction System for Axial Flux Yokeless and Segmented Armature Machines. *IEEE International Electric Machines and Drives Conference (IEMDC),* Miami, FL, USA, 21-24 May 2017.

Vergteeg, H. and Malalasakera, W. (1995) *An Introduction to Computational Fluid Dynamics The Finite Volume Method.* England: Longman Scientific and Technical, Longman Group Ltd.

Vilar, Z., Patterson, D. and Dougal, R. (2005) Thermal Analysis of a Single Sided Axial Flux Permanent Magnet Motor. *31st Annual Conference of IEEE Industrial Electronics Society, 2005. IECON 2005.* Raleigh, NC, USA, 6-10 Nov. 2005, s.n.

Wahsh, S., Shazly, J. and Yassin, A. (2016) Steady State Heat Conduction Problems of AFPMSM Using 3D Finite Element. *2016 Eighteenth International Middle East Power Systems Conference (MEPCON).* Cairo, Egypt, 27-29 Dec. 2016, s.n.

Wallis, L., Leonardi, E., Milton, B. and Joseph, P. (2002) 'Air Flow and Heat Transfer in Ventilated Disc Brake Rotors with Diamond and Tear-Drop Pillars'. *Numerical Heat Transfer, Part A: Applications*, 41(6-7), pp. 643-655.

Wang, C., Qu, R., Li, J., Fan, X., Li, D., and Lu, Y. (2017) Rotor Loss Calculation and Thermal Analysis of a Dual-Stator Axial-Flux Permanent Magnet Machine with Combined Rectangle Shaped Magnets. *International Conference on Electrical Machines and Systems (ICEMS).* Sydney, NSW, Australia, 11-14 Aug. 2017, s.n.

Wang, R., Kampar, M. and Dobson, R. (2005) 'Development of a thermofluid model for Axial field permanent-magnet Machines'. *IEEE Transactions on Energy Conversion,* 20(1), 80-87.

Wildi, T. (2006) *Electrical Machines, Drives and Power Systems*. Estados Unidos: Pearson Education.

Woolmer, T. (2009) *The Yokeless and Segmented Armature Machine Developed for the LIFECar.* Unpublished PhD thesis. Oxford: University of Oxford.

Woolmer, T. and McCulloch, M. (2006) Axial Flux Permanent Magnet Machines: A New Topology For High Performance Applications. *Hybrid Vehicle Conference.* IET the Institution of Engineering and Technology.Coventry,

Woolmer, T. and McCulloch, M. (2007) Analysis of the Yokeless And Segmented Armature Machine. IEEE International *Electric Machines & Drives Conference*, Antalya, Turkey,

Xia, C. (2002) Spray/Jet Cooling For Heat Flux High To 1KW/cm2. *Eighteenth Annual IEEE Symposium Semiconductor Thermal Measurement and Management*, CA, USA, 159-163 .

YASA Motor Ltd. (2017) The YASA P400 Series of Electric Motors. [online] available from <http://www.yasamotors.com/wp-

content/uploads/2015/09/YASA_P400_Product_Sheet.pdf> [29 August 2017].

YASA Motors Ltd. (2017) The YASA Product Range. [online] available from <http://www.yasamotors.com/products/> [29 August 2017].

Yuan, Z., Saniei, N. and Yan, X. (2003) 'Turbulent heat transfer on the stationary disk in a rotor-stator system'. *International Journal of Heat and Mass Transfer*, Vol. 46, 2207-2218.

Zhang, L. and Jin, Y. (2011) "Effect Of Blade Numbers On Aerodynamic Performance And Noise Of Small Axial Flow Fan". *Advanced Materials Research* 199-200, 796-800

Zhang, S., Xu, J., Junak, J., Fiederling, D., Sawczuk, G., Koch, M., et al. (2012) Permanent Magnet Technology for Electric Motors in Automotive Applications. *2012 2nd International Electric Drives Production Conference (EDPC),* Nuremberg, Germany, IEEE.

APPENDICES

Appendix A : Industrial Contributions

Timeline of YASA machine evolution for rotor cooling technique

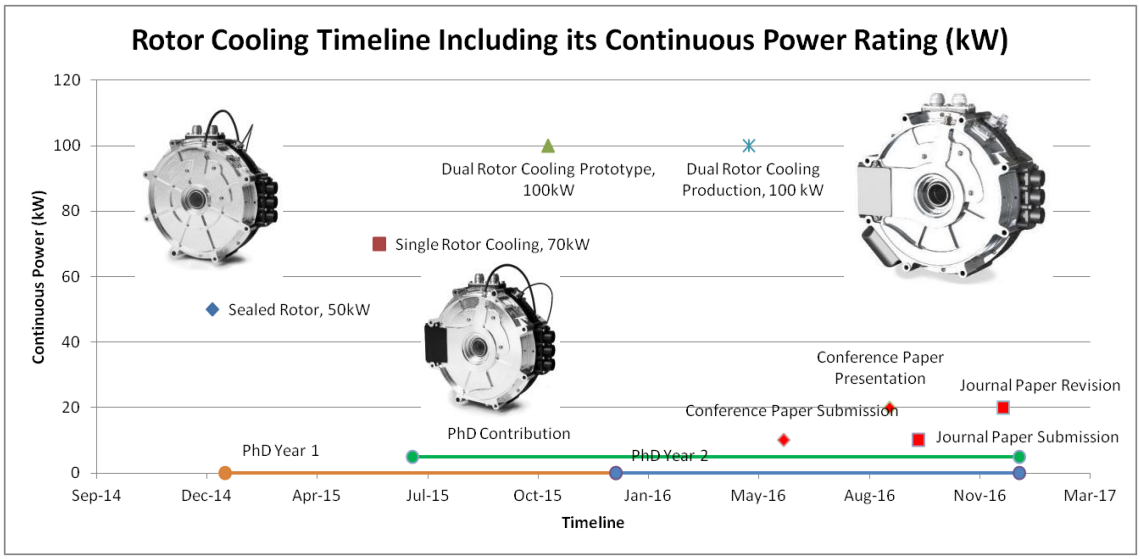

The findings has been accepted by the machine manufacturer (also the as the sponsored body of this PhD) to be used in their product. After a year of the PhD, the production of high performance YASA machine was on sales. The product is targeted for high-powered automotive manufacturer.

Since then, the rotor cooling technique has been gradually evolving to suit automotive car manufacturer the requirements.

Appendix B : Example of the MatLab code for plotting

```
clear all;
load FanPerfm.txt;
x1=FanPerfm(:,1);
y1=FanPerfm(:,2);
y2=FanPerfm(:,3);
y3=FanPerfm(:,4);
y4=FanPerfm(:,5);
y5=FanPerfm(:,6);
y6=FanPerfm(:,7);
y7=FanPerfm(:,8);
y8=FanPerfm(:,9);
y9=FanPerfm(:,10);

figure
plot (x1,y1,x1,y2,'--',x1,y3,'LineWidth',1.5);
ylim([0.002 0.018])
xlabel('RPM');
ylabel('Mass Flow Rate (kg/s)');
legend('Backward Curved','Radial','Pillar');

figure
plot (x1,y4,x1,y5,'--',x1,y6,'LineWidth',1.5);
ylim([0 90])
xlabel('RPM');
ylabel('Pressure Rise (Pa)');
legend('Backward Curved','Radial','Pillar');

figure
plot (x1,y7,x1,y8,'--',x1,y9,'LineWidth',1.5);
ylim([0 80])
xlabel('RPM');
ylabel('Windage Losses (W)');
legend('Backward Curved','Radial','Pillar');


figure
subplot(1,3,1)
plot (y1,y4,'LineWidth',1.5);
ylim([0 70])
xlabel('Mass Flow Rate (kg/s)');
ylabel('Pressure Rise (Pa)');
yyaxis right
plot (y1,y7,'--','LineWidth',1.5);
ylim([0 70])
ylabel('Windage Losses (W)');
grid on;
title('Backward Curved');
legend('Fan Curve','Windage Curve');

subplot(1,3,2)
plot (y1,y5,'LineWidth',1.5);
ylim([0 70])
xlabel('Mass Flow Rate (kg/s)');
ylabel('Pressure Rise (Pa)');
yyaxis right
plot (y1,y8,'--','LineWidth',1.5);
ylim([0 70])
ylabel('Windage Losses (W)');
grid on;
title('Radial');

subplot(1,3,3)
plot (y1,y6,'LineWidth',1.5);
ylim([0 70])
xlabel('Mass Flow Rate (kg/s)');
ylabel('Pressure Rise (Pa)');
yyaxis right
plot (y1,y9,'--','LineWidth',1.5);
ylim([0 70])
ylabel('Windage Losses (W)');
grid on;
title('Pillar');
```